Low-Dose STEM Characterisation of Nanoscale Calcium Carbonate Particles

Robert William Mitchell Hooley

Submitted in accordance with the requirements for the degree of Doctor of Philosophy

School of Chemical and Process Engineering

The University of Leeds

September 2019

The candidate confirms that the work submitted is his own, except where work which has formed part of jointly-authored publications has been included. The contribution of the candidate and the other authors to this work has been explicitly indicated overleaf. The candidate confirms that appropriate credit has been given within the thesis where reference has been made to the work of others.

Declaration

Publications

Chapter 4 contains data reproduced from a peer reviewed publication in the *Journal of Physics, Conference Series*

Hooley, R.W.M., Brown, A.P., Kulak, A.N., Meldrum, F.C., Brydson, R.M.D., 2017. A Quantitative Evaluation of Electron Beam Sensitivity in Calcite Nanoparticles. **Journal of Physics: Conference Series** *902*.

The experimental work and interpretation were carried out by the candidate, Alex Kulak and Fiona Meldrum assisted in the synthesis of the calcium carbonate particles. The candidate prepared the manuscript, with assistance in proofreading and editing from Rik Brydson and Andy Brown.

Chapter 5 is a reproduction of a peer reviewed publication in *Micron*

Hooley, R., Brown, A., Brydson, R., 2019. Factors affecting electron beam damage in calcite nanoparticles. **Micron** *120*, 25-34.

The experimental work and interpretation were carried out by the candidate. The candidate prepared the manuscript, with assistance in data interpretation, proofreading and editing from Rik Brydson and Andy Brown.

Funding

Funding for this research was provided through the EPSRC Centre for Doctoral Training in Complex Particulate Products and Processes (CP^3-CDT) through grant number EP/L015285/1 and acknowledges co-funding from Thermo-Fisher Scientific (formerly FEI Co). Funding for the FEI $Titan^3$ Themis microscope was provided through EPSRC grant EP/M028143/1.

Copyright

Abstract

This thesis forms a framework for the reliable identification and quantification by transmission electron microscopy (both conventional and scanning) of discrete particle crystallinity in nominally amorphous, nanoscale calcium carbonate particles used industrially as fuel detergents. The foundations of this framework are built on understanding and quantifying the progressive radiolytic damage of ~50 nm calcite nanoparticles. The degradation pathway of calcite involves disruption of the crystal lattice, the formation of pores, and the transformation from $CaCO_3$ to CaO and CO_2. The damage threshold for the loss of lattice integrity at 300 kV in CTEM was determined to be $2.7x10^7$ e^-nm^{-2}.

Microscope operating conditions were optimised to maximise the extracted analytical information, whilst minimising the extent of electron beam damage. It is shown that STEM offers significant benefits over CTEM, however only in the presence of hydrocarbon contamination, increasing the fluence threshold for the detection of irradiation-induced faults in the calcite lattice to over 1.8×10^8 e^-nm^{-2} for 300 kV STEM in wide-angle bright field operation.

These conditions were used to characterise and quantify the incidence of discrete crystallinity in nominally amorphous ~5 nm fuel detergent particles, which were found to crystallise following ~$3x10^7$ e^-nm^{-2} at 300 kV CTEM irradiation. Quantification of discrete crystallinity was achieved by automated imaging, and random sampling. This revealed a low incidence of inherent vaterite crystallinity of 1 in 5000 particles which was not detected using conventional laboratory based analytical techniques such as X-ray diffraction and Fourier Transform Infrared spectroscopy.

In addition, STEM imaging was used to observe the deliberate, solvent-induced destabilisation of the amorphous fuel detergent particles, demonstrating agglomeration, aggregation, and eventual crystallisation into vaterite over 28 days. This was again detected by STEM prior to conventional laboratory analytical techniques, making a compelling case for low-dose STEM imaging to be used as a form of process control for the synthesis of the fuel detergent particles.

Acknowledgements

My utmost thanks go to my supervisors, Rik Brydson and Andy Brown, this would not have been possible without your passion, patience and willingness to share your knowledge. You have both taught me so much, and helped me to develop, I hope to pass on your teachings and do you proud. I have thoroughly enjoyed working with you both and can't speak highly enough of my time with you.

My thanks are extended to all of the staff and students in the Leeds electron microscopy group and LEMAS centre, especially Nicole, John, Zabeada, Stu, and Mike for their wonderful support, patience, and motivation. To Fiona Meldrum and Alex Kulak, for the warm welcome into your group and the world of calcium carbonate.

I would also like to thank FEI/Thermo Fisher Scientific for funding and supporting this research, in particular: David Beamer, David Foord, and Sorin Lazar for their help in arranging the visit to the Eindhoven Nanoport, and Maarten Wirix for invaluable assistance in collecting the probe corrected STEM data and use of the mapping software.

A shout-out to: Abdul, Alex, Anu, Arturs, Beth, David, Dewi, Joe, Jonno, Lewis, Mo, Pete, and Richard for the good humour, discussions, distractions, tea runs, biscuits, beer clubs, and cheese days, and to Wei and Andre, for the lesson that no matter what the literature says, there's always the opportunity to look "deeper". It would be remiss of me to forget to thank Darlo for his enthusiasm, humour and the many trips down curry mile!

To the Saturday afternoon fuddle at Headingley Golf Club, cheers for the encouragement and jokes, playing with you all was a lovely distraction. By the way, this is where your money went…

Thoko, thank you so much for being a great friend and collaborator, without your help the last two chapters of this thesis would be a bit sparse. I hope we have the opportunity to work together again, it's been a pleasure.

To my family, thank you for your love throughout, it means so much to have your encouragement and support behind me.

My final thanks are to my partner Rhiannon, your love, support, and enthusiasm has meant the world to me, I'm glad we got to share our PhD journeys together.

"Where the telescope ends, the microscope begins. Which of the two has the grander view?"

Victor Hugo

Contents

Table of Figures

Chapter 1. Introduction

1.1. Background

Calcium carbonate is a widely studied material in both academia and industry, where it is commonly encountered in crystalline geological forms and as a structural biomineral in both crystalline and amorphous forms (1). In both cases calcium carbonate is rarely found chemically pure, often precipitating with biopolymers, proteins, or doping atoms incorporated. The influence of these additives on the crystallisation process, and the material properties, is of interest to academic and industrial researchers. There are many investigations into calcium carbonate ranging from its use as a model system in studies of polymorphism and non-classical crystallisation, to the design, production, and mechanical testing of biomimetic structures and composites.

An example of research into calcium carbonate in an industrial context is in the form of synthetic fuel detergents, consisting of 5-10 nm particles of amorphous calcium carbonate, sterically stabilised by a surfactant. These particles are used to neutralise acid build-up in combustion engines caused by sulfur and nitrogen containing contaminants in fuels (2). There is interest into the structure-property relationship in these particles, with small, monodisperse, amorphous particles being preferred by manufacturers as they are more effective in use and more stable in storage. These particles are amorphous to X-ray diffraction, but X-ray absorption spectroscopy measurements have suggested the presence of some crystallinity (3). It is however difficult to distinguish by these techniques between crystallinity present in discrete crystals and a small crystalline core being present in all particles. As a result, there is interest in using more sensitive techniques to address this in a more specific manner i.e. at the individual nanoparticle level.

This is an ideal application for electron microscopy, where high resolution analysis down to the atomic scale could provide complementary information to bulk analysis from conventional lab-based techniques. Transmission electron microscopy (TEM), both conventional and scanning, are popular and powerful analytical techniques in the physical and biological sciences, for the

characterisation of ceramics, semiconductors, metals, and biological structures, amongst others. TEM is regularly used to provide information on structure and appearance across multiple length scales and is routinely coupled with elemental spectroscopy for compositional insights. From its origins in the 1930s, conventional TEM (CTEM) has been a common technique for materials analysis, and when high resolution scanning TEM (STEM) was introduced in the 1960s, it heralded a new era in spatially resolved analysis and chemical imaging (4, 5).

Whilst TEM can be used routinely for the structural and chemical analysis of many materials, some materials, including calcium carbonate can be altered by the electron irradiation, changing composition, bonding, appearance, or structure. In some cases, all of these properties are changed. This is due to electron beam damage, a complex problem arising from a combination of competing mechanisms, some of which cannot be completely eliminated. The electron beam is known to break bonds, induce crystallisation in amorphous specimens (and vice versa), remove material via sputtering, melt specimens, and coat specimens in hydrocarbon contaminants (6). Ultimately this results in images, compositions, and structures which are not representative of the pristine state. Despite the impact this can have on the accuracy and reliability of measured analytical information, it is often overlooked or under-appreciated by electron microscopists (7).

Previous studies of the fuel detergent particles have employed TEM imaging, diffraction and spectroscopy (3, 8, 9). However, these studies did not adequately consider the impact of electron irradiation-induced changes, and as such the accuracy and reliability of the measurements may be compromised. In order to study these particles with confidence, it is necessary to work under conditions where the influence of electron beam damage is minimised.

1.2. Research Aims and Objectives

The aim of this thesis is to apply high resolution TEM characterisation to the study of calcium carbonate-based materials. There is significant interest in the

nanoscale behaviour of calcium carbonate, especially in the interaction between calcium carbonate and additives. TEM would be a powerful technique to investigate this, provided that the influence of radiation damage is known and accounted for, and that the operation of the microscope can be optimised to extract the maximum amount of useable analytical information with minimal electron beam damage.

To achieve this aim, it is necessary to first understand some of the literature surrounding calcium carbonate and to summarise the appropriate underlying theories on radiation damage: how it operates, how it can be observed or quantified, and how it can be minimised. This is presented in the following literature review.

The specific objectives required to achieve the aims of this thesis are described in detail at the end of the literature review in section 2.5, but are briefly summarised below.

1) Produce and characterise a calcium carbonate-based model system to observe the progression of radiation damage and ascertain thresholds for electron beam damage under CTEM and STEM.
2) Compare the electron beam damage behaviour of the crystalline and amorphous calcium carbonate polymorphs, to determine whether polymorphism has an impact on electron beam sensitivity.
3) Determine the optimal microscope operating conditions for high resolution imaging or spectroscopy in calcium carbonate nanoparticles.
4) Compare TEM characterisation of a fuel detergent specimen to conventional analysis, investigate the presence of crystallinity in the fuel detergent specimens, and its potential origins.

1.3. Key Methods and Experimental Approach

The techniques employed in this thesis are described in detail in Chapter 3 and Chapter 4. A brief summary is presented to highlight the key techniques and some reasons for using them.

The key experimental technique in this thesis was transmission electron microscopy, which was used because it offers high resolution characterisation of a wide range of materials using imaging, diffraction and spectroscopy. Transmission electron microscopy was used to investigate the electron beam damage processes operating in calcite nanoparticles, this was done by collecting time-resolved bright field images, diffraction patterns, EDX spectra and phase contrast images at specific fluences.

The operating conditions of the microscope were optimised by comparing the measured damage thresholds at different accelerating voltages, in different illumination modes (CTEM compared to STEM) and with a thermally cleaned specimen compared to a contaminated specimen.

Annular Dark Field (ADF) and Wide-Angle Bright Field (WABF) STEM imaging were found to be fluence-efficient techniques for high resolution imaging of the fuel detergent specimen. ADF and WABF images provided useful complementary information on particle size and morphology (ADF), and crystallinity (WABF) at low incident fluences.

The approach taken to characterise the damage thresholds in all specimens included:

- Time-resolved phase contrast lattice imaging to provide a direct observation of the electron beam-induced degradation of the crystal lattice.
- Time-resolved EDX spectroscopy was used to investigate the loss of oxygen through the formation and release of carbon dioxide as a function of irradiation and accelerating voltage.

To characterise the fuel detergents, the approach taken used simultaneous WABF and ADF STEM imaging under low fluence conditions. The information acquired by STEM imaging was compared to conventional laboratory analytical techniques including FTIR, XRD and DLS, and synchrotron X-ray absorption spectroscopy measurements.

1.4. Thesis Outline

This thesis consists of 9 chapters. This introduction chapter is followed by a literature review in Chapter 2, which summarises some of the research undertaken in calcium carbonate, fuel detergents, electron beam damage, and low-dose STEM/CTEM. Chapter 3 contains the theoretical background to the experimental techniques used in this research, and Chapter 4 contains the experimental methods and material synthesis conditions used. Chapter 5 presents the synthesis, characterisation and electron beam damage of calcite nanoparticles. Chapter 6 demonstrates the optimisation of microscope operating conditions, including accelerating voltage, specimen cleanliness and illumination mode in order to maximise the electron beam damage threshold. The synthesis and characterisation of fuel detergent particles is detailed in Chapter 7, where the identification and quantification of discrete crystallinity is presented. Chapter 8 demonstrates the solvent-induced degradation of the fuel detergents by time-resolved bulk spectroscopy, STEM imaging, and electron diffraction. The results from chapters 5-8 are summarised in Chapter 9, and future research opportunities are discussed. The references and appendix follow.

Chapter 2. Literature Review

There is significant interest in accurate and reliable high spatial resolution analysis of calcium carbonate, through the application of low-dose electron microscopy. As such it is necessary to review some of the literature surrounding the fields of calcium carbonate, radiation damage, and low-dose electron microscopy.

2.1. Calcium Carbonate

2.1.1. Overview

Calcium carbonate ($CaCO_3$) is of widespread interest as a structural biomaterial and for its environmental and industrial importance. It is an important model system for fundamental studies of nucleation, growth and polymorphism in inorganic crystals (10). It is found in three anhydrous crystalline polymorphs, amorphous forms, and crystalline hydrated forms are also possible.

Polymorphism is the phenomenon in which a solid material can produce multiple crystal structures. For a material to be polymorphic, it must produce multiple crystal structures with no change in composition. Calcium carbonate is well known to exhibit polymorphism, with three anhydrous polymorphs commonly encountered (calcite, aragonite, and vaterite). Different polymorphs can be formed by varying the crystallisation conditions, including but not limited to: rate, supersaturation, solvent, temperature and impurity content.

Calcite is the most abundant naturally occurring form of calcium carbonate, it is commonly encountered geologically and biologically. Aragonite is a metastable polymorph of calcium carbonate which is found extensively in geological and biological forms, it is more thermodynamically stable than vaterite, but less stable than calcite. Vaterite is the least thermodynamically stable anhydrous crystalline polymorph of calcium carbonate, and also the least well understood in terms of crystal structure (11). Vaterite is not commonly encountered geologically but is an abundant biomineral.

In addition to the three anhydrous crystalline polymorphs, two hydrated forms of calcium carbonate are known, Monohydrocalcite ($CaCO_3.H_2O$) and Ikaite ($CaCO_3.6H_2O$). Amorphous calcium carbonate is commonly encountered in biomaterials, however due to its low thermodynamic stability it is not encountered geologically.

Calcium carbonate is used industrially in complex multicomponent mixtures, examples include: as a polymer filler to improve mechanical properties (12), as a paint filler to reduce costs and for rheological properties (13), in pharmaceuticals as an active ingredient in oral dose formulations (14), as a key component in the production of Portland cement (15, 16), and also in amorphous form as fuel detergents in combustion engines (2).

Biologically, calcium carbonate is often found in structural composites, typically embedded in a biological polymer matrix, an example of this being iridescent nacre in mollusc shells (17). The biological formation of calcium carbonate is of significant research interest, especially around the behaviour of calcium carbonate with biological polymers and additives during crystallisation, and how they affect the crystal structure and habit formed (18-20). The structural composites formed from calcium carbonate and bio-polymers are of interest for their high strength and other mechanical properties such as toughness (21).

2.1.2. Thermodynamics

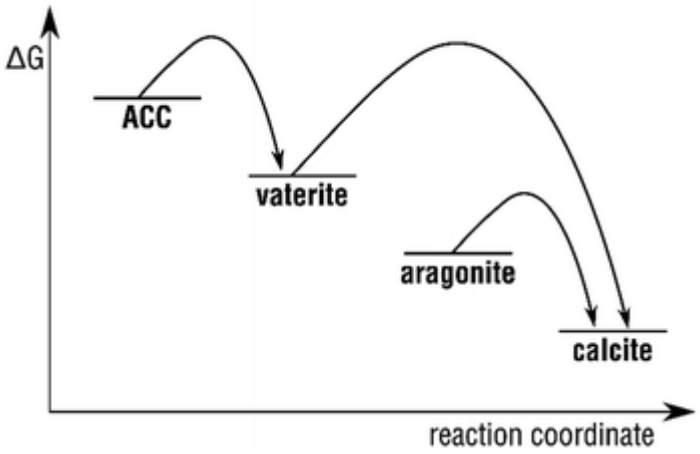

Figure 2.1 Schematic representation of the relative energetic stabilities of calcium carbonate polymorphs, the black arrows indicate observed solid state phase transitions (modified from (22)).

Calcite is the most thermodynamically stable polymorph of calcium carbonate, being widely encountered in biological and geological forms. Aragonite is a metastable phase of calcium carbonate, however it is only marginally less stable than calcite, meaning that it is stable enough to exist in geological form, though it can undergo solid-state transformations into calcite (23). Vaterite is the least thermodynamically stable crystalline form of calcium carbonate, readily transforming directly to calcite, bypassing aragonite (22). Amorphous calcium carbonate (ACC) is an unstable form of calcium carbonate commonly encountered biologically where it is used as a precursor to vaterite crystallisation, it is often found in a hydrated state (24). ACC will readily transform to vaterite, which can inherit a share of disorder in the carbonate arrangements found in the amorphous state (25).

2.1.3. Calcite

Calcite has a hexagonal unit cell, with a trigonal space group. The unit cell parameters are a=b=4.99 Å, c=17.06 Å and $\alpha=\beta=90^{o}$, $\gamma=120^{o}$. This is shown in the simulated unit cell in Figure 2.2.

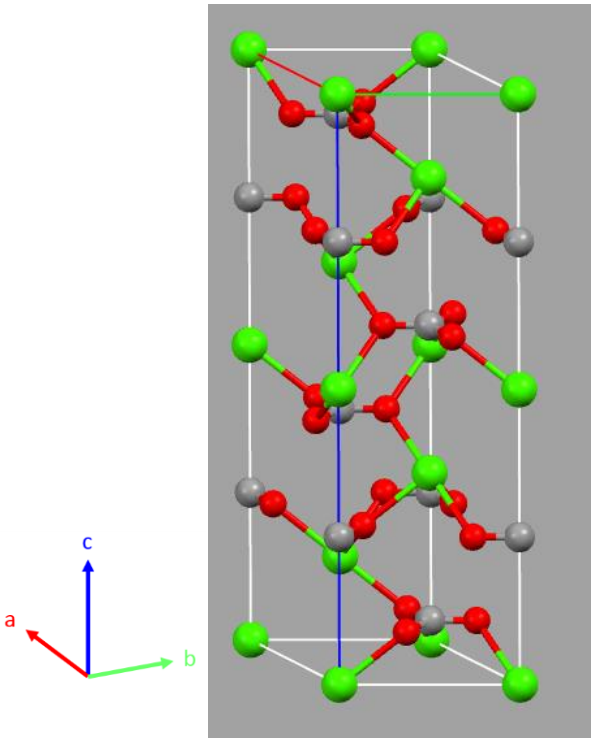

Figure 2.2 Simulated unit cell of calcite, using the structure proposed by Graf (26). Calcium atoms are green, oxygen atoms are red, and carbon atoms are grey.

Calcite displays a primitive rhombohedral cell, which is seen in its crystal morphology as distinctive rhombohedral crystals, or rhombs. The primitive cell has dimensions a=b=c= 6.375 Å and $\alpha=\beta=\gamma=60^{o}$.

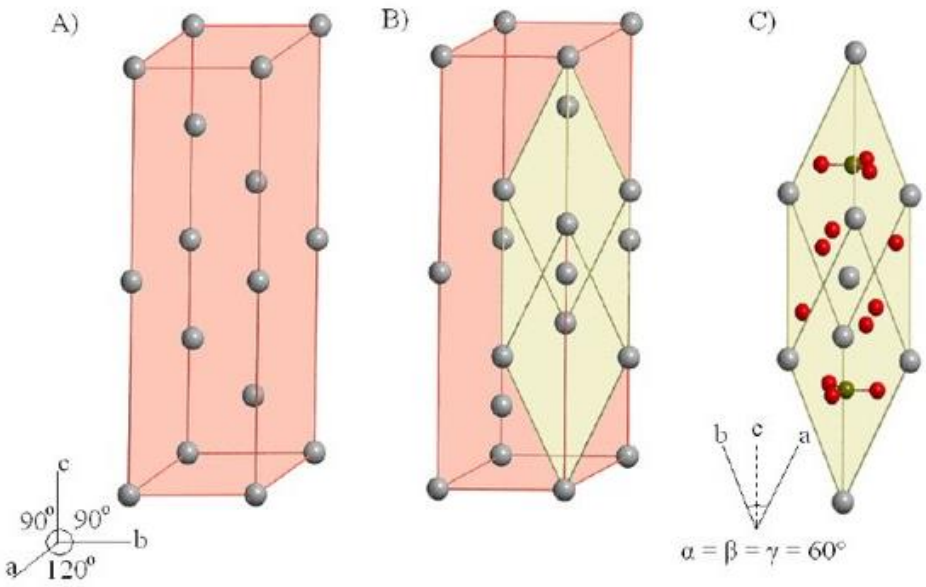

Figure 2.3 The calcite structure. A) Unit cell, showing calcium atoms only B) the relation between the primitive rhombohedral cell and the unit cell, showing calcium atoms only. C) The primitive rhombohedral cell, where red atoms are oxygen, gold atoms are carbon and grey atoms are calcium (27).

As calcite is abundant in limestone, it is the most common polymorph used for industrial applications. Calcite can be synthesised and crystallised through multiple pathways, as such it is commonly used as a model system for investigating the impact of $CaCO_3$ additives on crystallisation and crystal habit (28). Due to its abundance and thermodynamic stability, the structure of calcite is well known and has been characterised by multiple analytical methods.

2.1.4. Aragonite

The orthorhombic crystal structure of aragonite is well known, with a=4.96 Å, b=7.97 Å, c=5.74 Å and α=β=γ=90°. The simulated unit cell is shown in Figure 2.4.

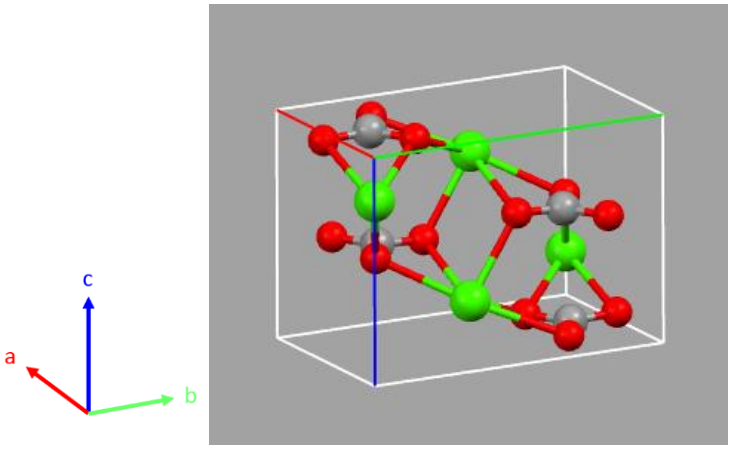

Figure 2.4 Simulated unit cell of aragonite, using the structure proposed by De Villiers (29). Calcium atoms are green, oxygen atoms are red, and carbon atoms are grey.

Aragonite is not commonly used industrially as phase-pure aragonite typically only precipitates at high temperature (65^{o}C) or with additives, forming long needle-like crystals which can make separation challenging (30). There would be no inherent benefit to using aragonite over calcite for compositional purposes, however there are some structural applications exploring aragonite (31). It is a common biomineral, being found in mollusc shells as flat plates in nacre composites, and in the endoskeletons of *Scleractinia* corals (32).

2.1.5. Vaterite

Vaterite is a metastable form of calcium carbonate, with a complex crystal structure that is not fully understood. It is most commonly encountered biologically as a structural biomaterial, where it is thought to form from an amorphous calcium carbonate precursor. Whilst vaterite was first synthesised in 1894, there has been significant debate regarding its crystal structure, with multiple potential structures published. Christy (33) presented a review of a number of published structures, to determine the impossible, unlikely, and possible structures. It was concluded that none of the currently published structures fully describe the crystal structure of vaterite, but when all are considered some insights into the structure can be gained. The major challenge in characterising the structure of vaterite is the disorder present in the arrangement of the carbonate ions. It has been postulated that different synthesis conditions (biologically mediated or lab synthesised) may affect the

disordering of the carbonate ions and produce subtle differences in the crystal structure (33-36). For the purposes of this thesis, the crystal structure proposed by Mugnaioli et al (34) was used for diffraction pattern analysis. It is considered to be a likely structure by Christy (33), and is experimentally derived through electron diffraction tomography. It is similar structure to a theoretical structure proposed by Demichelis et al (37), which was energy minimised using Density Functional Theory (DFT) calculations and revealed some distortions to the structure. The structure proposed by Mugnaioli was also used by Kathyola et al, for analysis and fitting of X-ray absorption spectra and X-ray pair distribution function data (38, 39).

The monoclinic vaterite unit cell proposed by Mugnaioli has dimensions a=12.17 Å, b=7.12 Å, c=25.32 Å, α=γ=90^{o} and, β=99.2^{o}, this cell is shown schematically in Figure 2.5.

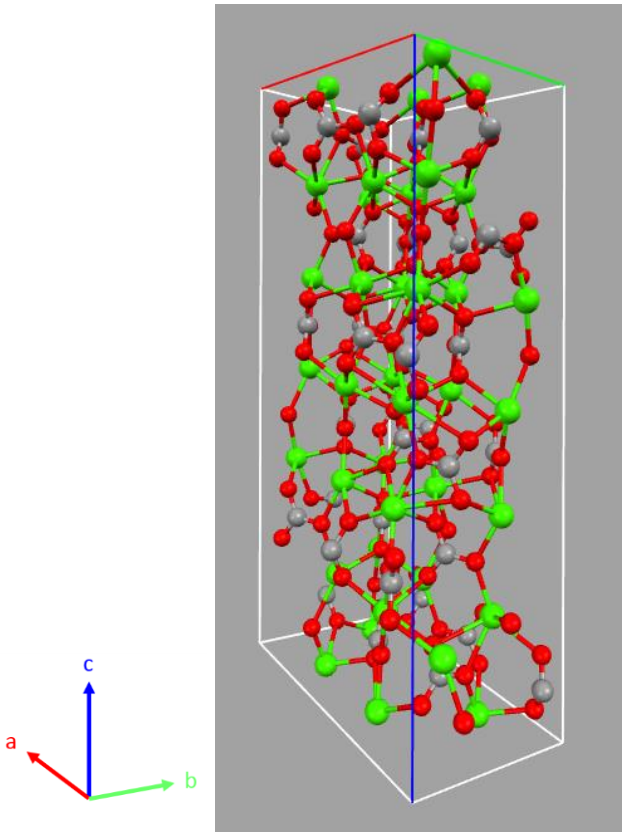

Figure 2.5 Simulated unit cell of vaterite, using the structure proposed by Mugnaioli et al (34). Calcium atoms are green, oxygen atoms are red, and carbon atoms are grey.

Biologically vaterite is commonly formed from an amorphous calcium carbonate precursor, being found across a wide range of biomaterials (40, 41). Due to its thermodynamic instability, biological vaterite is stabilised by polymeric and inorganic additives, which prevent or inhibit transition into calcite (42).

Vaterite is not commonly used industrially due to its poor thermodynamic stability and poorly understood crystal structure, however there has been some research into using vaterite for pharmaceuticals and personal care products (43). Vaterite has been investigated as a method for drug delivery as it is possible to form vaterite particles with a porous or hollow structure. A pharmaceutical agent can be co-precipitated with vaterite, and could be encapsulated within hollow or porous vaterite particles (44). As vaterite has a relatively high solubility, the vaterite particles would release the active pharmaceutical ingredient as it dissolves in the body or delivery media (43).

2.1.6. Amorphous Calcium Carbonate (ACC)

Amorphous calcium carbonate is most commonly encountered biologically, where it is considered to be a precursor to the formation of crystalline vaterite. Amorphous calcium carbonate has been widely studied in the context of biomineral research, where it is of interest into how additives and polymers affect its crystallisation behaviour (45, 46). There is also interest into how templating can affect the crystallisation of amorphous calcium carbonate, whether polymers can affect the final structure, or induce localised ordering in the amorphous phase (10). Pure amorphous calcium carbonate can easily be made to crystallise, however it can be stabilised by adding polymers, surfactant or inorganic additives (47).

Jacob et al (48) showed that amorphous calcium carbonate can be made to crystallise under the electron beam when attempting to perform high resolution CTEM characterisation of vesicles in bivalves. However, they did not characterise the crystalline product formed meaning it is uncertain whether crystalline calcium carbonate was formed, or crystalline calcium oxide (the damage product of radiolysis in calcium carbonate). They showed that

amorphous calcium carbonate is found in a growth region of the bivalve, intermingled with crystalline domains, however they were unable to definitively state whether some crystallinity was induced by the electron beam. No electron fluences are mentioned or quantified in this study.

Pouget et al (49) used low-dose cryo-TEM to investigate the crystallisation of amorphous calcium carbonate into vaterite. They used cryo-TEM to take ex-situ “snapshots” of the crystallisation process, which was observed using low-dose diffraction, CTEM imaging and electron tomography. They showed that from solution, calcium carbonate forms pre-nucleation clusters which agglomerate to form amorphous calcium carbonate particles. These particles then aggregate and crystallise to form vaterite. This process could be mediated by a polymer, which initially stabilises the amorphous particles. With further aggregation the polymer layer then templates the crystallisation into vaterite, stabilising one orientation and permitting crystallisation of a chosen crystal habit. As the authors considered the impact of electron irradiation, choosing cryo-TEM and low-dose operation, it is unlikely that their results have been impacted by electron irradiation.

2.1.7. Overbased Fuel Detergent Particles

Industrially produced nanoscale (~5-10 nm) calcium carbonate particles, (thought to be amorphous from XRD measurements) stabilised by a surfactant shell are commonly used as fuel detergents. Their function is to neutralise acid build-up in combustion engines, caused by impurities in the fuel used. Their performance and stability are related to their size and structure, with a small monodisperse particle size and amorphous structure preferred, though their internal structure is poorly understood.

They are proposed to have the approximate structure shown in Figure 2.6, of an amorphous calcium carbonate core, with an amorphous calcium hydroxide shell, surrounded by a sulfonate surfactant. The particles are overbased as they contain an excess of base (calcium carbonate) present in the cores to neutralise the acidic surfactant used to synthesise them (2). Thus, they act as

reservoirs of basic material to aid in the neutralisation of acid build-up when the detergent particles dissolve.

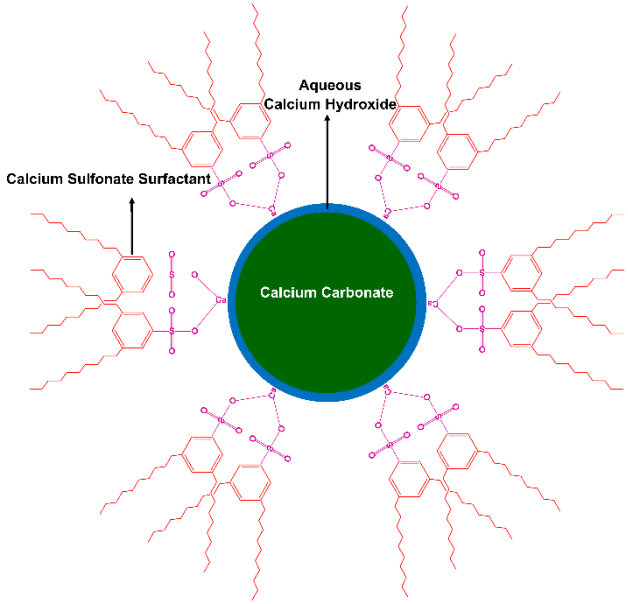

Figure 2.6 Schematic representation of industrially synthesised fuel detergent particles, the blue layer represents calcium hydroxide (39).

These particles are added to engine oils and fuels to neutralise acid build-up from fuel combustion, which produces acidic by-products through the oxidation of sulfur and nitrogen containing contaminants. These by-products can cause significant corrosion in the engine and lead to mechanical breakdown. The manufacturers prefer a small particle size with the core being amorphous, as this leads to rapid dissolution and acid neutralisation. They are concerned that a crystalline fraction may affect the particle stability in storage or use, as crystalline particles may destabilise the amorphous particles through agglomeration. For industry, a reliable method to rapidly investigate the core size and structure would be of significant interest.

Synthesis

Markovic (50) and Roman (51) have previously presented the synthesis of the fuel detergent particles, this process is used industrially (52, 53). The multistep procedure is shown in detail in Chapter 4 but follows the general outline of:

1) Neutralisation of sulfonic acid with calcium hydroxide to form the calcium sulfonate surfactant in toluene, water, and methanol.

2) Carbonation of remaining calcium hydroxide with carbon dioxide, forming the overbased sulfonate detergent ($nCaCO_3 \cdot Ca(R–SO_3)_2$).
3) Heating of the carbonated mixture to allow for the particles to grow to a final size.
4) Distillation to remove the water and methanol solvents used to suspend the calcium hydroxide.
5) Centrifugation to remove the toluene.
6) Vacuum distillation to remove trace water, toluene, and methanol.

Characterisation

The fuel detergent particles have previously been characterised by Cizaire et al (3), Markovic et al (50), and Mansot et al (54). Where Cizaire used XPS (X-ray Photoelectron Spectroscopy), ToF-SIMS (Time-of-Flight Secondary Ion Mass Spectrometry), XANES (X-ray Absorption Near Edge Structure), and EFTEM (Energy Filtered TEM), Markovic used SANS (Small Angle Neutron Scattering), and Mansot used bright field CTEM imaging, EELS (Electron Energy Loss Spectroscopy), EFTEM and XANES. These present a combination of bulk spectroscopy and more specific imaging techniques.

Markovic et al (50) presented a SANS study of the overbased fuel detergent particles, they determined the particle size of the fuel detergents to be around 4-13 nm excluding the surfactant shell. They do not characterise the particle structure or chemistry. It is unknown what effect the specimen preparation methods have on the measurements, as they condensed a solution by adding acetone until the particles came out of suspension, the supernatant was removed, and the residue dried before being suspended in toluene. It is possible that by introducing a polar solvent, the stability of the particles is affected, causing agglomeration which may affect the final particle size measurements; this was not considered by the authors.

Mansot et al (54) discussed sample preparation methods for the CTEM analysis of the overbased detergent particles. They found no benefit to cryo freeze-fracture replication with Pt/C shadowing over conventional drop-

casting for imaging purposes, with their images showing 10-20 nm particles (Figure 2.7).

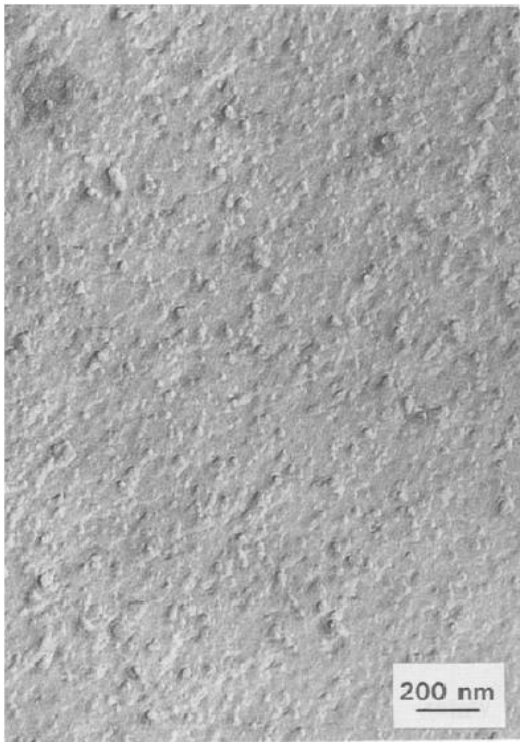

Figure 2.7 BF-CTEM image of a freeze-fractured specimen containing the calcium carbonate particles (54).

Their EFTEM results demonstrated a carbon-based shell surrounding a calcium containing core, presumably the surfactant surrounding the amorphous calcium carbonate, shown in Figure 2.8 and gave a comparable particle size of 5-10 nm.

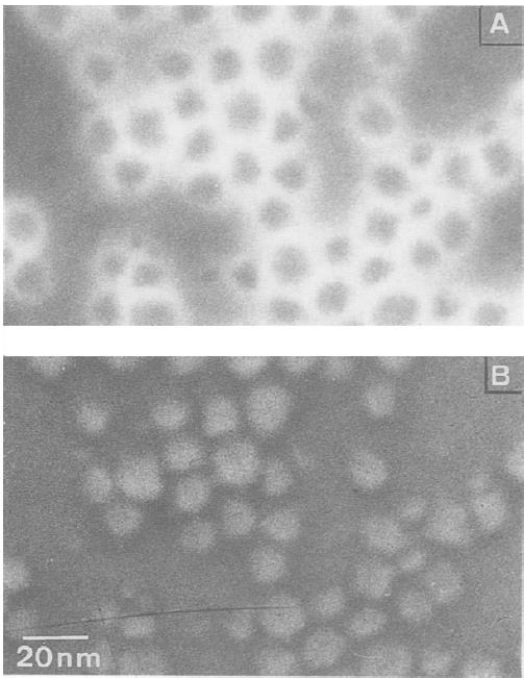

Figure 2.8 EFTEM images of the calcium carbonate particles A) Carbon *K*-edge, B) Calcium $L_{2,3}$-edge (54).

XANES spectra taken by Mansot et al (54), shown in Figure 2.9A indicated that the particles were amorphous, as a resonance feature seen in calcite (shown by the black arrow) correlated to the alignment of carbonyl groups is not present, suggesting disordered cores. This was corroborated by analysis of the radial distribution function, this is a Fourier transform of the EXAFS spectrum which plots the photoelectron scattering profile as a function of radial distance from the absorbing atom. In this case it showed that there was no ordering beyond 3.2 Å, suggesting no long-range ordering was present, though they did not compare the RDF to an amorphous calcium carbonate reference material.

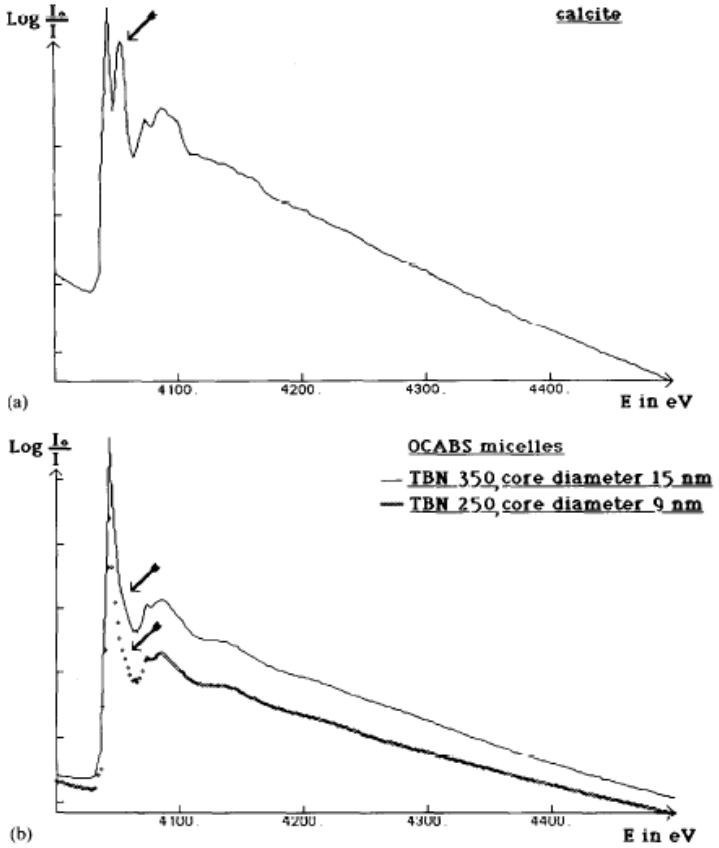

Figure 2.9 Ca k-edge XANES spectra of A) calcite and B) two overbased fuel detergent specimens (54).

Cizaire et al (3) used electron diffraction to reveal the amorphous nature of the particles, along with images indicating the particle sizes present were between 5-10 nm, shown in Figure 2.10.

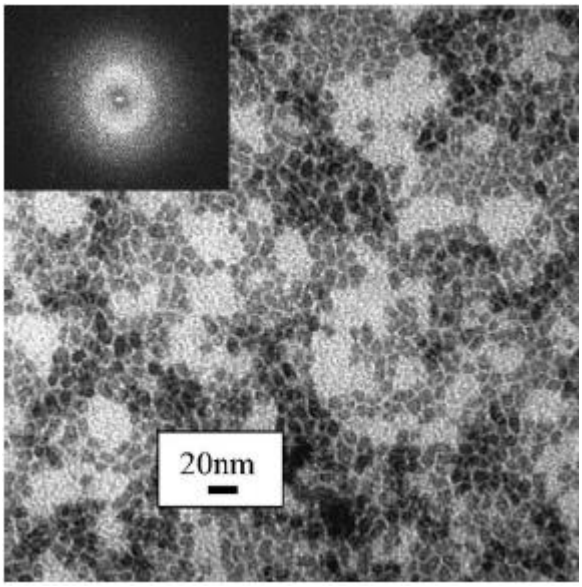

Figure 2.10 BF-CTEM image and inset electron diffraction pattern of the overbased detergent particles (3).

To enhance image contrast they employed energy filtered EFTEM, to reduce inelastic scattering contrast using the zero-loss peak, carbon plasmon filtered imaging and calcium $M_{2,3}$ edge filtered imaging was used to investigate the surfactant and the core.

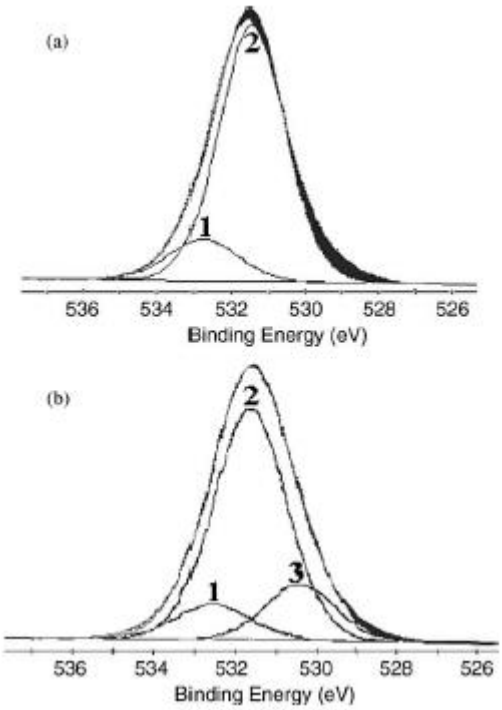

Figure 2.11 Oxygen 1s XPS spectra of the overbased fuel detergent particles from Cizaire et al (3), A) is fit with calcium sulfonate 1) and calcium carbonate 2), B) is fit with calcium sulfonate 1), calcium carbonate 2), and calcium hydroxide 3). Black regions indicate peak residuals.

The XPS spectra in Figure 2.11 showed that it was possible to fit calcium carbonate, calcium hydroxide and calcium sulfonate to the O1s peak in the detergent particles XPS spectrum. A better fit was obtained with the addition of the calcium hydroxide component, when compared to the fit obtained with only calcium carbonate and calcium sulfonate. This correlated to ToF-SIMS results suggesting the calcium hydroxide is present in a shell around the calcium carbonate core. XANES and EFTEM results showed that the particles contained calcium carbonate, and the carbon *K*-edge XANES showed weak scattering features that may correspond to calcite crystallinity alongside the amorphous calcium carbonate. However, it was not certain whether the calcite crystallinity was present in all particles or in discrete crystalline particles.

2.1.8. Summary

Calcium carbonate is a material with significant interest from academic and industrial researchers and would provide a useful model system for demonstrating practical applications of low-dose electron microscopy. As calcium carbonate is known to be electron beam sensitive, some literature into radiation damage is present. However there have been few attempts to thoroughly characterise the electron beam-induced changes to calcium carbonate in a quantitative manner.

The fuel detergent particles provide an industrial application where low-dose electron microscopy can provide specific insights to correlate with bulk analysis. For example, it can be used to investigate the presence of crystallinity on an individual nanoparticle scale, whilst minimising the impact of electron beam damage. Previous TEM studies on the fuel detergent particles did not consider the impact of electron beam damage on the measured data, which may have implications for the accuracy of measurements, with structure, particle size, and composition known to be affected by electron irradiation.

Low-dose CTEM/STEM offers significant sensitivity and specificity of measurements down to the atomic level and would be an ideal technique to

investigate these materials with. However, an understanding of the processes behind radiation damage, and how it can affect materials is also necessary.

Specimen selection

Calcium carbonate was chosen as a model system as it is widely encountered in industrial, geological and biological systems. Calcium carbonate also displays polymorphism with three crystalline anhydrous forms of varying thermodynamic stability. As such it may provide information on whether composition or relative thermodynamic stability is a more important factor in a materials electron beam sensitivity. Specimens of crystalline calcite, aragonite and vaterite were chosen as they are the anhydrous crystalline polymorphs and cover a range of thermodynamic stabilities. The fuel detergent specimen was chosen as it is a case study specimen that will benefit from the application of TEM/STEM to its characterisation. As the fuel detergents are amorphous, they will provide an insight into whether the electron beam damage behaviour is different in amorphous calcium carbonate, compared to crystalline forms. The fuel detergent specimen is available due to an existing collaboration with Dr. Thokozile Kathyola.

2.2. Radiation Damage

Radiation damage is a significant yet often underappreciated issue in electron microscopy. The specimen in an electron microscope is subject to a hostile environment of high vacuum and high flux ionising radiation. The bombardment of a thin specimen with high energy charged particles is almost inevitably going to cause some form of alteration. Radiation damage is seen in many areas, from nuclear reactors to medical therapies, and is caused by the deposition of energy from charged particles (such as electrons), neutral particles (neutrons) or from photons, including X-rays and ultraviolet light.

Due to the complex nature of electron-specimen interactions, many radiation damage mechanisms are poorly understood, or are only understood in detail for a limited number of materials. In many cases multiple damage processes act concurrently, making the deconvolution of the impact of each mechanism difficult. However, by manipulating the operating conditions of the microscope

and observing the changes to the progression of electron beam damage, it is possible to gain some understanding on the dominant damage processes, and then potentially mitigate against it.

Egerton proposes that radiation damage processes can be classified as either elastic or inelastic mechanisms based on how the incident electron transfers energy to the specimen (6). The following section outlines the main radiation damage mechanisms, their common manifestations and some of the materials in which they are known to operate.

2.2.1. Elastic Interactions

Elastic specimen interactions arise through Coulombic interactions of the incident electrons and the nuclei of specimen atoms. The interaction of the nucleus and incident electrons results in electrostatic forces being applied to the incident electrons, which can deflect incident electrons by varying degrees.

If an incident electron is scattered through a small angle θ, the energy transfer is very small (usually <1 eV) as demonstrated in equation 2.1 which demonstrates the scattering angle dependence of energy deposition, and equation 2.2 which demonstrates the maximum energy transfer possible.

$$E = E_{max} \times sin^2(\theta/_2)$$

(3.1)

$$E_{max} = E_0(1.02 + \frac{E_0}{10^6})/(465.7 \times A)$$

(3.2)

In both equations, E corresponds to the energy transferred to the atom, E_0 is incident electron energy and E_{max} is the maximum energy that can be transferred to the system (assuming θ = 180° from complete electron backscatter), all in eV. θ corresponds to the scattering angle and A is the atomic number (55).

Displacement Damage

Displacement damage relies on the conservation of momentum from incident electrons. When the energy transferred from an incident electron to the atom, E, is above a threshold energy (E_d), atoms are susceptible to displacement. They may be knocked into interstitial spaces (Frenkel defects), or out of the lattice, forming a vacancy defect (known as Schottky defects in ionic materials). These both produce imperfections in the crystal lattice, reducing order and acting as nucleation sites for dislocations, cracks and further degradation (6, 55).

At low scattering angles, the $\sin^2(\theta/2)$ term in equation 2.1 maintains a low energy transfer; however, at larger scattering angles or higher incident electron energies, the energy transfer becomes larger and more significant, as E_{max} is high. High scattering angles can be indicative of strong electron-nucleus interactions, such as a direct hit and deflection.

The displacement threshold energy is a function of crystal structure, atomic weight and bonding strength, some examples are shown in Table 2.1, together with the minimum incident energy for which displacement is observed (E_0). This minimum incident energy is then used with equation 2.2 to extract the displacement energy. The displacement energies of most materials shown in Table 2.1 are within the reach of many commercially produced TEMs, excluding gold, and to a lesser extent copper.

Material	**Displacement energy (eV)**	**Minimum incident energy for displacement to occur (keV) (E_0)**
Graphite	30	140
Diamond	80	330
Aluminium	17	180
Copper	20	420
Gold	34	1320

Table 2.1 Atomic displacement energies and required incident energy to displace an atom from several elemental materials (6, 56).

Sputtering

Sputtering damage occurs when the momentum transferred from the incident electron is sufficient to remove surface atoms. Where displacement damage operates mainly in the bulk of a sample, sputtering operates on the top and bottom surfaces of the sample. Equation 2.1 and equation 2.2 still hold true for sputtering, but surface atoms can be displaced into the vacuum rather than being forced into an interstitial space. This, coupled with the lower bonding energy displayed by surface atoms as they have fewer bonds, reduces the displacement energies required for sputtering. While some sputtering occurs on the top surface of a sample, the majority occurs on the exit side as the momentum is transferred to the sample along the beam axis, towards the bottom of the sample.

Using equation 2.2, E_{max} is often taken as the sublimation energy (the energy required to change one mole of a substance from solid to gas) when the incident energy is above the sputtering threshold energy ($E_{max} = E_s$). Samples containing elements with a low atomic number are more susceptible to sputtering, as lighter elements generally have lower sublimation energies (57).

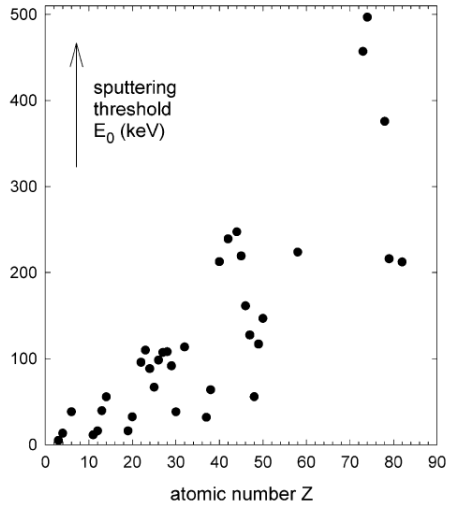

Figure 2.12 The correlation of sputtering threshold and atomic number, using equations 2.1 and 2.2 (6).

Under standard TEM operating conditions (up to 300 kV), sputtering can be expected for most light to medium atomic number elements. As seen in Figure 2.12, which is derived from equation 2.2 where sublimation energy is used as

E_{max} and E_0 is extracted as the incident energy required for sputtering to occur (sputtering threshold).

In STEM, the high current density of the focussed probe can induce highly localised sputtering, known as “hole-drilling”. An example of this in calcite can be seen in Figure 2.13 from Murooka et al (58). The dark central point in the ADF image (right) is the thinnest region of the sample, the lighter region surrounding it is believed to be hydrocarbon contamination or re-deposition of sputtered material causing further scattering.

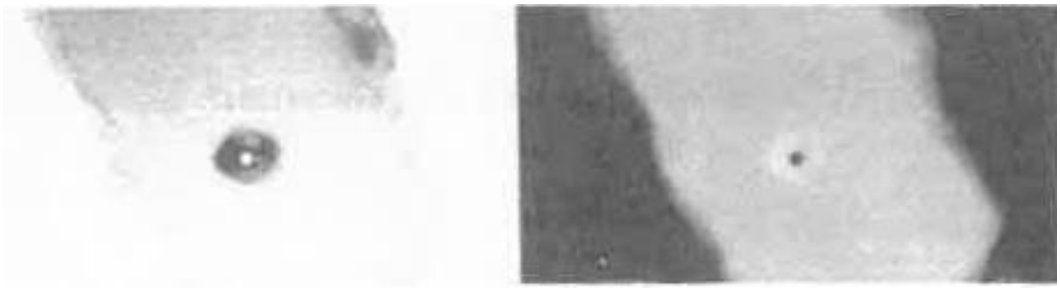

Figure 2.13 An example of STEM hole drilling in calcite at 100 kV, both in bright field (left) and annular dark field (right) imaging modes (58).

Hole-drilling can be avoided by reducing the current in the STEM probe, and by reducing the dwell time of the STEM probe. If this is not possible then the beam should be blanked (electrostatic or electromagnetic deflection of the incident beam off the specimen) when the probe is stationary.

2.2.2. Inelastic Interactions

Inelastic specimen interactions involve the deposition of energy through the electrostatic interaction of a fast incident electron with electrons in a specimen. The incident electron loses an amount of energy related to the strength of the interaction, this can either be low losses from inter-band transitions or plasmon interactions (~10-30 eV), or relatively large losses from core excitation events subsequently causing characteristic X-ray emission.

Radiolysis

Radiolysis is a primary inelastic damage mechanism, the incident electron causes ionisation events which excite and cleave chemical bonds, unlike

knock-on and displacement processes, where the incident electron interacts with atomic nuclei. Above a threshold energy, valence electrons are promoted to excitons (bound electron-hole pair states) and conduction band electrons are excited as plasmons (oscillations of valence band electron density) (59). This threshold comes about as atomic electrons and nuclei are locally bound, the threshold is commonly taken to be between 5-30 eV, as demonstrated by the broad plasmon resonance peak seen in EEL spectra (60). The lifetime of this excited state varies between materials but is typically in the order of picoseconds before the de-excitation/decay process occurs.

Radiolysis is believed to be the dominant damage mechanism for inorganic and insulating materials where efficient radiolysis mechanisms exist, more specifically, where efficient recombination of electron-hole pairs is allowed. Hobbs (61) stated that efficient recombination is more likely in insulating materials, as the excitons remain localised and have a high likelihood of recombination, making them more sensitive to radiolysis. Cazaux (62) also stated that insulators are susceptible to radiolysis as the electrical equilibrium is slow to recover at the atomic scale, as there is limited conduction of electrons to or from the surrounding areas. The recombination of the excitons cause the energy introduced by the excitation process to be dissipated into the material, which may cause bond breakage or localised heating. This has been demonstrated for alkali metal halides by Itoh (63) and, Kabler and Williams (64). Metals show a strong plasmon resonance in EEL spectra, however they are not susceptible to radiolysis as the excitations are delocalised too rapidly by the conduction of electrons (typically < femtoseconds) for radiolysis to occur (61).

A de-excitation mechanism proposed by Cazaux (62) for covalently bonded materials may be applicable to the carbonate group of $CaCO_3$. They propose that the initial electronic excitation is followed by the emission of an Auger electron, which escapes the material leaving the excited atom missing one or more electrons. In poorly conductive materials the electronic equilibrium cannot be reached by transfer of electrons from the surrounding area and so to compensate, the charged species is ejected from its initial site. As this

mechanism is proposed only for covalently bonded materials, it may have some applicability to the carbonate group. However it does not consider resonance structures, which are a feature of the carbonate group, as there is a carbon-oxygen double bond that is shared between the three oxygen atoms, it is assumed that each carbon-oxygen bond has an equal probability of being the double bond, and as such the bonding electron density is distributed across all three bonds, however one oxygen atom is ionically bonded to the calcium atom and this bond will affect the distribution of electron density in the carbonate group.

In the de-excitation process, the deposited energy can also be lost as electromagnetic radiation, for example characteristic X-ray emission, visible light which can be measured by cathodoluminescence, or as localised heating, which may cause damage to sensitive materials (65).

The inelastic cross section

$$\sigma_i = \int \left(\frac{d\sigma_i}{dE}\right) dE = (In_a t)^{-1} \int \left(\frac{dJ}{dE}\right) dE \qquad \textbf{(2.3)}$$

σ_i is the inelastic cross section for a thin specimen of a given material with thickness below the inelastic mean free path length. Where I is incident beam intensity, J(E) is an integrated energy loss, t is specimen thickness and n_a is number of atoms per unit volume (66). From the inelastic cross section in equation 2.3, it can be seen that radiolysis is directly related to the amount of energy deposited in the sample. The deposited energy can be changed in multiple ways, changing the sample thickness, beam intensity or incident energy. Thicker samples have more atoms in the path of the incident electron, increasing the chance of inelastic scattering events occurring. A more intense beam will send more electrons through the sample, meaning there are more opportunities for inelastic scattering events. Increasing the accelerating voltage will reduce the energy deposition, as the inelastic cross section is inversely proportional to the incident electron energy, high energy electrons will have fewer opportunities to interact in a given material. While reducing acceleration voltage will reduce the susceptibility to knock-on and

displacement damage, for materials susceptible to radiolysis it will serve to exacerbate the problem. This is linked to the idea of the dose-limited resolution, discussed in section 2.2.5.

The energy deposited by an incident electron can be presented in terms of a stopping power for radiolysis. This is a measure of the energy deposited per unit distance of an electron passing through a specimen shown by equation 2.4 (66).

$$S_i = n_a \int E \left(\frac{d\sigma_i}{dE}\right) dE = n_a E_m \sigma_i = \frac{E_m}{\lambda_i} \quad \textbf{(2.4)}$$

The stopping power for inelastic scattering, where n_a is the number of atoms per unit volume, E is the incident electron beam energy, E_m is the mean inelastic energy loss per collision, σ_i is the cross section, and λ_i is the inelastic mean free path. This can be used to optimise specimen thickness to minimise the extent of radiolysis, a thinner sample will have a lower stopping power, and will absorb correspondingly less energy, however this also means that thinner samples will display weaker inelastic signals, and also weaker elastic contrast (as the elastic cross section also depends on 1/E). This is encapsulated in the “dose-limited resolution” equation discussed in section 2.2.5. The stopping power can also be used to calculate the total energy deposition in a specimen, to correlate energy deposition with physical or chemical changes (67).

Progression of damage

Chiu and Jeng (68) noted that radiolytic beam damage is a progressive mechanism, affecting short range order first, i.e. the loss of outer diffraction spots in SAED. This is most likely due to the introduction of localised point defects, which disrupt short range order whilst leaving long range packing mostly unaffected. Cazaux (62) suggests that radiolysis occurs initially at the surface of single crystals and at the grain boundaries of polycrystalline materials, as the electrons in those locations are generally less strongly bound, observations supported by Rodriguez-Navarro et al (69) where CaO

nucleation is seen on $CaCO_3$ particle edges after thermal and electron beam-induced decomposition.

Delocalisation of inelastic scattering

Egerton (70) demonstrated experimental and theoretical evidence for delocalisation in inelastic scattering, suggesting that radiolysis events can be induced in regions several nanometres away from where the incident electron interacts directly with the specimen, as shown in Figure 2.14, i.e. valence band electronic excitations can be excited at a distance. This becomes a more significant problem when using STEM, as radiolysis can be induced and detected in regions outside of the probe illumination, as demonstrated in Figure 2.15.

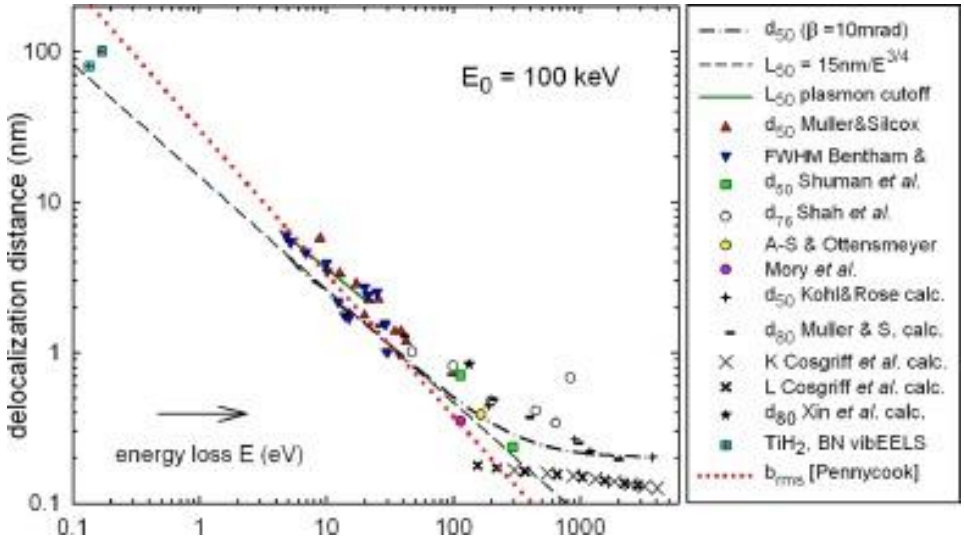

Figure 2.14 Delocalization length of inelastic scattering *L*(*E*), adjusted to an incident energy of E_0 = 100 keV. Where b is the classical impact parameter at 100 kV, in nm.

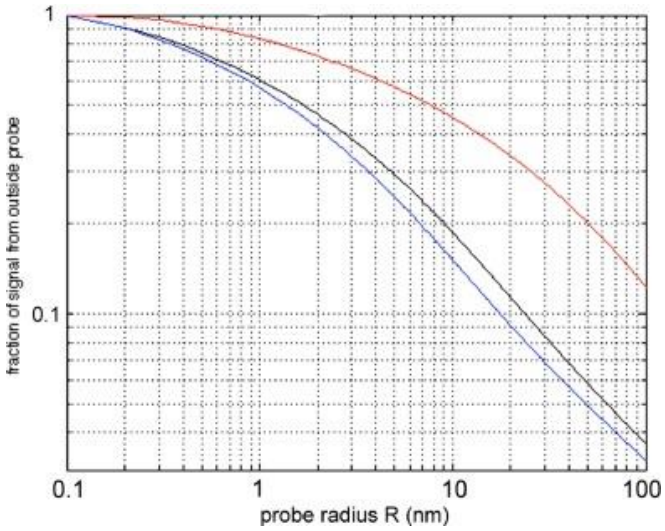

Figure 2.15 Fraction of the inelastic scattering occurring outside an electron probe of radius *R for an energy loss E*. Red curve: *E* = 0.45 eV, E_0 = 60 keV, black curve: *E* = 6 eV, E_0 = 200 keV, blue curve: *E* = 6 eV, E_0 = 60 keV.

For cases where the beam is large, as in CTEM imaging, the fraction of the measured signal obtained from outside of the beam diameter is relatively low. Whereas with small probes, as in STEM, a large fraction of the signal is from regions not being actively illuminated. Whilst high energy loss signals can be localised with relative ease, low loss signals (responsible for radiolysis) will be limited in spatial resolution due to this scattering delocalisation.

Radiolysis in carbonate materials

Cater and Buseck (71) showed that the radiolytic damage of dolomite ($Ca_{0.5}Mg_{0.5}CO_3$) occurs via a metastable $Ca_{0.5}Mg_{0.5}O$ phase, before the production of separate CaO and MgO crystallites. They stated that due to the radiolysis process happening at room temperature, the process must be diffusion-less. They also did not observe phase separations consistent with diffusion when compared to ex-situ high temperature conditions. They also observed the reduction of damage when increasing the electron acceleration voltage from 100 to 500 kV, consistent with radiolytic damage. Rodriguez-Navarro et al. (69), stated that the type of energy used to transform $CaCO_3$ to CaO does not affect the decomposition mechanism (i.e. either electron irradiation or thermal heating). They also proposed three stages for the decomposition of $CaCO_3$: energy transfer to the reaction interface (via

excitation of electrons into the conduction band), fission of the O-C bond to produce CaO and CO_2 (via de-excitation of the excited electrons to the ground state), and diffusion of CO_2 through the product layer. They believed that the rate limiting step is the fission of the O-C bond, and that the diffusion of CO_2 is not rate limiting due to the presence of pores and voids induced by the volume change of $CaCO_3$ to CaO facilitating its egress to vacuum or air. There is a difference of 19% in density between $CaCO_3$ and CaO, with calcite having a density of 2.71 g/cm^3 and CaO having density of 3.34 g/cm^3.

There is still debate on the mechanisms of radiolysis, but a fundamental study into the radiation effects on carbonates at an atomic level is beyond the scope of this thesis.

Electron beam-induced heating

Inelastic scattering involves energy transfer from incident electrons to the sample, through electronic excitations and de-excitations (radiolysis). As the excitation and de-excitation of electrons causes rearrangement and movement of atoms, energy is dissipated as heat.

In high thermal conductivity materials, heating is not a significant concern as the localised hotspots can be dissipated with relative ease. Heating may however become a problem in low conductivity materials, where a significant temperature rise may be possible, leading to sample degradation through melting, sublimation or annealing.

Heating damage can be mitigated through the active cooling of a sample by a cryogenic holder. It is also believed that by using STEM, the induced heating becomes localised, allowing for the heat to dissipate more rapidly from a small spot due to the higher surface area to volume ratio of the heated region (72). It has been noted that in SEM, scanning at 24 scans per second (TV scan rate) may reduce temperature build up by a factor of 10 when compared to a stationary probe of the same size and current (73).

The amount of heat deposited per incident electron can be calculated for thin samples (thickness < inelastic mean free path) using equation 2.5 (6), which

balances heat loss due to radial and surface conduction against the heat generated by an incident electron beam of diameter d. Here I is incident beam current, t is sample thickness, λ is inelastic mean free path, κ is thermal conductivity, σ is the Stefan Boltzmann constant, and ε is emissivity. R_0 is radial conduction distance (the maximum heat affected radius at thermal equilibrium), T_0 is the initial temperature.

$$I\langle E(eV)\rangle\left(\frac{t}{\lambda}\right) = \frac{4\pi\kappa t(T - T_0)}{\left[0.58 + 2ln\left(\frac{2R_0}{d}\right)\right]} + \pi\left(\frac{d^2}{2}\right)\varepsilon\sigma\left(T^4 - T_0^4\right)$$

(2.5)

The temperature rise for calcium carbonate (calcite) was calculated at several electron beam conditions using equation 2.5, the results are presented in Table 2 for isolated 50nm particles.

Conditions	Beam diameter (nm)	Temperature rise (K)
Wide beam	500	0.01
Condensed beam	20	0.02
STEM probe	0.1	0.08

Table 2.2 Temperature changes in calcite due to electron beam-induced heating, calculated using equation 2.5. Using t=50 nm (assuming particle thickness is the same as particle size), R_0=50 nm (no conduction between particles), λ=80 nm (approximate inelastic mean free path of calcite at 200 kV), ε=0.5, κ=5.5 W/m/K (thermal conductivity of calcite), I=1 nA and an average energy loss of 30 eV.

For calcite, it appears that under common imaging conditions, beam-induced heating is not a significant concern, a statement corroborated by several studies on beam-induced heating in both metals and bio-minerals (6, 74). In fact, to reach a temperature rise close to the thermal decomposition point of $CaCO_3$ in air (825 ^oC), an average energy loss of 100 keV would be required for a 20 nm beam, half of the energy of the 200 keV incident electron beam. In addition to this, the amorphous carbon support film would have degraded

prior to this temperature, which has not been observed in literature studies of irradiation damage of calcium carbonate. However, when considering the vacuum in a TEM, the thermal decomposition temperature will be lower than in air due to the reduction of carbon dioxide vapour pressure. Even when considering this, the electron beam-induced thermal decomposition of calcite is unlikely.

Charging

Electrostatic charging can be a significant issue in nonconductive or thick materials. Charging effects occur when the number of electrons retained by, or generated by the specimen is larger than the number of electrons conducted out of the sample. High levels of charging in a specimen may produce a mechanical force which can cause damage to samples and may tear the carbon support film of a TEM grid, or the specimen itself. Charging in the bulk of a specimen can affect the paths of incident electrons, influencing imaging, diffraction and spectroscopy (75).

Cazaux (62) linked the emission of electrons from radiolytic damage to the positive charging of a sample on the top and bottom faces. This is partly compensated by the conduction of absorbed electrons in the sample but can become significant in poorly conductive materials. Susceptibility to charging is related to the electrical conductivity of the material. The main method to combat charging is to reduce the beam current and increase the accelerating voltage so that fewer electrons undergo inelastic interactions, allowing the specimen to dissipate the absorbed electrons (6).

Charging can be mitigated through coating the sample with a conductive material, often an evaporated carbon film, however this can be obstructive to high resolution imaging and may affect analytical information such as EDX or EELS signals due to the spurious detection of carbon in the coating, or due to increased X-ray absorption as a result of increased sample thickness (62).

Hydrocarbon Contamination Deposition

Whilst hydrocarbon contamination does not damage the specimen itself, it adversely affects the quality of imaging and often renders sample regions unusable for imaging or spectroscopy. Hydrocarbon residues on the sample or microscope, usually arising from impurities, surface dirt, or seal lubricants are vaporised in the column vacuum and are attracted to charged regions on the specimen, and the edges of the electron beam where the greatest charge gradient exists. This is demonstrated in Figure 2.16, where the shape of the contamination deposits can be seen for different electron beam sizes (76).

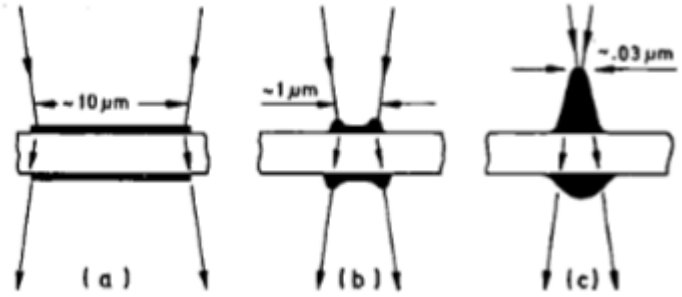

Figure 2.16 Contamination build-up morphology as a function of electron beam size, for a) broad beam low magnification imaging, b) condensed beam for HRTEM imaging, and c) focussed STEM probe.

Most contamination comes from surface diffusion of sample borne contaminants towards the sites of high charge gradient. The electron beam then polymerises the hydrocarbons, immobilising them. In wide beam operations, this contamination manifests as a thin disc of contamination under the beam, and a thicker ring around the edge of the beam in HRTEM, in small condensed beam operations such as STEM the contamination forms a peak or spot where the beam sits or is scanned.

With the probe in motion in STEM, hydrocarbon contamination deposition has the effect of laying down a layer of amorphous carbon in the imaging area. This can hinder imaging through reduction of contrast in images by effectively increasing the thickness of the specimen and support film. This means that a higher fraction of electrons are scattered by the amorphous film layer, which can raise the contribution of background scattering to the image, influencing the image contrast. In HRTEM imaging, the amorphous layer can affect the

phase of the exiting electrons, reducing image quality and impeding phase reconstructions.

There are several strategies for mitigating hydrocarbon contamination, however not all sources of contamination can be eliminated conveniently. These include:

- Heating the sample to thermally desorb hydrocarbons, care must be taken to avoid altering the sample when using this method.
- Plasma or ion cleaning, can be used to remove contaminants via the reaction of oxygen plasma or ozone with the contamination layer, this forms H_2O, CO, CO_2 or low molecular weight hydrocarbons with a high vapour pressure, these are then removed by the vacuum (77).
- Cooling the same to cryogenic temperatures will reduce the mobility of hydrocarbons on the sample surface, reducing the contamination rate under the electron beam (78).

A commonly used method to reduce the impact of hydrocarbon contamination is the “beam-shower”, where the beam is defocussed and spread over a large area, allowing for the hydrocarbons to deposit over a wide area as an ultrathin layer. Whilst not an ideal method, as contamination is still present, no extra sample processing steps are involved (79, 80). This method is less useful when working on some electron beam sensitive materials, as even small amounts of irradiation can be sufficient to damage crystallinity or compositional information.

Examples of surface contamination can be seen in Figure 2.17 and Figure 2.18, in both figures it can be seen that the surface coating from hydrocarbon contamination can obscure fine detail, reducing the image resolution.

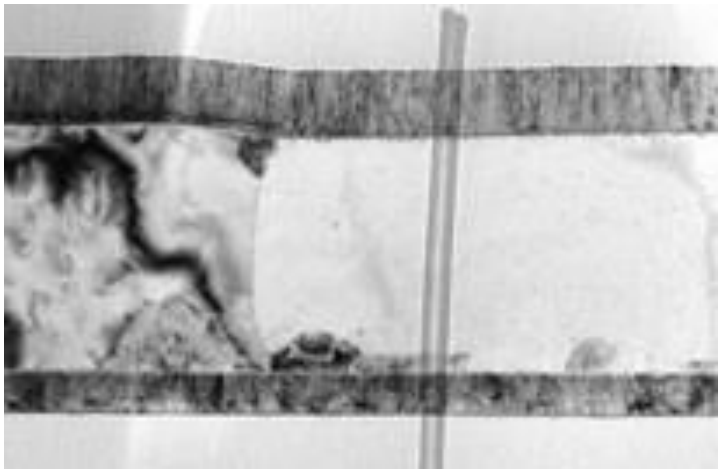

Figure 2.17 Hydrocarbon contamination deposited after a STEM line-scan, seen as the vertical line passing down the image (81).

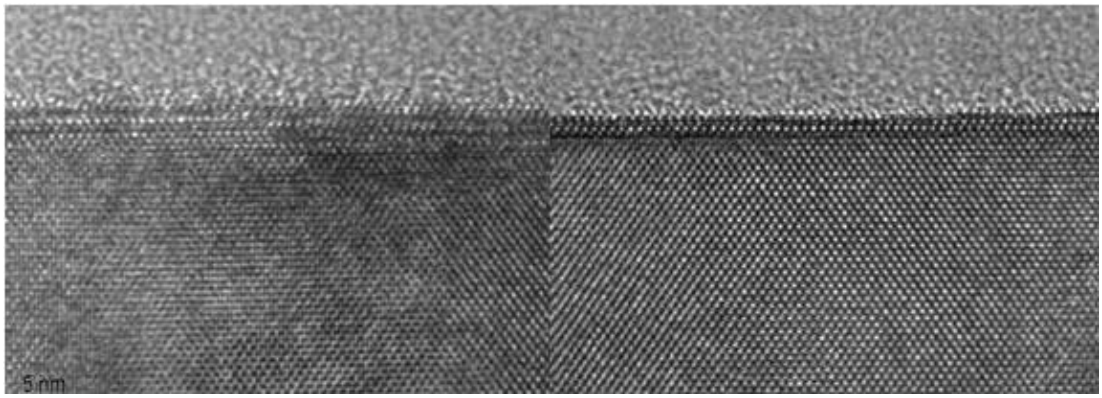

Figure 2.18 CTEM of a lamellar sample before (L) and after (R) ion/plasma cleaning showing much improved contrast and clarity after plasma cleaning (81).

The intentional deposition of a specimen coating of controlled thickness has been discussed as a method of extending the lifetime of particles under irradiation. Conductive coatings have been used to aid in charge dissipation, and metallic coatings have been applied to the exit surface of a specimen to reduce sputtering damage by preventing mass loss (6, 82). It is possible that the deposition of hydrocarbon contamination can be beneficial in a similar manner, either by aiding in charge neutralisation, obstructing surface diffusion of damage products or by facilitating thermal conduction (62, 72). In a study by Ward et al (83), it was observed that below a critical STEM probe current density the damage mechanism transitioned from sputtering to contamination deposition. In this case, the rate of hydrocarbon deposition exceeded the rate of sputtering and the deposited contaminants prevented further mass loss.

However, the deposition of hydrocarbon contamination is generally not controllable, as such, care should be taken that the potential increase in specimen lifetime is not outweighed by poorer image resolution or contrast. The potential benefits of hydrocarbon contamination are explored further in Chapter 6 where the characteristic fluences for the electron beam degradation of calcite nanoparticles are measured with and without the presence of hydrocarbon contamination.

2.2.3. Terminology of Radiation Damage

Medical and nuclear physicists take absorbed dose to be the amount of energy deposited per unit mass. This is given in units of Grays (Gy), which corresponds to one joule of energy deposited per kilogram of mass.

However, electron microscopists often erroneously use the term dose to mean fluence, the number of electrons incident on a unit area. To approximate dose in electron microscopy, the electron fluence, the density (ρ) and inelastic mean free path (IMFP) (typically ~100 nm but this is dependent on electron accelerating voltage) should be known, and average energy loss (E_L) can be approximated as plasmon losses, typically 10-30 eV (84). This results in:

$$Grays = Fluence\ (C/cm^2) \times \left(\frac{E_L\ (eV)}{IMFP\ (nm)}\right) \times \left(\frac{10000}{\rho\ \left(\frac{g}{cm^3}\right)}\right) \quad \textbf{(2.6)}$$

This equation only considers the impact of inelastic energy transfer, however elastic scattering also produces electron beam damage through knock-on and sputtering damage. The relative contribution of elastic and inelastic scattering to electron beam damage has been considered by Egerton (84), where it was determined that for an organic specimen, the rate of knock-on damage is several orders of magnitude smaller than the rate of radiolysis damage, and thus can normally be negated for organic specimens at 100 kV.

Low-dose electron microscopy is somewhat of a misnomer, a more accurate name should be low-fluence electron microscopy, as typical “low-dose”

methods involve reducing the electron fluence to reduce the number of potential damage events, this does not influence the dose deposited per electron, but reduces the dose received by the specimen overall. For a specimen under irradiation, the dose can be reduced by increasing the electron acceleration voltage whilst maintaining the same fluence.

The following tables define some commonly used terms and offer conversions between units used in radiation physics.

Term	Definition	Common Units
Fluence	Number of electrons incident upon a unit area.	Electrons per square nanometre ($e^{-}nm^{-2}$). or Electrons per square Angstrom ($e^{-}Å^{-2}$)
Fluence Rate or Flux	Rate at which a number of electrons pass through a unit area.	Electrons per square nanometre per second ($e^{-}nm^{-2}s^{-1}$). or Coulombs per square centimetre ($C^{-1}cm^{-2}$)
Dose	Ionising radiation energy deposited in a material per unit mass.	Grays (Gy).
Dose Rate	Rate of ionising radiation energy deposition per unit mass.	Grays per second (Gys^{-1}).

Table 2.3 Terminology of commonly used radiation units and their definitions

Original unit	Converted unit	Multiplication factor
$e^{-}nm^{-2}$	$e^{-}Å^{-2}$	0.01
$e^{-}nm^{-2}$	$Amps^{-1}m^{2}$	6.242
$e^{-}nm^{-2}s^{-1}$	$C^{-1}cm^{-2}$	62420

Table 2.4 Conversion factors for common fluence, flux and dose units

2.2.4. Implications of Radiation Damage

For many materials, radiation damage is a limiting factor for spatial or spectral resolution, meaning that detailed analysis at small length scales, or high spectral resolution remains a challenge.

Radiation damage manifests itself in many forms: destruction of crystallinity, loss of mass, atomic displacements, disrupted bonding. All of which have implications on the information that can be gathered using electron microscopy. For example, it would be remiss to implicitly trust compositional information from a sample shown to lose mass under irradiation. However, the conditions required for operation on electron beam sensitive materials often preclude high resolution imaging or spectroscopic studies.

Low beam currents mean that long exposure times would be required to form an image or spectrum of a given signal to noise ratio, increasing the likelihood of specimen motion or stage drift. Low beam currents make focussing by eye challenging, as images appear faintly on the viewing screen or camera, and hence achieving optimum focus can be time consuming and prone to error. Using short exposure times with a moderate beam current can introduce noise to images, which can reduce overall contrast.

Rather than using just the critical dose or fluence as a measure of a materials irradiation sensitivity, materials can be compared using the measurement of the smallest region from which meaningful signals can be acquired without being compromised by irradiation and electron beam-induced damage. This provides a measure of how electron dose limits the resolution permitted.

2.2.5. Dose Limited Resolution

Reducing the accelerating voltage is known to increase radiolysis but also increases elastic and inelastic scattering, thus the signal to damage ratio would appear to have no relation to accelerating voltage. This would suggest that there is no benefit to adjusting accelerating voltage in the microscope, however this is an oversimplification.

Instead Egerton (57) introduced the concept of the “dose limited resolution” (DLR) where the impact of microscope operation, detection hardware, specimen dimensions, and statistical noise are also considered. Here the dose-limited resolution is presented as the size of the smallest region from

which meaningful signals can be acquired. The DLR is demonstrated for low contrast imaging as:

$$\delta = \frac{(SNR)(DQE)^{-\frac{1}{2}}\left(\frac{FD}{e}\right)^{-\frac{1}{2}}(2)^{\frac{1}{2}}}{|C|}$$

(2.7)

Where δ is the DLR, SNR is the signal to noise ratio, typically ~5 to satisfy the Rose criterion (The Rose criteria state that for a signal to be considered significant, it should have an intensity at least 3-5 times higher than the background/noise level (85)). DQE is the detective quantum efficiency, which refers to the efficiency of a detector in converting incident electrons into an imaging signal. Low values of DQE correspond to detectors which require large incident currents to form images for example fibre optic coupled CCD detectors demonstrate a low DQE due to the inefficiency involved in illuminating the scintillator, losses through fibre optic transmission of the scintillator light, and losses in the CCD due to noise. F is the fraction of electrons collected by the detector, this is considered to be nearly 100% for CTEM phase contrast imaging, and ~25% for STEM wide angle bright field imaging in a non-aberration corrected system (86) (explained further in section 3.3.4), D is the dose (or more strictly fluence) applied to the specimen, e is the electronic charge and C is the absolute contrast. F can be approximated for an amorphous or polycrystalline specimen in bright field CTEM imaging when t is the specimen thickness and λ_e is the mean free path for elastic scattering as:

$$F = e^{\left(\frac{-t}{\lambda_e}\right)}$$

(2.8)

Through this, it is possible to see that by changing specimen thickness t or accelerating voltage (and thus the mean free path for elastic and also inelastic scattering), the electron collection efficiency can be improved. Egerton

presented this in Figure 2.19 for an organic specimen which reduces the produced image contrast exponentially on irradiation, this is common for organic specimens, which lose lattice integrity following an exponential decay where C = image contrast, C_0 is initial contrast, D is incident electron dose and D_c is the critical dose or fluence. This is demonstrated in equation 2.9.

$$C = C_0 e^{\left(-\frac{D}{D_c}\right)} \tag{2.9}$$

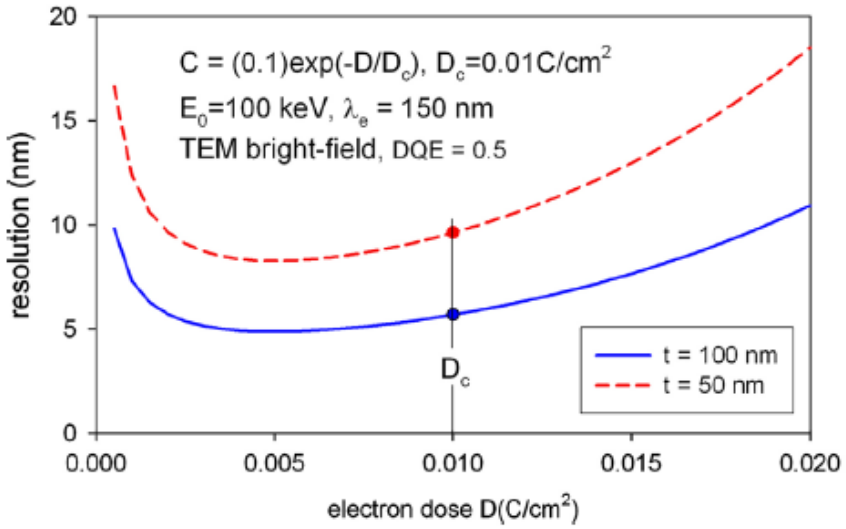

Figure 2.19 Dependence of DLR on incident electron dose, where SNR = 5, DQE = 0.5, C_0 = 0.1, λ_e = 150 nm and D_c=0.01C/cm^2 (typical of an organic specimen exposed to 100 keV electrons).

From Figure 2.19 it can be seen that by simply increasing the specimen thickness, the dose limited resolution increases by a factor of 2, due to the increased electron collection from the thicker specimen. This is due to the larger number of scattering events occurring, producing a larger signal, with the damage per unit volume being constant. This increases the signal to damage ratio.

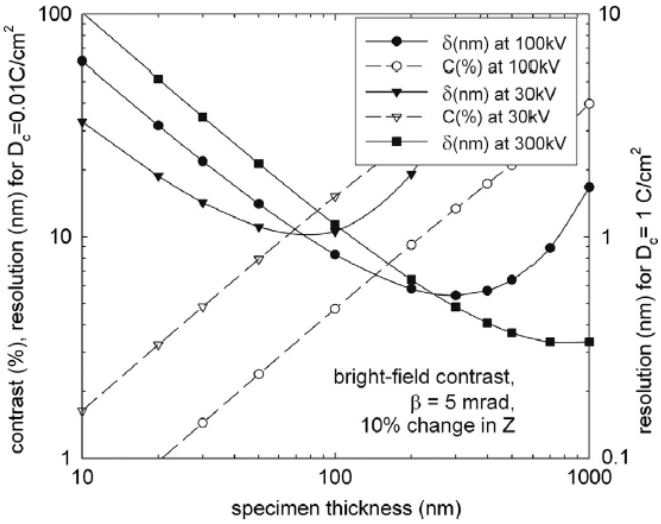

Figure 2.20 Influence of specimen thickness on the contrast (C) and dose limited resolution (δ) as a function of accelerating voltage.

By increasing the specimen thickness, the DLR will reduce and the contrast will increase, however at large thicknesses, F reduces as fewer transmitted electrons are collected, and dynamic diffraction effects become more significant. This means the DLR has an optimum thickness value (minimum DLR) and deteriorates above or below this, as is demonstrated in Figure 2.20. Higher accelerating voltages can be used to optimise this for thicker specimens due to the reduction in elastic scattering, however the optimum thickness for 300 kV operation is almost 1 μm, which would introduce chromatic aberrations (Figure 2.20). In thin specimens, lower accelerating voltages will provide higher contrast, but at the risk of higher radiolysis damage through increased inelastic scattering.

The implications of the dose-limited resolution are that the operating conditions of the microscope, and the specimen dimensions can be adjusted to extract the maximum amount of information permitted prior to damage onset. In addition, equation 2.7 also considers that changing from CTEM to STEM illumination may improve the DLR, as STEM photomultiplier detectors display an improved DQE compared to the CCD cameras used in CTEM imaging, however this may be balanced out by the reduced electron collection efficiency for STEM compared to CTEM. For example phase contrast STEM is ~25% efficient on an uncorrected STEM system and phase contrast CTEM is considered to be ~100% efficient (57, 87). There is the potential for a

different critical dose/fluence in STEM operation due to the change in illumination from continuous irradiation to “pulsed” irradiation when the probe moves away from a pixel. In this case the material may have the opportunity to dissipate charge build-up. This means that for an electron beam sensitive material, there may be benefits to not only adjusting the accelerating voltage and specimen dimensions but considering the choice of the illumination mode as well.

2.3. Observing and Quantifying Electron Beam Damage

This section summarises and discusses several different damage studies performed on either calcium carbonate or similar electron beam sensitive materials, including: organic crystals, hydroxyapatite bio-minerals, and asbestos.

A common term used when discussing beam damage is the characteristic dose or fluence (D_c) for a particular stage of damage in a material. The characteristic dose is the energy deposited in a material required for the reduction of a given parameter to 1/e of its original value, for example the reduction in diffraction spot intensity. A material can have several characteristic doses for different manifestations of damage, for example the change in composition measured by EDX may have a different characteristic dose to the reduction of crystallinity observed by diffraction. The characteristic dose can be used to compare the electron beam sensitivities of multiple materials, and can be used to correlate the sensitivity to chemical structures (88). Although as previously discussed, a characteristic electron fluence is more often reported in practice.

2.3.1. Imaging

Imaging theory is explained in detail in section 3.2, section 3.3 and section 3.5. This section will present some uses of CTEM imaging in the study of calcium carbonate based materials.

The change in appearance of a sample that is not subject to any other external stimuli, (i.e. use of a heated stage in the electron microscope, intentional

chemical reaction or in-situ stressing) can be used to identify the effects of electron beam-induced degradation. Under electron irradiation, particles may shrink or change in contrast, pores may form, and crystal facets may be damaged. Many of these are difficult to quantify accurately but can be a useful tool for probing the onset of electron beam damage. Some recently reported examples of electron beam damage in calcite are shown in Figure 2.21 and Figure 2.22.

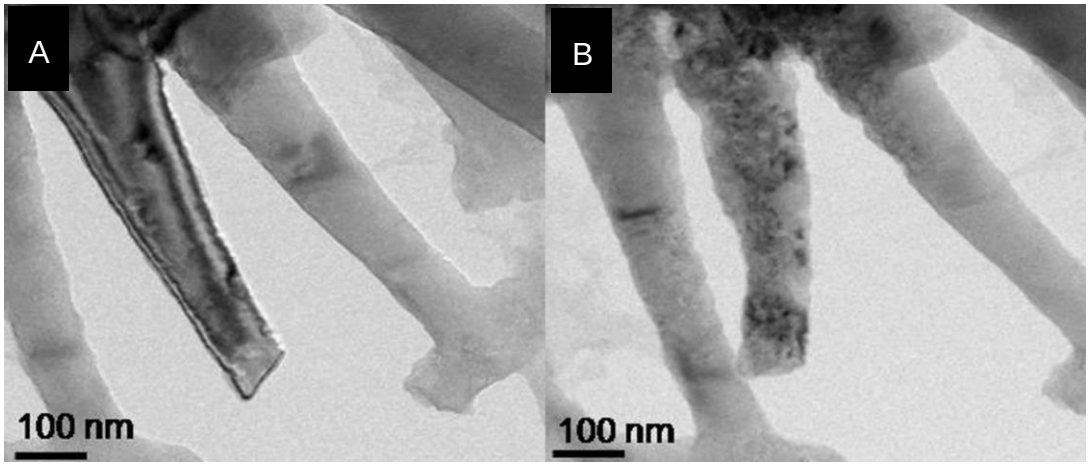

Figure 2.21 BFTEM of sectioned *E.Huxleyi* coccolith A) before and B) after irradiation at 300 kV, accumulated fluence ~3x10^{7}e^{-}nm^{-2} (89).

In a study by Hoffmann et al (89), (displayed in Figure 2.21), an irradiated region of $CaCO_3$ based coccolith significantly deformed under irradiation (Figure 2.21B) with a severe bend in the crystal. Bragg contrast in the pre-irradiated image showed that the central flake is a single crystal (Figure 2.21A). The presence of black spots on the irradiated flake was consistent with diffraction contrast from nucleated CaO crystallites (Figure 2.21B). Lighter regions on the irradiated crystal may show a reduction in sample thickness, consistent with mass loss.

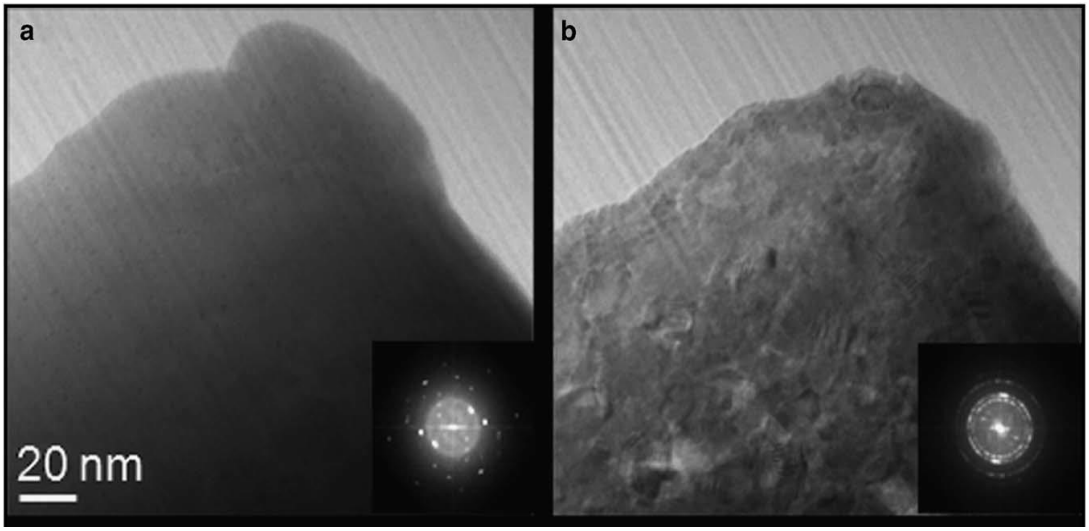

Figure 2.22 BFTEM of calcite following 80 kV irradiation, showing a mottled and damaged particle surface, accumulated fluence 1.4x10^{8} e^{-} nm^{-2} (90).

Golla-Schindler et al (90) showed in Figure 2.22, that under 80 kV irradiation a calcite specimen appeared to gain a mottled appearance and projected surfaces appeared rougher, consistent with pore formation and mass loss from the crystal facets. The inset Fourier transform showed that the particle has transitioned from single crystal calcite (Figure 2.22a), to polycrystalline calcium oxide (Figure 2.22b).

In a study on hole-drilling (a form of surface sputtering, often seen in STEM) in calcite by Murooka et al (58), the damage sites could easily be observed in both BF and DF-STEM imaging. An example of this has been previously shown and described in Figure 2.13.

2.3.2. Diffraction

Electron diffraction theory is covered in detail in section 3.4, this section presents some examples of diffraction studies of electron beam sensitive materials, including calcium carbonate.

Using electron diffraction, it is possible to observe the change in intensity of the diffraction spots or rings as a function of the accumulated electron fluence. In crystalline organic specimens under electron irradiation, the outer diffraction spots which correspond to smaller lattice spacings fade first, as

point defects are formed and weaker intermolecular bonds are broken, this initially affects short range ordering without significantly affecting long-range packing (68). Following this, the lower angle spots will begin to fade as more significant damage occurs. Eventually no crystalline diffraction pattern will be observed as the specimen becomes amorphised. Extracting the intensity of the diffraction spots and plotting them as a function of cumulative electron fluence can identify the fluence required to reduce the spot brightness to 1/e of original brightness, known as the critical fluence. An example of this can be seen in Figure 2.23 as part of a study by Eddleston et al (91) on theophylline, an organic crystal of interest to the pharmaceutical industry.

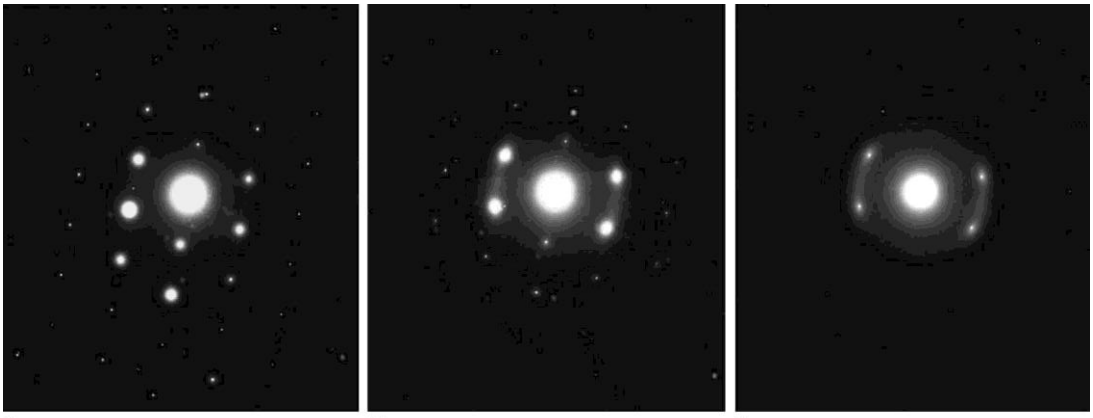

Figure 2.23 Loss of crystalline diffraction spots in the <100> zone axis diffraction pattern of theophylline (form II) after approximately 2, 20, and 40 min, SADP scalebar not provided (91).

The same technique was used in a study by Cattle et al (92), where the critical fluence was evaluated as a function of multiple experimental parameters to ascertain the optimal operating conditions for working with theophylline. It was observed that the optimal conditions were 300 kV accelerating voltage, liquid nitrogen cooled sample holder and a graphene support film under the sample. These conditions increased the critical fluence from 2500 to 4250 $e^{-}nm^{2}$ over standard conditions (200 kV, ambient temperature and continuous carbon film support grid). This is not a significant increase, being less than a factor of 2 greater than the standard conditions.

This is commonly observed in organic materials, but for calcium carbonate, the changes in the diffraction pattern follow a different route, single crystal

calcium carbonate diffraction spots have been shown to transform to polycrystalline calcium oxide diffraction rings. This is well known for calcium carbonate, though the onset of electron beam damage has not been thoroughly probed (93, 94).

Hoffmann et al (89) showed diffraction patterns of a calcium carbonate specimen prior to and following irradiation, to determine whether the specimen preparation route affected the electron beam damage of biological or geological calcium carbonate. They determined that neither FIB preparation nor etching with distilled water affected the electron beam sensitivity. However, they did not actually observe the onset of electron beam damage, instead showing that electron beam damage was present at the same high fluence. An example of the diffraction patterns produced are shown in Figure 2.24.

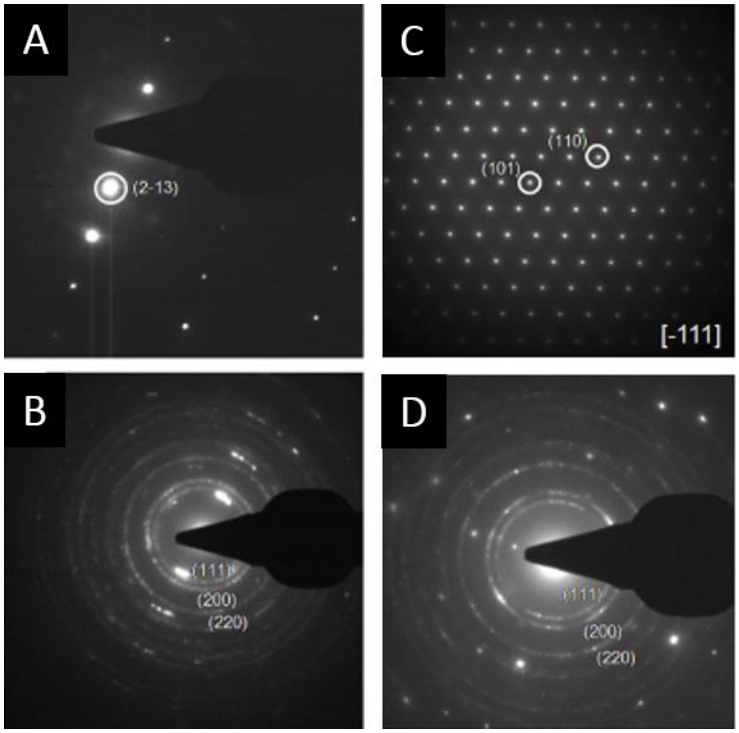

Figure 2.24 Selected area electron diffraction of A) biogenic calcium carbonate specimen prior to irradiation B) the same specimen following ~ $3x10^7$ e^-nm^{-2} at 300 kV in CTEM, where significant polycrystalline CaO formation is seen. C) geological calcite prior to irradiation, D) following ~ $3x10^7$ e^-nm^{-2} at 300 kV in CTEM, where the same CaO crystallisation is seen (89). SADP scalebar not provided.

Hoffmann showed that upon irradiation, single crystal calcium carbonate degraded into polycrystalline calcium oxide. Calcite crystallinity was

maintained, as in image D, both single crystalline calcium carbonate and polycrystalline calcium oxide can be seen coexisting, suggesting a progressive degradation which does not entirely disrupt the calcite crystallinity. From these results, it is apparent that to measure the onset of electron beam damage in calcium carbonate, the appearance of calcium oxide rings should be probed as a function of accumulated electron fluence.

2.3.3. Spectroscopy

An alternative method for quantifying damage is to quantify the ratios of characteristic elemental peak intensities in energy dispersive X-ray or Electron energy loss spectra of specimens under irradiation. As atoms are removed from the specimen through either radiolysis or sputtering, the X-ray or EELS signal intensity for that particular atom type will reduce. In addition to compositional quantification, EELS may also be able to show changes in bonding or co-ordination for specimens which do not lose mass on irradiation, by investigating the edge shape in features in the ELNES (Energy Loss Near Edge Structure). The underlying theories of energy dispersive X-ray spectroscopy and electron energy loss spectroscopy are presented later in section 3.6.1 and 3.6.2 respectively.

EDX

Eddisford et al (95) used EDX to characterise the damage of hydroxyapatite $Ca_{10}(PO_4)_6(OH)_2$ by plotting the peak ratios of Ca:P ratio (initially ~1:1.5) in the specimen as a function of electron fluence, to demonstrate the compositional changes seen observed irradiation, this is shown in Figure 2.25.

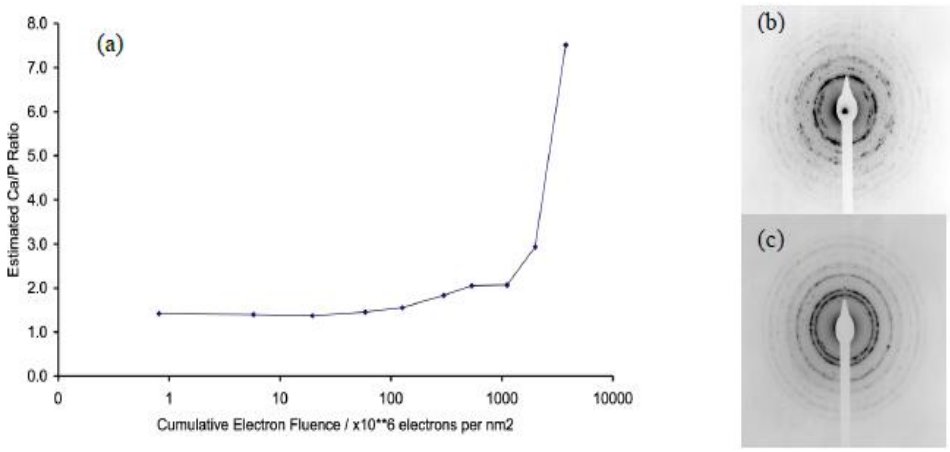

Figure 2.25 a) EDX ratios of calcium to phosphorous in hydroxyapatite. b) Diffraction pattern before and c) after irradiation at 200 kV (95).

They showed that following irradiation, the ratio of Ca to P increased due to phosphorous being removed from the sample by radiolysis, through which the material degrades from $Ca_{10}(PO_4)_6(OH)_2$ to CaO. A corresponding change in the diffraction pattern can also be observed between Figure 2.25b and c, where calcium hydroxyapatite spots have disappeared, and calcium oxide diffraction rings appeared.

Martin et al (96) presented an example of electron beam damage in asbestos (chrysotile) fibres, measured by EDX spectroscopy. They measured the peak intensities of magnesium to silicon from the initial composition of $Mg_3(Si_2O_5)(OH)_4$ when the fibres are irradiated. Through this they found the beam damage of chrysotile had a direct dose rate dependence, and that irradiating and blanking the beam between measurements to “pulse” the irradiation extended the lifetime of the fibres, presumably allowing the specimen to return to thermal equilibrium or dissipate charge build-up between measurements.

Electron Energy Loss Spectroscopy

The theory of EELS signal formation and collection is covered in section 3.6.2, the following section describes some uses of EELS to study electron beam damage in calcium carbonate-based materials.

Hoffmann et al (89) presented low-loss, carbon-*K*, calcium-$L_{2,3}$ and oxygen-*K* edge spectra of geologically derived calcite before and after beam damage occurs, shown in Figure 2.26. The most significant changes were seen in the low-loss and oxygen-*K* spectra, where the peak shapes and positions are altered. Changes in the low-loss spectrum are indicative of the influence of irradiation on the plasmon excitation behaviour in the specimen, with the spectrum showing a stronger and sharper plasmon resonance centred around 40 eV. Changes around 20-30 eV may be attributed to the Ca $M_{2,3}$ edge, situated at 25 eV, showing more strongly from the loss of oxygen and carbon low-loss signal. The changes in the oxygen-*K* edge spectra correspond to changes in the bonding characteristics of the carbonate group associated with the excitation and fission of bonds. The carbon *K*-edge peak at ~305 eV reduced in intensity following irradiation, likely related to the loss of carbon through carbon dioxide out-gassing. A residual carbon signal remains in the damaged spectrum, as it is uncertain whether this spectrum represents an entirely damaged specimen (complete conversion to CaO is shown below by Golla-Schinder et al), or whether the carbon signal is produced by a carbonaceous contaminant or the support film. The calcium $L_{2,3}$ edge showed very little change, suggesting no loss of calcium.

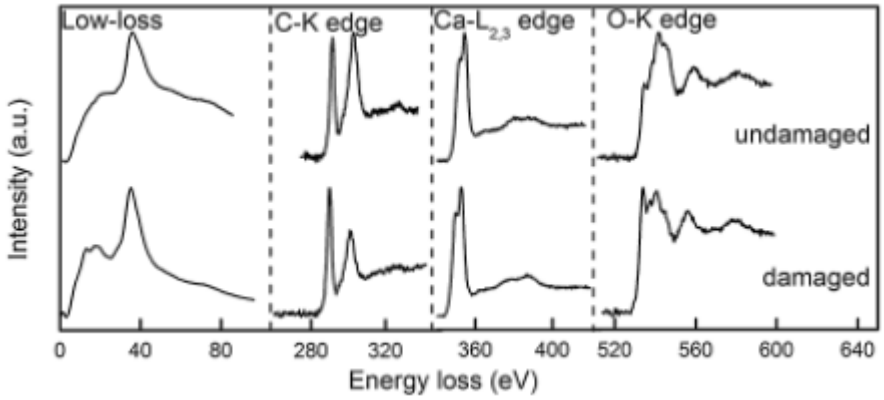

Figure 2.26 Core loss and low loss EELS spectra of Iceland Spar calcite under irradiation at 300 kV, accumulated fluence > 10^7 e^-nm^{-2} (89).

Golla-Schindler et al (90) presented a time-resolved EELS study of the same carbon-*K*, calcium $L_{2,3}$ and oxygen-*K* edges of geologically derived calcite, this study showed much more significant changes to the spectra over a longer experiment (90 mins of irradiation at 80 kV with a flux of $4x10^4$ $e^-nm^{-2}s^{-1}$).

Irradiation proceeded to the extent that the carbon-*K* edge signal became almost entirely eliminated, consistent with complete conversion of $CaCO_3$ to CaO. Significant changes were again be seen in the oxygen-*K* edge, corresponding to the loss of CO_2 and the destruction of the carbonate group (Figure 2.27c).

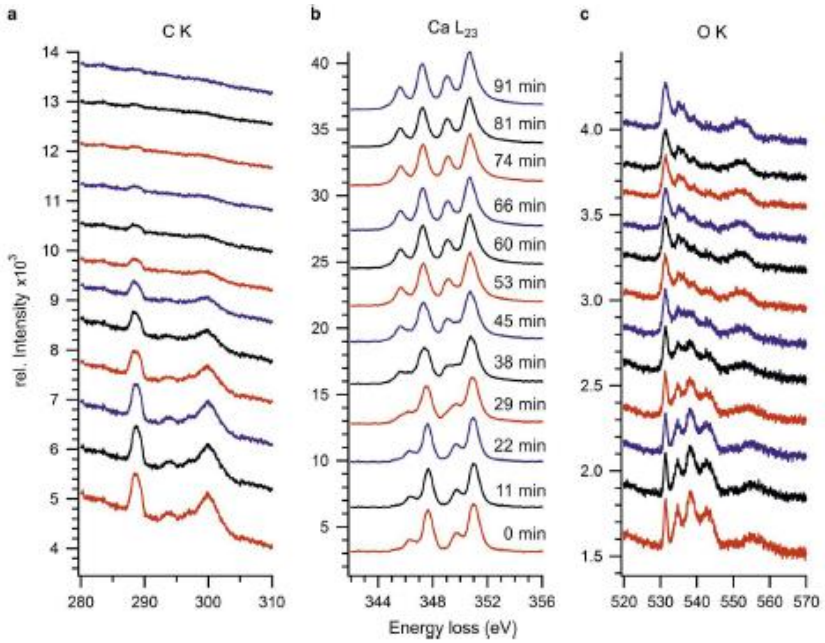

Figure 2.27 Raw, unprocessed time-resolved EELS spectra of calcite under irradiation at 80 kV and $4x10^4$ $e^-nm^{-2}s^{-1}$. Time series proceeds from the bottom to the top of the figure.

Walls et al (97) presented a study on hole-drilling in STEM of calcite, using EELS to investigate the extent of mass loss occurring in Figure 2.28. In this study, characteristic signals of the carbon-*K*, calcium-*L* and oxygen *K*-edges were used as indicators of mass loss, reduction of the signal intensity was assigned to the mass loss of that element. The calcium signal showed a small reduction under irradiation indicating some sputtering, though this was not significant and may be attributed to spectrum noise. There were more significant changes in the intensity of the carbon and oxygen *K*-edges, presumably from the loss of carbon dioxide through radiolysis.

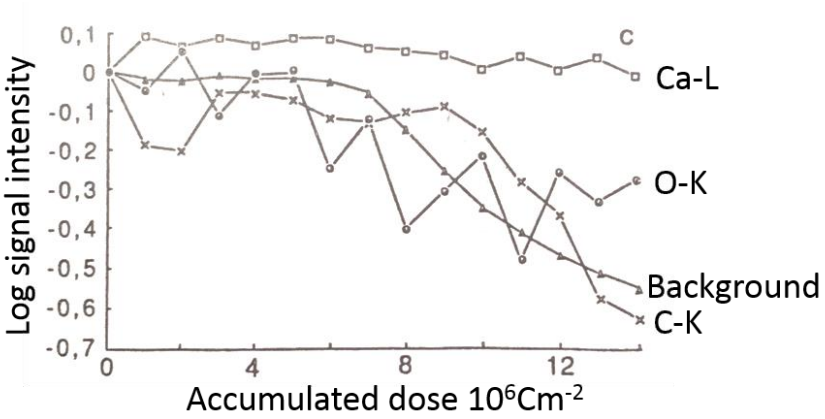

Figure 2.28 Calcite EEL spectrum integrated edge intensity plotted as a function of accumulated dose under 100 kV irradiation (97). 1 Cm^{-2} is equivalent to 6.25 $e^{-}nm^{-2}$.

Murooka and Yuan (98) used EELS to probe the appearance of a feature in the carbon *K*-edge EELS in calcite as a function of accumulated fluence. The feature, labelled B_D (289.8 eV) was only visible in damaged samples. The appearance of B_D was correlated to the reduction in intensity of a neighbouring feature, labelled B_π (290.3 eV), the reduction of B_π was consistent with changes in the carbon-oxygen bonding in the carbonate group of calcium carbonate. A graph of integrated intensity of both BD and B_π is shown in Figure 2.29.

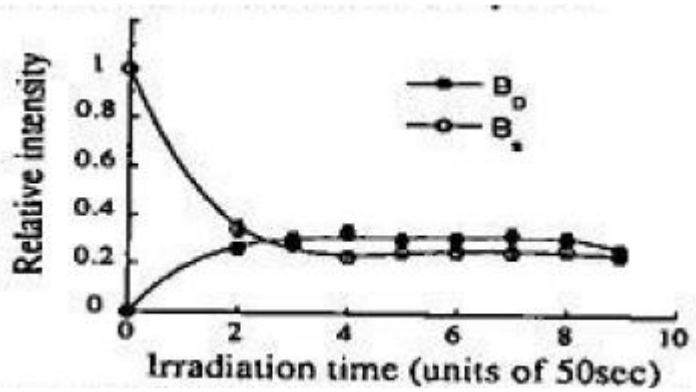

Figure 2.29 Integrated intensity of BD and Bπ features in the carbon-K edge in irradiated calcite, electron flux ~10^5 $e^{-}nm^{-2}s^{-1}$ electron beam voltage 100 kV. The points which decrease in intensity correspond to the Bπ feature in the carbon K-edge (98).

From Figure 2.29, between 0 and 100 seconds, the sample was significantly degraded, this corresponded to an accumulated flux of ~10^7 $e^{-}nm^{-2}$ at 100 kV.

Due to the low time resolution of this dataset, it is not known exactly when this degradation occurred.

From the previously presented damage studies on calcium carbonate, the apparent damage threshold is in the region of ~10^7 e^-nm^{-2}, however, these studies have used various voltages and criteria for determining damage., Thus it is necessary to investigate the electron irradiation-induced degradation of calcium carbonate with more closely defined indicators of damage.

2.4. Electron Beam Damage Mitigation Techniques

Several methods are currently used to reduce the impact of electron beam damage, these include:

2.4.1. Low-Dose Electron Microscopy

Whilst the electron dose can be reduced by increasing the microscope accelerating voltage, low-dose electron microscopy more typically involves reducing the incident electron fluence, to reduce the dose.

In CTEM, the incidence fluence can be reduced in several ways: The beam can be spread over a large area using the condenser lens system. A small condenser aperture can be used to exclude a larger proportion of the beam prior to reaching the specimen. The electron source extraction voltage can be reduced, this reduces the number of electrons which enter the high-tension accelerator. The spot size can also be reduced to reduce the electron beam diameter, a small spot size means the beam diameter will be small, and thus will have to be spread.

In STEM, the fluence can be reduced by: Controlling the incident probe current using the spot-size controls, or source extraction voltage. The pixel dwell time can be reduced, so that the probe spends a shorter amount of time on each pixel. The scan region size can be increased, which will increase the specimen pixel size and reduce the number of electrons per unit area.

In some S/TEM systems, complete continuous control of the probe or beam current is not possible due to the electron optical design. However, a

monochromated electron source will permit the complete continuous control of probe/beam current, meaning that any chosen probe/beam current can be used without significant impact on the alignment, beam/probe size, or focus (99).

Buban et al (100) presented an investigation into low-dose aberration corrected STEM imaging of $SrTiO_3$, they showed that they could reduce the fluence by reducing the probe current and pixel dwell time without impacting the image resolution. They found that the images were affected by streaking caused by the maximum readout speed of the STEM detector system, the maximum speed of the scanning coils, or noise from a small probe current. The images were not visually interpretable, though they did display features down to 2 Å, when they were processed by FFT.

The following sections introduce other techniques used alongside or as an alternative to reducing the probe current or reducing the pixel dwell time.

Subsampling, Sparse Sampling, or Compressed Sensing with Image Reconstruction

Subsampling is a relatively new technique in low-dose STEM imaging, based on the use of compressed sensing where the rastered beam is blanked or deflected to reduce the pixel count of the image. Subsampling reduces the overall incident electron fluence and thus allows the charge or heat to dissipate before the next raster. Subsampling is summarised in schematic form in Figure 2.30, where only the red pixels are sampled. Subsampling can reduce the scan fluence by up to 95%, but in practice using 20% of the original scan fluence will still yield high quality images when reconstructed, as seen in Figure 2.31.

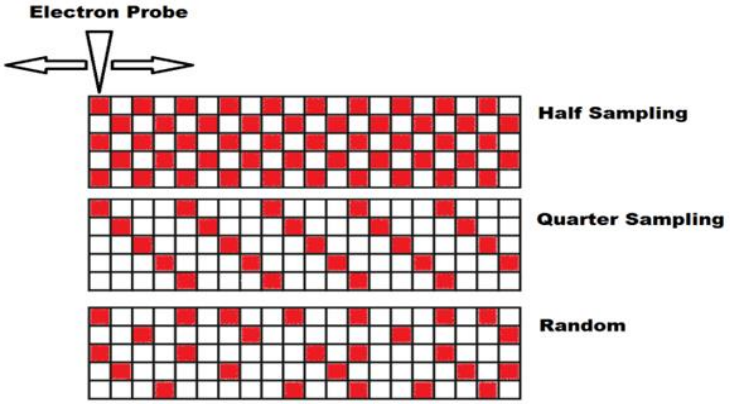

Figure 2.30 STEM subsampling regimes. Red pixels indicate pixels where signals are collected.

Subsampled images require computational reconstruction prior to interpretation, these reconstruction algorithms, which include “in-painting” generally require the subsampling to be random, which complicates the scan hardware and sampling required. In painting allows for the sparse sampled image to be reconstructed to a state that is more easily interpreted by filling in the missing pixels. An example of random subsampling and in-painting can be seen in Figure 2.31, on a $SrTiO_3$ specimen.

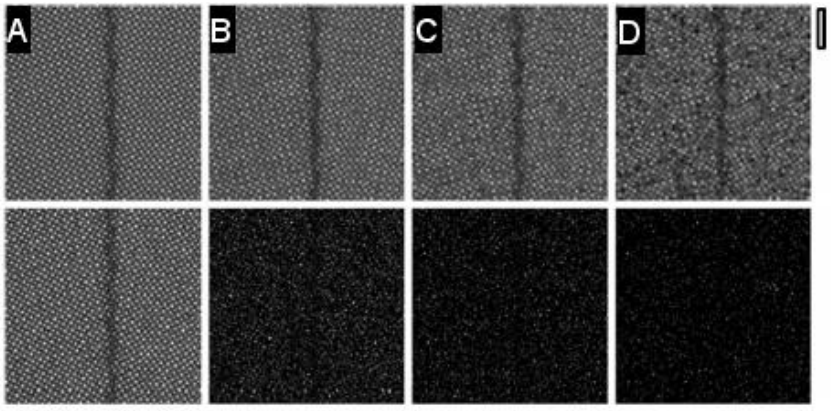

Figure 2.31 A-D (left to right) – Examples of subsampling and reconstruction of a grain boundary in $SrTiO_3$. A) Fully sampled, B) 20% sampled, C) 10% sampled D) 5% sampled. The top half shows the reconstructed image and the bottom half shows the subsampled image prior to in-painting (101).

Though this method is new, it shows considerable promise, major details can still be seen at around 5% sampling and fine detail is seen at 20%. The major limitations of this method include the susceptibility to artefacts and the large

computational requirements for the reconstruction process. However, as with any reconstruction, having a poor image to begin with will yield a poor result.

Kovarik et al (102) used a high flux electron probe with sparse sampling on calcium carbonate. While the probe current was high, the flux was only applied to 20% of the specimen pixels, meaning that the specimen as a whole received relatively little dose, the partially sampled image was then reconstructed, this is shown in Figure 2.32.

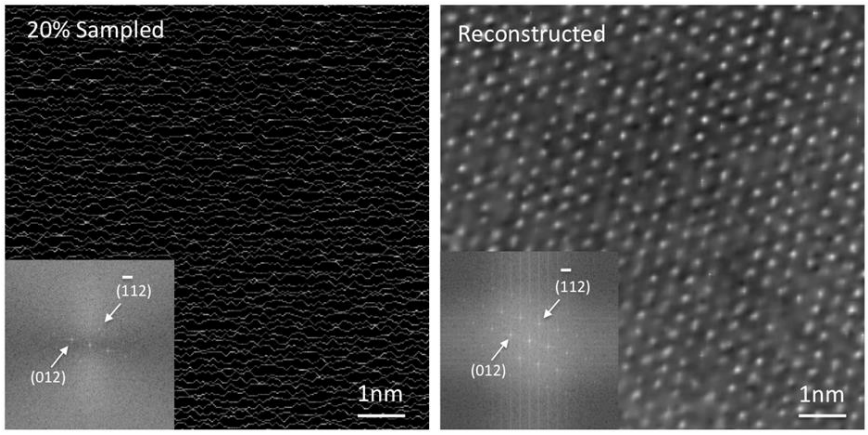

Figure 2.32 Left) 20% sparse sampled HAADF image of calcium carbonate. Right) reconstructed HAADF image of calcium carbonate, showing localised amorphisation after an accumulated fluence of $3.2x10^5$ e^-nm^{-2}. The inset FFT shows the lattice spacings visible in the image (102).

In this study, an atomic resolution image of a calcite sample was taken at 200 kV with an accumulated fluence of $3.2x10^5$ e^-nm^{-2}. At this accumulated fluence, some localised amorphisation was visible as blurring in the image, the authors noted that subsequent images showed significant amorphisation and beam damage although did not provide images of this. This would again support a critical fluence of the order of 10^7 e^-nm^{-2}.

Non-rigid registration and frame averaging

Non-rigid registration is a technique developed to reduce scan distortions in STEM imaging, it allows for drift, scan distortions and mechanical instabilities to be removed from images, by summing multiple sequentially acquired images together and applying a registration algorithm (103). This means that multiple low-fluence images can be acquired and then summed to form higher

fluence images. Images with a low signal to noise ratio, which cannot be visually interpreted, can hence be summed to form an image with a higher signal to noise ratio and thus be easily interpreted (104).

Frame averaging is useful for materials which display a direct dose rate dependence of damage, meaning that a low fluences can be used for imaging and then the frames summed to form a high fluence image (105).

2.4.2. Cryo-EM

For Cryo-TEM imaging, particles are suspended in an aqueous solution then plunge frozen in liquid ethane, to avoid ice crystallisation and the redistribution of material. This forms an amorphous ice phase that holds the particles in place. Cooling the sample helps reduce localised heating and has also been shown to reduce radiolysis by slowing down atomic movements (72). Cryo-TEM is a common biological technique, but is becoming more widely used for non-biological specimens (106), nanomaterials (107) and investigations into nanoparticle uptake into cells (108).

Cryo-TEM is commonly used for structural biology and protein crystallography as high-resolution images of averaged protein structures can be determined without having to form large crystals for X-ray analysis. By avoiding crystallisation, it is possible to determine structures in representative conformations and arrangements and to more rapidly produce structural models of proteins and biological media (109, 110).

The spatial resolution of cryo-TEM is less than for standard specimens in CTEM/STEM due to the thicker samples and amorphous scattering from the ice matrix. However recently, spatial resolutions of 2.2 Å have been demonstrated which show information on structural water molecules and protein-ligand hydrogen bonding (111).

Whilst the amorphous ice matrix reduces specimen damage through heating, it may also reduce diffusion processes and also damage reaction rates, however, it does not completely protect against knock on damage. As a result, biological samples are susceptible to damage, leading to the practice of

imaging thousands of particles and averaging them to get information on their structure, this is known as Single Particle Analysis (112). However, single particle analysis can only be applied to samples with repeatable structures, which can be assumed to be the same, allowing them to be averaged. As such, this will not work with conventional nanoparticles or soft matter samples as their structures and morphologies will have differences, and averaging non-repeating structures will provide spurious structural data (113).

Another concern is that the cooling of specimens may lead to a phase transition or a different structural conformation. In this case it would be pertinent to compare experimental data with simulated structures or to perform multiple experiments to compare structures (114).

Evans et al (115) performed low-dose and cryo-STEM on organic crystalline specimens, however, the low signal to noise ratio typical of both low-dose and cryo-STEM images meant that significant image reconstructions had to be undertaken before analysis or image interpretation was possible.

As previously mentioned, Pouget et al (49) used cryo-TEM to investigate the early stages of nucleation in calcium carbonate. By using low flux SAED, along with bright field CTEM imaging, they were able to observe the crystallisation of amorphous calcium carbonate to vaterite.

Cryo-protection, which is related to cryo-TEM, does not involve embedding the sample in an amorphous ice matrix, instead the sample is actively cooled whilst in the microscope. This was successfully implemented in a study of organic crystals by Cattle et al (92). It was shown that by cooling the organic theophylline specimens to -190^{o}C, the critical electron fluence increased by only 10%, though when coupled with the use of a graphene support film, the critical fluence increased by 70%.

2.4.3. Scanning Moiré Fringe Imaging

Scanning moiré fringe imaging (SMF) is a relatively new technique for the imaging of crystalline electron beam sensitive materials. SMFs are formed from the interference of two overlaid lattices, which must be similar in

periodicity but not identical. This produces a set of Moiré fringes which effectively represent a magnified (and possibly rotated) image of the real lattice.

In SMF, the artificial scanned lattice produced by the rastered electron probe interferes with the atomic lattice of a crystalline material. A schematic example produced by S'ari et al (116) is shown below in Figure 2.33, where the artificial lattice and real lattice can be seen.

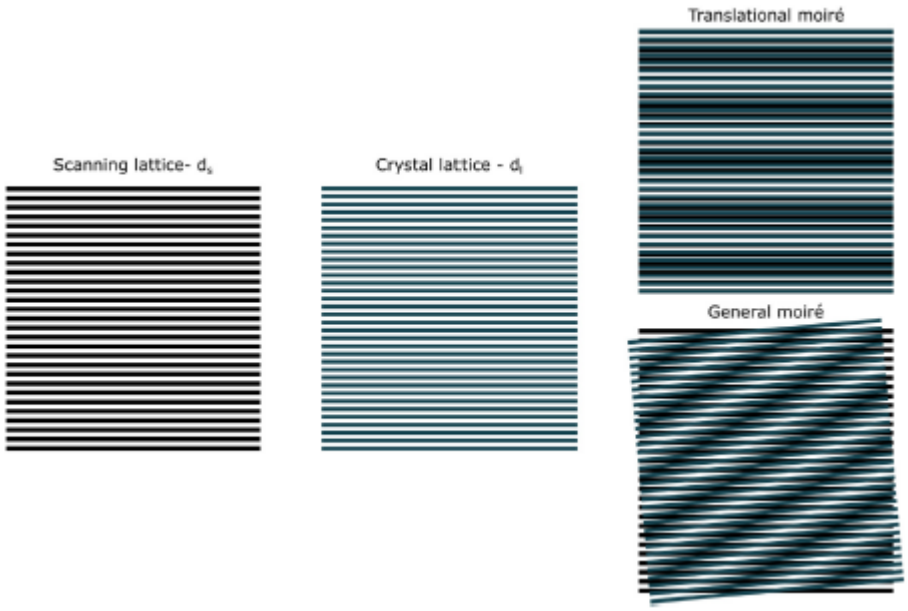

Figure 2.33 The scanning lattice (d_S) and crystal lattice (d_I) of similar sizes overlay to form translational moiré fringes, with no angular mismatch, and general moiré fringes with an angular mismatch.

The magnification of the SMF is related to three parameters, the STEM magnification, which determines specimen pixel size and thus d_s (the scanning lattice spacing), the size of the crystalline d-spacings in the real lattice d_l and β, the angular relative angle between d_s and d_l (117).

S'ari et al (116) have demonstrated SMF imaging on crystals of theophylline, where SMF imaging produced indirect phase contrast lattice imaging, where direct lattice imaging was precluded due to electron beam damage. Their imaging was able to demonstrate the presence of crystalline defects, as the moiré fringes magnified these features.

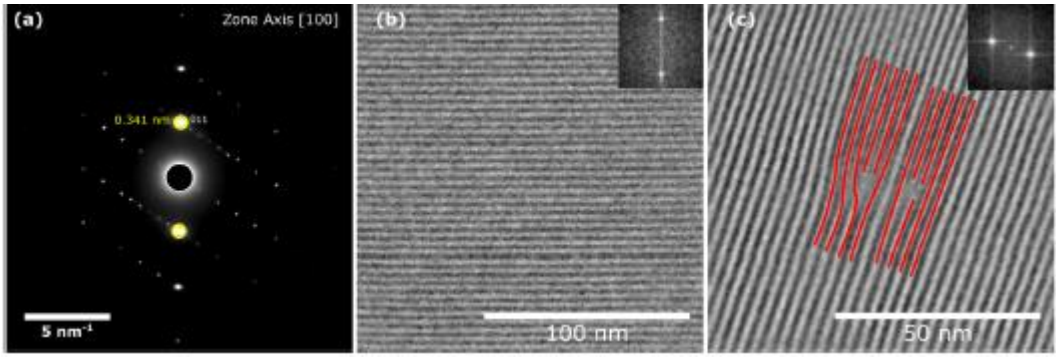

Figure 2.34 SMF of theophylline A) SAED aligned along the <100> zone axis, the scan direction was aligned to the 0.34 nm (011) reflection B) BF-STEM image of the SMFs where d_s = 0.33 nm and d_l = 0.34 nm. C) Fourier filtered images of a different crystal area showing magnified dislocations in the SMFs, using the same d_s and d_l. Scan fluence exceeds 29 $e^{-}Å^{-2}$ for each image.

The benefits of using SMF imaging is that lattice information can be acquired at lower magnifications than direct lattice imaging. This means that a lower fluence is received by the specimen, as STEM fluence is directly proportional to magnification. However the downside to using SMF imaging, is that the specimen can receive significant irradiation from the alignment process, where the SAED is collected and the STEM scanning lattice aligned before imaging can commence (116).

2.5. Directions for Research

There is significant scope for CTEM/STEM based research into calcium carbonate. An area of interest to industry is the CTEM/STEM characterisation of calcium carbonate-based fuel detergent particles. Research collaborators and the detergent particle manufacturers are interested in correlating specific studies of the structure of these particles with bulk analysis from conventional lab-based spectroscopies and synchrotron X-ray measurements. CTEM/STEM based studies will be able to contribute information on whether the particles display crystallinity in all particles as a crystalline core, or whether there are individual discrete crystalline particles dispersed amongst an amorphous majority.

However, as the fuel detergent particles are a challenging specimen due to their size (<10 nm) and weak image contrast, it would first be pertinent to

measure and optimise microscope operation using a pure crystalline calcium carbonate model system. This would be used to investigate the progression of electron beam damage in calcium carbonate, highlighting its effects on crystal structure, particle size and composition as a function of electron fluence, to produce a baseline threshold measurement of damage in calcium carbonate. From this an indicator of electron beam damage can be chosen. This should then be used to determine whether the specimen is too badly damaged to continue specific analytical techniques.

The fuel detergent particles can be investigated with optimised microscope operating conditions and an appreciation of the influence of electron irradiation on the potential results obtained. The particles can be characterised with the intention of measuring particle core size and determining the presence of any crystallinity and its structure, with the knowledge that irradiation effects are minimised or at least considered. Thus, the findings of this literature review map onto the project aims previously mentioned:

- Chapter 5 presents the synthesis and solid-state characterisation of the calcite reference specimen. This chapter also demonstrates the electron induced irradiation damage of calcite and the selection of damage thresholds.
- Chapter 6 presents the optimisation of the microscope operating conditions, where the chosen damage thresholds for calcite are investigated at different accelerating voltages and illumination modes.
- Chapter 7 shows the characterisation of the fuel detergent particles through conventional analytical techniques, and through low-dose CTEM/STEM imaging and electron diffraction. In addition, this chapter also shows the determination and quantification of the presence of discrete crystallinity in the nominally amorphous material system.
- Chapter 8 demonstrates the solvent-induced degradation of the fuel detergent particles through the application of time-resolved low-dose CTEM/STEM imaging and diffraction, along with conventional analytical techniques.

Chapter 3. Experimental Theory

This chapter summarises the background theories of the characterisation techniques used, along with the physical foundations of transmission electron microscopy and image contrast formation.

3.1. Transmission Electron Microscopy

3.1.1. Background

The transmission electron microscope was invented in 1931 by Ernst Ruska and Max Knoll, it was based on work by Hans Busch who demonstrated that magnetic fields could act as lenses for electrons, allowing for the focussing of electron beams (118). This was then developed into the conventional TEM which by 1933 was able to surpass the resolution of light microscopes (about 550 nm)(119-122).

The principle behind electron microscopy is that the wavelength of the radiation limits the resolution, so by reducing the wavelength, smaller features can be resolved. This is shown for light by the Abbe equation shown as equation 3.1, where d is the spatial resolution and λ is wavelength (123). NA corresponds to the numerical aperture, a dimensionless number that characterises the maximum half-angle at which light can enter the lens/optical system:

$$d = \frac{\lambda}{2n\,sin\,\alpha} \approx \frac{\lambda}{2NA}$$

(3.1)

The development of the TEM was based on the de Broglie hypothesis (124), that matter in motion can exhibit wave-like behaviour and that the wavelength is related to the kinetic energy as λ is wavelength, m is the rest mass of a particle at velocity v, and h is Planck's constant.

$$\boldsymbol{\lambda = h/mv}$$

(3.2)

By increasing the kinetic energy and hence velocity of electrons through increasing the accelerating voltage, their wavelength would decrease and thus the resolution would improve following equation 3.3 (124), where m_0 is the rest mass of an electron:

$$\lambda_e \approx \frac{h}{\sqrt{2m_0\left(1+\frac{E}{2m_0c^2}\right)}}$$

(3.3)

This led to the development of microscopes that use high voltages to accelerate electrons to high velocities. Generally, CTEM/STEMs operate between 80 and 300 kV, giving electron wavelengths of between 4.1 pm and 1.9 pm respectively, however the actual resolution is limited by lens aberrations and mechanical stability (see section 3.1.3).

Following Ruska and Knoll's CTEM development, Manfred von Ardenne redesigned the instrument to place the image forming lenses above the specimen, as the electrons passing through the specimen would only need to be collected, not focussed, this was an early attempt at STEM imaging. Following further development, these ideas helped form the basis of Scanning Electron Microscopy (SEM) (125), for the surface analysis of materials.

Albert Crewe developed the high resolution STEM in Chicago during the 1960s (4). Through realising the shortcomings of conventional thermionic electron sources, field emission sources were investigated, which offer a lower electron energy spread and higher brightness. This, tied in with improvements in vacuum technology, ultimately gave the Crewe STEM the resolution that Ardennes's prototypes lacked, allowing for the imaging of isolated thorium and uranium atoms on a carbon film in 1970 (126). Crewe further developed his STEM prototypes, eventually allowing for motion pictures of atomic movements and interactions, and ultimately sub-nanometre spatial resolution (127).

3.1.2. CTEM and STEM Hardware

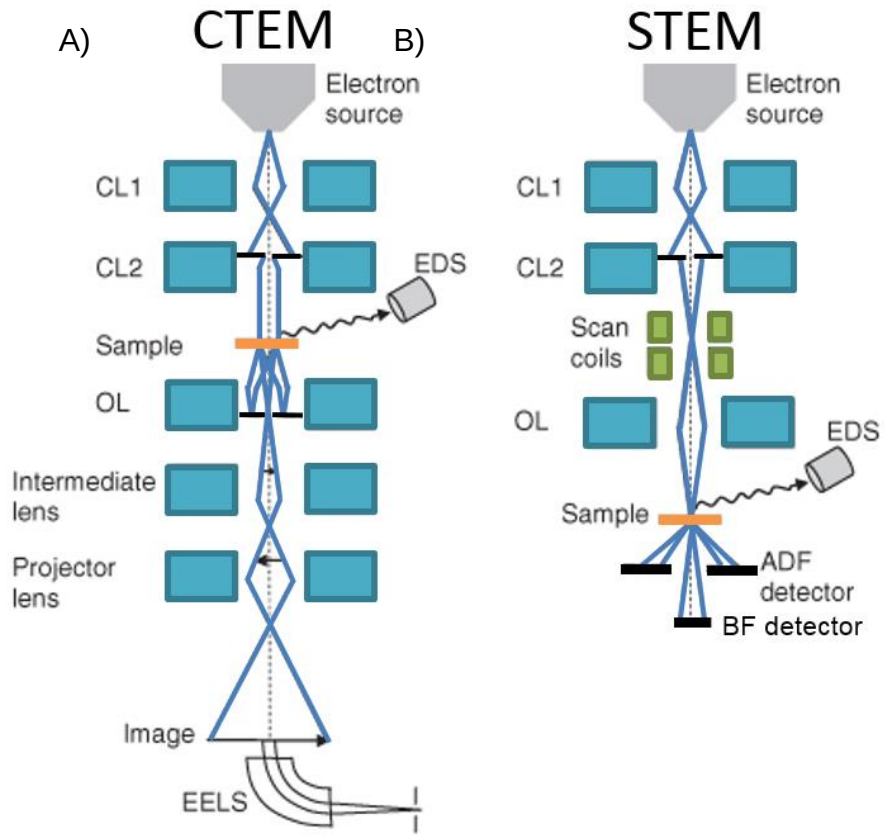

Figure 3.1 Schematic representation of (A) CTEM and (B) STEM instruments, the blue line corresponds to the electron path, CL corresponds to condenser lens, OL corresponds to objective lens (modified from (128)).

Conventional TEM (Figure 3.1A) uses a parallel beam of electrons to illuminate a specimen, images are formed by an objective lens (OL) and projected onto a CCD or CMOS camera. Changing between imaging and diffraction in CTEM involves either projecting the back focal plane (for diffraction) or the image plane (for imaging) of the OL onto the viewing screen/camera, as both the diffraction pattern and image are simultaneously present in the microscope (Figure 3.2).

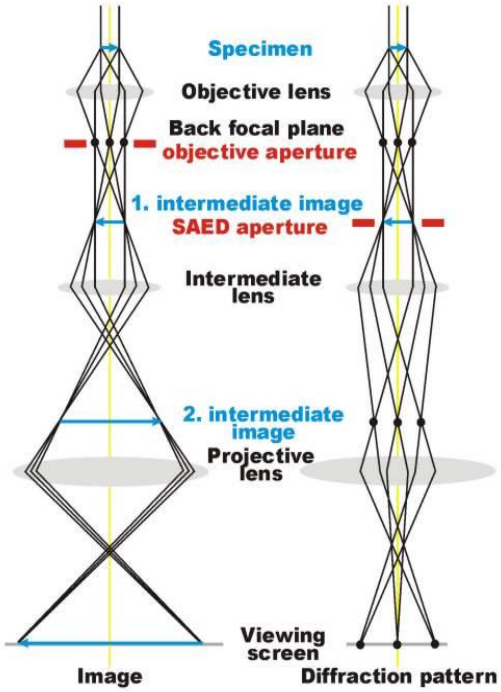

Figure 3.2 Schematic representation of Left) CTEM bright field imaging and Right) selected area electron diffraction (129)

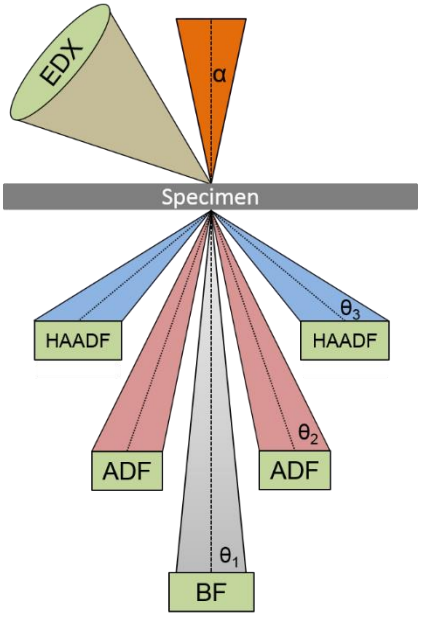

Figure 3.3 Schematic representation of STEM imaging detector positions, where α = Probe convergence semi-angle, θ_1 = Bright field detector angle, θ_2 = ADF detector angle, θ_3 = HAADF detector angle. For EELS measurements, the BF detector is retracted, and the beam passes into the EEL spectrometer.

STEM systems (Figure 3.1B) form images by rastering a focussed convergent probe across the specimen. This makes the imaging system very flexible as multiple imaging signals can be acquired at once. As the detectors do not

need to be spatially resolved, bright field and dark field images can be collected at the same time with suitably designed detectors. As the probe is rastered, it also means that elemental or chemical information can be spatially resolved, producing maps of elemental distribution, or bonding characteristics. An example of typical STEM detector configurations is shown in Figure 3.3, the detector collection angles can be changed by adjusting the strength of post specimen projector lenses. Typical STEM detector collection semi-angles are in the region of ~7 mrad for bright field, 17-100 mrad for annular dark field, and 80-200 mrad for high angle annular dark field imaging. For STEM-EELS measurements, the bright field detector is retracted to allow for the electrons to pass into the spectrometer.

3.1.3. Aberrations

Lens aberrations are one of the major limiting factors in terms of microscope resolution and contribute to the reason electron microscopes do not resolve at the electron wavelength (~1.97 pm for 300 kV electrons). Lens aberrations cause a deviation between intended focus and actual focus for a proportion of scattered electrons. Lens aberrations are caused by anisotropy in the magnetic fields of the lenses, and can be corrected for using systems of multipole magnetic lenses. Two of the more commonly encountered lens aberrations are outlined below.

Chromatic Aberrations

Chromatic aberrations (C_c) are formed when there is an energy spread of the electrons used for imaging, this means that the fixed lens cannot focus all electrons to the same point. This results in electrons coming from a point on the specimen, form a disc in the image, reducing resolution. The formation of chromatic aberrations are shown in Figure 3.4.

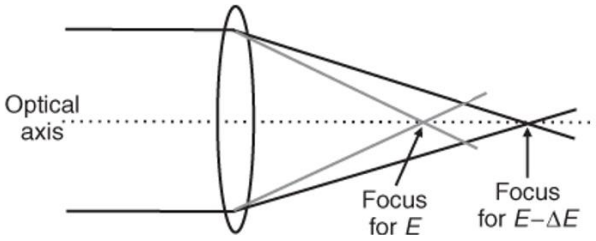

Figure 3.4 Ray diagram showing chromatic aberration formation (130).

Chromatic aberrations can be reduced by using a monochromator on the electron source, to ensure that incident electrons have a relatively small energy spread. Chromatic aberrations are a more significant problem when working with thick specimens, as the specimen itself induces energy shifts to the transmitted electrons, through plasmon excitation and core loss events.

Spherical Aberration

Spherical aberrations (C_s), are formed by electrons passing through the lens magnetic field off the optic axis. Electrons passing through the edge of the lens are focussed to a different point than those passing through close to the optic axis. C_s is the most significant detriment to resolution.

Image formation due to spherical aberrations is shown in Figure 3.5, where the focal point of the electrons further from the optic axis deviates from the on axis Gaussian focus point, electrons further from the optic axis are deflected more strongly and are focussed more strongly.

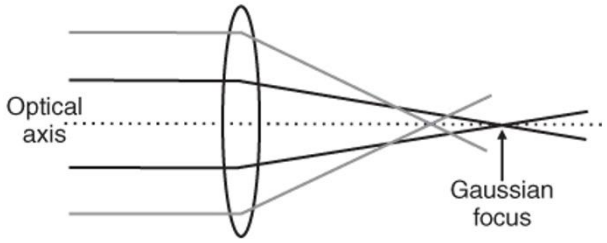

Figure 3.5 Ray diagram showing the impact of spherical aberration on image formation (130).

Spherical aberrations can be corrected for in both CTEM and STEM, C_s aberration correctors are known as “image correctors” for CTEM and “probe correctors” for STEM systems, microscopes with both image and probe correction lenses are known as “double corrected”. Correcting for C_s in STEM can mean that a larger probe convergence angle can be used and thus smaller probes, and a higher probe current can be used without compromising probe size, when compared to non-aberration corrected microscopes. A large probe convergence angle makes the assumption of reciprocity between CTEM and STEM more valid. Reciprocity theory is covered in section 3.3.4

3.1.4. The Ronchigram

The Ronchigram is a shadow image of the specimen formed by a convergent probe in the diffraction plane, the Ronchigram is the zero-order diffraction disc of the convergent beam electron diffraction (CBED) pattern. The Ronchigram is highly sensitive to STEM probe focus and aberrations, as such it is commonly used to focus and align the probe prior to STEM imaging.

The Ronchigram is a highly magnified image of the specimen, the magnification and image contrast is focus dependent. A well aligned Ronchigram should have a central region with constant intensity, over which the probe forming aperture should be placed to block aberrated rays, this is shown by feature 3 in Figure 3.6. Astigmatism in the probe forming lens will distort the shape of the Ronchigram, making it non-symmetrical, this can be easily diagnosed and corrected for using lens stigmators.

The outer ring-shaped features in the Ronchigram are the rings of infinite magnification and are formed by chromatic aberrations. These are shown below in Figure 3.6 as 1) and 2) respectively.

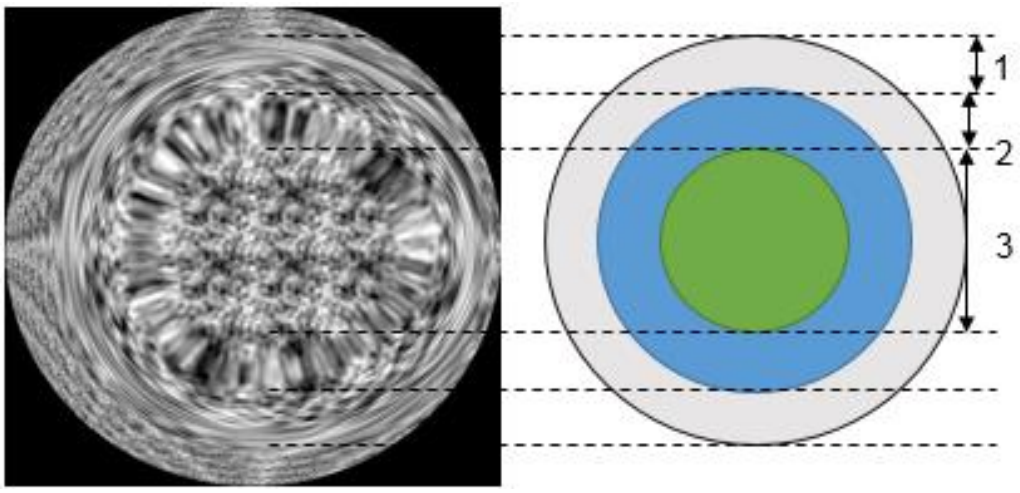

Figure 3.6 Simulated Ronchigram for an amorphous specimen (131). 1) corresponds to the ring of infinite radial magnification, 2) is the ring of infinite azimuthal magnification and 3) is the magnified shadow image of the amorphous specimen (132).

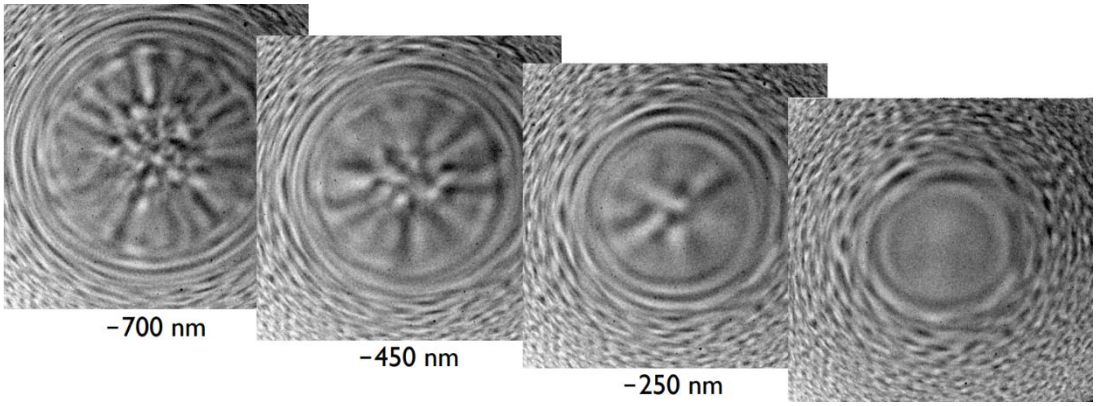

Figure 3.7 The influence of defocus on the electron Ronchigram on an amorphous carbon film, as defocus is reduced the rings of infinite magnification decrease in size, at their minimum the focus is similar to Scherzer defocus in BF-CTEM (132).

In Figure 3.7, the effects of adjusting probe focus on the Ronchigram can be seen, at optimum focus (on right hand side) the central region shows almost flat contrast, this flat central region is the aberration free optimum probe diameter. In a microscope without aberration correcting lenses, the optimum probe convergence semi-angle is of the order of ~10 mrad, whereas in a spherical aberration corrected probe, it is possible to achieve probe convergence semi-angles of up to ~40 mrad (133).

3.2. Bright field Imaging

Bright field imaging is an overarching term for images formed using un-scattered or weakly scattered electrons. Bright field images of supported particles will show darker scattering or diffracting features on a light background, as electrons passing through the support film will typically not scatter out of the objective aperture and will form an image. Contrast is formed from Bragg diffraction or inelastic scattering of electrons out of an objective aperture, or by absorption of the incident electrons by the specimen. In CTEM the scattered electrons are excluded from the image by the use of an objective aperture, and in STEM the camera length is modified so that only the un-scattered electrons reach the bright field detector. The setup of BFTEM is demonstrated schematically in Figure 3.8

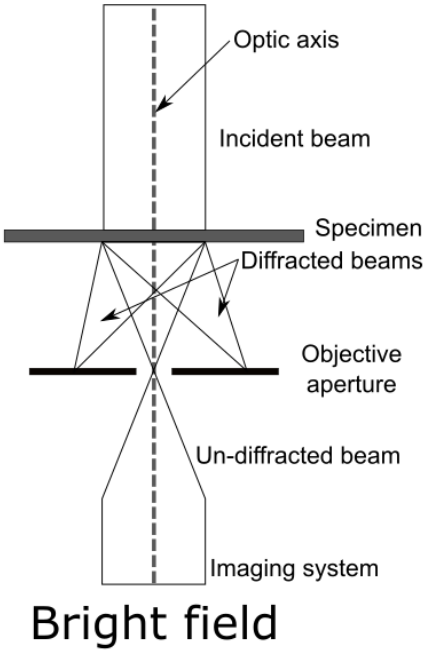

Figure 3.8 Bright field CTEM image formation with an objective aperture centered on the optic axis in the back focal plane.

There are several contrast mechanisms within bright field imaging which use the same optical arrangement, they include:

3.2.1. Mass Thickness, or Absorption Contrast

Mass-thickness contrast is formed from the incoherent Rutherford scattering of incident electrons by the specimen (134). The cross section for Rutherford scattering has a strong dependence on atomic number, as a result material containing heavy atoms will scatter more readily. The same phenomenon is observed for thick specimens where the likelihood of scatter is larger than for thin specimens of the same composition, as the mean free path is fixed. Heavily scattering regions will deflect more electrons off-axis out of an objective aperture, and fewer electrons will contribute to the final image.

3.2.2. Diffraction Contrast

Diffraction contrast is formed from coherent scattering from diffracting crystalline specimens or through diffuse scattering from amorphous specimens (134). As the diffracted electrons are excluded from image formation by an objective aperture, diffracting crystallites appear dark. The extent of diffraction is related to the orientation of the crystallite, with

crystallites aligned along a zone axis diffracting more strongly, thus appearing darker than weakly diffracting crystallites.

Strong diffraction contrast is formed by tilting the specimen into “two-beam” conditions, where only the un-scattered beam and one diffraction spot appear brightly in the diffraction pattern. In these conditions with an appropriately placed objective aperture, complementary information is provided by bright field diffraction contrast and dark field images.

3.3. Phase Contrast Imaging

Phase contrast is a more complex contrast mechanism involving constructive interference between the un-scattered and diffracted electrons. The diffraction of electrons by a crystalline lattice causes a shift in the phase of the scattered electrons relative to the un-scattered electrons. When the un-diffracted and diffracted beams are brought back together in the imaging plane, the constructive interference of these beams produce intensity fringes related to the lattice periodicity of the specimen. Rather than obstructing the diffracted beams with a small objective aperture, as in diffraction contrast BF imaging, phase contrast imaging uses a large or even no objective aperture to collect multiple diffracted beams. Phase contrast CTEM image formation is summarised schematically in Figure 3.9, and phase contrast STEM in Figure 3.14

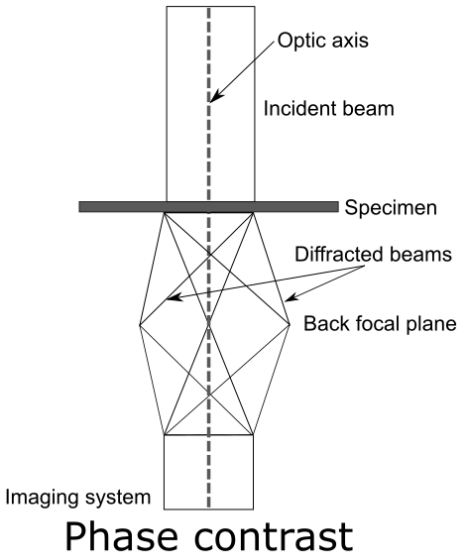

Figure 3.9 Schematic representation of phase contrast CTEM imaging, with no objective aperture in the back focal plane.

For two interfering beams 0 (un-diffracted beam) and g (diffracted beam), where g is a reciprocal lattice vector, lattice fringes are produced in thin specimens, with periodicity varying for different values of g' allowing for the lattice spacing to be inferred from the spacing of the intensity fringes in the image. However, the position of the fringes is not directly indicative of the position of the lattice planes in the specimen.

For thin specimens consisting of light atomic weight atoms, the weak phase object approximation is employed, where it is assumed that the specimen does not cause a change in beam amplitude, and only causes a phase shift. It is also assumed that weak phase objects only display single scattering, with no dynamic diffraction effects.

3.3.1. Contrast Transfer Function (CTF)

The contrast transfer function of the objective lens modulates the phases and amplitudes of the electron wave in the back focal plane, it is represented in equation 3.4 where T(k) is the transferred contrast at a given spatial frequency, C_s is the spherical aberration of the objective lens, λ is the wavelength, k is the spatial frequency and Δf is the defocus (134).

$$T(k) = \frac{1}{2}\pi C_s \lambda^3 k^4 + \pi \Delta f \lambda k^2$$

(3.4)

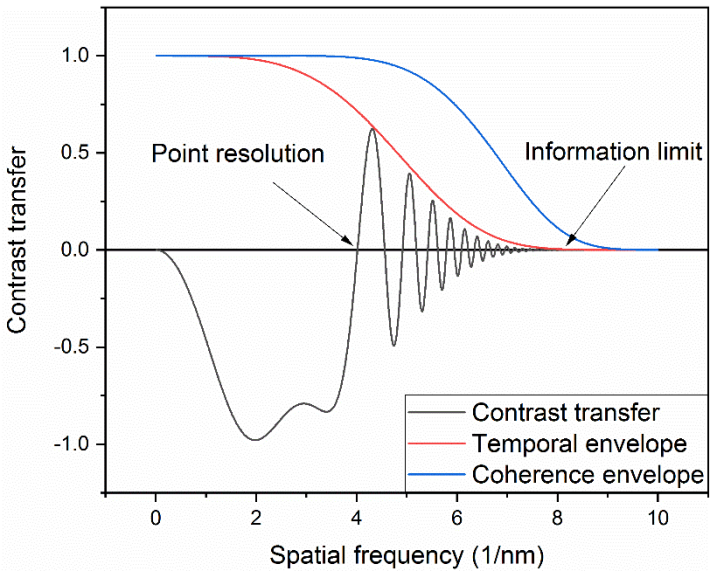

Figure 3.10 Simulated contrast transfer for a 300 kV FEG-TEM at Scherzer defocus with coherence and temporal envelopes applied, simulated using CTF calculator by D.R.G Mitchell (135).

The CTF is used to evaluate and represent image contrast, and resolution in microscopes. On the CTF plot, when the CTF is negative, a positive phase contrast occurs, and atoms will show up dark on a light background. When the CTF is positive, the electrons will appear bright on a dark background. Due to the oscillations of the transferred contrast with changing spatial frequency, the contrast can rapidly invert, this contrast inversion makes image interpretation challenging and requires image simulations using multi-slice methods (136). The spatial frequency at which the CTF axis is crossed for the first time, when the microscope is set to Scherzer defocus (see below), is known as the point resolution. At spatial frequencies past this point, the images cannot be directly interpreted. The information limit is the spatial frequency at which phase information can no longer be carried by the CTF, this is the size of the smallest lattice detail observable with an instrument (137).

Envelope functions are applied to demonstrate the influence of temporal and spatial coherence. The temporal coherence envelope is caused by instability

in the objective lens currents, acceleration voltage, chromatic aberrations and energy spread variations in the beam. The spatial coherence envelope is caused by the convergence of the incident electrons and the virtual source size.

3.3.2. Scherzer Defocus

Scherzer defocus is a defocus value Δf to give the best point resolution and is given where C_s is the spherical aberration coefficient, and λ is the wavelength by:

$$\Delta f_{Scherzer} = -1.2\sqrt{C_s\lambda}$$

(3.5)

Scherzer determined that optimal defocus conditions were dependent on electron wavelength λ and spherical aberration C_s. In order to maximise the point resolution, the microscope should be operated under Scherzer defocus conditions, as this is where defocus balances C_s (138).

3.3.3. The Fast Fourier Transform

High resolution phase contrast imaging, and HAADF-STEM imaging commonly use the Fast Fourier Transform (FFT) to aid in image interpretation. The FFT is an algorithm which converts a function from the spatial domain into the frequency domain (139). This has the effect of separating the different frequencies present in an image, which are then represented with their relative orientations. When used on a phase contrast lattice image, the result of this is similar to a selected area diffraction pattern, where the spacing and orientation of the repeating fringes are plotted radially, however an FFT of an image contains a contribution from the lens (including aberrations, defocus and astigmatism). An example of this is shown below in Figure 3.11, where the FFT of a HAADF-STEM image of a $SrTiO_3$ lattice shows single crystal character, aligned along the <001> zone axis (100).

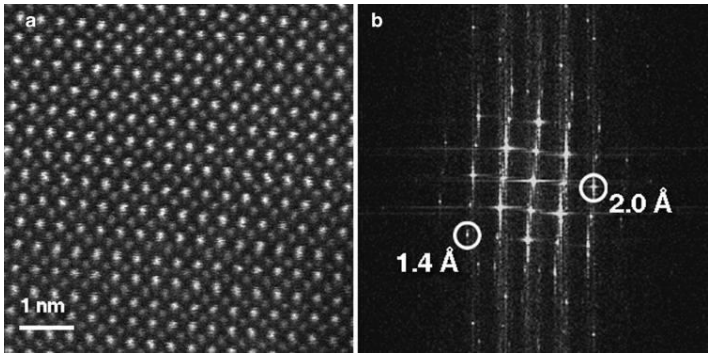

Figure 3.11 A) HAADF-STEM image of $SrTiO_3$ lattice, with FFT shown in B) the visible spots show representation of the crystal structure and the d-spacings of the resolved features (100).

As the FFT detects repeating features, it is commonly used as a pseudo diffraction pattern on a phase contrast or HAADF lattice image, where the FFT size and position can be selected, this allows for highly specific diffraction analysis after original image acquisition. By selecting spots on the FFT and applying a reverse FFT, pseudo dark field images can be produced from bright field images, to locate regions scattering to a chosen reflection. However, these spots should display sufficient signal to noise ratio (>3) to ensure that false fringes are not generated from noise.

3.3.4. Reciprocity in CTEM and STEM Imaging

Reciprocity is the principle of time-reversal symmetry between CTEM and STEM, resulting in image contrast that is complementary under certain conditions. Time-reversal symmetry means that the electrons would follow the same path through the optical system if their direction were reversed and the source and detector were interchanged, this is shown in Figure 3.12 for CTEM and STEM. Whilst reciprocity is generally used to compare between phase contrast in CTEM and STEM, it has also been shown that hollow-cone dark field CTEM is comparable to ADF-STEM through reciprocity (140). In this thesis, reciprocity was only considered in the context of phase contrast imaging.

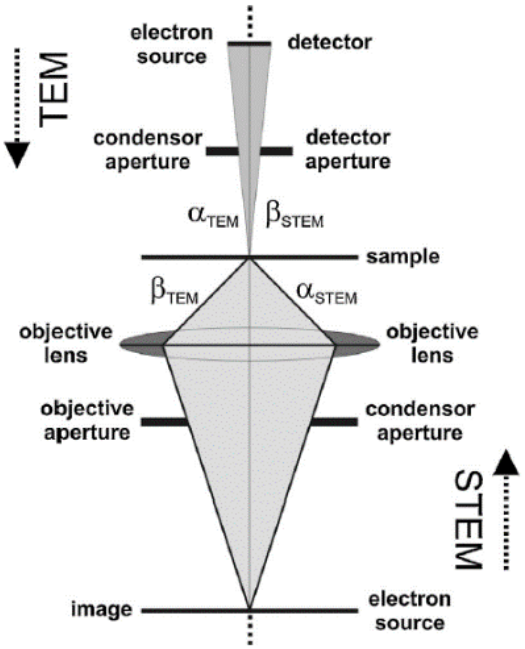

Figure 3.12 Representation of reciprocity between CTEM and STEM imaging. Reciprocity is achieved if $\alpha_{STEM} = \beta_{TEM} >> \beta_{STEM} = \alpha_{TEM}$, where α are convergence angles and β are detection/collection angles (141).

For reciprocity between CTEM and STEM several conditions must be met by the electron optical systems in the CTEM and STEM, these include:

- STEM probe convergence angle is the same as CTEM objective aperture angle.
    - This implies the probe convergence semi-angle is large, as a large objective aperture is required for CTEM phase contrast imaging.
- STEM bright field collection semi-angle is the same as CTEM beam convergence.
    - This implies a small bright field STEM collection angle as CTEM illumination is assumed to be near parallel.
- Spherical aberrations must be the same in CTEM and STEM operation
    - This implies the electron optical systems are identical, either all aberrations are corrected, or none are.
- Detectors must not be phase sensitive

    - This is inherent as standard CCD/CMOS cameras in CTEM and STEM photomultiplier detectors are not phase sensitive, and are only sensitive to intensity.
- Incoherent illumination
    - A heated tungsten filament electron source is an incoherent source and offers reciprocity with a standard detector, however a FEG source offers more coherent illumination and would require a coherent electron detector to ensure reciprocity.

There are several issues with fully reciprocal phase contrast imaging:

Due to the small BF STEM detector collection angle required, dose efficiency is poor, as most of the incident electrons are excluded from image formation, with collection efficiency estimated at ~1% (86, 87). This is in order to reduce the absorption or mass-thickness contrast by only sampling the overlapping diffracted disks (see Figure 3.14). Humphreys (142) stated that by reducing the collection efficiency, it was necessary to use large incident fluences to produce images with appropriate signal to noise ratios. By supressing mass-thickness and diffraction contrast by using a smaller BF-STEM detector, thin specimens or non-diffracting features can be challenging to observe. This can make image interpretation challenging, especially under low-dose conditions, where the signal to noise ratio is lower. An example of this is shown below in Figure 3.13A:

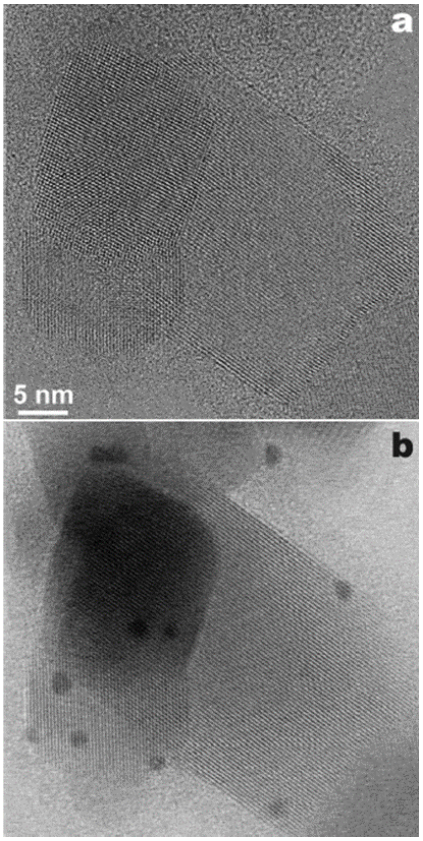

Figure 3.13 BF-STEM images of Pt particles on TiO_2 crystals, a) reciprocal phase contrast, b) Wide-angle bright field imaging (non-reciprocal phase contrast) (scale is the same for both images) (141)

In Figure 3.13A, the platinum nanoparticles cannot be clearly observed in the reciprocal phase contrast image, whereas the mass-thickness contrast contribution in Figure 3.13B shows them more clearly. Wide angle bright field (WABF) imaging is performed by setting the bright field detector to a larger collection angle than is indicated by reciprocity, thus phase contrast is combined with mass-thickness contrast and diffraction contrast features. This breaks the assumption of reciprocal imaging; however, it does provide phase contrast with larger electron collection efficiencies. WABF is schematically represented below in Figure 3.14, where the differences in the collection conditions can be seen. In modern STEM systems, with post-specimen lenses, it is possible to change between these conditions by adjusting the camera length of the diffraction pattern on the detector system.

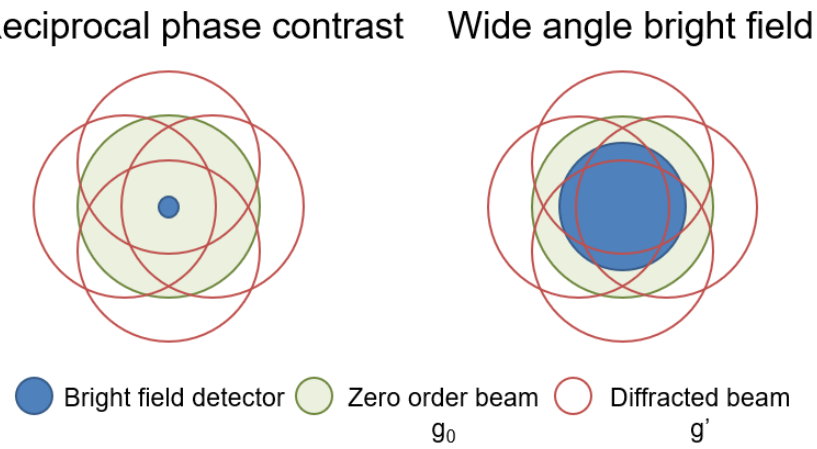

Figure 3.14 Schematic representation of reciprocal phase contrast and wide-angle bright field collection conditions.

Sader et al (87) proposed using wide angle bright field imaging as an alternative to phase contrast in STEM, this is in order to improve electron collection efficiency whilst producing phase contrast. The bright field detector was set to be slightly smaller than the undiffracted beam to exclude the majority of aberrated electrons and avoid suppressing phase contrast by allowing too many undiffracted electrons to form the image. This allowed them to extract high resolution phase contrast lattice images of vermiculite at lower fluences than were possible when using reciprocal phase contrast conditions. They proposed using a collection semi-angle set to 50% of the probe convergence semi-angle to achieve ~25% electron collection, these collection conditions were optimised for a non-aberration corrected STEM system and were developed following Rose (86). For a C_s corrected STEM, they propose setting the bright field collection semi-angle to 66% of the probe convergence semi-angle, which would collect nearly 50% of the transmitted electrons.

3.4. Selected Area Electron Diffraction (SAED)

SAED is a crystallographic technique, where a parallel electron beam is passed through a sample and elastically scattered by the atomic planes following the Bragg equation below, where n is the diffraction order, λ is the electron wavelength, d is lattice spacing and θ is the scattering angle.

$$n\lambda = 2dsin\theta$$

(3.6)

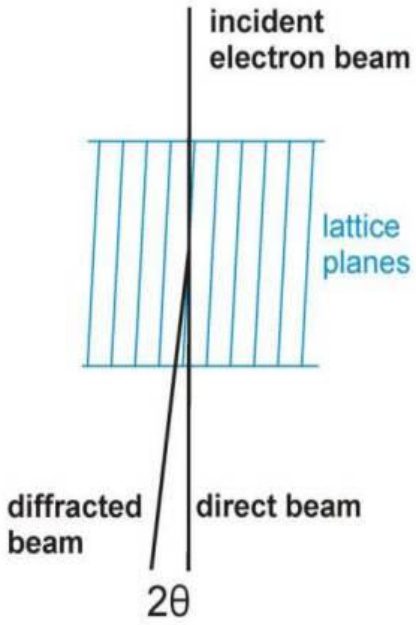

Figure 3.15 Schematic of Bragg diffraction in CTEM, 2θ is the scattering angle between the direct beam and the diffracted beam (129).

Through this the scattering angle can be related to the d-spacing, allowing for images of the diffraction pattern to be converted into a list of lattice plane spacings present in the specimen. To extract the d-spacings from the CTEM diffraction pattern, the radius of the diffraction rings or spots and the operating conditions of the microscope must be used, as is shown in equation 3.7, where r is the diffraction radius, λ is the electron wavelength, L is the camera constant and d is lattice spacing.

$$r = \frac{L\lambda}{d}$$

(3.7)

Each spot in the diffraction pattern corresponds to conditions where the Bragg equation is satisfied. After passing through the sample, the diffracted beam is passed through a selected area aperture in the intermediate image plane, allowing for diffraction information on localised on the specimen to be

transmitted. This means that diffraction patterns can be captured specifically based on chosen features in the image, for example crystallographic studies of individual nanoparticles, grain boundaries, or interfaces.

Both single crystal and polycrystalline SAED are commonly used. When studying the effects of electron irradiation on single crystal materials, the crystallinity of the particle is often affected, and these changes show up clearly in the diffraction pattern. For example, in a study by Hoffman et al (89), SAED was used to investigate calcium carbonate-based materials under electron irradiation. It could be clearly observed from the diffraction patterns that previously single crystal calcite had transformed into polycrystalline calcium oxide, as shown by the rings formed in the diffraction pattern. This is shown in Figure 3.16B.

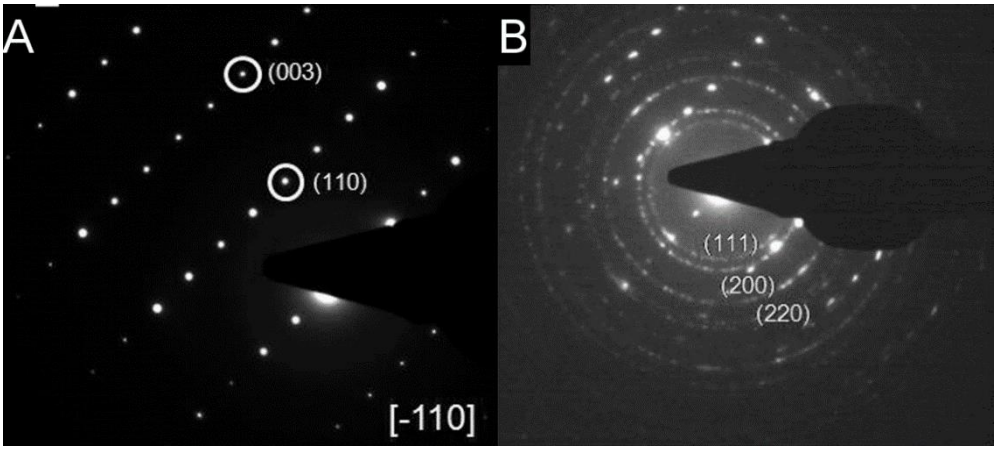

Figure 3.16 Geological calcite (Iceland Spar) A) before irradiation B) after irradiation, accumulated fluence ~3x10^{7} e^{-}nm^{-2} at 300 kV (89). SADP scalebar not provided.

It can be seen that some of the single crystal calcite (shown by the spot pattern) is still present, though polycrystalline calcium oxide rings are also clearly visible in pattern B, the zone axis or orientation of the single crystal calcite was unaffected, though in some smaller particles the electron beam can induce movement and the particle can become reoriented.

3.5. Dark Field Imaging

Dark Field imaging forms images only from scattered electrons and discards the transmitted electrons (134). Dark Field CTEM (DF-CTEM) and Annular

Dark Field STEM (ADF-STEM) produce images formed by diffracted electrons, and High Angle Annular Dark Field STEM (HAADF-STEM) images are formed by higher angle Rutherford scattered electrons. Dark field images show bright specimen features on a dark background, as the background does not scatter electrons to form contrast, this is not an inversion of bright field imaging contrast, but the provided contrast can be complementary.

DF-CTEM imaging is demonstrated schematically in Figure 3.17, where the incident beam, is tilted so that the chosen diffracted beam passes through an objective aperture placed on the optic axis.

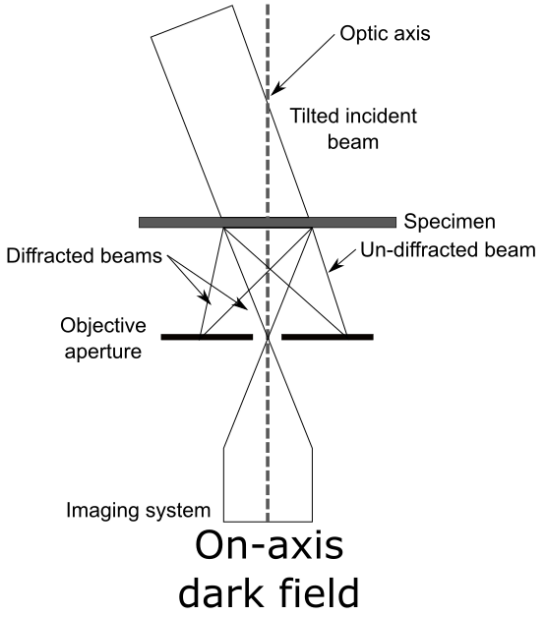

Figure 3.17 Schematic representation of on-axis dark field CTEM image formation, the objective aperture is centred on the optic axis and the diffracted beam of choice is deflected onto the optic axis and through the aperture.

3.5.1. Dark Field CTEM

CTEM dark field imaging uses an objective aperture in the back focal plane to form the image only from diffracted electrons. This excludes the un-diffracted electrons, instead only crystallites that diffract through the objective aperture show up in the image. It is common practice to place the objective aperture on the optic axis, and deflect the diffraction pattern by tilting the incident beam so that the chosen reflection passes through it. This gives improved resolution

when compared to keeping the direct beam on axis and displacing the objective aperture to the chosen reflection, as deviating from the optic axis introduces spherical aberrations. Dark field images are not simply inverted bright field images, they contain complementary information on the size and location of diffracting features.

A comparison of BF-CTEM and DF-CTEM is shown in Figure 3.18, from Jacob et al (48), where electron beam-induced crystallisation is observed in amorphous calcium carbonate. The white spots in the DF image show newly diffracting regions.

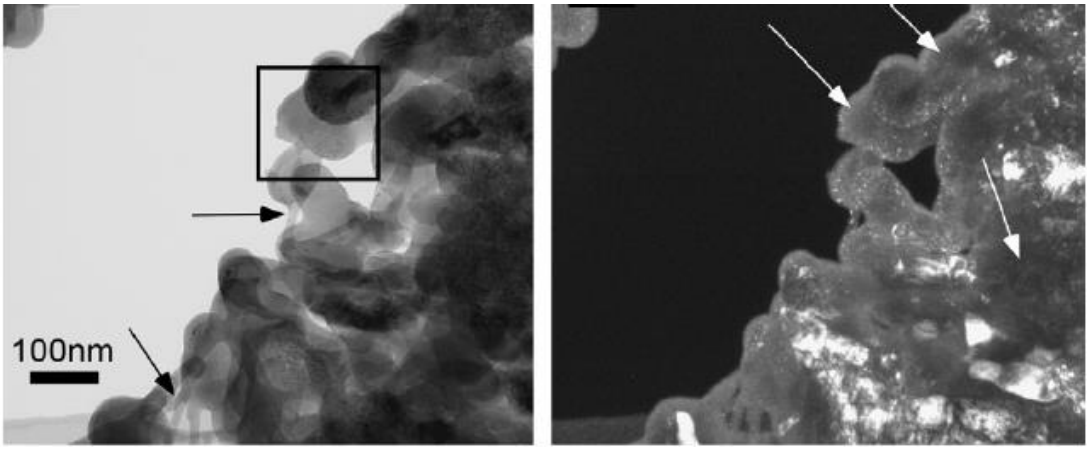

Figure 3.18 BF (left) and DF (right) of electron beam-induced crystallisation in biogenic amorphous calcium carbonate. The black box in the bright field image shows the region which was irradiated heavily, when compared to the dark field image, many white crystallites can be seen (48).

In standard dark field CTEM imaging, only a fraction of the scattered electrons are used and whilst this is useful when investigating a single diffraction spot, this can be time consuming when attempting to investigate where multiple reflections of the same family of diffraction originate. Using hollow cone DF imaging, the incident beam is tilted so that the diffracted beam passes through an on axis objective aperture, and the beam is rotated so that the diffracted electrons continually pass through this aperture. This means that rather than sampling e.g. specific (111) spots individually, all of the {111} reflections can be imaged simultaneously if a sufficiently small objective aperture is used to only sample one diffraction ring. This can significantly increase the signal

produced, as multiple diffraction spots are sampled, increasing the dose efficiency. The hollow cone dark field approach is related to annular dark field STEM imaging by reciprocity, where diffracted or scattered electrons are collected on a ring-shaped annular scintillator photomultiplier detector.

3.5.2. Annular Dark Field -STEM

ADF-STEM images, like in DF-CTEM, are formed by the Bragg diffracted electrons, or electrons scattered by an amorphous specimen, though no objective aperture is used. Diffracting regions appear bright, giving diffraction contrast analogous to DF-CTEM.

As ADF-STEM uses an annular scintillator photomultiplier detector, it is able to collect a large proportion of the scattered electrons, making it more dose efficient than DF-CTEM, however it does not display the same specificity in terms of forming images with individual Bragg reflections.

At low collection angles, (25-50 mrad) it has been demonstrated that crystal orientation contrast is possible, allowing for strain mapping and grain size analysis. Lower collection angles display more significant orientation contrast as the image is constructed from beams with low Miller indices. This is known as Low-Angle Annular Dark Field (LAADF) (143).

In addition, annular bright field STEM imaging is possible, where the image is formed an outer region of the diffracted beam. This provides light element contrast with atom columns appearing dark on a white background. However, this technique is not used in this thesis and will not be discussed in further detail.

3.5.3. High Angle ADF-STEM (HAADF)

HAADF-STEM forms images from the high angle Rutherford scattered electrons, and excludes Bragg diffracted and un-scattered electrons. This provides an image with contrast related to the composition and thickness of a specimen. Rutherford scattered electron intensity (I_{HAADF}) is related to the atomic weight of the scattering atom, through equation 3.8 where Z is atomic

number, α is probe convergence angle and k is the wavenumber (144). As thickness increases, Rutherford scattering increases, and the HAADF image intensity is no longer solely atomic number dependent.

$$I_{HAADF} \approx \frac{4Z^2}{\alpha_0^2 \Delta k^4} \quad \textbf{(3.8)}$$

HAADF produces images which can be directly interpreted, as contrast is related to atomic number, heavier atoms appear brighter and thus atomic positions can be directly interpreted, unlike in phase contrast images (145). As HAADF imaging excludes most electrons, it is not a dose efficient technique when used alone, however it is commonly combined with EELS spectrum imaging to make simultaneous use of the electrons passing through the middle of the annular detector to perform elemental images as well.

HAADF imaging is more sensitive than BF-STEM to high atomic number elements and is relatively dose inefficient due to the high scattering angles employed. Meaning it often requires high incident fluences to produce an adequate signal to noise ratio in images. Thus, it is of limited use for calcium carbonate and was not used as an imaging technique in this thesis, as such it will not be discussed in any further detail.

3.6. Electron Spectroscopy

3.6.1. Energy Dispersive X-Ray Spectroscopy (EDX/EDS)

EDX provides elemental information based on the emission of characteristic energy X-rays from the irradiated specimen, caused by incident beam-induced electronic excitations. This allows for the rapid extraction of compositional information at a variety of length scales.

For characteristic energy X-ray emission, an incoming electron excites and removes an inner shell electron bound to an atom in the specimen. To rectify this, an outer shell electron drops (in energy) to fill the vacant orbital. The excess energy is emitted in the form of an X-ray; the energy of this X-ray is

characteristic of the orbital it is emitted from and drops into i.e. the energy difference. For example, X-rays emitted by the transition of electrons from the calcium *L* to the *K* shell has an energy of 3.69 keV and is known as a K_α X-ray. A schematic diagram of electron stimulated X-ray generation is shown in Figure 3.19.

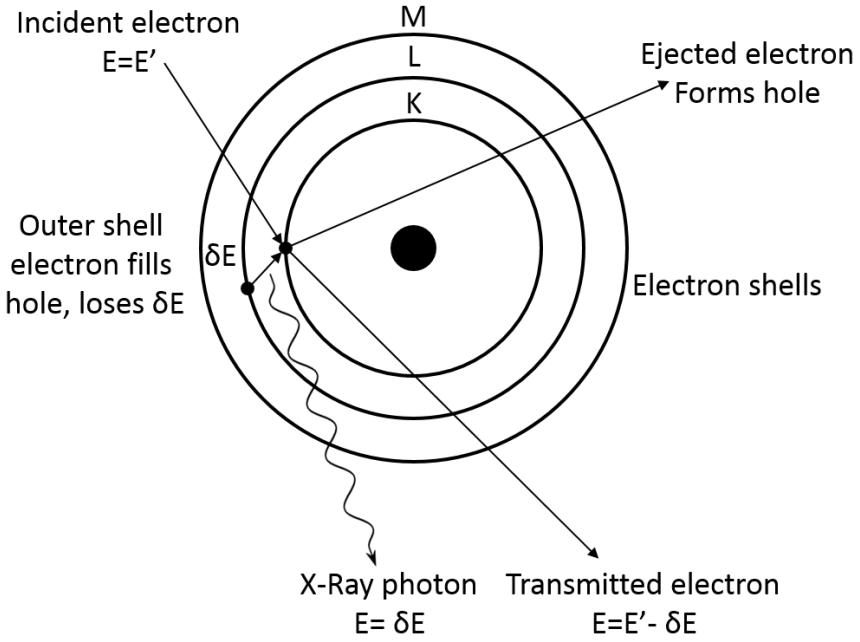

Figure 3.19 Schematic of electron stimulated characteristic X-ray emission, the incident electron removes an inner shell electron and the resulting electronic de-excitation emits an X-ray of characteristic energy.

The number of characteristic X-rays produced by an element in a material is a function of many parameters, some material based, and some instrumentation based, as can be seen in equation 3.9 (146). Where I_A' is equal to the number of characteristic X-rays of element A generated per second, N_o is Avogadro's. number, A_A is atomic weight, i_p is probe current, e is electronic charge, ρ is sample density, t is sample thickness, ω is fluorescence yield, C is concentration, Q is cross section and S is a partition fraction, all specific to element A.

$$I'_A = \frac{N_o}{A_A} \cdot \frac{i_P}{e} \cdot \rho \cdot t \cdot C_A \cdot Q_A \cdot S_A \cdot \omega_A$$

(3.9)

X-ray Detection and EDX Detectors

There are several common types of EDX detectors available commercially, including lithium drifted silicon detectors (SiLi), intrinsic germanium detectors, and silicon drift detectors (SDD). Silicon drift detectors are becoming the most commonly used overtaking SiLi detectors, as these do not require cryogenic cooling, have larger solid angles due to the size of the detector chips, and are capable of operating at higher count rates (147, 148).

If an emitted X-ray reaches the EDX detector, it causes an ionisation event in the silicon detector crystal, producing electron-hole (e-h) pairs. The e-h pairs are collected by electrodes on the surface of the detector crystal, the number of e-h pairs produced from an ionisation event is related to the energy of the incident X-ray, and thus the current measured by the detector is correlated to incident X-ray energy. Ultimately this allows for the formation of a spectrum of the incident X-ray energy and number of counts over a set measurement time.

Artefacts

If multiple incident X-rays ionise the detector at the same time, the detector will consider this to be a single X-ray whose energy is the sum of the simultaneous X-rays. If not detected and removed from the spectrum, these are called sum-peaks. Often the processing software is generally able to detect the larger than expected current, and discount it from the spectrum to avoid spurious signals. This is known as a pulse pile-up correction, pulse pile-ups are a common issue when working with a high incident beam current or elements with a high fluorescent yield.

Incident X-rays can themselves stimulate emission inside the detector crystal, producing silicon K_α X-rays which can be detected. This is known as internal fluorescence and can result in Si K_α peaks appearing in the spectrum, when no silicon is present in the sample.

In cases where only part of the incident X-ray energy is converted into e-h pairs, a Si K_α X-ray can be generated and detected. The remaining incident X-ray energy is then converted into e-h pairs which show up as a peak with a measured energy reduced by the energy of a Si K_α X-ray, this is known as an escape peak. For example, a Ca K_α X-ray has energy of 3.69 keV, less a Si K_α X-ray of energy 1.74 keV would produce an escape peak of 2.1 keV, a similar energy to phosphorous and sulfur K_α X-ray energies.

These artefacts must be identified and removed from captured spectra in order for quantification to be accurate, though this is mostly done automatically by processing software, some artefacts may remain.

EDX Quantification

Spectra are quantified by comparing integrated peak areas to either a known standard, or theoretical standard for a given incident electron current and accelerating voltage. For theoretical standards, silicon is commonly used. Equation 3.10 is used to give an initial value for elemental concentration, where C is composition of element A, I is characteristic line intensity for element A and *k* is the concentration ratio.

$$\frac{C_A}{C_A^{standard}} = \frac{I_A}{I_A^{standard}} k_A \qquad \textbf{(3.10)}$$

The Cliff-Lorimer method shown in equation 3.11 does not use a known standard, instead simultaneously capturing the intensities from two elements in the sample and calculating a concentration ratio for them. Where C is composition of the element, I is characteristic line intensity for each element and *k* is the concentration ratio for both elements, known as the Cliff-Lorimer Factor. For this method, C_A+C_B must equal 100%.

$$\frac{C_A}{C_B} = \frac{I_A}{I_B} k_{AB} \;\; where \;\; k_{AB} = \frac{\frac{k_A}{k_{Si}}}{\frac{k_B}{k_{Si}}}$$

(3.11)

This is considered a semi-quantitative method, as the standards have not been measured for a specific instrument, accelerating voltage or beam current. They present a reasonable approximation, but are not fully quantitative. This would require measurements of standards under the same operating conditions and instrumentation as the specimens to be quantified.

In many cases, semi-quantitative EDX by the standard-less approach can be accurate to ± 5-10 %wt for most elements, with a minimum detectable fraction of 0.1-1%wt. However light elements (Z<11) are hard to accurately quantify due to their low fluorescent yield of X-rays (134). Light elements have fewer electrons, making them harder to ionise, and have a higher tendency to emit Auger electrons rather than characteristic X-rays on electronic de-excitation (149). If X-rays are generated, they have a higher likelihood of absorption by the sample itself or a surface contaminant, as light element X-rays have low energies, making them more likely to be absorbed.

Other considerations for accurate quantification include: background subtraction and avoiding the use of overlapping peaks. A background spectrum must be collected under the same conditions as the spectra under investigation (acquisition time, electron flux and accelerating voltage) that considers the support film, column vacuum and column generated X-rays. This allows for the subtraction of spurious counts which can skew quantification. Overlapping peaks require deconvolution prior to quantification, which can introduce inaccuracies in the peak intensity, compounding inaccuracy in the quantification of the chosen peaks.

The specimen thickness is implicated in the accuracy of quantification, especially for light elements. As light element X-rays are more likely to be absorbed due to their lower photon energy, and thick specimens provide more

opportunities for absorption, the implication is that EDX will underestimate the composition of light components in thick specimens. This can be avoided by using thinner specimens for light element quantification.

STEM-EDX

Whilst CTEM can produce single spectra for a selected area determined by the size of the electron beam, STEM is more spatially resolved, i.e. information is collected on a pixel by pixel basis, meaning that maps can be built up from EDX spectra, this allows for the position of high elemental concentrations to be deduced and overlaid with imaging information. At high magnifications this can be a highly powerful tool to aid in the understanding of atomic distributions and their influence on material structures.

Applications of EDX

When considering electron beam damage, EDX has been used to probe sample mass loss occurring as a function of electron fluence, losing atoms of a particular element will reduce the X-ray counts and thus the reported composition will change. Examples from Eddisford and Martin have previously been discussed in section 2.3.3.

The major problem with using EDX on electron beam sensitive materials, is that acquiring high quality spectra requires a large number of characteristic X-rays to be detected, meaning that the sample will have to endure high electron fluences, possibly altering the composition of the sample and producing unrepresentative spectra from the onset. This is because X-rays are produced isotropically i.e. in all directions over 4π steradians, and EDX detectors have a finite size, for example the Super-X EDX system used on the FEI Titan microscope covers 0.7 steradians, ultimately this means that detection efficiency is relatively low.

Using EDX with a low electron beam fluence conditions will lead to spectra with low signal to noise ratios for the peaks, which in turn may lead to inaccurate and unreliable quantification. Before quantitative EDX can be

undertaken, there must be an appreciation of any likely compositional changes under irradiation.

3.6.2. Electron Energy Loss Spectroscopy (EELS)

Electron energy loss spectroscopy is a powerful analytical technique which provides information on the composition, bonding and electronic properties of materials (60). EELS measures the amount of energy lost by electrons which have undergone inelastic scattering, elastically scattered or diffracted electrons do not lose energy and thus do not contribute to the low-loss or core-loss EELS spectrum.

To perform EELS, the transmitted electrons are passed through a magnetic prism to separate the electrons based on their energy, the electrons are then projected onto a camera to record a spectrum, where the electrons position on the camera is related to their energy. An example spectrum is shown below in Figure 3.20, where the multiple regions of the spectrum can be seen.

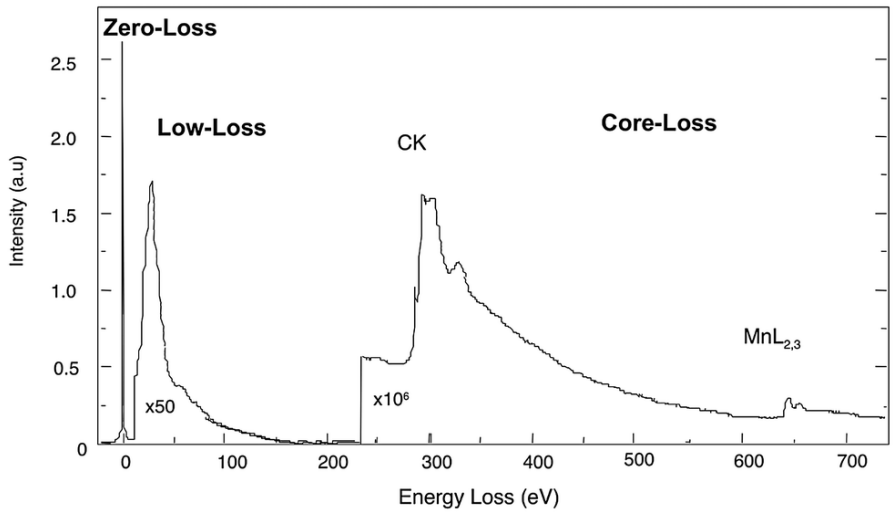

Figure 3.20 Example EELS spectrum showing the zero loss peak, low loss and core-loss region with carbon K and manganese L_{2-3} edges (150).

Zero-loss peak (ZLP) – The zero-loss peak is formed from transmitted or diffracted electrons which have not undergone any inelastic interactions. The ZLP has the highest intensity as the majority of electrons do not interact inelastically. The width of the ZLP is used to measure the energy spread of the electron beam and align spectra.

Low-loss region - Low-loss EELS features present in the 0-50 eV region of the spectrum are formed from collective oscillations of valence electrons, and the transitions of valence electrons into the conduction band. In addition to plasmon losses, phonon losses caused by lattice vibrations, are present but are typically between 10-100 meV and are generally indistinguishable from the ZLP for non-monochromated microscopes. The low-loss region can be used to approximate the specimen thickness, by comparing the integrated intensity of the low-loss region and the zero-loss peak (151, 152). This can then be used to map the thickness of a specimen to assess suitable regions for analysis. Low-loss signals can also be used to extract information on the band structure and dielectric properties of the specimen.

Core-loss region – core-loss EELS features correspond to characteristic energy loss events caused by the ionisation of atoms in the specimen, the high intensity peak at the start of a core-loss spectrum corresponds to the ionisation energy of that elements electronic shell. These ionisations occur when core electrons are excited into higher energy states, either bound states or free electron states, by the incident electron (60). Integrating the core-loss EELS edges for selected elements can be used for atomic quantification, in a similar manner to EDX, though with higher light element sensitivity. This is limited to a maximum energy loss of ~3 keV due to the poor signal to noise ratio at higher energy losses and hardware limitations .

However, the core-loss EELS edges can provide more information than solely composition, including bonding, nearest atomic neighbours, and coordination state. The core-loss edge consists of two regions, the energy loss near edge structure (ELNES), and the extended energy loss fine structure (EXELFS), these regions are shown in Figure 3.21. These regions are complementary to the XANES and XAFS regions measured in X-ray absorption spectroscopy respectively (mentioned further in section 3.7.6).

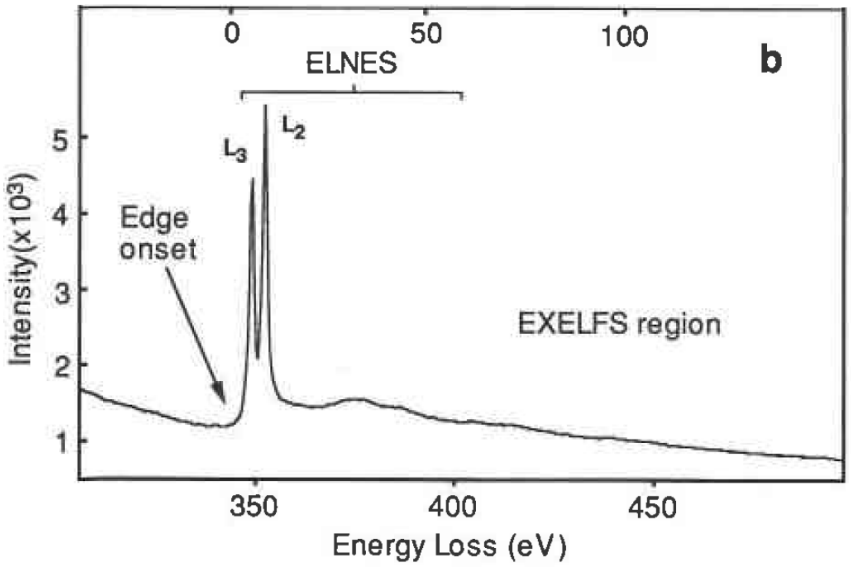

Figure 3.21 The ELNES and EXELFS regions of a calcium $L_{2,3}$-edge (153).

The ELNES region is found within ~50 eV of the ionisation edge, these features are formed from the multiple elastic scattering of the ionised electron into unoccupied states above the Fermi energy level. Quantification of the features in the ELNES can be used to investigate electronic structure, density of states, valence and co-ordination (106, 154).

The EXELFS region generally begins ~50 eV above the ionisation edge, however there is often some overlap with the ELNES region. EXELFS features are formed from single scattering of an ionised electron when it has sufficient energy to escape the atom and act as a free electron. This free electron can be diffracted by the specimen, and this diffraction causes the oscillations in intensity seen in EXELFS spectra, this can be used to extract geometric information on bonding, including bond lengths and nearest atomic neighbours (155).

An area of significant interest in EELS, is the use of chemical fingerprinting to determine between different forms of the same element. For example: EDX is only able to determine the presence and approximate quantity of an element, whereas EELS is able to determine between different oxidation states or bonding states. An example of this would allow the operator to determine between iron particles containing Fe^{2+} or Fe^{3+} atoms using the iron $L_{2,3}$-edge, or to determine between amorphous carbon, diamond, and graphite solely

using the carbon *K*-edge core loss spectrum (154). However, measuring chemical shifts or chemical fingerprints require strong signal to noise ratios, and thus significant electron doses.

As EELS only makes use of inelastic interactions, much like EDX it is not a dose efficient technique. In principle EELS has a higher detection efficiency than EDX, as the transmitted and inelastically scattered electrons are strongly forward peaked, enhancing collection, however it suffers from a large background signal, especially in thick specimens. Even with these downsides, EELS and spectrum imaging have been used in electron beam sensitive and cryogenically prepared materials (106, 107). However, an understanding and consideration of the electron beam damage process is essential to ensure that observations are representative of the pristine material and not induced by the electron beam.

EELS was not used as an experimental technique in this thesis as time resolved EDX measurements were able to demonstrate the electron beam compositional changes effectively. In addition, previously published work by Golla-Schindler et al (90), Hoffmann et al (89), and Murooka et al (58, 98, 156) elegantly demonstrated the time resolved electron beam damage of calcium carbonate using EELS. As EELS was not used as an experimental technique in this thesis, it will not be discussed in any further detail.

3.7. Bulk Material Characterisation Techniques

3.7.1. Fourier Transform Infrared Spectroscopy (FTIR)

FTIR spectroscopy collects information from attenuation of incident infrared light by the specimen. The attenuation is measured as a function of incident wavelength, over a wide spectral range simultaneously. Molecular bonds possess resonant frequencies and absorb energy from light related to their structure at these frequencies, where the absorbed frequency matches the bond vibrational frequency. “IR-active” molecules display vibrational modes associated with changes in the dipole moment of bonds, where symmetric and asymmetric distortions of bonds are seen when energy is absorbed.

FTIR-ATR (Attenuated Total Reflectance) uses a high refractive index crystal under the specimen to form an evanescent wave of the infrared light, this wave refracts internally, and some intensity impinges on the sample in contact with the crystal. Upon leaving the crystal after interacting with the specimen, the remaining light is detected, and a Fourier transform is taken of the data produced. FTIR-ATR has the advantage of having simple sample preparation, with liquids and solid specimens being measured in their native state with no further preparation required. From this, rapid measurements can be taken with high sensitivity, as the evanescent IR light wave samples the specimen multiple times before the light is detected. ATR measurements allow for thick, or heavily absorbing specimens to be measured, due to the limited penetration depth of the incident light, which had previously precluded standard FTIR by transmission measurements.

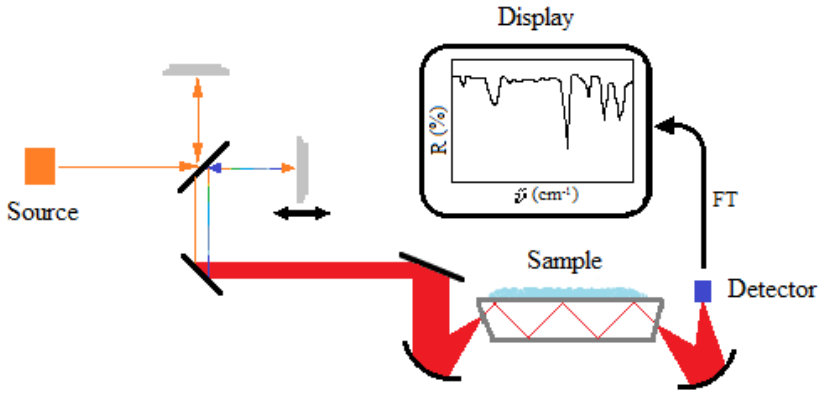

Figure 3.22 Schematic of FTIR-ATR spectrometer operation (157)

FTIR spectra show characteristic sharp peaks, or wide bands based on the absorption of a particular bond, these bands can be used to characterise specimens by identifying functional groups and their relative abundance. Complex mixtures of molecules will result in complex spectra, due to the overlapping absorptions from the IR-active components, meaning that for mixtures, reference spectra should be used to inform peak assignments.

The region between 500 cm^{-1} and 1500 cm^{-1} is commonly known as the fingerprint region, and can be used to determine which compound or molecule is present. For example, the spectra of the crystalline calcium carbonate polymorphs, in Figure 3.23 show some similarities in the fingerprint region,

with the absorption features occurring at the same wavenumber, but with different shapes or relative intensities.

The reference spectra used to investigate the calcium carbonate materials in this thesis are shown in Figure 3.23, the calcium carbonate specimens were synthesised and characterised following methods outlined in Chapter 4. Solvent and surfactant references were characterised as received from the manufacturer. For an amorphous calcium carbonate reference, collected spectra were compared to the ACC spectrum presented by Benning et al (158).

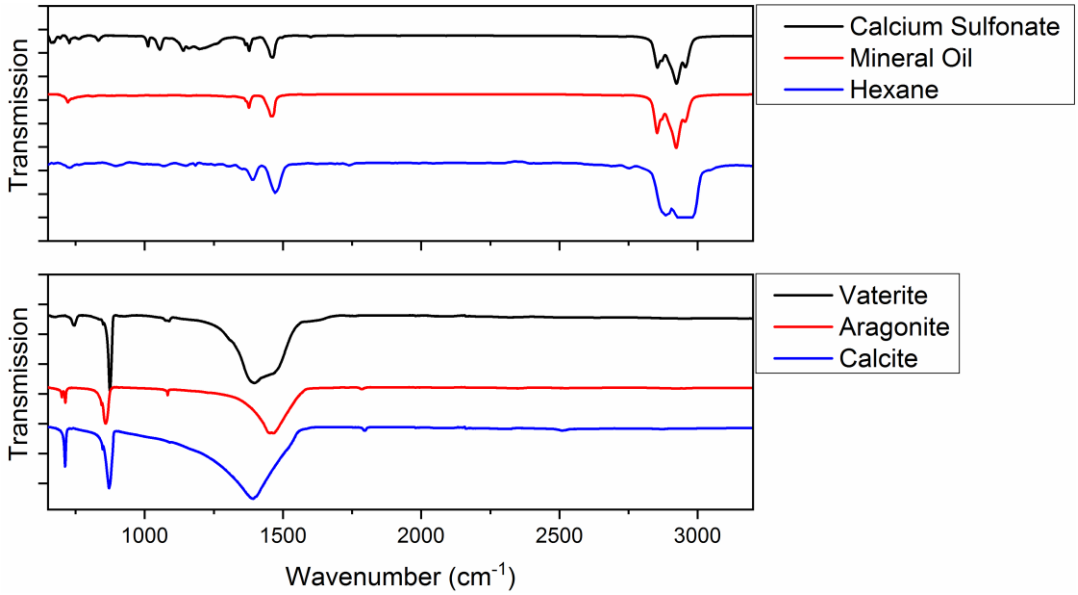

Figure 3.23 FTIR spectra of crystalline calcium carbonate polymorphs, calcium sulfonate surfactant, mineral oil and hexane (data courtesy of T. A. Kathyola)

3.7.2. Dynamic Light Scattering (DLS)

Dynamic Light Scattering is a technique commonly used for particle size measurement using laser scattering. DLS measures the Brownian motion of particles suspended in solution, where the hydrodynamic radius is related to the speed of motion, with small particles moving more rapidly. DLS is typically used for particles smaller than 1 µm as larger particles are more likely to settle. The diameter is calculated assuming that the particle is spherical, thus there is error in measurements for elongated or rod-like particles, but for more isotropic morphologies this is a reasonable assumption.

For reliable DLS measurements, the solvent viscosity and temperature must be known, as well as the specimen refractive index. As the measurement is related to the ability of a particle to diffuse in the solvent, the diameter reported is the hydrodynamic diameter, the diameter of a sphere with the same translational diffusion coefficient as the particle. The translational diffusion coefficient is dependent on particle size, solvent viscosity, solvent temperature, the surface structure the concentration of particles, and the ions present in the solvent (159, 160).

The hydrodynamic diameter is calculated from the Stokes-Einstein equation, shown below in equation 3.12 (160). Where d(H) is hydrodynamic diameter, D is the translational diffusion coefficient, T is the absolute temperature, k is the Boltzmann constant and η is the viscosity of the suspending media.

$$d(H) = \frac{kT}{3\pi D\eta}$$

(3.12)

When d<λ/10 for the incident laser light, typically 60 nm for He-Ne laser, the light scattering is isotropic, and the scattering intensity is proportional to d^6, and also proportional to $1/\lambda^4$. Meaning that a 50 nm particle will scatter approximately 10^6 more light than a 5 nm particle, as such scattering can be dominated by relatively small numbers of large particles. Due to this, the average particle size reported by DLS is only appropriate for monodisperse particle systems, however the dispersity can be investigated from the plot of intensity or number against particle size. DLS is thus unsuitable for mixed particle systems, and materials prone to agglomeration as in-situ agglomeration will affect measurements as they are being taken.

DLS plots hydrodynamic diameter against either the scattering intensity, or the number of scattering events, each providing complementary information. As large particles scatter more than smaller particles, the scattering intensity plot is skewed towards larger particle sizes by poly-disperse or agglomerated materials. Whilst the measured average hydrodynamic is not representative of the entire system, intensity plots can provide information on agglomeration,

as small fractions of agglomerated material can be detected easily. The number plot simply presents the number of scattering events against hydrodynamic diameter, this means that the plot is not dominated by intense scattering from large particles. Number plots will provide information on the more common hydrodynamic diameters present, but may not demonstrate low levels of agglomeration or small fractions of larger particles.

3.7.3. X-ray Diffraction (XRD)

X-ray diffraction is a commonly used technique for solid material analysis, it is most frequently used to provide information on crystal structure, though it is also routinely used to examine crystallite sizing, surface and inhomogeneous strain, and perform quantitative phase analysis. X-rays are typically formed from characteristic emission from an electron beam incident on a metallic anode, meaning that the source is not inherently monochromatic. Lab diffractometers can use multiple wavelengths of X-ray, with copper K_α being the most common, with a wavelength of 1.54 Å.

XRD relies on Laue scattering theory where the incident X-ray is diffracted by atomic planes, with constructive interference of the diffracted X-rays forming peaks in intensity, detected as a function of diffraction angle following Braggs law. In contrast to electron diffraction, powder X-ray diffraction patterns are formed from the reflected X-rays, not transmitted. For XRD measurements using a Bragg-Brentano θ-2θ geometry, the specimen is tilted to angle θ relative to the fixed X-ray source throughout the scan, and the X-ray detector is rotated to angle 2θ. For a polycrystalline or powder specimen, all possible diffraction peaks should be observed in the scan, provided there is no preferred orientation or crystallographic texture in the sample.

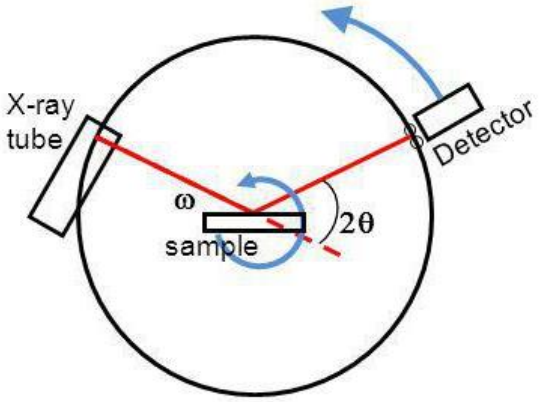

Figure 3.24 Schematic of θ-2θ X-ray diffraction, where ω is the incident X-ray angle.

XRD has the benefits of requiring minimal sample preparation and rapid acquisition times, though is hampered by Scherrer broadening of peaks in nano-crystalline specimens. Powder XRD does not have the ability to investigate symmetry, making solving an unknown crystal structure more challenging than in single crystal XRD.

Phase purity can also be extracted from XRD, through the use of quantitative phase analysis, it is assumed that multiple phases in a sample will contribute to diffraction patterns in a component proportional to the sample volume fraction. Like all diffraction based techniques, there is a minimum mass fraction (MMF) required for phase purity measurements, small phase components may not have sufficient atomic planes to form a significant diffraction signal, the lower limit is generally accepted to be around 5% by volume, but this is dependent on the crystallite size of the minority phase (161).

3.7.4. Raman Spectroscopy

Raman spectroscopy is a light scattering technique based around the interaction of a monochromatic laser with vibrational states in a material. It is a rapid technique used for quick fingerprinting of crystal structures as the vibrational states probed by the incident photons are related to chemical

bonding and symmetry in materials. It is a commonly used technique for calcium carbonate fingerprinting as it is able to conclusively differentiate between polymorphs, and analysis can be localised onto small sample regions (≈1-10 μm spatial resolution if done in an optical microscope) (162). Raman spectroscopy is not significantly affected by the presence of water, meaning that it can be used during or immediately after a reaction has finished (163).

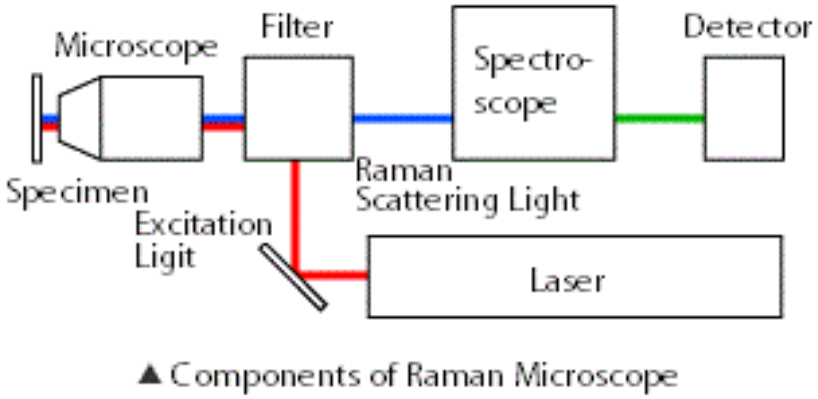

Figure 3.25 Schematic representation of Raman microscopy (164).

In practise, a light microscope is used to aim a laser onto a sample, the incident photons reflect off the sample and interact inelastically with phonons in the material. If the material absorbs energy from the laser, it will emit a photon of lower energy, is known as a Stokes scattering event, and if the material loses energy by emitting a photon of higher energy, it is an anti-Stokes scattering event. The light from the laser which has not interacted with the sample i.e. has simply reflected off (the parent laser line), is removed by a monochromator, the light corresponding to sample interactions is projected onto a CCD camera and the wavelengths are extracted (163).

Unlike IR spectroscopy, Raman does not require the creation of a dipole during bond vibration, meaning that symmetrical vibrations can be observed, these would be invisible to IR spectroscopy as they does not produce a permanent dipole. If a molecule has a centre of symmetry, Raman active vibrations would not be visible in the infrared spectrum.

The wavelength shifts correspond to specific interactions of the incident photons with chemical bonds or molecular alignments, for example, vaterite

displays two wavelength shifts at 1075 and 1091 cm^{-1}, and these correspond to different orientations of the carbonate group in the unit cell. Calcite and aragonite have more rigid carbonate orientations and thus do not display this double wavelength shift, only one (41). A summary of the Raman shifts for the anhydrous polymorphs can be seen in Table 3.1.

Polymorph	**Raman shift cm^{-1}**							
Calcite	157	282	713	1086				
Aragonite	155	208	701	1085				
Vaterite	115	207	266	301	743	751	1075	1091

Table 3.1 Raman shifts of the anhydrous calcium carbonate polymorphs (41, 46, 165, 166).

It should be noted that the intensity of the laser source used in Raman spectroscopy can induce heating in the specimen and thus induce alteration of composition or structure. Care should be taken to avoid causing damage using this technique by reducing the laser intensity until damage is avoided.

3.7.5. Scanning Electron Microscopy (SEM)

Scanning electron microscopy is a surface sensitive electron microscopy technique. Similar to STEM, SEM uses the rastering of a focussed electron probe to form images in a serial manner, with multiple analytical signals produced including EDX. Information on particle shape and surface topography are extracted through secondary electron (SE) imaging, where low energy electrons are emitted from beam-induced ionisations in the sample. Backscattered (incident) electron (BSE) images produce compositional contrast based on atomic weight, regions with high atomic weight scatter electrons more readily than light atomic weight regions, giving contrast where heavy regions show up brightly. SEM typically uses accelerating voltages between 1-30 kV for surface analysis, some modern SEM systems are capable of operating in STEM mode for appropriately thin specimens, but lack resolution due to lens aberrations. SEM resolution in bulk specimens is limited by lens aberrations and the interaction volume of the

beam with the specimen, lower voltages produce lower interaction volumes and are more surface sensitive.

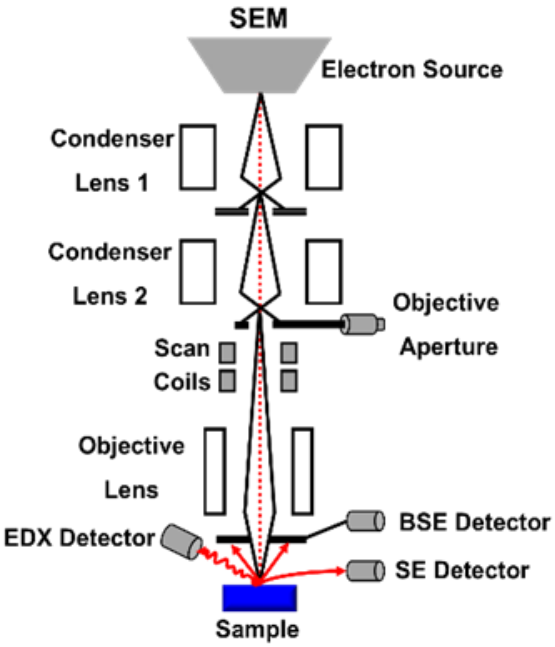

Figure 3.26 Schematic representation of a scanning electron microscope, showing electron beam path, and conventional lens and detector positions (128).

Whilst SEM is a valuable tool for imaging and elemental analysis, it is unable to readily provide information on crystallinity in samples, particularly in nano-particulates, for this reason it is necessary to combine SEM with diffraction-based techniques, either XRD, phase contrast CTEM/STEM imaging or SAED.

3.7.6. X-ray Absorption Spectroscopy (XAS)

X-ray absorption spectroscopy (XAS) is a complementary technique to EELS, as it measures the absorption of specific wavelengths of X-ray by a specimen. XAS relies on the use of a tuneable X-ray source to measure the X-ray absorption coefficient over a range of incident X-ray energies, corresponding to a characteristic atomic absorption energy. XAS generally uses a synchrotron radiation source, as the X-rays must have a high intensity, and the energy spread must be tightly monochromatic but also readily tuneable. Measurements of specimens can be taken in either dry solid, aqueous

dispersion or liquid state, sampling either transmitted X-ray intensity, X-ray fluorescence intensity, or photoelectron yield produced by the X-ray beam.

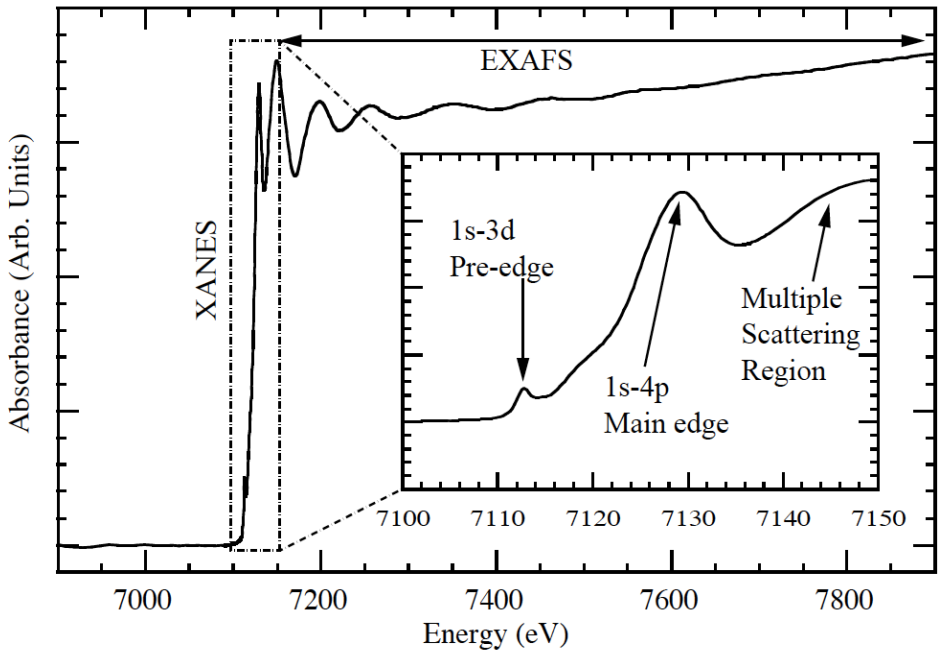

Figure 3.27 XAS spectrum showing the XANES region and the EXAFS regions of the Fe *K*-edge (167).

X-ray absorption spectra encompass both XANES (X-ray Absorption Near Edge Structure) and EXAFS (Extended X-ray Absorption Fine Structure), these regions are indicated in Figure 3.27. Where XANES shows features based on the multiple scattering resonances of excited core electrons to bound states at energies 50-100 eV above the core ionisation potential. EXAFS features are formed from single scattering events of the ejected photoelectron.

The EXAFS region can be processed to extract the radial distribution function, which gives the nearest neighbouring atoms for a chosen atom, this can build up a picture of bonding in a material (168). The XANES region can be fit using Gaussian peaks to investigate the energies of the electronic excitations. The XANES region is often characteristic of the valence state of an atom, as such it can be used to fingerprint compounds present in mixtures, or the different oxidation states present.

Chapter 4. Experimental Methods

4.1. Specimen Synthesis

Aragonite, vaterite and fuel detergent specimens were synthesised by Dr. Thokozile Kathyola as part of her PhD studies, using the methods presented below. These methods were directly reproduced with permission from Dr. Kathyola (39). Calcite was synthesised by the author.

4.1.1. Calcite

Calcite nanoparticles were synthesised following the methods outlined by Hari et al (169). Calcium oxide was prepared from calcined Fisher Scientific AR grade calcium carbonate, heated to 900 ^{o}C for 5 hours. Carbon dioxide was bubbled through a stirred suspension of 0.03 M calcium oxide in 200 ml Milli-Q deionised water. The pH of the suspension was monitored throughout; once the pH had reduced from 12 to 7 and stabilised, the resulting mixture was centrifuged at 8000 rpm for 30 mins and the precipitates dried at 50 ^{o}C for 6 hours.

4.1.2. Aragonite

Aragonite was synthesised using a variation of the method proposed by Kitamura et al (170). 1.61 M of sodium carbonate (in 126 ml of water) was added to 0.21 M calcium hydroxide (in 82 ml of water) *via* dropwise addition. The reaction mixture was continuously stirred and maintained at a temperature of 70 °C. The dropwise addition and stirring were maintained for 30 and 60 minutes respectively. The resulting white precipitate was filtered, washed with water and ethanol, and dried under vacuum for 24 hours.

4.1.3. Vaterite

Vaterite was synthesised using the method proposed by Shivkumara et al (171). 1 M of sodium carbonate (in 20 ml of water) was added a solution of glycine (0.16 M in 200 ml of water). The mixture was stirred for 30 minutes before 0.03 M of calcium chloride dihydrate (in 20 ml of water) was added.

The mixture was stirred for 60 minutes after which a white precipitate was filtered, washed with water and ethanol, and dried under vacuum for 24 hours.

4.1.4. Overbased $CaCO_3$ Fuel Detergents

The overbasing process, based on literature (9, 172), was carried out in two stages. The first stage consisted primarily of the synthesis of particles and the second stage involved the removal of solvents and solid sediments from the colloidal dispersion. The detergent synthesis and isolation can be separated into six steps i.e.

Step 1) Neutralisation – Reaction of sulfonic acid ($R–SO_3H$) with calcium hydroxide ($Ca(OH)_2$) to produce calcium sulfonate ($Ca(R–SO_3)_2$) surfactant:

$$2R\text{-}SO_3H + Ca(OH)_2 \longrightarrow Ca(R\text{-}SO_3)_2 + 2H_2O$$

The reactor was configured for reflux (Figure 4.1) and charged with toluene (240 ml), methanol (177 ml), water (14 ml), and mineral oil (about 6% of the required total volume of ~200 ml). Calcium hydroxide (1.54 M) was then added to the vessel, followed by the addition of 170 g of sulfonic acid (molarity not known as the surfactant chain is proprietary) and a smaller amount of toluene in semi-batch mode. The temperature during this process ranged from 28 to 40 °C (172) and the system was operated at stirrer speeds ranging from 0 to 400 rpm depending on the material being added and its associated viscosity. Following the completion of the neutralisation process (measured by pH), an aliquot of the dispersion was taken to isolate the non-carbonated calcium sulfonate surfactant.

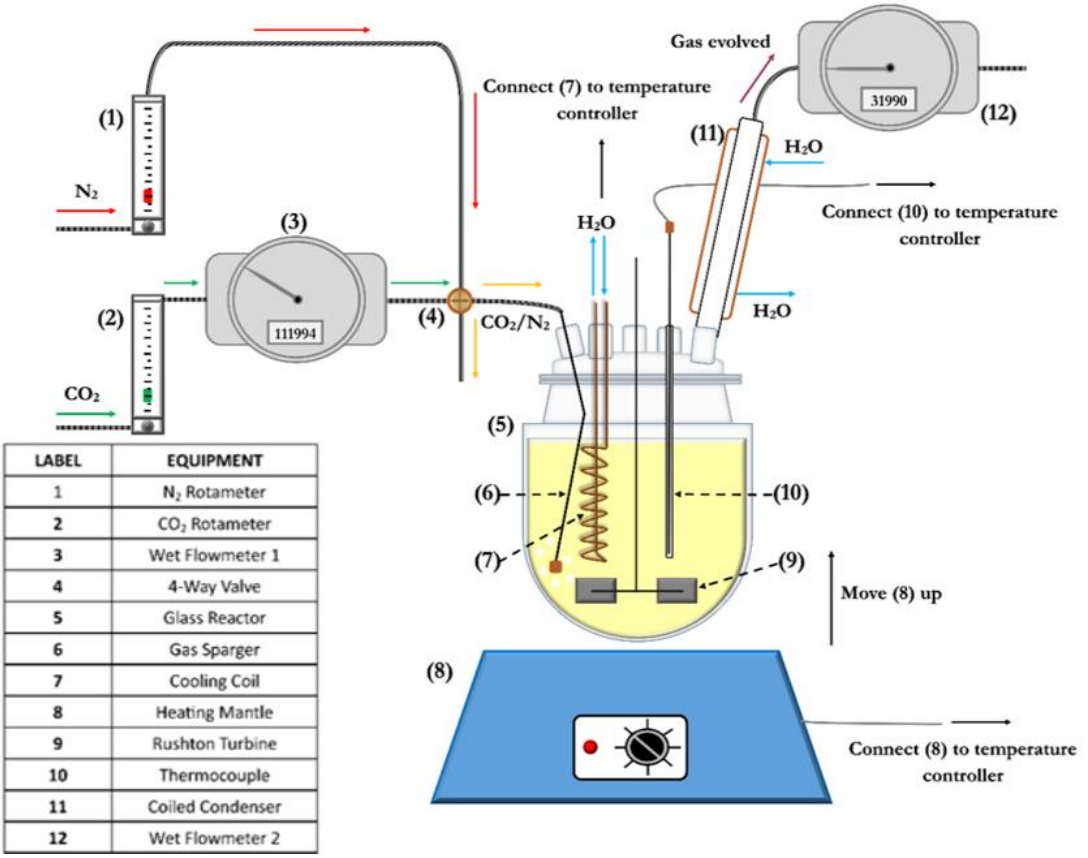

LABEL	EQUIPMENT
1	N_2 Rotameter
2	CO_2 Rotameter
3	Wet Flowmeter 1
4	4-Way Valve
5	Glass Reactor
6	Gas Sparger
7	Cooling Coil
8	Heating Mantle
9	Rushton Turbine
10	Thermocouple
11	Coiled Condenser
12	Wet Flowmeter 2

Figure 4.1 Schematic of the conventional lab setup (in reflux mode) for the synthesis of calcium sulfonate neutral surfactants and overbased detergents (39).

Step 2) Carbonation – Reaction of $Ca(OH)_2$ with carbon dioxide (CO_2) to form overbased sulfonate ($nCaCO_3 \cdot Ca(R–SO_3)_2$) detergent:

$$Ca(R\text{-}SO_3)_2 + (n+x)Ca(OH)_2 + nCO_2 \xrightarrow{CH_3OH} nCaCO_3 \cdot Ca(R\text{-}SO_3)_2 + xCa(OH)_2 + nH_2O$$

The second step initially required setting a carbon dioxide (CO_2) flowrate that ensures a 3-hour reaction. To account for the exothermic nature of the carbonation reaction, a cooling coil connected to a temperature controller was inserted in the vessel to maintain the reaction temperature at about 28 °C.

Step 3) Heat Soak – The post-carbonation mixture was heated to 30°C to allow for reaction completion and growth of the carbonate particles and to reduce the formation of sludge and sedimentation. During this time, a second charge of 56% of the mineral oil is added to the reactor.

Step 4) Polar Distillation – The reactor setup was changed to distillation configuration (as can be seen in Figure 4.2) to remove the polar (water and methanol) solvents. This involved increasing the temperature above the boiling point of the two solvents i.e. greater than 100 °C. The remaining mineral oil was added during distillation. Subsequently, the dispersion was diluted with a specified amount of toluene, ensuring the methanol to toluene volume ratio is within the 0.1 to 0.6 range (173).

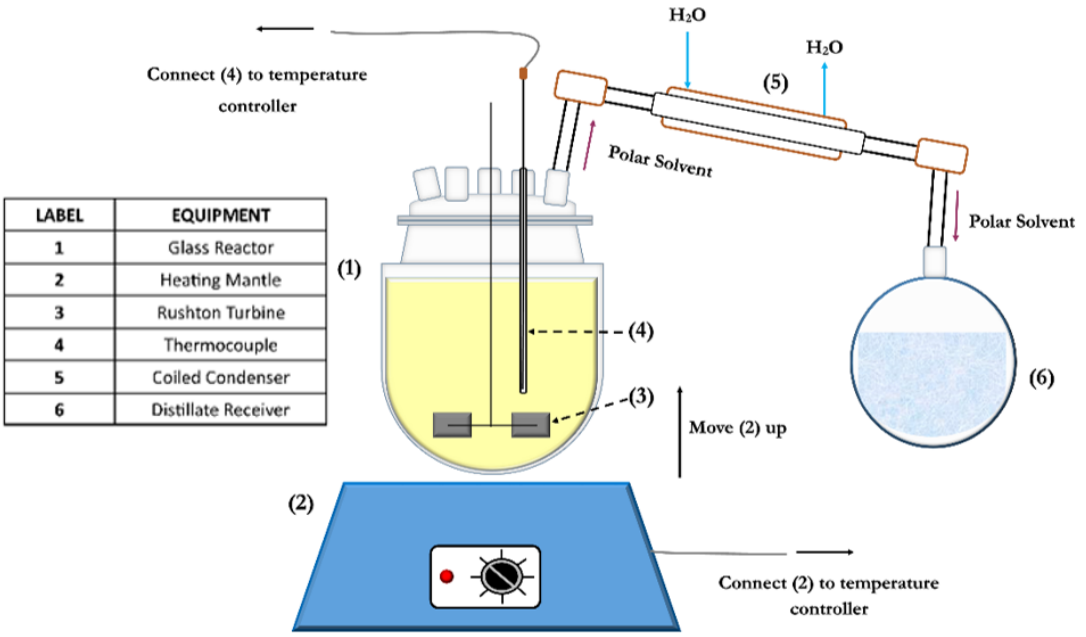

Figure 4.2 Schematic of the of the conventional lab setup (in distillation mode) for the removal of the polar and non-polar solvents from the oil dispersion containing calcium sulfonate neutral surfactants and overbased detergents (39).

Step 5) Centrifugation – the non-polar (toluene) solvent was removed from the post-carbonation dispersion in a three-step distillation: the first step was to centrifuge the entire reaction mixture for an hour in order to remove all residual solids from incomplete carbonation of $Ca(OH)_2$ and $CaCO_3$ crystallisation. The sediment-free fluid containing suspended detergent particles was then put back into the reactor.

Step 6) Non-polar Distillation – The hydrocarbon solvent and some water was distilled using the same setup as for the methanol distillation (Figure 4.2) but with the addition of a vacuum and re-insertion of the gas sparger for a

nitrogen purge. This distillation was achieved by increasing the reactor temperature from ambient to a temperature greater than 130°C (174).

Particle separation through dialysis

Samples of the detergent particles were separated from the reaction mixture using dialysis through a latex membrane with a hexane or heptane solvent. A schematic of the separation equipment is shown below in Figure 4.3.

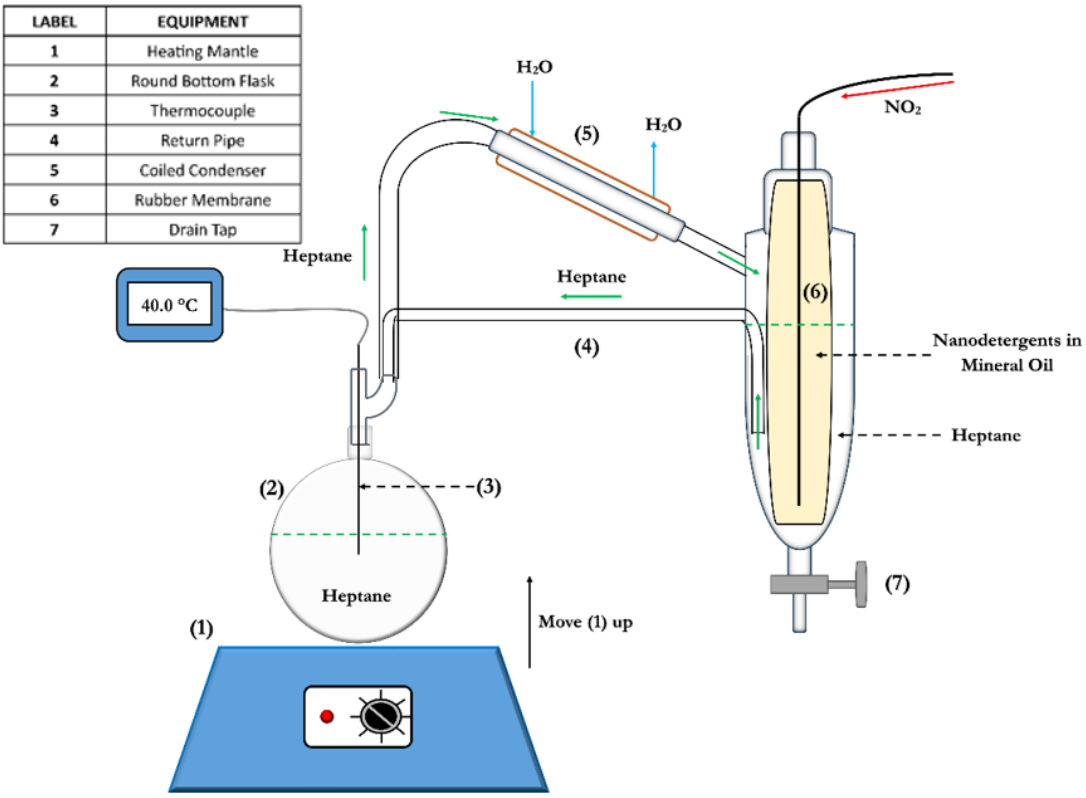

Figure 4.3 Schematic of the dialysis equipment used to separate the detergent particles from the mineral oil reaction mixture (39).

30 g of the as-synthesised mixture was diluted in 45 ml of heptane/hexane and placed in the dialysis membrane (item 6) in Figure 4.3. 250 ml of heptane/hexane was added to the round bottom flask and was heated to 100^{o}C so that fresh solvent would pass through the condenser and replenish the dialysis vessel. Nitrogen was bubbled into the dialysis membrane for agitation.

Following separation, the fuel detergent particles were suspended in hexane for analysis. For CTEM/STEM applications, the fuel detergent particles were drop cast onto an ultrathin amorphous carbon support film on a lacy carbon

film with a copper grid (Agar Scientific). Once the solvent had evaporated, the particles were ozone cleaned using a Hitachi ZoneSEM cleaner. All imaging of the detergent particles took place using a FEI low background double tilt analytical TEM sample holder.

4.2. Bulk Materials Characterisation

4.2.1. X-ray Diffraction

X-ray diffraction was carried out on a Bruker D8 Advance diffractometer, equipped with a Cu K_α X-ray source and Bragg-Brentano geometry, a 3mm focussing slit was used on the X-ray source and a Vantec position sensitive detector was used for pattern collection. Suspended particles were deposited into a Silicon sample holder and left to dry prior to analysis. Diffraction scans were taken between 20^o and 100^o with a step size of 0.033^o and a time per step of 0.15s. Peak fitting was performed in Panalytical HiScore+, using the ICSD PDF4+ database. Scans of the sample holder were also taken under the same conditions, to determine whether background features are present in the specimen or the sample holder.

4.2.2. Raman Spectroscopy

Raman spectroscopy was performed with a Renishaw inVia Raman Microscope, using a 785 nm laser with a scan range of 100-1200 cm^{-1}. The spectral resolution of this system is approximately 10 cm^{-1}, and spatial resolution (laser spot size) is approximately 1 µm. Suspended particles were deposited onto a glass microscope slide and air-dried prior to measurements. Peak positions were compared against literature references (shown in section 3.7.4). In the calcite spectra, the baseline intensity rises between 1000 and 1200 cm^{-1}, this is a fluorescence background effect from the glass slide and has no implications for the Raman shifts (175). In some cases, a broad peak can be seen at 380 cm^{-1} this corresponds to water (176).

4.2.3. Scanning Electron Microscopy

A Hitachi SU-8230 FEG-SEM was used to characterise the shape and size of the calcite particles following synthesis. A specimen was prepared by drop-

casting particles suspended in ethanol onto a copper TEM grid with a holey carbon film. The specimen was imaged at 20 kV, using an in-lens secondary electron detector.

4.2.4. Fourier Transform Infra-Red Attenuated Total Reflectance

FTIR-ATR measurements were performed using a Thermo-Nicolet IS-10 spectrometer with a ZnSe ATR crystal. The final spectra were built up from an average of 4 spectra measured between 650 and 4000 cm^{-1}, at a resolution of 4 cm^{-1}. The calcite specimen was measured dry, with the powder deposited directly onto the ATR crystal, the fuel detergent specimens were drop cast and measured whilst hexane was still present. Background spectra were taken after the ATR crystal had been cleaned.

4.2.5. X-ray Absorption Near Edge Structure

XANES measurements were acquired by Dr Thokozile Kathyola at the Diamond Light Source synchrotron using end station B18. The energy range covers the calcium *K*-edge at 4000-4600 eV. The measurements were taken on dried powder and fuel detergents, under a helium atmosphere in total electron yield (TEY) collection conditions.

4.2.6. Dynamic Light Scattering

DLS measurements were performed using a Malvern Zetasizer Nano ZS system, at 20 ^{o}C with three measurements taken sequentially. The calcite specimens were suspended in ethanol and measured in a disposable polystyrene cuvette, and the fuel detergent specimens were suspended in hexane, and measured in a glass cuvette. The density of the synthesised particles was taken to be 2.71 g/cm^3 (density of calcite), the viscosity of the ethanol solvent was set to 1.2 $mPas^{-1}$ at 20^{o}C and the refractive index of the synthesised particles was set to 1.5.

4.3. 200 kV CTEM Imaging, Diffraction and EDX

CTEM imaging and diffraction experiments were carried out in a FEI Tecnai F-20 FEG-TEM with an Oxford Instruments X-Max 80 mm^2 EDX detector and

a Gatan Orius CCD. Controlled irradiation at several electron fluxes was applied to the calcite nanoparticles, bright field mass-thickness contrast images and selected area diffraction patterns; using an aperture which defined a ~200 nm diameter at the specimen, were taken at fixed timed intervals. Prior to imaging and diffraction, the electron beam was blanked and the fluence reduced to avoid unintended irradiation.

To find suitable particle clusters at low magnification, the beam was spread using the second condenser lens to lower the incident fluence. The particles were centred on the optic axis at low magnification and low incident fluence, then the beam was blanked, the magnification increased, and the electron beam condensed to a pre-set current corresponding to a known electron flux. This was in order to minimise the exposure of the specimen to unintended irradiation, however it was exposed to some irradiation during focussing and searching, this was incorporated into the first time point, by measuring the incident electron fluence rate and approximately timing the specimen's exposure. This meant that the first time point did not correspond to zero accumulated fluence, but was typically below 5% of one second of the chosen fluence rate for imaging or diffraction, meaning that the typical error on the first time point was below 1%, which was propagated throughout the time resolved data series. The larger source of error was from the time measurement, which was considered to be up to 10%, this produced an error in the accumulated fluences of 10%. Both of these sources of error are combined in the vertical error bars in Figure 5.14. The horizontal error bars reflect errors in the measurement of the electron flux using the fluorescent screen and an internal calibration provided by the manufacturer.

4.3.1. Bright Field CTEM Imaging

Time-resolved BF-CTEM images were interpreted in FIJI to extract information on the onset of pore formation in calcite nanoparticles (177). The thresholding tool was used to observe the appearance of bright regions in the particles as a function of accumulated fluence. Brighter regions in the bulk of a particle are the result of mass loss, and are likely pores or voids. An example

of how the thresholding process was applied to a cluster of particles is shown in Figure 4.4.

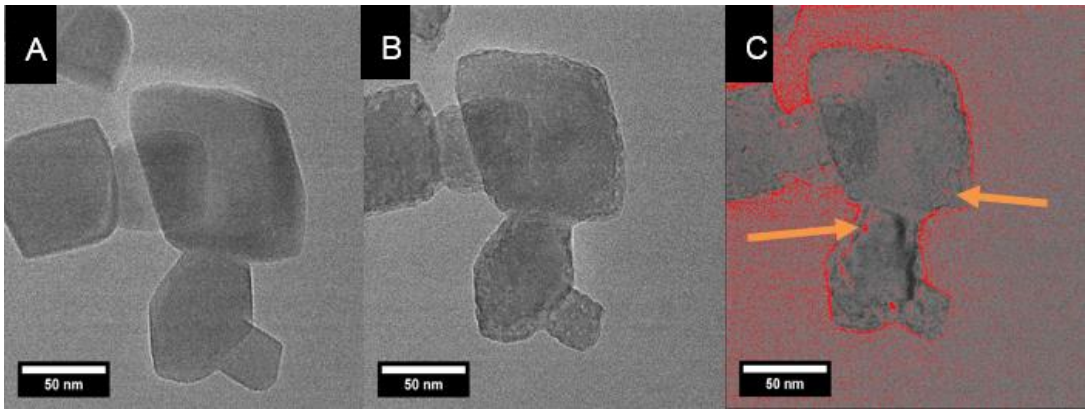

Figure 4.4 A) undamaged particle. B) Damaged particle showing light regions consistent with pore formation. C) Image B with a brightness threshold applied, red regions correspond to regions brighter than the image threshold.

This method was adequate to identify the presence of pores (shown with the orange arrow in Figure 4.4), but not for the quantification of pore size, as changing the threshold level would change the measured pore size for a given image.

4.3.2. Diffraction

Diffraction patterns were analysed using the Gatan digital micrograph software package. The d-spacings were extracted by measuring the distance between opposing diffraction spots, or measuring the diameter of diffraction rings, these were divided by 2 and converted from 1/nm to angstroms by taking the inverse of the distance and multiplying by 10. These spacings were compared to those of known d-spacings of the crystalline calcium carbonate polymorphs and calcium oxide.

The presence of polycrystalline calcium oxide in SADPs was investigated by analysing the CaO {111} and {200} diffraction rings at d spacings of 2.77 Å and 2.41 Å respectively. SADPs were processed using the “reveal weak reflections” tool in the Difftools plugin for Gatan Microscopy Suite 3.11 (178). This plugin applies a reciprocal cube root to the image pixel values, the cube root compresses the dynamic range, and the negative power inverts the image

to give black spots on a white background. Following this, a line profile was drawn from the centre of the diffraction pattern, through a region with no diffraction spots. The presence of two diffraction rings indicated by arrows in the line profile was indicative of the CaO {111} and {200}. The appearance of these diffraction rings were used as an indicator of electron beam-induced phase transformation in the crystal structure in calcite nanoparticles.

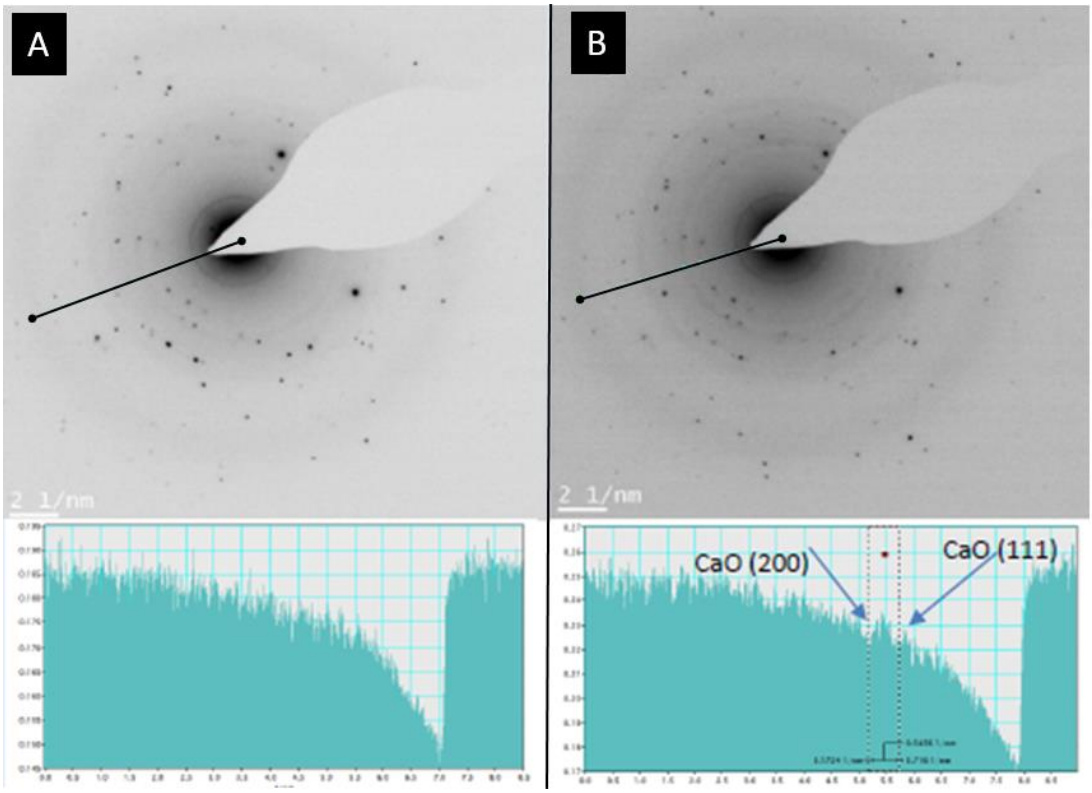

Figure 4.5 Selected area diffraction pattern (top) and integrated line profiles (bottom) from locations indicated by the black lines in the SAED of the calcite particles A) before the calcium oxide rings are detected B) after calcium oxide rings were detected.

4.3.3. Dark Field CTEM Imaging

Off-axis DF-CTEM images were formed with an objective aperture inserted around a section of the calcium oxide {111} and {200} rings in the back focal plane. Images were taken in both bright field and dark field imaging modes whilst the particle was irradiated. Fluences were not quantified.

4.3.4. EDX

A cluster of calcite particles was continually irradiated at a flux of 2.6×10^4 e-$nm^{-2}s^{-1}$ and successive EDX spectra were collected with an acquisition time of

30 s each. The background was subtracted using the method outlined in section 4.4, to reduce the impact of oxygen contamination in the support film on the quantification of the O:Ca atomic ratio. Spectra were analysed using the DTSA-II software package (179), for background subtraction and peak integration of the Ca K_α and O K_α peaks. From this the k-factor was calculated assuming that the first spectrum corresponded to undamaged calcite, of perfect stoichiometry, giving a ratio of oxygen to calcium of 3:1. No absorption or fluorescence corrections were used in the quantification, as all damage experiments were carried out in the same specimen environment and it was assumed that these would be the same. In addition absorption and fluorescence are generally considered to be negligible in TEM-EDX applications (146).

4.4. Background Subtraction for EDX Measurements

Multiple spectra, typically 5, were acquired from a region of the carbon film close to the irradiated particles, using the same conditions as for the particle spectra, these were averaged to produce a background spectrum for subtraction from the calcite spectra. This was done in order to reduce the impact of residual oxygen found in and on the carbon film on the quantification of oxygen in the calcite particles.

4.4.1. Oxygen Contamination

Oxygen is not typically quantified by EDX spectroscopy, as light elements have low fluorescence yields and their low energy X-rays can be easily absorbed by the specimen. There are also specimen related artefacts which can reduce the accuracy of oxygen quantification, any adsorbed water will produce oxygen X-rays, as will oxygen containing contaminants present in the specimen, TEM grid, support film, or microscope column. Oxygen contamination has been seen qualitatively through STEM-EDX mapping, shown in Figure 4.6, where oxygen was detected in the support film. Oxygen was not detected in the column vacuum, as the contaminant signals are localised to the support film.

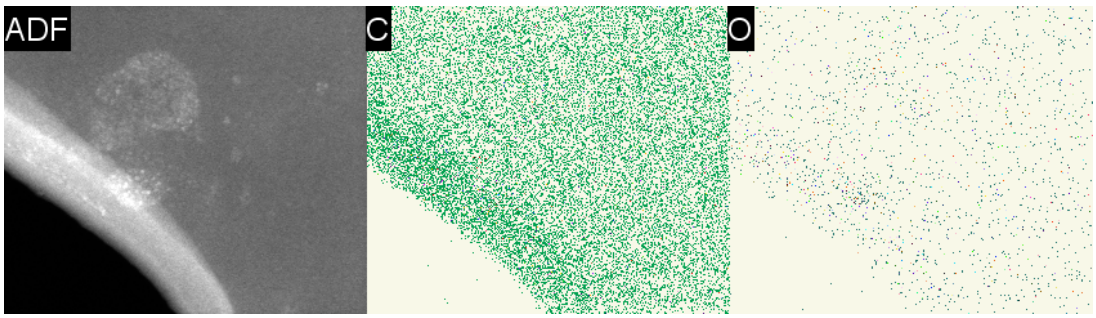

Figure 4.6 STEM-EDX map showing the presence of oxygen in the carbon support film.

An example of the background is shown in Figure 4.7, where a calcite spectrum and a background spectrum are overlaid, a relatively small oxygen peak can be seen in the background spectrum.

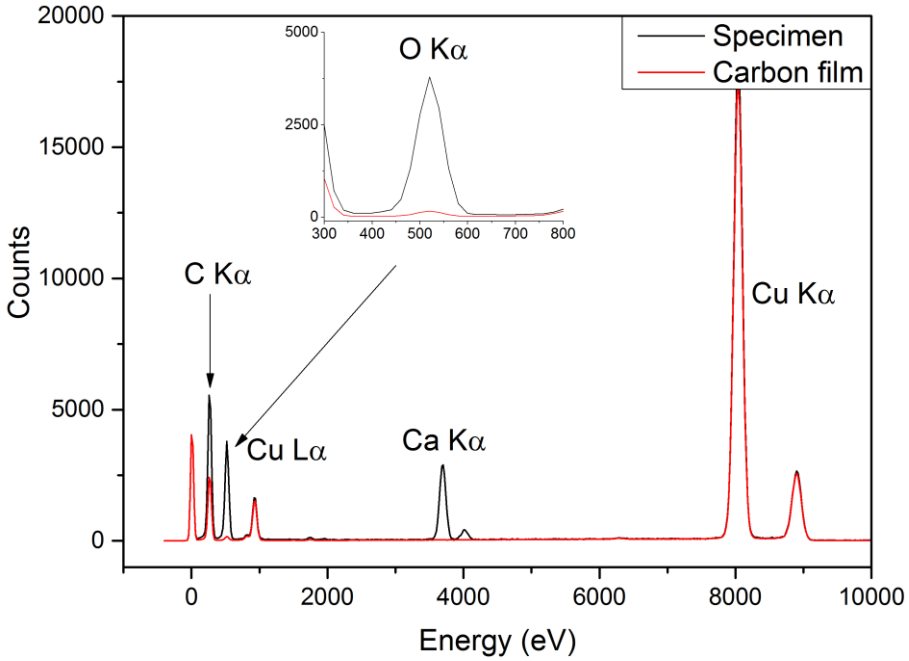

Figure 4.7 CTEM-EDX spectrum of the specimen and an area of the lacy carbon support film with no specimen present, both spectra were taken under the same acquisition conditions. The background spectrum is averaged from 5 spectra taken from the same region to reduce background noise.

The source of the contaminants on the film is not known, though it is believed that they are present at the point of manufacture, may be introduced during specimen transfer from ambient conditions to the vacuum, or are fixed as a contaminant by the electron beam during spectrum acquisition. Hydrocarbon contamination often contains oxygen, either through the deposition of silicon

dioxide SiO_2 from silicone vacuum greases, or through deposition of water molecules previously desorbed by the vacuum which have migrated towards the electron beam (78, 180, 181).

4.5. Quantitative Investigation into Beam Damage in Calcite

4.5.1. Comparing CTEM and STEM Irradiation Using Time-resolved Phase Contrast Lattice Imaging

A comparative study of electron beam sensitivity in STEM and CTEM was performed in a FEI Titan^3 Themis G2. Phase contrast (PC) CTEM lattice images were taken at 80 kV and 300 kV with an electron flux of 3.8×10^5 $e^- nm^{-2} s^{-1}$ at 380,000 times magnification on a Gatan OneView CCD. Phase contrast STEM images were taken at 300 kV with a probe current of 40 pA, 16 µs dwell time and a specimen pixel size of 81.7 pm at 910,000 times magnification giving an averaged fluence of 1.2×10^6 $e^- nm^{-2}$ per scan. The probe convergence semi-angle was 10 mrad, giving a 1.4 Å probe, the bright field detector collection semi-angle was set to 7 mrad and the ADF detector collection semi-angle was set to 17-100 mrad, at a camera length of 460 mm. The FFTs of both CTEM and STEM images were compared to investigate changes in crystallinity induced by electron irradiation.

For STEM imaging, the probe was focussed onto the ultrathin carbon support film using the Ronchigram in a region within ~10 nm of the scan window. The probe focus was adjusted until the central region of the Ronchigram displays near flat contrast (similar to Figure 3.6). To ensure the STEM phase contrast conditions were sufficiently sensitive at low fluences, a calcite specimen was imaged using a 1 pA probe current, 81.7 pm pixel size and 20 µs dwell time Figure 4.8).

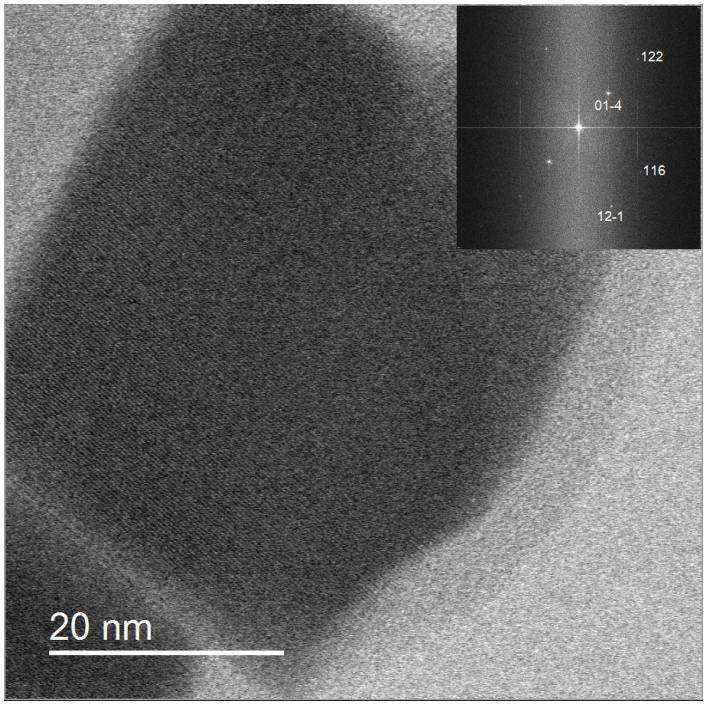

Figure 4.8 Calcite nanoparticle imaged under low-dose conditions, showing a 1.6 Å calcite (122) d-spacing (scan fluence = 1.65x10^4 e$^-$nm^{-2}).

This demonstrated that the STEM collection conditions were sensitive enough to detect a lattice in the calcite specimen at low incident fluxes, and that the resolution obtained was ~1.6 Å

4.5.2. Comparing the Impact of Accelerating Voltage on Mass Loss Using Time-resolved EDX Spectroscopy

EDX measurements were taken on a FEI Titan^3 Themis G2 with a Super-X EDX system, using a FEI low background analytical double tilt sample holder. Spectra were taken on clusters of particles at a fluence of 3.5x10^4 e$^-$nm^{-2}s^{-1}, 15s spectra (for 300 kV) and 30s spectra (for 80 kV) were taken consecutively with the beam blanked between acquisitions. The spectra were quantified, and the backgrounds subtracted following the procedure in section 4.4.

4.5.3. In-Situ Bake Out

To reduce the impact of hydrocarbon contamination during STEM imaging, a calcite sample was drop cast from ethanol onto a silicon nitride MEMS heater grid (DENS Solutions) and loaded into the microscope in a DENS Solutions wildfire single tilt holder. The hydrocarbon contamination was quantified first

with the sample unheated, by measuring the contamination growth perpendicular to particle facets after each scan, using ADF-STEM imaging at 320,000 times magnification, 10 µs dwell time, 40 pA probe current and at a camera length of 460 mm, giving an ADF collection semi-angle range of 17–100 mrad. Measurements of contamination thickness were taken using line profiles in the Gatan Microscopy Suite software package, with a 5-pixel integration width, this is shown in Figure 4.9. The sample was then heated to 75 °C and held for 16 hours before cooling to 25 °C over the course of 1 hour. Following heat treatment, the contamination build-up was then quantified using the same method on a fresh region of the sample, to ensure contamination desorption.

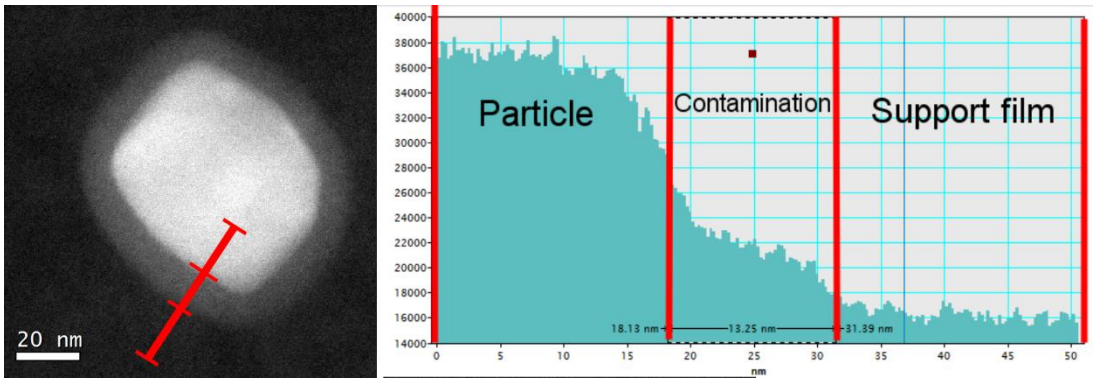

Figure 4.9 Quantification of hydrocarbon contamination buildup on calcite nanoparticles in STEM imaging.

Following cleaning, the calcite particles were imaged at high resolution using the STEM phase contrast conditions outlined in section 4.5.1. The FFTs were processed using the “Reveal weak reflections” function in Difftools and were used to observe any electron beam damage.

4.6. TEM Characterisation of Fuel Detergent Particles

4.6.1. Initial CTEM Characterisation

Low magnification CTEM imaging and selected area electron diffraction were carried out on the FEI Titan microscope at 300 kV. Bright field imaging was performed with and without a 6 mrad objective aperture centred on the optic axis. Electron diffraction was carried out with a selected area aperture inserted corresponding to 3 µm diameter region of illumination on the specimen.

4.6.2. Particle Size Measurement Using STEM

ADF-STEM imaging was used to provide a measure of the particle size of the detergents. Images were processed using FIJI (177) using a brightness threshold to separate the particles from the support film, and to measure the particle size using the Feret diameter. The Otsu thresholding algorithm and the same brightness threshold were used for all images measured for particle sizes. The nearest neighbours and hence approximate surfactant chain length was measured on these particles using a FIJI script (182).

4.6.3. Electron Beam Damage of Fuel Detergent Particles

Time-resolved BF-CTEM lattice imaging was used to measure the critical fluence of the fuel detergents. A beam current of 0.5-1 nA at a magnification of 380,000 times was used, producing a flux of 1.9-3.8x10^5 $e^-nm^{-2}s^{-1}$. The method used was the same as previously described for the calcite nanoparticles in section 4.5.1. For the detergent particles, the critical fluence was taken to be the fluence at which crystalline CaO was seen in the FFT of the image.

4.6.4. Low-Dose STEM Characterisation of Fuel Detergent Particles

Low-dose STEM imaging was performed with a probe current of 10 pA and a camera length of 460 mm, giving detector collection angles of 7 mrad and 17-100 mrad for bright field and annular dark field respectively, this follows the recommendations of Sader et al (87), to produce phase contrast with relatively efficient electron collection. The dwell time was set to 10 µs per pixel, the pixel size was 81.7 pm for high resolution scans giving fluences per scan of 9x10^4 e^-nm^{-2}. If crystallinity was discovered in a particle, the d-spacings present in the FFTs were compared to known d-spacings of the crystalline calcium carbonate polymorphs, calcium hydroxide (synthesis precursor), and calcium oxide (the beam damage product of calcium carbonate).

4.6.5. Aberration Corrected STEM Imaging

Aberration corrected STEM imaging was performed on a FEI Titan^3 Themis Z equipped with a CEOS ASCOR C_s corrector, at the Thermo Fisher Eindhoven Nanoport. The microscope was operated at 300 kV, with the probe convergence semi-angle set to ~20 mrad. The BF detector collection semi-angle was 17 mrad, and the ADF collection semi-angles were approximately 32-150 mrad.

4.6.6. "Random" Sampling

As a baseline for the quantification of crystallinity, the specimen was imaged in 50 locations, chosen without prior knowledge, i.e. no low magnification screening. However, images with significant sections of thick carbon support film were excluded after capturing. These regions were imaged using standard low-dose ADF and BF STEM conditions, as outlined in section 4.6.4. The particles were counted in all images using FIJI, using the same methods as in section 4.6.2 and the incidence of crystallinity manually counted. Crystallinity was confirmed by the presence of crystalline spots in the FFT of the phase contrast image and compared to known structures.

4.6.7. Wide Area Mapping

An aberration corrected Titan^3 Themis Z was used for wide-area mapping controlled by the Thermo Fisher MAPS software (183). The MAPS software was configured to image a 7x7 µm region using ADF-STEM imaging, with a pixel size of 70 pm, a probe current of 10 pA, and a dwell time of 10 µs, the ADF collection semi-angles were approximately 32-150 mrad. This produced in a fluence of $5x10^5$ e^-nm^{-2}. The MAPS software compensated for stage drift and backlash, however the scan region was set to overlap the image tiles by 20% to aid in reconstruction of the map. Due to software limitations it was not possible to use the bright field detector simultaneously.

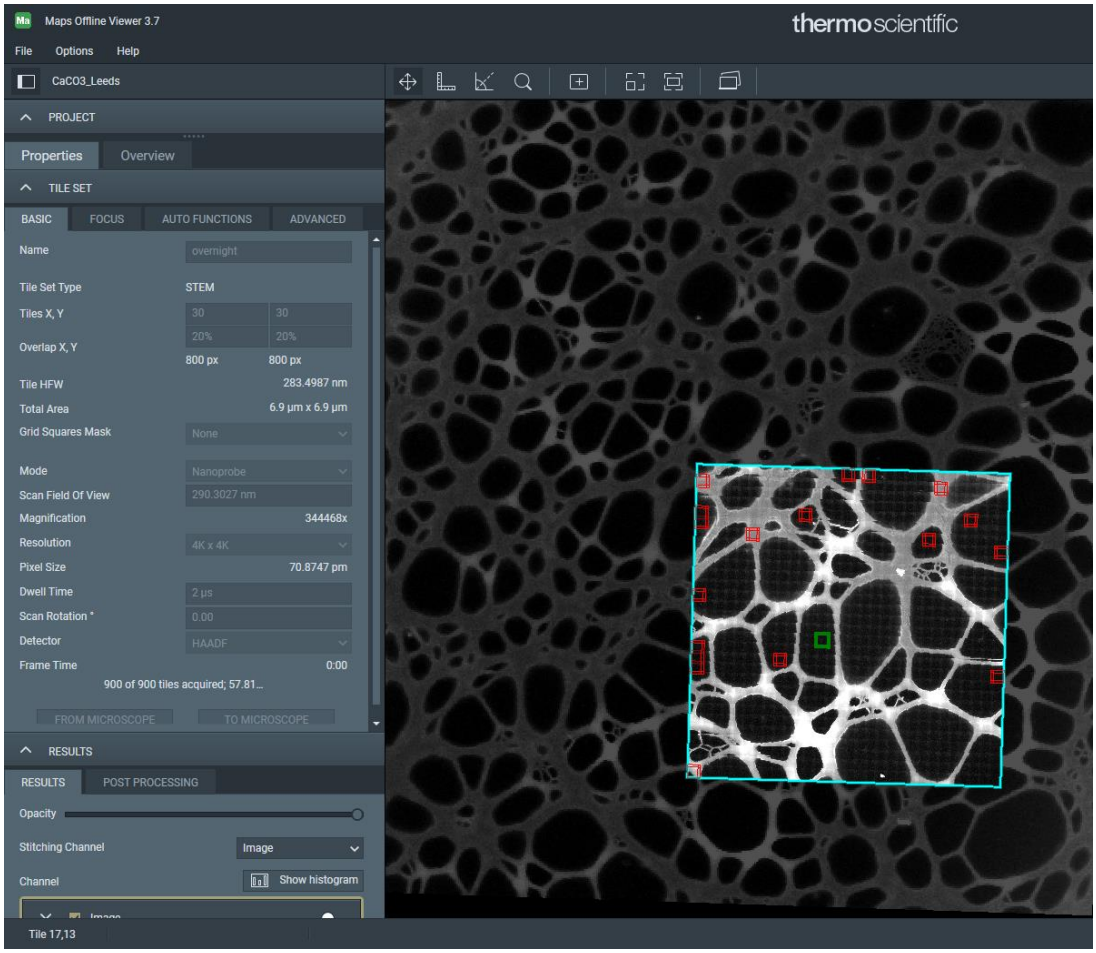

Figure 4.10 The MAPS software interface, showing the imaging conditions in the left panel for the individual tiles and the map as a whole. The green tile is the currently selected tile, the red tiles could not be automatically stitched together and were aligned manually.

A screenshot of the MAPS software interface presented in Figure 4.10 shows the composite wide area map built up from smaller images. The low-magnification background image is used to define the approximate region which will be mapped using the pre-set imaging conditions.

Following mapping the wide-area image was then segmented into 50 smaller regions using FIJI (177) to make processing the dataset more manageable on a standard desktop PC. The particles were counted using the same method as in section 4.6.2. The incidence of crystallinity was manually measured, by comparing particles which were visibly larger than average, displayed enhanced diffraction contrast relative to their non-crystalline neighbours

(~20% brighter when measured using FIJI) and were not formed from obvious particle superposition, as this was noticed during the random sampling experiments.

4.7. Solvent Effects on Fuel Detergent Stability

4.7.1. "Proof of Concept" Experiments into Methanol Effects

Approximately 2% methanol by volume was added to a sample of the fuel detergent particles suspended in hexane, the specimen was sonicated for 15 minutes, and then left for 4 days prior to analysis by STEM and FTIR. STEM imaging took place with a 10 pA probe current, with the BF collection semi angle set to 7 mrad, and the ADF collection semi-angles set to 17-100 mrad. EDX mapping was performed with a 100 pA probe current and a 2 µs dwell time. Selected area electron diffraction was carried out using an aperture which defined a region of 100 or 200 nm diameter, at a camera length of 285 mm, the aperture size was chosen depending on particle size, in order to fit only one entire particle inside the aperture wherever possible.

4.7.2. Time-resolved Measurements

1 drop (~50 µl) of methanol was added to 3 ml of the dialysed fuel detergent particles suspended in hexane and the mixture was sonicated for 15 minutes. The specimens were then left for various times between 1 and 28 days and were measured by DLS, FTIR, XRD, STEM imaging and SAED using the previously outlined methods. All STEM imaging, EDX mapping and electron diffraction measurements were carried out using the same conditions as the "proof-of-concept" experiments.

Diffraction patterns were analysed using the Gatan digital micrograph software package. The d-spacings were extracted by measuring the distance between opposing diffraction spots, or measuring the diameter of diffraction rings, these were divided by 2 and converted from 1/nm to angstroms by taking the inverse of the distance and multiplying by 10. These spacings were compared to those of known d-spacings of the crystalline calcium carbonate polymorphs, calcium hydroxide, monohydrocalcite, ikaite, and calcium oxide.

The zone axis of single crystal diffraction patterns were extracted using the Weiss zone law and confirmed by overlaying a simulated diffraction pattern of that zone axis on the experimental pattern to confirm.

Chapter 5. Quantifying and Thresholding Electron Beam Damage in Calcite Nanoparticles under 200 kV CTEM Irradiation

5.1. Introduction

In this chapter, the characterisation and irradiation study of a calcite nanoparticle model system is described, the first part of the chapter will cover the general characterisation of the nanoparticles through various analytical methods. The second part of the chapter will detail qualitative observations of the progression of electron beam damage, and the quantification of these processes in calcite nanoparticles, as they degrade into calcium oxide.

In-house synthesis of calcite nanoparticles produced a phase pure product, with a tight particle size distribution, though susceptible to aggregation. The polymorph and purity were determined by Raman spectroscopy, X-ray diffraction, SEM, and CTEM via bright field imaging and electron diffraction. DLS was used for particle size and dispersion measurement when suspended in ethanol.

Following characterisation, the calcite nanoparticles were used to investigate electron beam irradiation using a FEI Tecnai F20 TEM, in both a qualitative and quantitative manner, through imaging, diffraction and EDX spectroscopy. Bright field imaging showed visible degradation, giving a damage threshold for the formation of pores and voids across the particle. Electron diffraction provided a fluence threshold for the appearance of calcium oxide crystallites, signifying that diffraction information is no longer of a single phase. It was found that these observations had no dependence on electron fluence rate, only on total accumulated fluence. Dark field imaging gave a qualitative indication of where calcium oxide nucleation occurs. High resolution lattice imaging by CTEM gave a direct observation of the damage process and the associated fluence required for the destruction of calcite crystallinity. EDX spectroscopy gave insights into the mass loss process occurring under irradiation, and how the extent of mass loss can be correlated to phenomena visible in CTEM images.

5.2. Calcite Model System Characterisation

5.2.1. Powder X-Ray Diffraction

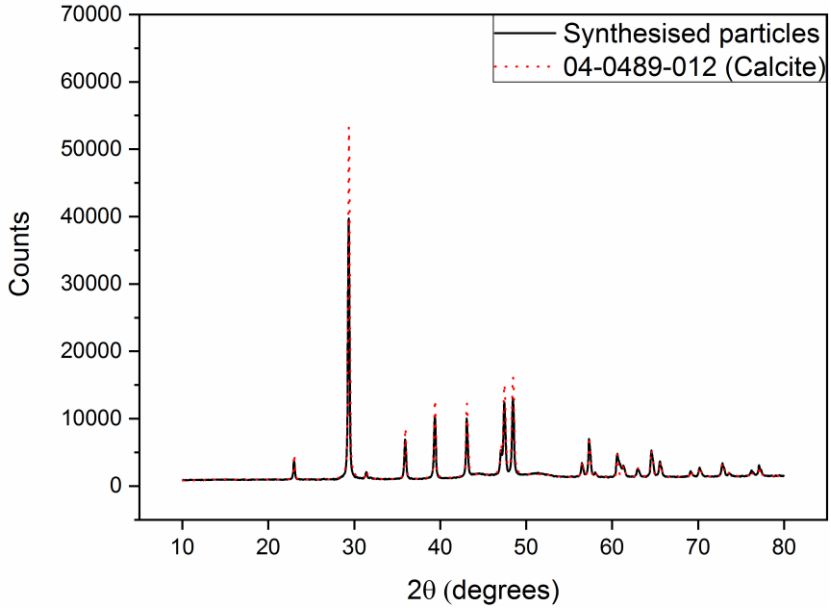

Figure 5.1 X-ray diffractogram of synthesised particles, overlaid with ICDD pattern 04-012-0489 for calcite.

XRD showed that the synthesised material was solely calcite with no traces of crystalline impurities of either unreacted precursor or other calcium carbonate polymorphs.

5.2.2. Raman Spectroscopy

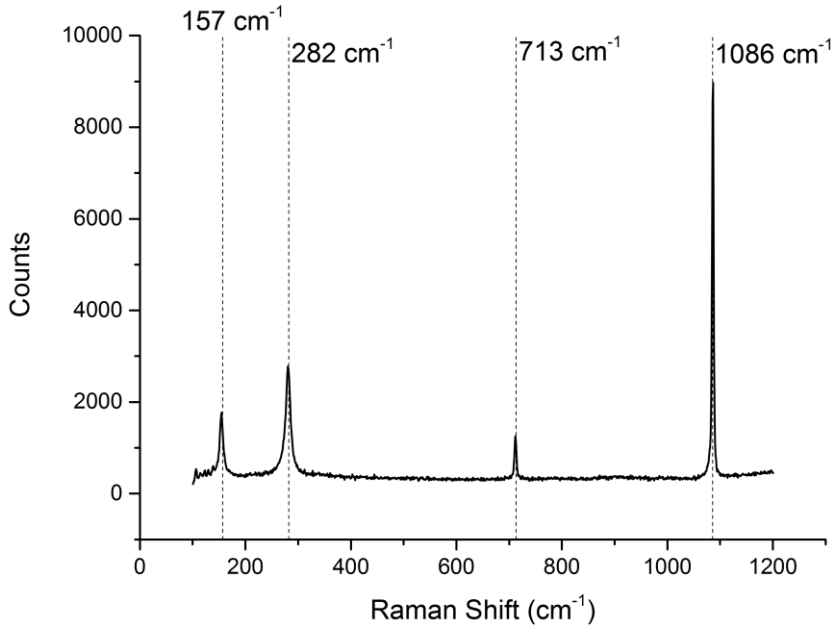

Figure 5.2 Raman spectrum for synthesised particles

From the Raman spectrum shown in Figure 5.2, it can be seen that the peak positions were consistent with published calcite references (indicated by dotted lines) (46, 165, 166). No additional peaks corresponding to impurity phases of unreacted precursor, or other crystalline calcium carbonate polymorphs were present, consistent with X-ray diffraction.

5.2.3. Scanning Electron Microscopy

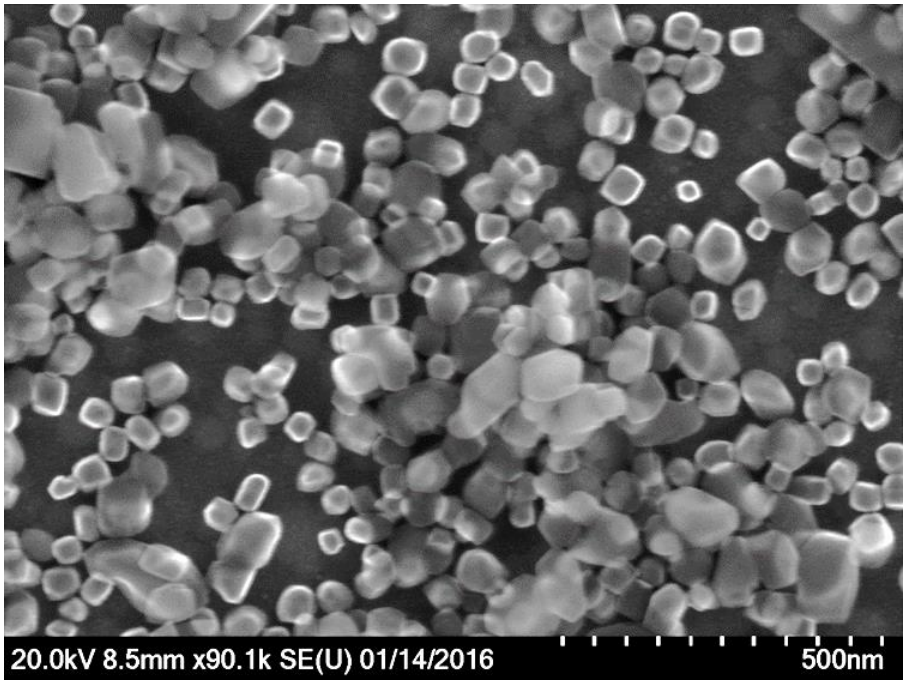

Figure 5.3 Secondary electron image of synthesised calcite particles drop cast onto a holey carbon film, supported on a copper TEM grid

The micrograph in Figure 5.3 shows the synthesised calcite particles have a faceted rhombohedral morphology, with particles randomly oriented on the support film (184).

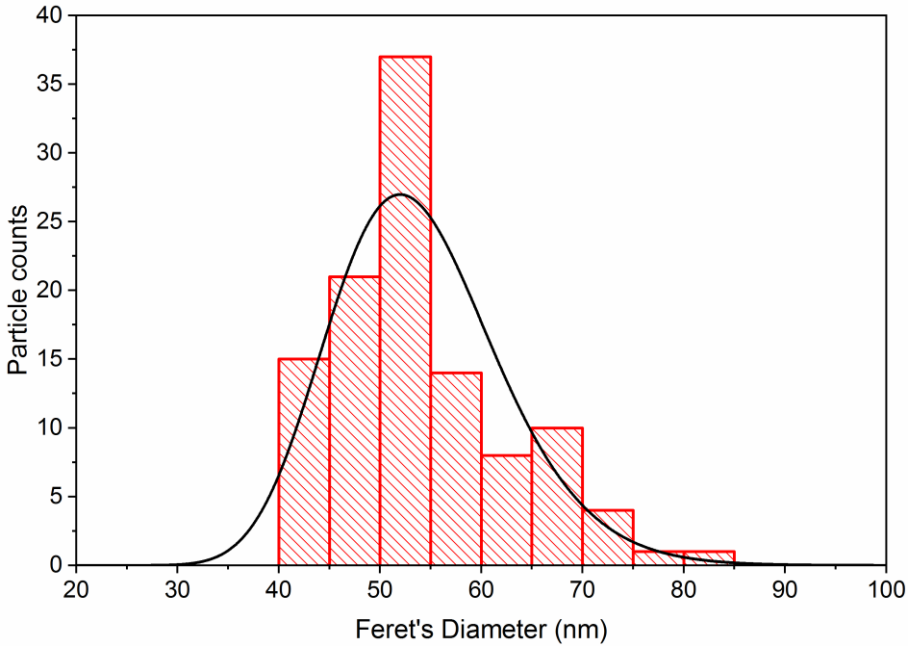

Figure 5.4 Histogram of the Feret's diameter of synthesised calcite primary particles measured via ImageJ. Mean particle size is 54 nm with a standard deviation of 9 nm, black line shows a lognormal distribution.

Using ImageJ (185, 186), the Feret's diameter was measured and calculated to be an average of 54 nm with a standard deviation of 9 nm. The particle size distribution closely follows a log-normal distribution, commonly seen for particles formed under a random nucleation and growth regime, where nucleation and growth are continually occurring, shown on the histogram by the black line (187).

5.2.4. Dynamic Light Scattering

Dynamic light scattering intensity plot of the calcite particle size when suspended in ethanol, this provided a primary particle size of ~50 nm, however agglomeration is visible in the intensity size distribution, as the particle size is seen to increase over consecutive measurements.

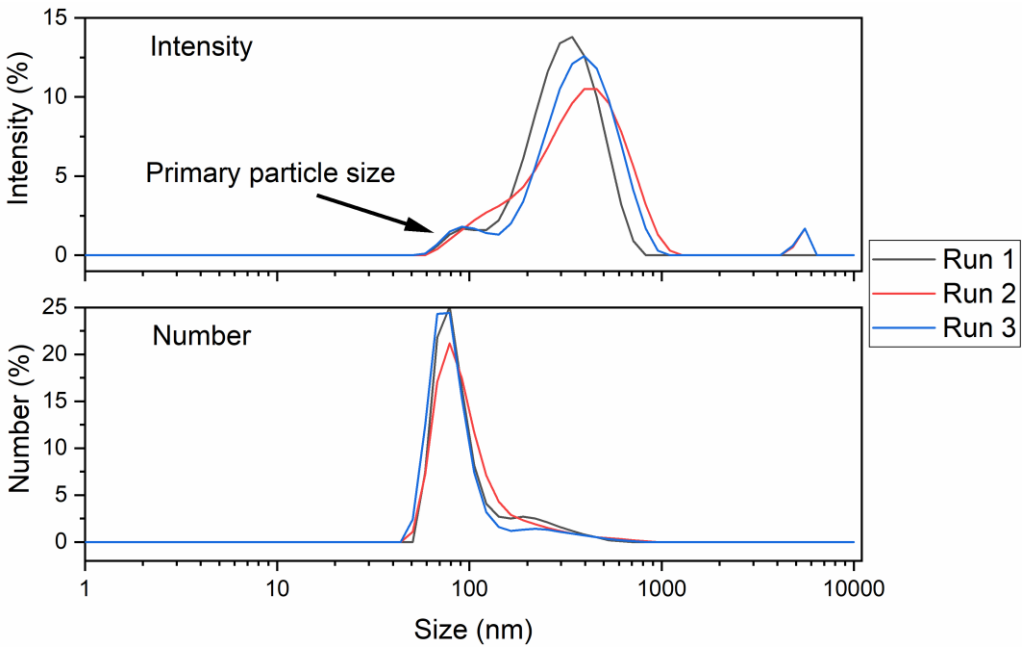

Figure 5.5 DLS particle size distribution of calcite nanoparticles in ethanol taken consecutively, 10 seconds between runs.

The DLS size intensity measurements showed agglomeration of the calcite particles, however size intensity measurements are skewed by larger particles or agglomerates, due to this the size numbers plot should be used in correlation. The DLS number size plot shows that the majority of the particles have a particle size of ~55 nm, with a small fraction being found in agglomerates, seen in the shoulder around 100-200 nm, these same agglomerates dominate the DLS intensity size plots. Agglomeration of the calcite particles is not a significant issue for this research as CTEM/STEM measurements can be taken from isolated primary particles

.

5.2.5. Transmission Electron Microscopy

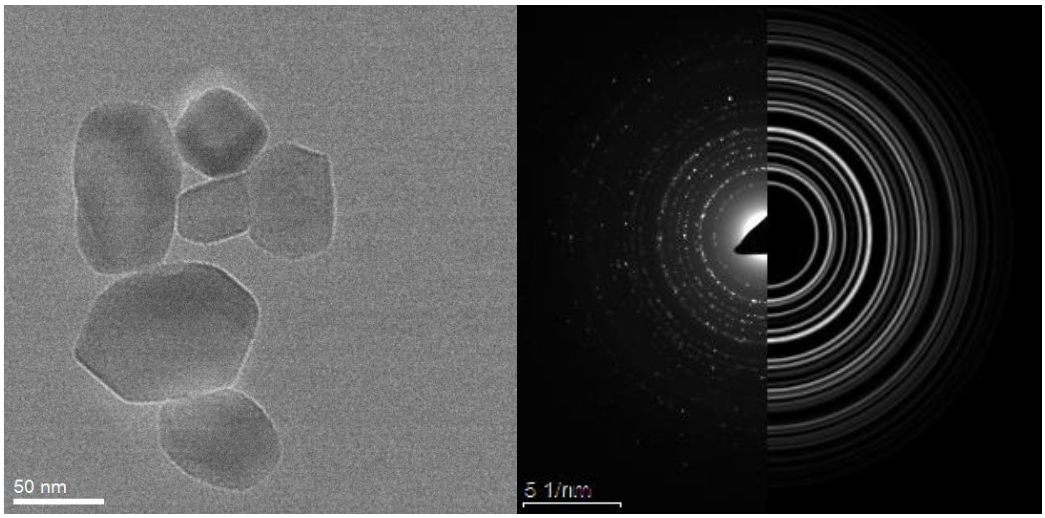

Figure 5.6 BF-CTEM and SAED of synthesised calcite nanoparticles, with a simulated polycrystalline calcite diffraction pattern. (ICDD reference number for simulated calcite pattern 04-012-0489). SADP scalebar 5 1/nm.

Bright field CTEM imaging provided a primary particle size consistent with that measured by SEM and DLS. Electron diffraction shows that the particles display crystallinity consistent with calcite, when compared to a modelled calcite diffraction pattern.

The bright field CTEM images clearly show faceting and at high magnifications a continuous crystal lattice is seen across most particles. BFTEM imaging shows both aggregated, and agglomerated particles, Figure 5.6 shows an agglomerated cluster of particles, with an aggregated polycrystalline particle present also. Another example of this is shown below in Figure 5.7, where the grain boundary in an aggregate of two crystalline particles can be seen.

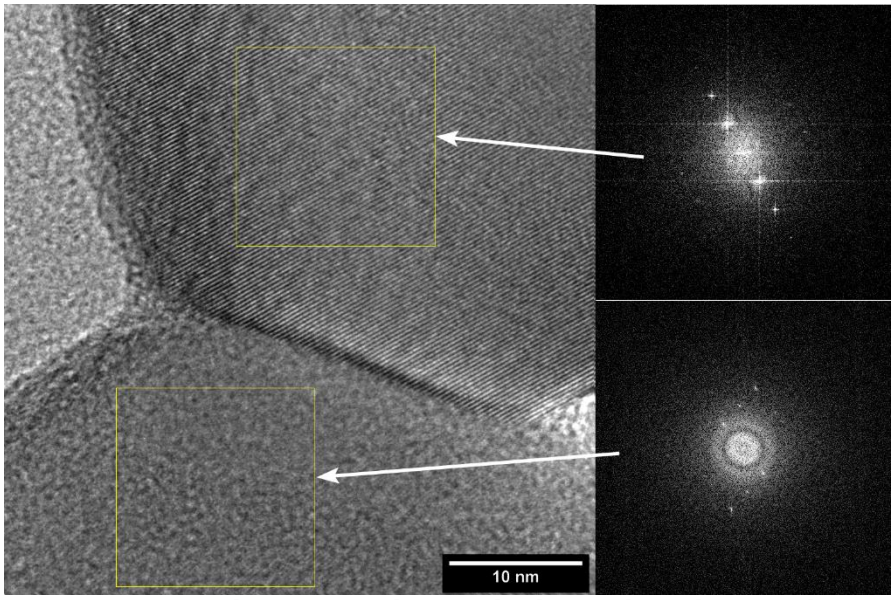

Figure 5.7 PC-CTEM image of the grain boundary in a polycrystalline calcite nanoparticle, showing crystallinity in both particles (indicated by FFTs), but misalignment between the crystal lattices. FFT image width 22 1/nm.

The most likely cause of the poly-crystallinity observed in a fraction of particles is the incidence of multiple nuclei adhering during crystallisation, rather than poly-crystallinity induced through the destruction of crystallinity in a single crystal particle. The FFTs indicate that both grains are single crystalline, but with a mismatch in orientation.

5.2.6. Summary

Calcite nanoparticles were synthesised rather than purchased in order to control purity and supply. The synthesis of calcite particles was successful, with production of nanoscale crystals of a narrow particle size distribution. Characterisation using CTEM, SEM, XRD and Raman did not detect any crystalline contaminants or unreacted calcium oxide precursor.

A narrow particle size distribution is advantageous for the measurement of radiation damage as there will be more consistency in fluence thresholds. Large or thick particles will absorb more dose for the same fluence than a small or thin particle, as dose is related to the energy deposited per unit volume; having a wide range of particle sizes would make fluence thresholds highly variable.

5.3. Electron beam damage study at 200 kV

The electron induced degradation of calcite was measured using 200 kV CTEM imaging, diffraction and EDX spectroscopy in a FEI Tecnai F20. This allows for multiple damage phenomena to be investigated, building up a thorough picture of how the degradation process affects the particle morphology, crystallinity and composition.

5.3.1. Bright Field CTEM Imaging

Bright field imaging was used to examine the influence of irradiation on the morphology of the particles, and to investigate any correlations between particle appearance and detectable structural or chemical changes, measured by SAED and EDX. As observed by bright field imaging, the irradiated particles display several stages of degradation: surface reconstruction, pore formation and shrinkage. The onsets of these stages are explained in the following section. These three visible stages agree with observations made by Golla-Schindler et al (90) and Hoffmann et al (89), though in their studies neither images nor fluences were quantified.

Surface Reconstruction

Firstly, it can be seen that the particle edges and corners break down, it appears that the original particle facets degrade into shorter “nanofacets” of different orientation and become more disordered with respect to the original facet, shown in Figure 5.8. Breakdown of the edges and facets is to be expected as the atoms at edges and corners are less strongly bound than bulk atoms, and are thus more susceptible to displacement, sputtering, or radiolytic bond fission. The onset of the surface degradation and reconstruction process was not quantified as it is a gradual process, with no reliable method for quantification.

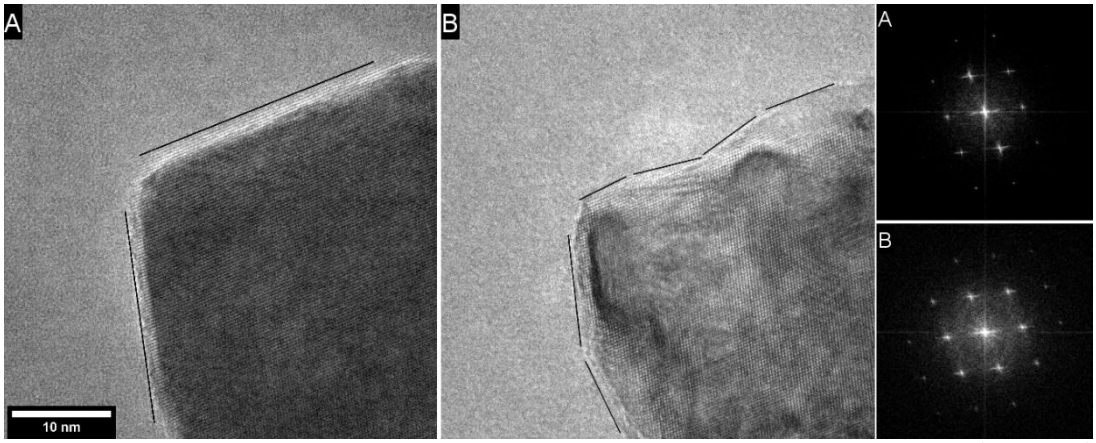

Figure 5.8 Example of surface reconstruction following $3.8x10^6$ e^-nm^{-2} with associated FFTs. Black lines schematically indicate the crystal facets present. The intensity of the FFT spots is seen to increase slightly in image B as the particle has moved and slightly reoriented towards the zone axis and is diffracting more than in image A, this is a well-known phenomenon (188). FFT image width 12 1/nm.

The crystalline lattice is disordered around the outside of the particle, in addition, internal disordering can be seen in the particle bulk. Here streaking of the calcite spots is seen in the FFT, arising from the disorder of the atomic planes in a manner similar to turbostratic graphite structures, this is shown in the FFT of Figure 5.8B. From these images, both internal and external disorder are observed, a more detailed discussion of time-resolved phase contrast imaging is presented in section 5.3.6.

Pore Formation

Following the degradation and reconstruction of the particle surface, pores begin to form in the crystals after receiving $2x10^6$ e^-nm^{-2}, initially the pores form near the edges of the crystals, but as irradiation progresses, further pore formation occurs in the bulk of the crystal. The location of these pores also ties in with the location of calcium oxide crystallites, observed through dark field imaging (presented in section 5.3.3). Pores are formed due to the transformation of $CaCO_3$ to CaO and the difference in density of the compounds. As such, the pores are often angular due to the shape of the CaO crystallites, this is shown by Figure 5.9, where pores with straight edges are seen in the irradiated particle.

As pores provide a direct route for CO_2 egress into the microscope vacuum, the radiolytic decomposition of $CaCO_3$ is not limited by the diffusion of CO_2 (69).

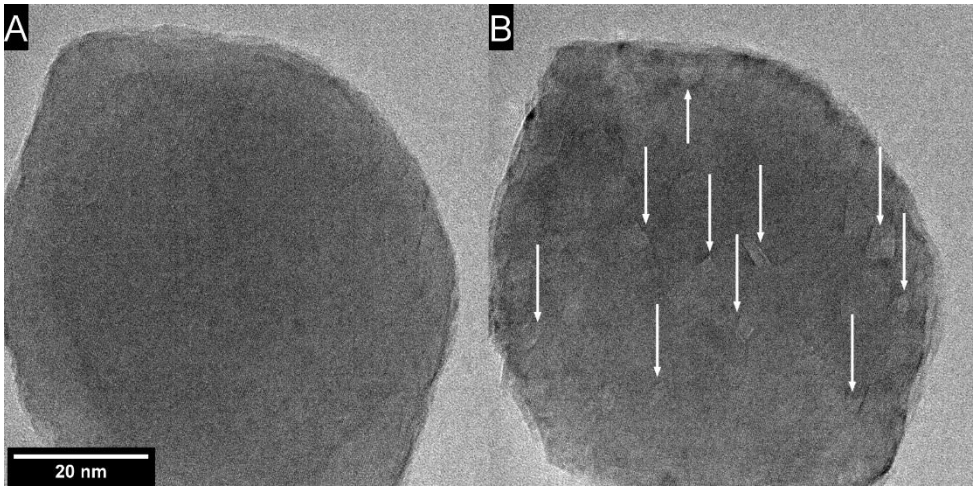

Figure 5.9 A) undamaged particles. B) Damaged particle following exposure to a fluence of $4.6x10^6$ e^-nm^{-2}. Arrows indicate light regions consistent with pore formation.

Pore formation manifests as bright regions in BF images, these correspond to thinner regions of the specimen, indicative of mass loss, examples of this can be seen in Figure 5.9. From these images it is also possible to observe the breakdown of the edges of the particles, where formerly pristine facets become jagged and are visibly damaged. These observations correlate with the results of dark field CTEM imaging, shown in section 5.3.3 and Figure 5.12.

The observation of pore formation is not new, however there has been no quantification of the appearance of pores with irradiation. The appearance of porosity in irradiated particles of calcite was previously described by Towe (94), followed by the crystallisation of nanoscale calcium oxide throughout the particle. Rodriguez-Navarro et al (69) mentioned the mottled appearance of irradiated particles, presumably due to pore/void formation and nucleation of calcium oxide. Wenk and Barber (189) showed examples of “spotty contrast” in calcite deposits found in carbonatite rocks (rocks with over 50% carbonate content) which appears as a function of time under observation in CTEM. This is likely the formation of pores and voids as they also mention the outgassing

of carbon dioxide, though it is possible that the contrast is due to crystallisation of calcium oxide as both phenomena would appear as dark spots on the irradiated particles.

Particle Shrinkage

Another stage of degradation observed via imaging is the shrinkage or densification of the calcite particles, this is due to the loss of carbon dioxide and the associated change in volume due to the conversion to calcium oxide. Shrinkage is a gradual process, when looking at particles following irradiation, significant loss of projected particle area can be seen in

Figure 5.10. In this study, the change in volume was not quantified with respect to dose, as the magnifications used for time-resolved imaging series were often low. An example of particle shrinkage is shown below in

Figure 5.10, after $3x10^7$ e^-nm^{-2} at 200 kV, the fluence is considered to be sufficient for complete conversion of calcite to calcium oxide (As measured subsequently by EDX spectroscopy in Figure 5.16), and the total area of the agglomerate is reduced by 32%.

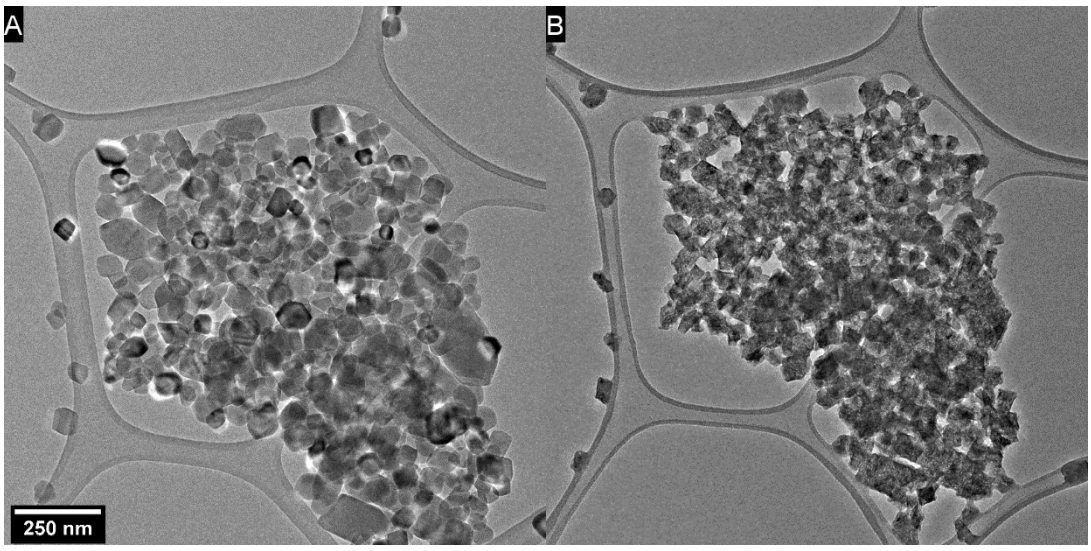

Figure 5.10 particle shrinkage caused by electron irradiation, in this example the projected area of the main agglomerate has reduced by ~30% following $3x10^7$ e^-nm^{-2}, (particle areas before and after irradiation measured using FIJI).

By considering the change in density between calcite and calcium oxide (2.71 and 3.34 $g^{-}cm^{-3}$ respectively) the change in volume would be expected to be approximately 19%, however this assumes a void and defect free material, which is not applicable for electron irradiated calcium oxide as pores, voids and polycrystallinity are present. Whilst an area change of ~30% is seen after significant irradiation, it is not possible to measure the change in volume without a measure of sample thickness using EELS, however this change in area gives a clear indication of particle shrinkage.

5.3.2. Selected Area Electron Diffraction

Selected area electron diffraction was used to quantify the onset of calcium oxide crystallisation, under irradiation calcium oxide was detected as polycrystalline rings in the diffraction patterns of calcite particles, following methods outlined in section 4.3.2. The presence of polycrystalline CaO has been noted in prior reports, however the onset has not been quantified with respect to fluence or dose. An example of the manifestation of CaO in diffraction patterns is shown below in Figure 5.11 and in the appendix where the images from a time-resolved irradiation experiment are shown.

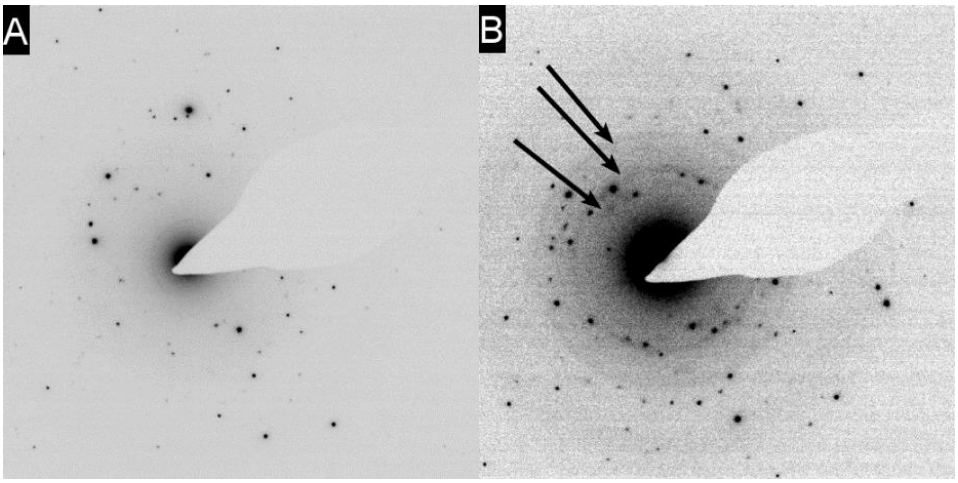

Figure 5.11 SADP of calcite nanoparticles prior to and following exposure to $3.8x10^6$ $e^{-}nm^{-2}$ at 200 kV, calcium oxide {111} and {200} rings are indicated by the arrows. SADP image width 26 1/nm.

Under irradiation, polycrystalline calcium oxide is detected by diffraction at fluences of $3.9x10^6$ $e^{-}nm^{-2}$ at 200 kV, shown in Figure 5.11, this is

approximately double the fluence at which pores form. It is likely that calcium oxide is present at the time of pore formation, however either the amount of crystalline calcium oxide is not sufficient for detection by diffraction, or it is non-crystalline and thus non-diffracting. It is possible that the degradation of calcium carbonate into calcium oxide proceeds through an amorphous intermediate of either calcium carbonate or oxide. This would not be detected through SADP as amorphous materials do not contribute diffraction information, only diffuse scattering which would increase the background intensity, this can be seen in Figure 5.11B but due to the low signal to noise ratio of this image, it is possible that this increase in background intensity is simply noise.

From the diffraction experiments it is shown that calcite and calcium oxide coexist, indicating a progressive degradation which does not directly affect the crystal structure of calcite across the entire particle. The most likely place for nucleation and crystallisation to occur would be around the edges and on the surfaces of the particle, forming pores or voids due to the shrinkage of calcium carbonate converting to calcium oxide. These pores and voids aid in the removal of carbon dioxide by providing a route for gas evacuation from the particle bulk to the microscope vacuum. This is supported by dark field imaging in which the image is formed using electrons from the calcium oxide diffraction rings, shown in section 5.3.3.

The progressive nucleation of calcium oxide is noted by Towe (94) Rodriguez-Navarro et al (69) and Hoffmann et al (89), where irradiated calcite displays both calcite diffraction spots, and calcium oxide diffraction rings concurrently. Similar observations were presented by Cater and Buseck (71) for the decomposition of dolomite ($Ca_{0.5}Mg_{0.5}CO_3$) under electron irradiation. Towe also stated that in some cases, there was a preferred orientation to the calcium oxide crystallites, where in one region the CaO (200),(220) and (100) reflections were observed normal to the calcite $(01\bar{1}2)$ reflection. This is known as topotaxy, or a topotactic transformation, which are solid state transitions that occur when the crystal lattice of a product phase has a crystallographically equivalent orientation to the reagent phase. However

other regions showed more random orientations, leading to the conclusion that multiple topotactic transformations are possible, and that topotaxy is not guaranteed. The diffraction patterns presented here showed no preferred orientation in the calcium oxide rings, and as these patterns were taken at the early onset of crystallisation, it is conceivable that preferred orientation develops following further irradiation, and that early stage crystallisation is more random in orientation.

Whilst Hoffmann et al (89) provides some quantification for the appearance of calcium oxide, it falls short of quantifying the fluence at which calcium oxide first appears, rather showing that extensive formation of calcium oxide is present at two similar fluences for two different sample preparation methods. Hoffmann provides a fluence of $1x10^5$ e^-nm^{-2} at 300 kV above which damage occurs, this is not a useful damage threshold as the form of damage is not stated. The electron flux used is not stated, but can be assumed to be ~10^5 $e^-nm^{-2}s^{-1}$ as the presented figures make reference to an accumulated fluence of $3x10^7$ e^-nm^{-2} over 5 minutes of irradiation.

5.3.3. Dark field CTEM Imaging

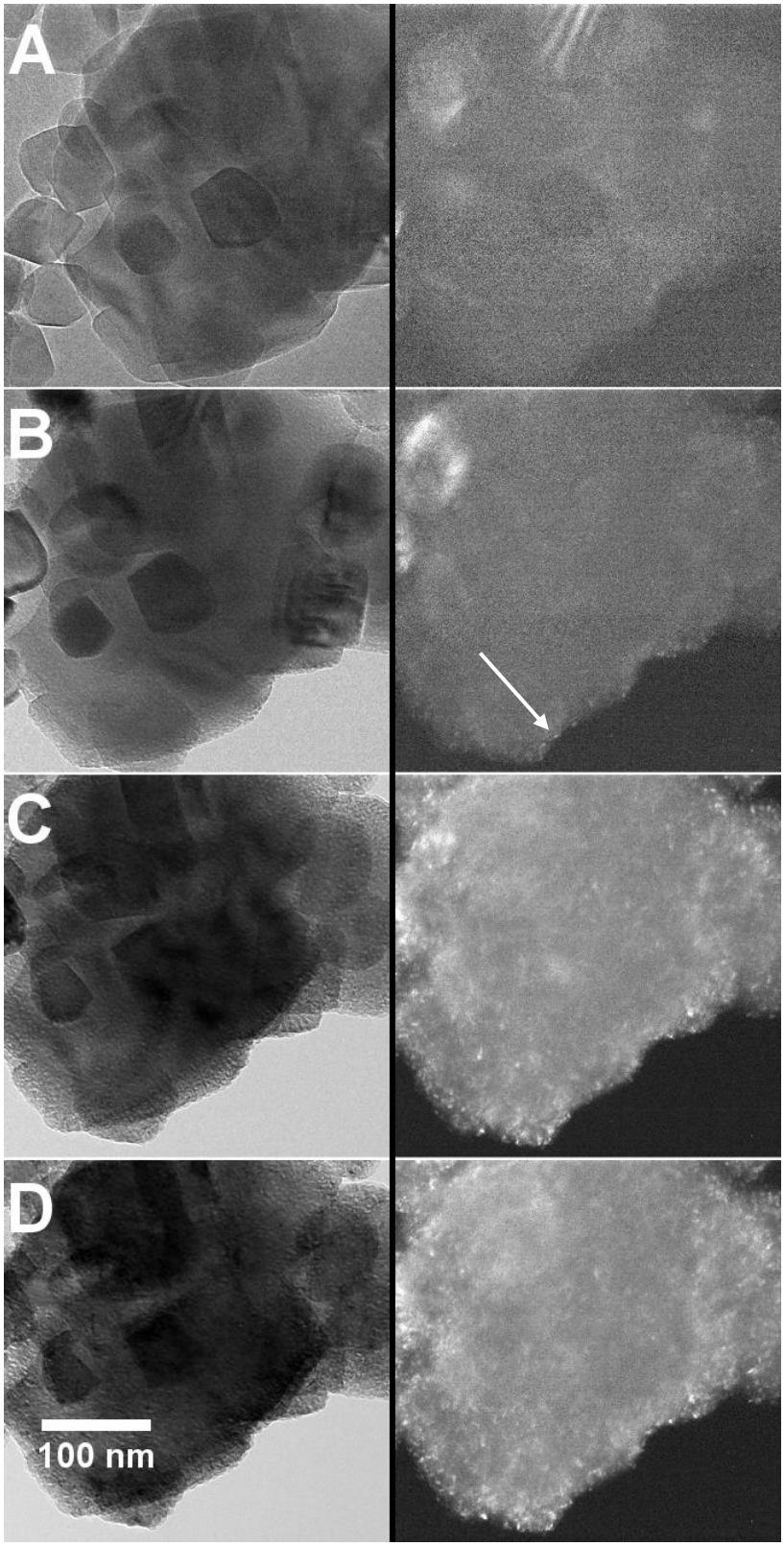

Figure 5.12 Correlative BF (left) and DF (right) images of calcite particles under progressive electron irradiation. Dark field images formed from electrons scattered to the calcium oxide (111) and (200) rings. Electron fluences and beam flux were not measured.

Frame A shows the particles before significant irradiation, the crystal structure is pristine and shows no nucleation of calcium oxide crystallites or pore formation.

Frame B shows some initial nucleation of calcium oxide around the edges of the particle in the DF image, indicated by the arrow. The BF image shows degradation of the particle edges and mottling from pore/void formation through the particles preceding calcium oxide nucleation.

Frame C shows nucleation of calcium oxide through the particle bulk, nucleation is no longer limited to the edges of the particle, but there are more crystallites around the edges. The bright field images show that the particle is significantly damaged with voids and pores across the bulk, giving a mottled appearance.

Frame D shows further nucleation of calcium oxide through the particle, with nucleation spread throughout the particle. The bright field image also shows further degradation, with more porosity visible.

Through dark field imaging, it was observed that calcium oxide initially nucleates around the edges of calcite crystals under irradiation. Following further irradiation, nucleation sites were formed in the bulk of the crystal. This is to be expected as the atoms on the edges of crystals have more disrupted bonding environments than the core atoms, and thus are more weakly bound giving them a higher probability of escaping the crystal should their bonds break. Cazaux (62) remarked that radiolysis damage progresses from the outside of particles towards the core. This is also consistent with the observations in section 5.3.1, where lighter regions in the image, consistent with pore/void formation were observed at the edges of the crystals first, before being seen in the bulk of the crystal.

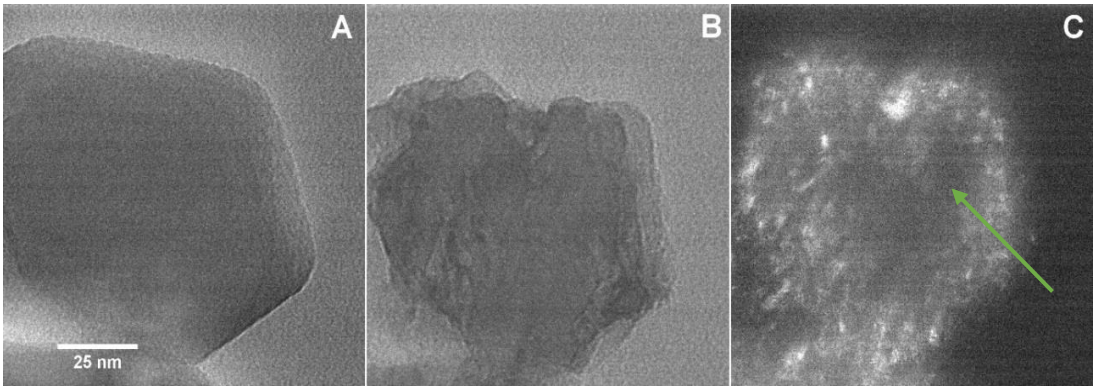

Figure 5.13 A) BF image of calcite particle before irradiation, B) BF image of same particle after irradiation, C) DF image of same particle after irradiation (objective aperture centred over calcium oxide diffraction rings).

From Figure 5.13 B and C) it can be seen that while the particle appears to be heavily damaged, the core of the particle does not show significant calcium oxide nucleation (indicated by the arrow). This is in agreement with the diffraction experiments, as even when calcium oxide diffraction rings were detected, calcite diffraction spots were still visible (Figure 5.11B). This suggests a progressive nucleation of calcium oxide from the surfaces of calcite crystals towards the core. This progression of damage is noted by Ruiz-Agudo et al (190) for calcite samples under electron irradiation. Burrage and Pitkethly (93) mention seeing the appearance of CaO crystallites around crystal defects, grain boundaries or cracks when aragonite crystals are irradiated. This suggests that disrupted bonding environments, like those seen at defects and particle surfaces, are the most susceptible to radiolysis.

5.3.4. Rate Dependence of Electron Beam Damage

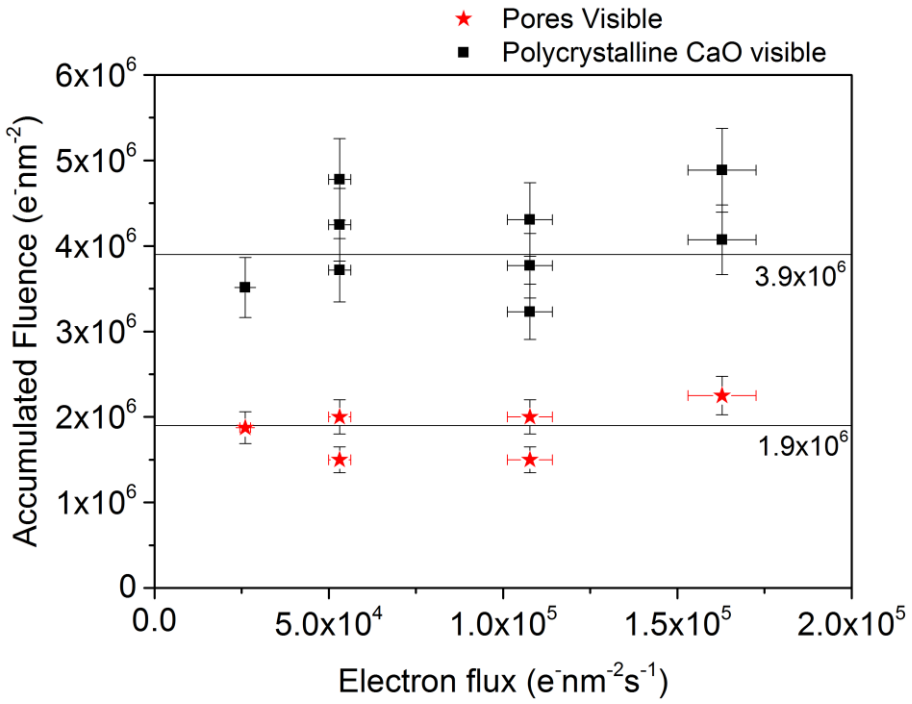

Figure 5.14 Measured damage thresholds as a function of electron fluence rate at 200 kV. Horizontal lines are averages.

The presence of a rate dependence of electron beam damage was investigated using multiple electron fluence rates for irradiation damage studies on the formation of pores and calcium oxide crystallisation. Bright field imaging and diffraction were used to probe the two stages of degradation, it was found that there was no dependence of electron fluence on either damage threshold at the measured fluences, within error. This can be seen from the graph in Figure 5.14, where the average damage thresholds have been plotted for both the appearance of pores in bright field images, and the appearance of calcium oxide in the diffraction pattern. As there is no rate dependence it gives options for how to operate prior to damage occurring, it should be equally valid to work under high fluence rate conditions for short experiments, or to work under low fluence rate conditions for longer durations.

Since the damage process is not diffusion limited nor is a healing reaction possible due to the irreversible loss of CO_2 and considering that critical fluences for visible damage phenomena are independent of electron flux it is

suggested that the electron beam damage of calcite is a linear process, i.e. the damage rate displays no electron flux dependence (191). This has implications for future research using STEM imaging, as STEM offers an improved irradiation lifetime over CTEM for radiation sensitive materials displaying a non-linear/inverse dose rate dependence i.e. increasing fluence rate does not cause a linear increase in damage rate, typically diffusion limited damage processes. In the case of calcite, which displays a linear relationship between fluence rate and damage rate, the extent of damage was directly proportional to the accumulated fluence and so it would be expected that there would be no inherent benefit to the use of STEM over CTEM to avoid damage. However, STEM does have different operational considerations which may be advantageous, including; concurrent imaging and spatially resolved spectroscopy, off specimen focussing using the Ronchigram, and the potential for enhanced heat and charge dissipation by the rastering of the probe.

5.3.5. Energy Dispersive X-Ray Spectroscopy

EDX spectroscopy was used to give a direct observation of the mass loss occurring under irradiation. The loss of carbon dioxide could be picked up by investigating the decrease in oxygen and carbon K_α peak intensities. Any reduction in calcium peak intensity would suggest the presence of knock-on or sputtering damage occurring as calcium, along with oxygen and carbon are susceptible to knock-on damage above 100 kV as demonstrated by Figure 2.12 in the literature review.

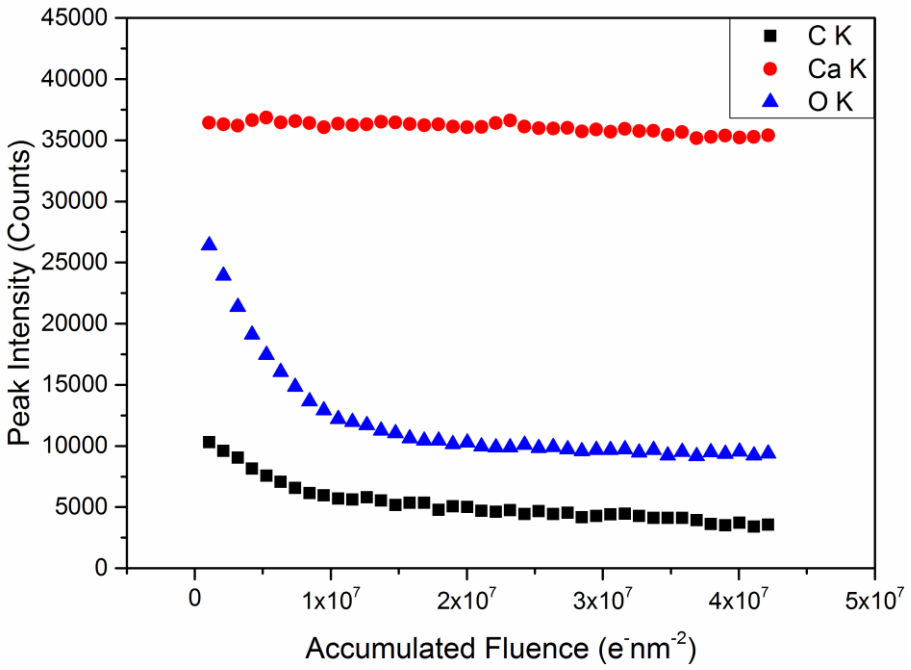

Figure 5.15 Change in integrated K_α peak counts for calcite under 200 kV irradiation, as measured by EDX.

Figure 5.15 shows the changes in composition of calcite under irradiation, from this it can be seen that there is a reduction in carbon and oxygen peak areas due to the removal of carbon dioxide by radiolysis, but there is no significant change in the calcium peak intensity. This suggests that calcite is mostly susceptible to radiolysis, with no significant or detectable amounts of calcium being removed by knock-on or sputtering damage at 200 kV, however this may not be the case at higher accelerating voltages, where knock-on damage is more prevalent, or at higher fluences. Whilst there is a loss of both carbon and oxygen, it is not possible to examine whether the stoichiometry of the mass loss products exactly matches CO_2. This is because there is the likelihood that the carbon support film is being damaged by the beam and is losing mass as well, and the possibility that hydrocarbon contamination growth is affecting the signals produced as oxygen and carbon are known constituents of hydrocarbon deposits.

Pore formation is not immediate upon irradiation, however mass loss onsets immediately, thus it is likely that surface mass loss occurs prior to pore formation. This is corroborated by the DF-CTEM images showing CaO crystallisation near the surfaces of particles, indicating surface degradation

occurring (Figure 5.12 and Figure 5.13). Pores are not required for early mass loss, as CO_2 from the surface degradation is released directly into the vacuum.

Rodriguez-Navarro et al (69) stated that the de-excitation process resulting in bond fission is likely the rate limiting step here because the resulting transformation of calcite to calcium oxide would leave sufficient pores and voids for rapid out-diffusion of CO_2, meaning the process is not diffusion limited. The exponential form is instead due to the slowing of the radiolysis process (Figure 5.15 and Figure 5.16). As irradiation progresses, the number of fissile O-C bonds decreases, thus the mean free path for radiolytic events increases, meaning that the cross section for radiolysis decreases.

When considering the appearance of calcium oxide in the diffraction patterns, there would need to be a large enough loss of carbon dioxide to form sufficient calcium oxide to be detectable in diffraction, as there must be a minimum amount of crystalline material present and be of a large enough crystallite size for diffraction to occur. The image capture device is also implicated in the detection limit for electron diffraction, as sufficient signal from diffraction spots must be received to exceed the noise threshold of the microscope camera, weak diffraction signals may also be hidden by strong diffraction signals due to the high dynamic range in the image.

The characteristic fluence for mass loss using EDX was taken to be the reduction in O:Ca ratio from 3:1 (stoichiometric calcium carbonate) to 1.8:1, a reduction of 1/e. The data in Figure 5.16 is taken from multiple degradation time series and is processed in terms of O:Ca ratio, carbon has not been quantified.

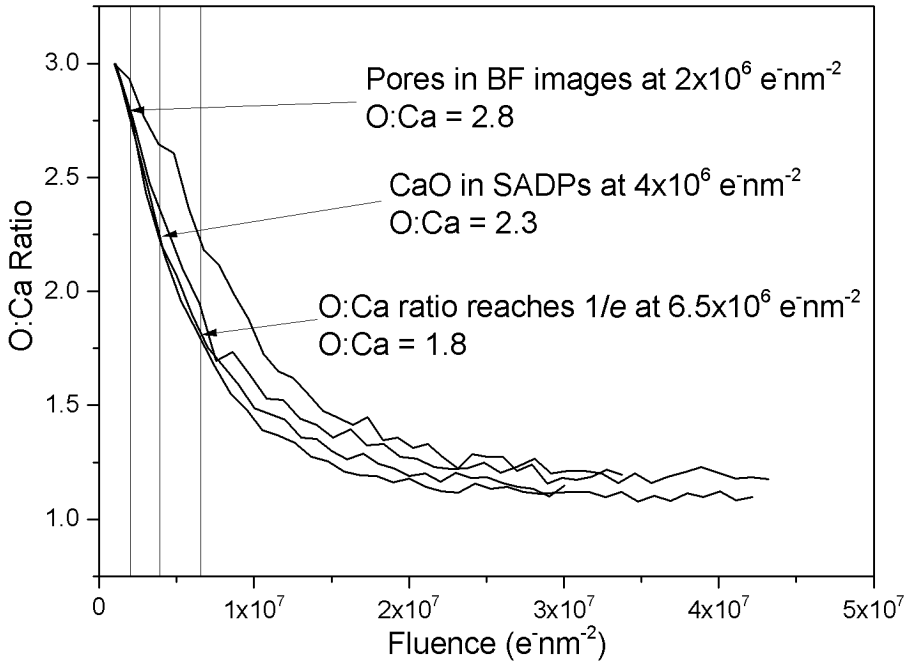

Figure 5.16 Reduction of O:Ca ratio in calcite as measured by EDX at 200 kV in CTEM.

From Figure 5.16 it can be seen that the O:Ca ratio decreases from 3:1 to ~1.2:1 as the specimen is irradiated. The decay of O:Ca K_α peak area ratio follows an exponential form, with the characteristic or critical fluence for the reduction of O:Ca atomic ratio to 1/e giving an indication of the rate of mass loss. The characteristic fluence threshold for mass loss at 200 kV was 6.5×10^6 $e^- nm^{-2}$. Pore formation is seen at a fluence of ~2×10^6 $e^- nm^{-2}$, by this fluence the O:Ca ratio has reduced to ~2.8:1. Crystalline CaO is seen in diffraction patterns by ~4×10^6 $e^- nm^{-2}$, by which the O:Ca ratio has decreased to ~2.3:1. These measurements indicate that once visible degradation of the image and diffraction pattern has occurred, compositional measurements will not be representative of the original material, within acceptable errors.

The assumption used for the quantification of the O:Ca ratio is that the first spectrum is representative of undamaged calcium carbonate i.e. O:Ca ratio is 3:1, this would infer that the end-point of the degradation would be when the O:Ca ratio is 1:1 for pure calcium oxide. It can be seen that the observed end-point is slightly above 1:1, there are several reasons why this may be the case: Oxygen contamination in the support film, or hydrocarbon deposition on the specimen would skew the ratio to be higher than 1:1. Stoichiometry is likely to

be disrupted at grain boundaries and defects, as the calcium oxide produced is nano-crystalline and will have a large relative proportion of grain boundary and thus will likely have non-stoichiometric regions which may skew the ratio of O:Ca. It is also possible that the error is due to the detection of light elements in EDX, though this would more likely skew the ratio to lower oxygen content as oxygen is often underestimated due to its low X-ray energy and hence low fluorescent yield in comparison to calcium. The lower energy of oxygen X-rays also means that they have a larger propensity to be absorbed by the material itself. The most likely explanation is that the first spectrum of a series is not representative of the pristine material and that some mass loss is occurring whilst the spectrum is being acquired.

Considering this, the compositional k-factor for O:Ca quantification could either be based on the initial ratio of O:Ca in calcium carbonate, or the ratio of O:Ca after the specimen has fully converted to calcium oxide. For example, in Figure 5.17 the O:Ca ratio has been plotted using two different k-factors. One k-factor is calculated assuming that the first spectrum is representative of the pristine calcium carbonate stoichiometry (O:Ca = 3:1), giving a k factor of 4.14. The other k-factor is calculated assuming the stoichiometry of the end-point is purely calcium oxide (O:Ca = 1:1), giving a k-factor of 3.77. The difference in O:Ca ratio between the two plots is approximately 10% throughout the damage series. A 10% error is considered reasonable for EDX analysis of light elements (192).

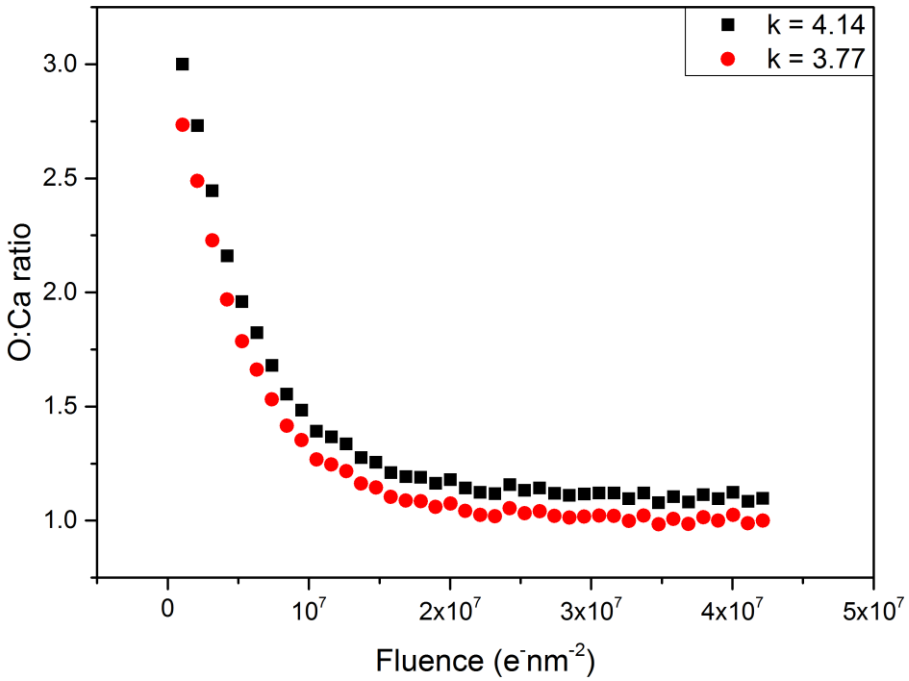

Figure 5.17 EDX degradation series of O:Ca ratio using different k-factors.

5.3.6. High Resolution CTEM Imaging

For a more direct observation of the manifestation of damage, and a more meaningful damage threshold for high resolution imaging, the electron beam-induced degradation of calcite was investigated using high resolution phase contrast CTEM. For the crystalline CaO damage product to appear in diffraction patterns, a significant amount of damage would have already occurred to the calcite particles. This is shown in the EDX results, where significant compositional changes have occurred at fluences lower than those at which damage is visible. For example, the O:Ca ratio would have decreased to ~2.4:1 before crystalline calcium oxide is seen in diffraction patterns (Figure 5.16).

A more direct measure of degradation is needed, which is applicable to high resolution imaging in both CTEM and STEM, and does not require switching between imaging and diffraction. High resolution phase contrast lattice imaging is applicable to both CTEM and STEM through the principle of reciprocity, and can provide a direct measurement of degradation under irradiation when coupled with the Fast Fourier Transform (FFT). As the FFT

displays a pseudo-diffraction pattern, any change to the crystallinity seen by phase contrast imaging will manifest as interpretable features in the FFT.

The degradation of the calcite lattice, as determined by the FFT of the high resolution CTEM image was chosen as the indicator of damage. An example of this is shown in Figure 5.18 where damage to the lattice shows as a streak or arc in the FFT, indicated by a white arrow. This does not necessarily correspond to the appearance of crystalline calcium oxide, but more the breakdown of crystallinity of the calcite lattice.

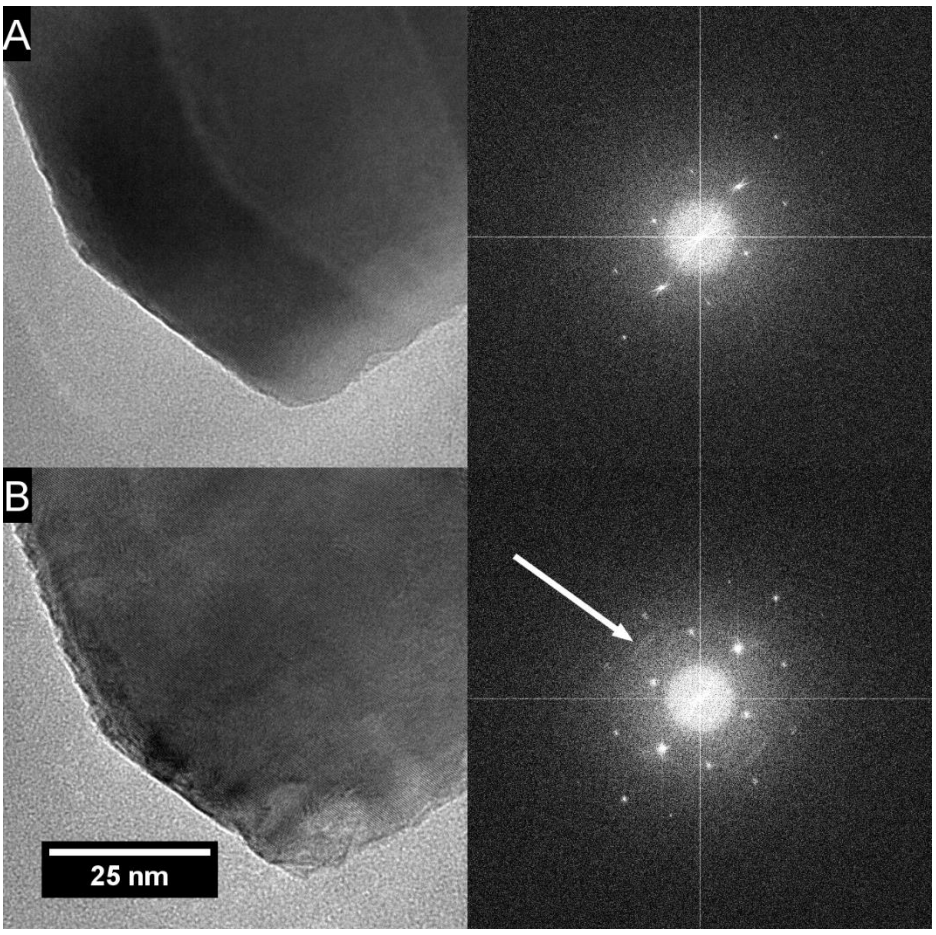

Figure 5.18 BF-CTEM image and FFT of pristine (A) and damaged (B) calcite particle showing degradation to the particle and the corresponding changes to the FFT. FFT image width 20 1/nm.

The visible arcing of the FFT spots is caused by the disruption of the calcite lattice by the incident electrons, the atomic planes are distorted or bent over a short range with respect to the pristine lattice, as shown in Figure 5.18.

This is a more severe threshold than the appearance of crystalline CaO in diffraction patterns, but is a more useful indication of electron beam damage for high resolution studies. Using the FFT to observe the onset of damage can be observed by both STEM and CTEM imaging, whereas selected area diffraction is limited to CTEM.

In terms of fluences, the initial breakdown of the FFT correlates well to the fluence threshold for pore formation. With the FFT beginning to break down at fluences of $2x10^6$ e^-nm^{-2} at 200 kV on average, with a standard deviation of 21%. This has significance in that even under low magnification operation, the breakdown of the FFT can be inferred through the appearance of pores or voids in the particle, meaning that the integrity of the particles is compromised and that imaging based analysis should cease.

5.4. Conclusions

Synthetic nanoparticles of calcite are an appropriate model system for the study of electron beam damage in calcium carbonate, the degradation can be observed using multiple analytical techniques, each having reliable fluence thresholds. In calcite, there was no observed fluence rate dependence of electron beam damage at the measured fluxes, meaning that there are excellent prospects for the application of low-dose, or dose limited microscopy.

By showing images and diffraction patterns at fluences below the damage thresholds, it demonstrates that it is possible to operate with confidence in the integrity of results acquired from beam sensitive materials. Sensible thresholds should be formed based on the information that can be obtained, and the accuracy of the results that can be achieved. However, careful measurements and observations must be made on the beam-induced damage process, to obtain the limits for a certain material. For calcite, the limits are shown in Table 5.1.

Threshold	Fluence ($e^{-}nm^{-2}$)
Pore formation	$1.9x10^{6}$
Lattice image degrades	$2.4x10^{6}$
Crystalline CaO seen in SADP	$3.9x10^{6}$
O/Ca ratio reduces by 1/e, as determined by EDX	$6.5x10^{6}$

Table 5.1 Summary of the damage thresholds extracted from 200 kV irradiation studies.

Using the lattice imaging damage threshold as a baseline, it will be possible to investigate influence of microscope operating conditions and other variables on the electron beam damage of calcium carbonate, including microscope voltage, imaging method, polymorph and specimen cleanliness. This will lead to the extraction of optimised conditions for analytical electron microscopy on calcium carbonate, and the ability of assess formulated products processed by less well-established routes.

A summary of the electron beam damage of calcite is found on the following page.

The damage of calcite undergoing continuous electron irradiation is summarised in the following Figure 5.19:

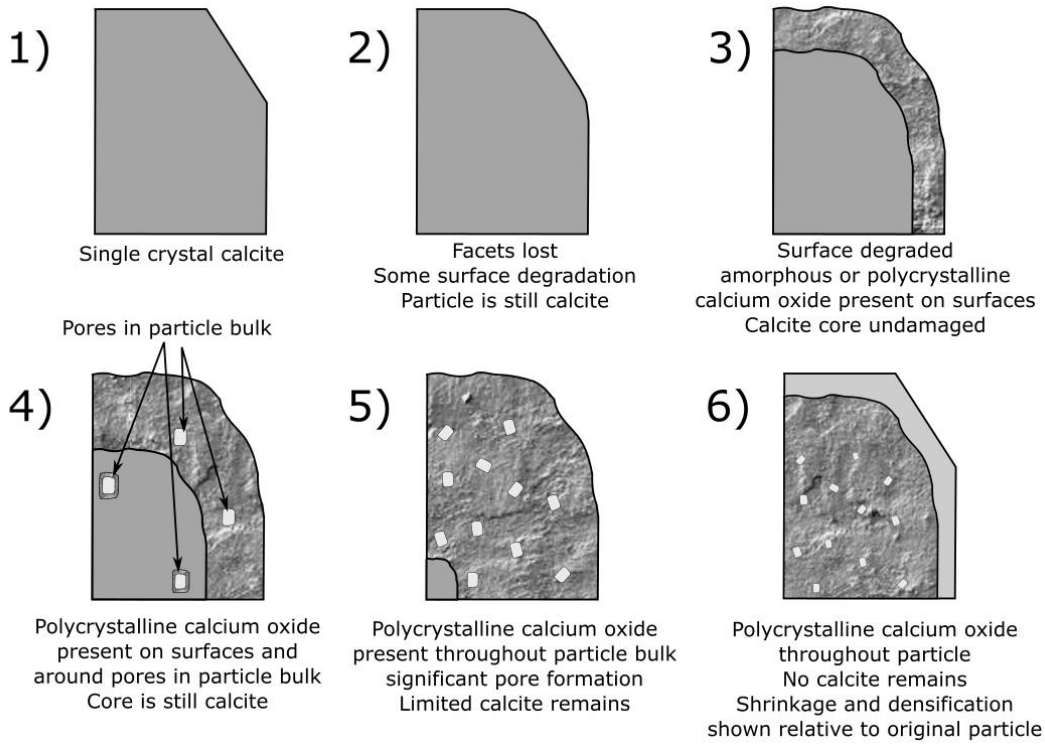

Figure 5.19 Schematic representation of the electron beam induced degradation of a single crystal calcite particle

1) Single crystal calcite prior to irradiation
2) Low levels surface degradation, facets are damaged, but the particle remains a single crystal of calcite
3) Surface faceting is destroyed, surfaces are either amorphous or polycrystalline calcium oxide, particle core is generally undamaged, but some pores may be present around the particle edges
4) Pores are seen throughout the bulk of the particle, polycrystalline calcium oxide is seen around the particle edges and around the pores, some undamaged calcite remains in the core
5) The particle is mostly polycrystalline calcium oxide, with only a small calcite content remaining. Pores are spread throughout the particle.
6) The particle entirely consists of polycrystalline calcium oxide, no calcite remains. Due to sintering and densification, the particle has shrunk significantly compared to the original calcite particle

Chapter 6. Factors Affecting Electron Beam Sensitivity in Calcite Nanoparticles

6.1. Introduction

This chapter details the investigation into experimental factors affecting the electron beam damage of calcite nanoparticles under electron irradiation by both CTEM and STEM in a FEI Titan^3 Themis, using time-resolved phase contrast imaging and EDX spectroscopy at both 80 kV and 300 kV accelerating voltages. This specifically covers instrument and specimen considerations, including: acceleration voltage, illumination mode (STEM or CTEM), specimen cleanliness, and crystal polymorph.

CTEM lattice imaging at 80 kV and 300 kV was used to investigate the difference in damage thresholds at two commonly used accelerating voltages. 300 kV CTEM imaging was then used as a baseline measurement to compare other voltages, illumination modes, and polymorphs. Time-resolved EDX spectroscopy provided insights into the mass loss occurring at both 80 kV and 300 kV, and how hydrocarbon contamination influences mass loss. 300 kV phase contrast STEM imaging was compared to CTEM imaging for both contaminated specimens and those thermally cleaned of hydrocarbons to observe the impact of hydrocarbon contamination on electron-induced lattice faults. Whilst it was concluded that STEM imaging has no inherent benefit to the lifespan of calcite when compared to CTEM, due to the linear damage rate dependence of calcite, or to the dose limited resolution, operational benefits were found, including off specimen focussing, simultaneous bright field and dark field imaging, and the protective properties of a hydrocarbon contamination layer.

Aragonite and vaterite specimens used in the study of polymorph stability were provided by Dr Thokozile Kathyola.

A significant part of the work presented in this chapter has previously been published in: Hooley, R., Brown, A., Brydson, R. (2019). "Factors affecting electron beam damage in calcite nanoparticles." Micron **120**: 25-34.

6.2. CTEM Lattice Imaging at 300 kV and 80 kV

Under 300 kV CTEM irradiation the fast Fourier transform (FFT) of phase contrast (PC) CTEM images of calcite nanoparticles began to show degradation of the calcite lattice, at an average fluence of 2.7×10^7 $e^- nm^{-2}$ with a standard deviation of $\pm 4 \times 10^6$ $e^- nm^{-2}$, (Figure 6.1b; spots in the FFT display some streaking/arcing at this fluence). This is not necessarily the nucleation of calcium oxide, but is the beginning of the breakdown of calcite crystallinity. Arcing of the FFT spots is caused by the disruption of the calcite lattice by the incident electrons, the atomic planes are distorted or bent over a short range with respect to the pristine lattice. This threshold is at a fluence just lower than that established for the onset of pore formation by bright field CTEM (191), shown in Chapter 5, section 5.3.1. Pores/voids were directly visible in the particle irradiated at 2.9×10^7 $e^- nm^{-2}$ and are indicated by the arrows in Figure 6.1b.

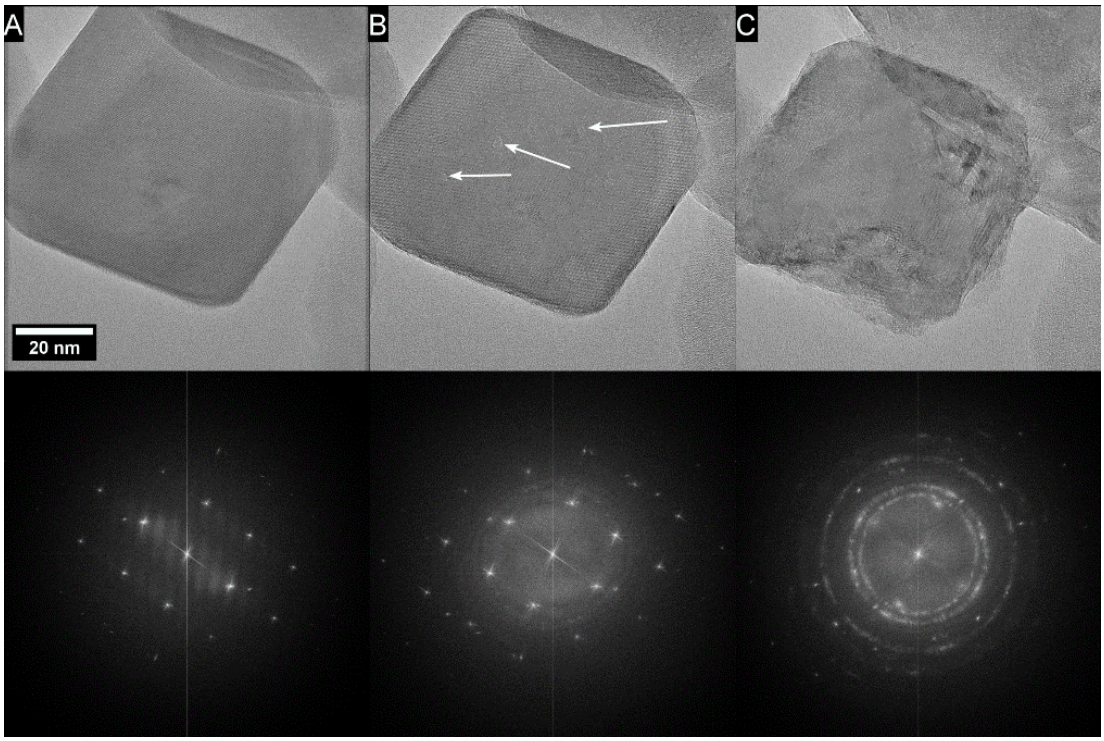

Figure 6.1 300 kV PC-CTEM images and corresponding FFTs (indicating the $[4\bar{4}1]$ zone axis orientation of a calcite nanoparticle) at accumulated fluences: A – 6.1×10^6 $e^- nm^{-2}$, B – 2.9×10^7 $e^- nm^{-2}$ and C - 1.7×10^8 $e^- nm^{-2}$. 20nm scale bar for CTEM images, arrows show pore formation in the calcite nanoparticle. FFT image width 20 1/nm.

Under similar PC CTEM imaging conditions but at 80 kV, the lattice began to degrade on average at 1.7×10^7 $e^- nm^{-2}$ with a standard deviation of ± 2×10^6 $e^- nm^{-2}$ a lower average fluence when compared to 300 kV operation; this is shown in Figure 6.2b, where the spots in the 80 kV FFT show the same streaking/arcing that occurs at 300 kV (Figure 6.1b). Working at higher accelerating voltages is expected to extend the damage threshold for materials sensitive to radiolytic fission since there is an increase in inelastic mean free path length at higher accelerating voltages and therefore less energy would be deposited in the material at a given fluence (e.g. Egerton (57)).

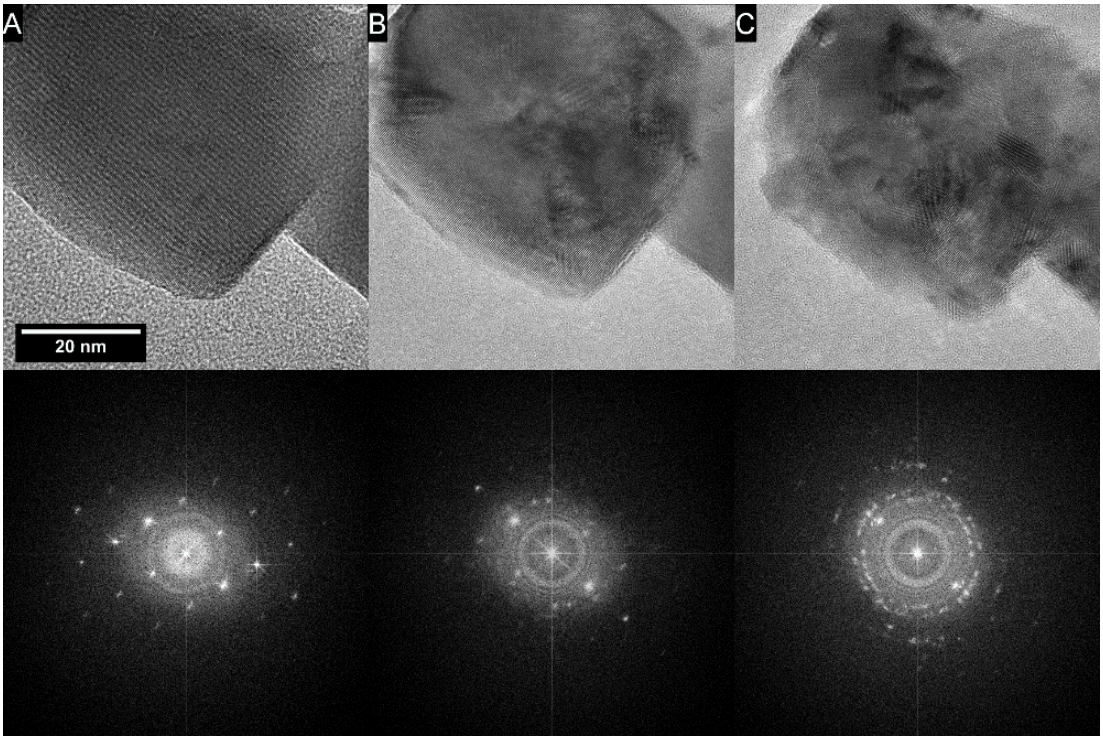

Figure 6.2 80 kV PC-CTEM images and FFTs (indicating the $[\bar{1}00]$ zone axis orientation of a calcite nanoparticle) at accumulated fluences of A) 4.8×10^6 $e^- nm^{-2}$ B) 1.7×10^7 $e^- nm^{-2}$ and C) 4.7×10^7 $e^- nm^{-2}$. 20nm scale bar for CTEM images, FFT image width 20 1/nm.

6.3. Influence of Polymorph on Electron Beam Sensitivity

Aragonite and vaterite crystals were also investigated to compare any difference in electron beam sensitivity across the different anhydrous calcium carbonate polymorphs, and to investigate the progression of damage, for

example whether the vaterite particles form aragonite or calcite as an intermediate phase as they are irradiated. This is shown in Figure 6.3, where under irradiation they were seen to form crystalline calcium oxide, in a similar manner to calcite, with aragonite and vaterite particles both losing lattice integrity after approximately 1.6×10^7 $e^- nm^{-2}$, with a standard deviation of ± 2×10^6 $e^- nm^{-2}$ for both. When compared to calcite nanoparticles, the damage threshold of vaterite and aragonite is approximately half, however this is not a conclusive study due to the larger particle size and thickness of the vaterite and aragonite crystals used. Qualitatively at least, it appears that for calcium carbonate, crystal structure does not have a significant impact on electron beam sensitivity, as the measured damage thresholds are all between 1.5-3.0×10^7 $e^- nm^{-2}$ for 300 kV CTEM irradiation.

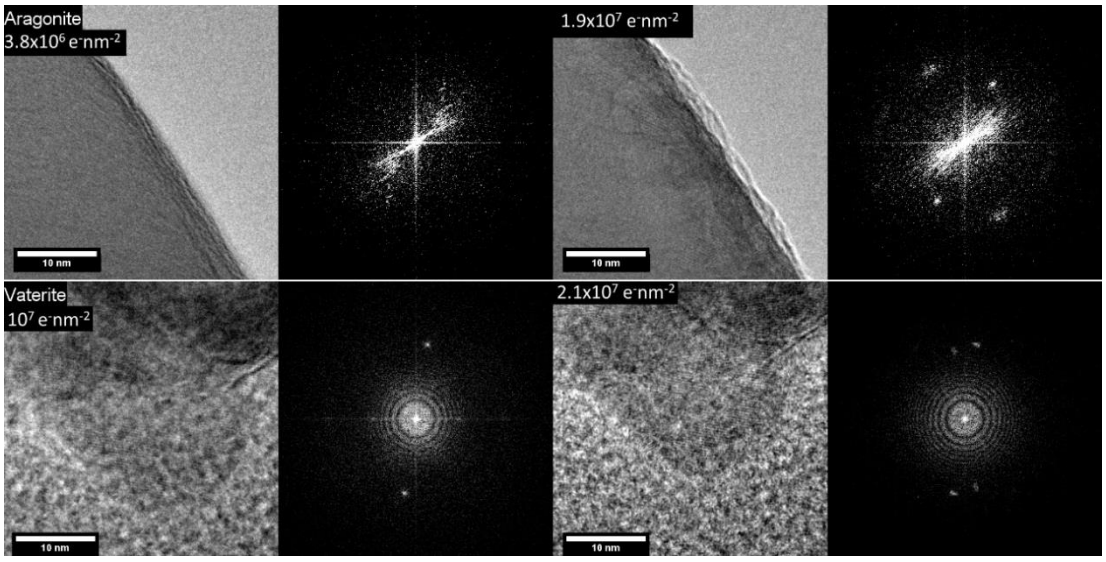

Figure 6.3 Time-resolved PC-CTEM images of aragonite crystals and vaterite crystals with associated FFTs. (Aragonite and vaterite crystals provided by T. Kathyola. FFT image width 10 1/nm for all FFTs.

6.4. Influence of Accelerating Voltage on Mass Loss

Whilst lattice resolution imaging provided insights into the degradation of calcite crystallinity, EDX spectroscopy can be used to investigate mass loss and its implications for compositional analysis. Any production and loss of carbon dioxide can be picked up by quantifying absolute changes in oxygen and carbon K_α EDX peak areas. Any reduction in the calcium K_α peak area would suggest the additional presence of knock-on or sputtering damage

occurring, likewise a continuing reduction in O:Ca ratio below 1:1 would indicate oxygen mass loss through sputtering. Calcium along with oxygen and carbon is likely to be more susceptible to knock-on damage above 80 kV (6).

Changes in the O:Ca K_α peak area ratio of calcite nanoparticles irradiated at 80 kV and 300 kV in CTEM showed a clear reduction in oxygen peak area, interpreted as the removal of carbon dioxide by radiolysis (Figure 6.4). No change was detected in the calcium peak area up to 10^8 e^-nm^{-2}, suggesting that calcite is mostly susceptible to radiolysis at these fluences, as no calcium is removed through knock on or sputtering, even at 300 kV although this may not be the case at even higher accelerating voltages or higher fluences.

At 80 or 300 kV, by 10^8 e^-nm^{-2} the measured O:Ca K_α peak area ratio approached a steady state value of approximately 1.2:1, where complete conversion of $CaCO_3$ to CaO would be expected to give 1:1. This small difference in measured and expected ratios was most likely due to the assumptions made when calculating the k-factor for quantification of the O:Ca atom ratio, although it is also possible that it is due to incomplete conversion of $CaCO_3$ to CaO, or that CO_2 remains trapped in the particles in closed pores/voids.

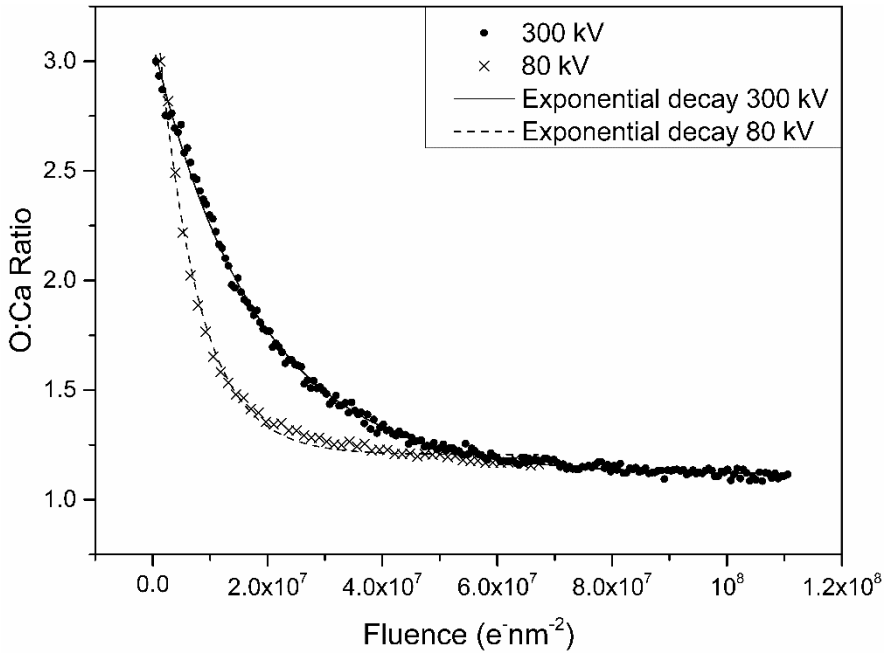

Figure 6.4 Influence of irradiation voltage on the reduction of O:Ca ratio determined by EDX spectroscopy in CTEM, with exponential fits to the decay curves also shown. Electron fluxes were $3.5x10^4$ $e^-nm^{-2}s^{-1}$ for both 80 and 300 kV.

The decay of O:Ca K_α peak area ratio follows an exponential form at both 80 and 300 kV irradiation, with the characteristic or critical fluence for the reduction of O:Ca atomic ratio to 1/e giving an indication of the rate of mass loss. The characteristic fluence threshold for mass loss at 300 kV was $2x10^7$ e^-nm^{-2}, whereas at 80 kV this was reduced to $8x10^6$ e^-nm^{-2}, in comparison the critical fluence for lattice imaging reduced from $2.7x10^7$ e^-nm^{-2} at 300 kV to $1.7x10^7$ e^-nm^{-2} at 80 kV. Rodriguez-Navarro et a (69) stated that the de-excitation process resulting in bond fission is the rate limiting step here because the resulting transformation of calcite to calcium oxide would leave sufficient pores and voids for rapid out-diffusion of CO_2. The existence of nanoporosity was supported by the BF-CTEM imaging already presented in section 5.3.1 and here in Figure 6.1 and Figure 6.2.

At fluences greater than 10^8 e^-nm^{-2} calcium carbonate was essentially transformed to polycrystalline calcium oxide. To make use of EDX information without significant compositional degradation, a suitably low fluence must be used, however this will lead to poor X-ray counts. Figure 6.5 displays the X-ray counts for individual calcite nanoparticles, irradiated for the same

accumulated fluence (of $1x10^6$ e^-nm^{-2} at a flux of $3.4x10^4$ $e^-nm^{-2}s^{-1}$) at 80 kV and 300 kV in order to evaluate whether the increase in X-ray counts provided by 80 kV operation outweighs the increase in damage.

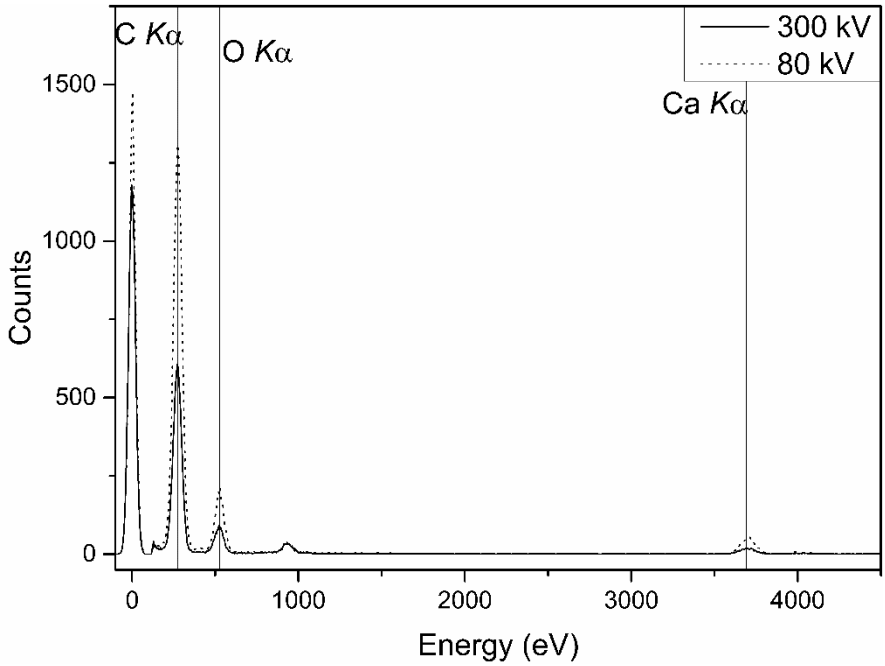

Figure 6.5 Averaged CTEM EDX spectra for individual calcite nanoparticles irradiated at 300 kV and 80 kV under the same accumulated fluence of $1x10^6$ e^-nm^{-2} at a flux of $3.4x10^4$ $e^-nm^{-2}s^{-1}$.

For the same total accumulated fluence, a single EDX spectrum acquired at 80 kV did indeed show an increased number of total counts and count rate over 300 kV operation (Figure 6.5). However, this increase in signal was almost exactly offset by the reduction in specimen lifetime: at 80 kV (relative to 300 kV) the average peak areas for Ca K_α and O K_α increased by a factor of 2.7 and 2.3 respectively, whilst the characteristic fluence for compositional change reduced by a factor of 2.4. At 300 kV, the same increase in X-ray counts could be achieved by simply collecting X-rays for longer whilst reaching the same extent of specimen damage as observed at 80 kV. This is well known (57) and arises since the dose (the energy) deposited in a specimen (of identical thickness) will be the same. This, coupled with the potential reduction in damage onset for phase contrast CTEM imaging (Figure 6.1 and Figure 6.2) indicated that there was no obvious benefit to the irradiation lifespan of calcium carbonate at 80 kV operation.

6.5. Intentional Contamination in CTEM

Time-resolved EDX measurements were performed on a specimen exposed to ambient conditions for several days. This allowed for significant adsorption of airborne hydrocarbons and contaminants. Upon irradiation in CTEM with a condensed beam of ~2 µm diameter (indicated by the white circle in Figure 6.7), contamination build-up was observed in EDX spectra and in bright field images, seen in Figure 6.6 and Figure 6.7 respectively.

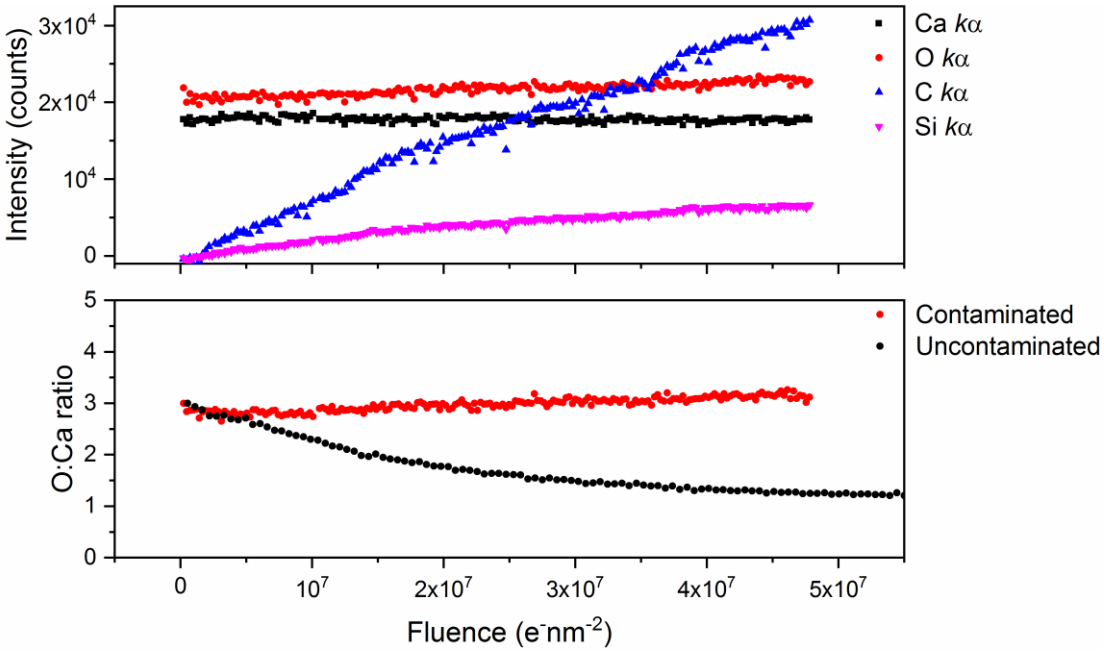

Figure 6.6 Top graph) Integrated peak intensities, Bottom graph) O:Ca ratios of time-resolved CTEM EDX spectra of a contaminated calcite specimen shown in Figure 6.7.

As shown in Figure 6.6 above, the time-resolved EDX spectra shows no reduction in the oxygen content, even after prolonged irradiation, in fact a slight increase in oxygen content is seen, presumably due to the deposition of oxygen containing hydrocarbons. The most significant change when compared to a standard calcite specimen is the significant growth of carbon over time, where standard calcite specimens show a loss of carbon due to the loss of CO_2. A minor decrease in the calcium signal is also seen, this is most likely due to absorption of calcium X-rays by the hydrocarbon contamination layer, rather than sputtering or knock-on damage, as no reduction of calcium X-ray counts was observed for a standard uncontaminated specimen

irradiated to higher fluences. Intentionally deposited carbon coatings have been shown to supress knock-on and sputtering damage when applied to the specimen beam exit side, presumably the hydrocarbon contamination can protect the specimen in the same manner (193).

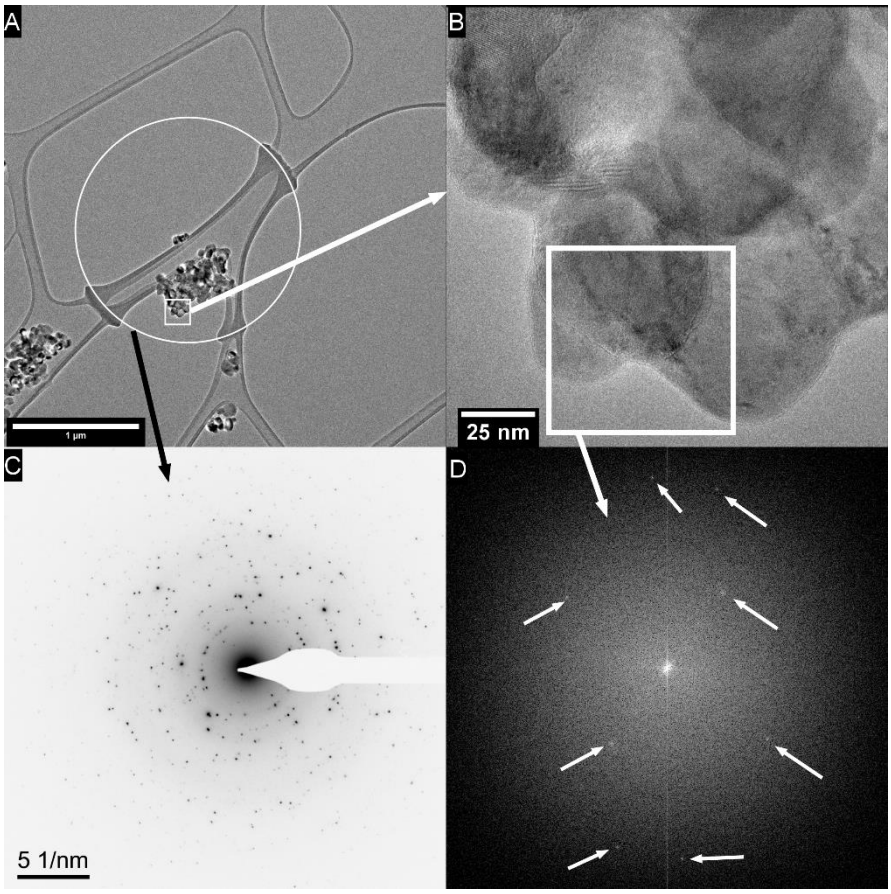

Figure 6.7 Intentionally contaminated calcite nanoparticles imaged in CTEM A) low magnification image B) High resolution image C) SADP from the particles within the highlighted circle in image A). D) FFT of indicated region in image B, showing calcite crystallinity (arrows) with no calcium oxide present. Fluence exceeds the damage threshold of an uncontaminated calcite specimen.

The diffraction pattern taken from the displayed particles, shows no crystalline calcium oxide present, however the high-resolution image does show some specimen degradation, manifesting as dark spots indicated by an arrow in Figure 6.7B. This suggests that a small amount of damage has occurred, however the crystallinity has not been damaged to the same extent as the standard uncontaminated sample at higher fluences (Figure 6.1).

It is possible that the build-up of contamination is protecting the specimen in several ways; by aiding the conduction of electrons, thus reducing the extent of radiolysis by supressing charge build-up; or by preventing the migration of molecular fragments and facilitating their recombination, meaning that there may be structural damage without significant chemical change. The reduction of radiolysis through charge mitigation is demonstrated by the reduced structural damage compared to the standard specimen, where it is visibly less degraded after the same fluence, and crystalline CaO is not detected. The reduced migration of molecular fragments would explain why there is limited loss of oxygen, as recombination or trapping of CO_2 would result in limited mass loss. Some mass loss is observed on the particle surface, seen in Figure 6.7B as surface degradation, and would likely be from early stages of irradiation, before the contamination layer is able to form and protect particle surfaces.

After the same fluence as the specimen in Figure 6.7, the O:Ca ratio in the standard uncontaminated sample would be ~1.3:1, however in the contaminated specimen, the O:Ca ratio has not decreased from an initial value of 3:1 (bottom graph Figure 6.6). When these results are taken alongside the STEM lattice imaging results, it is clear to see that the build-up of hydrocarbon contamination has beneficial qualities for minimising beam damage in calcite. It is seen that in either CTEM or STEM operation, a heavily hydrocarbon contaminated specimen will maintain structure and composition to higher fluences than a clean specimen.

6.6. Phase Contrast STEM Imaging

Under 300 kV STEM irradiation, crystalline CaO was not visible in the FFT of the PC-STEM image, even up to an accumulated fluence of 1.9×10^8 $e^- nm^{-2}$ shown in Figure 6.8. Despite the obvious formation of pores or bubbles, changes in projected shape of the particles and clear hydrocarbon contamination build up, the general form of the imaged calcite lattice is retained across these fluences. This possibly suggests that STEM may be a

better choice for prolonged imaging of calcium carbonate-based materials, at least where hydrocarbon contamination is present. This would suggest that the progression of radiolysis is limited by the hydrocarbon coating and that calcium oxide crystallization was completely inhibited. It is assumed that some amorphous CaO must have formed as mobile pores or gas bubbles were readily visible under the contamination layer, and CTEM EDX results show that significant mass loss could have occurred by this fluence with the O:Ca atomic ratio reduced to ~1.5:1.

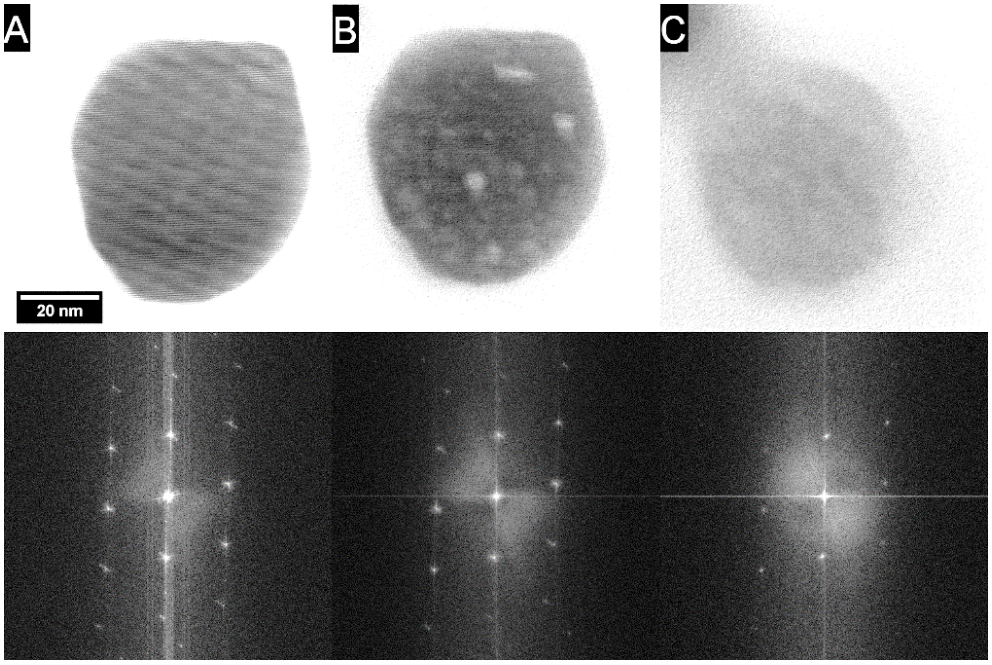

Figure 6.8 PC-STEM images and FFTs (indicating the $[4\bar{4}1]$ zone axis of the calcite nanoparticle) at different accumulated fluences: A 1.2x10^{6}; B – 2.7x10^{7} and C - 1.9x10^{8} e^{-}nm^{-2}. 20 nm image scale bar, FFT image width 12 1/nm.

The formation of a contamination layer may reduce the mobility of damage products by acting as a diffusion barrier, reducing the extent of mass loss, or acting to enhance the sample conductivity and hence charge build up in the specimen in a similar manner to intentionally deposited carbon coatings. However, it is not clear at this stage what is actually inhibiting the nucleation of CaO. Nonetheless, STEM imaging confirms that calcite degradation begins with a reduction in crystallinity. Eliminating or minimising the presence of hydrocarbon contamination should then reveal whether irradiation effects in STEM are similar to those already noted in CTEM.

6.6.1. Removal of Hydrocarbon Contamination

Removal of hydrocarbon contamination was achieved by heating the sample in an in-situ TEM heating holder at 75 ^{o}C for 16 hours in the microscope column to encourage thermal desorption of the contaminants. Prior to heat treatment, hydrocarbon contamination accumulated rapidly around particles, reaching an average of 15 nm thickness after 10 STEM scans, (Figure 6.10). Following in-situ heat treatment for 16 hours, little or no contamination was detected after 10 STEM scans and a significant reduction in contamination was seen even after as little as 10 minutes of in-situ heating at the same temperature (Figure 6.10).

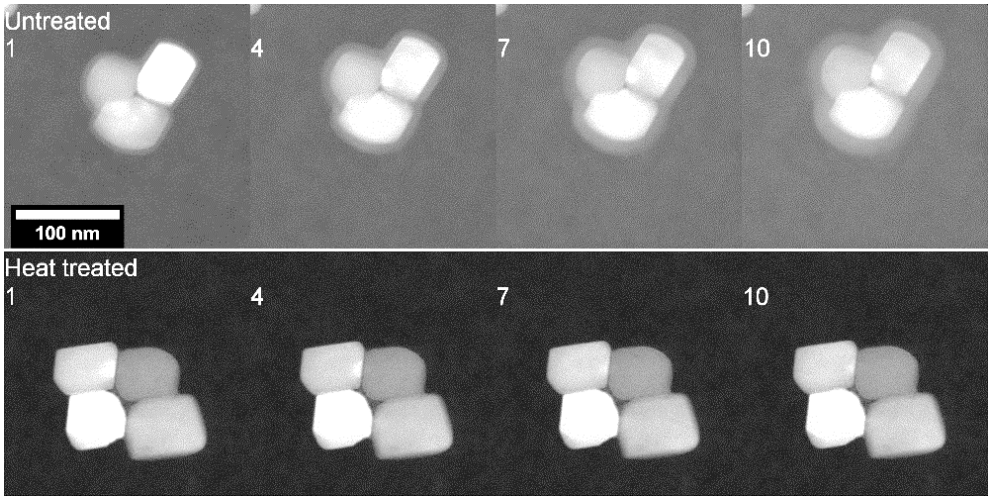

Figure 6.9 ADF-STEM images of calcite particles after 1, 4, 7 and 10 scans. Top row - prior to in situ heat treatment. Bottom row - after 16 hours of in-situ heat treatment at 75^{o}C, sample cooled to 25^{o}C before imaging. 100 nm scale bar.

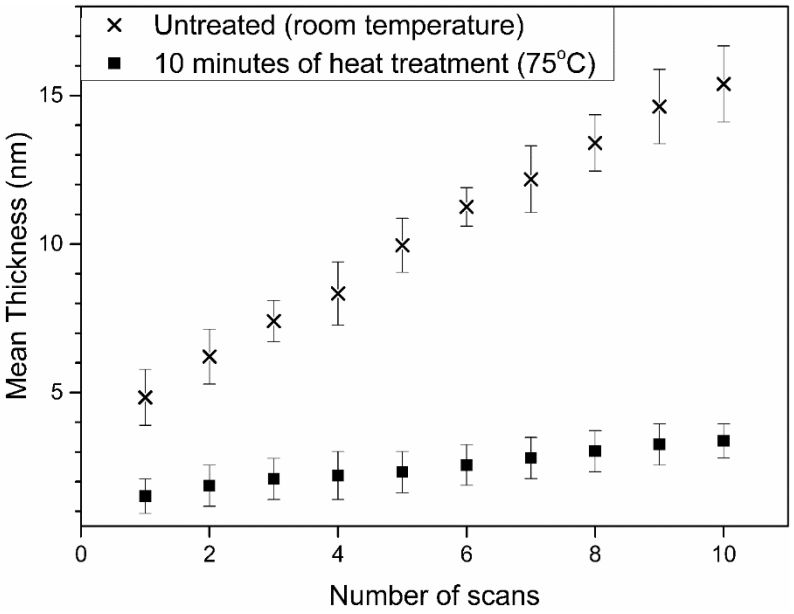

Figure 6.10 Observed thickness of the hydrocarbon contamination layer, measured by ADF STEM imaging, as a function of STEM scan number both at room temperature and following 10 minutes of in-situ heat treatment at 75 ºC. Error bars correspond to standard deviation from the measured mean.

The reduction of hydrocarbon contamination allowed for an investigation into the true electron beam sensitivity of calcite using 300 kV phase contrast STEM imaging. In STEM, without the presence of hydrocarbon contamination, calcite degraded at lower fluences than when contamination was present. On average, polycrystalline calcium oxide was seen in the FFT at ~1x10^{7} e^{-}nm^{-2} (Figure 6.11c), however dark features were seen in the images before this Figure 6.11b), with these features displaying crystallinity following further irradiation, these are likely beam-induced defects within the calcite lattice. This represents a similar fluence for the onset of calcite degradation as that observed using 300 kV CTEM illumination using an ultrathin amorphous carbon film to support calcite particles (2.7x10^{7} e^{-}nm^{-2}). A ~1-2 nm amorphous layer was seen around the calcite particles under CTEM irradiation (Figure 6.1), suggesting that a small build-up of contamination was present, however this did not appear to grow with continuing irradiation.

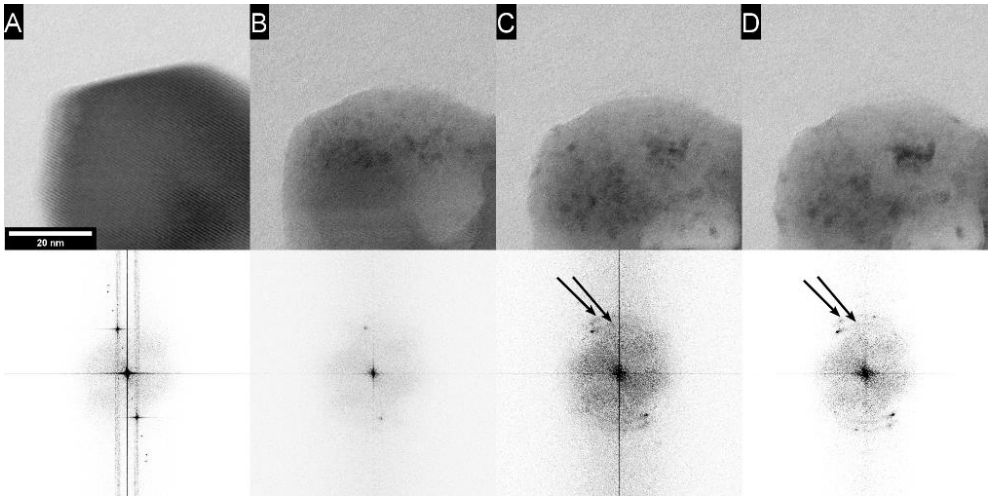

Figure 6.11 300 kV PC-STEM irradiation series and corresponding FFT processed with "reveal weak reflections" setting of Difftools plugin in GMS 3.11. A = $1.5x10^6$, B = $6x10^6$, C = $1.1x10^7$, D = $1.5x10^7$ e^-nm^{-2}, on a calcite nanoparticle following in-situ heat treatment. Image A and B display calcite crystallinity, polycrystalline calcium oxide is first detected in the FFT at $1.1x10^7$ $e\text{-}nm^{-2}$ indicated by the arrows in image C and D. 20 nm image scale bar, FFT image width 12 1/nm.

Repeated STEM scans (and associated FFTs) showed that cleaned calcite particles lost crystallinity before the nucleation of crystalline calcium oxide was detected, unlike in CTEM imaging. This was apparent in the FFTs in Figure 6.11 as the intensity of the amorphous scattering in the FFT increased whilst the crystalline calcite spot intensity concurrently reduced. In addition, the faceting of the irradiated particle degraded with increasing irradiation, with the original crystalline facets roughening and possibly rearranging into "nanofacets" before the particle becomes fully amorphous. This can be seen in the projected surface facet at the top of the particle in Figure 6.12, the original faceting, prior to irradiation (shown by the white lines), is seen to degrade into less well defined nanofacets, shown by the roughness on the particle faces.

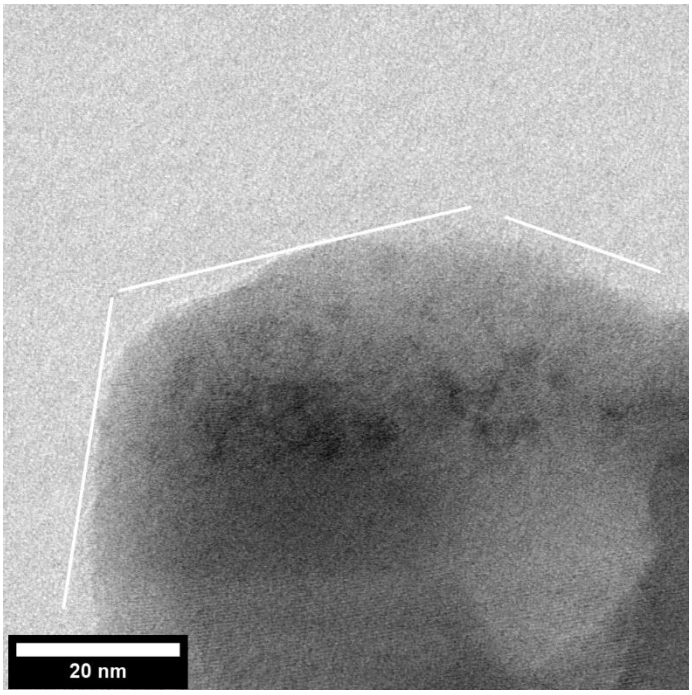

Figure 6.12 High resolution BF-STEM image of thermally cleaned calcite particle from Figure 6.11B, the white lines show the original faceting of the particle, from Figure 6.11A.

Taken together these results suggested the presence of an amorphous intermediate of either calcium carbonate, calcium oxide or both during the damage process, prior to the eventual crystallisation of calcium oxide.

6.7. Discussion

300 kV operation has been shown to have benefits over 80 kV for phase contrast imaging of calcite nanoparticles by CTEM (Figure 6.1 and Figure 6.2), this was due to the reduction in inelastic cross section giving an increase in the inelastic mean free path, which was beneficial for the lifespan of the particles, the reduced inelastic interaction at 300 kV means that there are fewer counts for EDX and EELS (Figure 6.5).

Whilst there was an increase in particle lifespan, the phase contrast image is predominantly formed from elastic scattering, and 300 kV operation displays a lower elastic scattering cross section than 80 kV, as the elastic cross section is ~$1/E_0$, thus the image contrast is reduced by a similar factor to the increase in particle lifespan. The reduction in EDX signal was also similar in magnitude to the increase in calcite specimen lifetime at 300 kV (Figure 6.4 and Figure

6.5), so the reduced sensitivity was offset by the increase in collection times required to achieve the same signal to noise level in EDX data (as discussed by Egerton (57).

Whilst increasing the accelerating voltage from 80 kV to 300 kV increased the critical fluence for the degradation of calcite, it reduces the image contrast proportionally, and thus it is expected that the dose limited resolution would remain unchanged (57). However, as the performance of the imaging detector is also a factor and the image contrast is affected by the detective quantum efficiency (DQE) and modulation transfer function (MTF), the imaging mode may have implications for the dose limited resolution. Photomultiplier based STEM detectors can be considered point detectors as they collect signals in a serial manner, and will display an improved MTF at standard collection conditions, as compared to a pixelated detector used for CTEM imaging (87). If STEM point detectors can be optimised for pulse readout, the MTF of STEM can be enhanced, improving the contrast and thus improving the dose limited resolution when compared to a CTEM CCD or CMOS camera with the same DQE (194).

STEM offers an improved irradiation lifetime over CTEM for radiation sensitive materials displaying a non-linear/inverse dose rate dependence i.e. increasing fluence rate does not cause a linear increase in damage rate, typically such damage processes are diffusion limited. In the case of calcite, which displays a linear relationship between fluence rate and damage rate and is not diffusion limited (191), the extent of damage was directly proportional to the accumulated fluence and so it would be expected that there would be no inherent benefit to the use of STEM over CTEM to avoid damage.

STEM operation does however offer advantages for calcium carbonate-based materials in terms of fluence efficiency for a fixed damage threshold including “off specimen” focussing and fine probe alignment using the Ronchigram on the support film to reduce pre-irradiation of the region of interest, and simultaneous phase contrast and elastic annular dark field imaging to identify regions of interest. Figure 6.8 and Figure 6.11 have shown that hydrocarbon

contamination generated by fine probe scanning appears to extend the damage thresholds in calcite nanoparticles, where a similar effect has been noted in the sheet silicate mineral biotite by Ward et al. (83). There are several potential reasons why contamination extends the lifetime of calcite under irradiation: the use of an intentionally deposited coating has been demonstrated to reduce knock-on and radiolysis induced sputtering damage in multiple reports (72, 83, 193, 195, 196). Fryer and Holland, (197) have suggested that for radiolysis, carbon coatings may aid in the recombination process of molecular fragments, as the fragments are retained in the original proximity by the carbon coat. By extension this mechanism would also reduce the mobility of damage products, in turn reducing the rate of mass loss for fragments which do not recombine. It is also likely that the contamination layer itself may aid in the dissipation of electrical charge and heat. Whilst irradiation-induced hydrocarbon contamination has benefits, a balance must be struck between extending the lifespan of beam sensitive materials, and the negative impacts of contamination build-up; including the reduction in image contrast, reduced X-ray counts due to absorption in the contamination layer and the interference of the signal from adventitious carbon in electron energy loss spectra.

In CTEM, phase contrast imaging has a high electron collection efficiency, however when imaging weak phase objects it is often challenging to achieve optimum focus visually, especially under low-dose conditions. Phase contrast STEM offers relatively poor collection efficiency of electrons when reciprocity conditions are used, but focussing is simplified using the Ronchigram of the support film. Also, by relaxing reciprocity conditions, it is possible to increase the collection efficiency of electrons, whilst forming phase contrast images (86). Previous work by Sader et al., (87) has shown it is possible to acquire phase contrast STEM images of adequate contrast and signal to noise ratio, whilst maintaining moderate collection efficiency by setting the bright field detector to be approximately half the size of the zero order STEM disc as originally theorised by Rose (86). The phase contrast STEM conditions used here followed those reported by Sader et al., (87) and therefore provided approximately 25% collection efficiency, with the bright field collection angle

being ~70% of the probe convergence angle. Whilst this is relatively low compared to CTEM, it is counteracted by the improved ease of focus using the Ronchigram, and retained the potential for simultaneous collection of multiple imaging and elemental signals.

Collection efficiency and signal to noise ratio can further be improved through recent developments in STEM integrated differential phase contrast (iDPC) using a segmented detector as well as focussed probe ptychography with a pixelated detector, where the signal to noise ratio is able to exceed CTEM phase contrast images (198, 199). Both iDPC and ptychography have shown promise for the study of beam sensitive materials and light element containing materials at atomic resolution due to the efficiency of electron collection at low probe currents.

Fluence-efficient imaging using STEM with a low probe current is a powerful tool for the study of radiation sensitive materials previously precluded or severely limited by CTEM investigation. Especially where both phase contrast and elastic annular dark field imaging can provide insights into structure and crystallinity. The conditions highlighted in this chapter will be used to aid in the characterisation of calcium carbonate-based fuel detergent particles, generally considered to be amorphous with a sub 10 nm particle size (2). In this case, diffraction contrast generated with STEM ADF imaging will aid in the identification of potentially crystalline regions and phase contrast will provide structural or polymorph information at high resolution, these imaging modes can be done concurrently, using low probe currents to minimise the impact of irradiation damage.

6.8. Conclusions

High voltage STEM has great potential for the analysis of calcium carbonate-based materials, offering opportunity for low fluence, high resolution imaging under suitable collection conditions. For the case of calcite nanoparticles, 300 kV STEM offers significant benefits over CTEM, however only where contamination is present, increasing the fluence threshold for the detection of irradiation-induced faults in the calcite lattice from 2.7×10^7 $e^- nm^{-2}$ for 300 kV

CTEM to over $1.8x10^8$ e^-nm^{-2} for 300 kV STEM. It was found that 80 kV operation offered no benefits for phase contrast imaging of calcite nanoparticles when compared to 300 kV operation, nor any benefits for EDX spectroscopy, where the characteristic fluence for mass loss reduced from ~$2x10^7$ e^-nm^{-2} for 300 kV to ~$8x10^6$ e^-nm^{-2} for 80 kV operation.

For fluence-efficient imaging of calcite nanoparticles, the optimal conditions include 300 kV STEM with simultaneous wide-angle bright field (WABF) and elastic annular dark field (ADF) imaging, this could routinely be coupled with EDX for compositional analysis.

Chapter 7. Correlative Characterisation of Overbased Calcium Carbonate Fuel Detergents

7.1. Introduction

This chapter demonstrates the characterisation of nano-sized calcium carbonate particles which are used as fuel detergents in combustion engines. This study combined bulk characterisation and specific localised information provided through imaging and spectroscopy in both CTEM and STEM using a FEI Titan^3 Themis and an aberration corrected FEI Titan^3 Themis Z. The first part of the chapter covers synthesis, separation from the reaction mixture using dialysis, and materials characterisation averaged over multiple nano-sized particles. The second part of this chapter demonstrates the challenges of electron beam characterisation at the level of individual nanoparticles, showing the progression and thresholding of electron beam damage. The final aspect of this chapter is the observation and quantification of discrete crystallinity in the nanoparticles.

The synthesised and dialysed fuel detergent particles were characterised using XRD, X-ray absorption near edge structure (XANES), FTIR spectroscopy and DLS. Following bulk characterisation, the specimen was investigated using electron microscopy, revealing amorphous nanoscale particles, which were susceptible to electron beam-induced crystallisation. The damage thresholds of the amorphous particles were compared to calcite nanoparticles, as well as aragonite and vaterite aggregates and were found to be approximately equal across all polymorphs.

Using low-dose STEM imaging, the particle core size distributions were characterised, and the presence of crystallinity was investigated at the individual nanoparticle scale. Crystallinity was found to exist in discrete particles, rather than as a crystalline core in all particles. Through sampling of a TEM specimen, the incidence of crystallinity was estimated to be ~ 1 particle in 7000. This was compared to wide-area mapping as an alternative method for quantification, where the incidence was estimated to be ~ 1 particle in 3000.

The research in this chapter was carried out in collaboration with Dr Thokozile Kathyola (University of Leeds). Dr Kathyola synthesised the overbased detergent specimen, aragonite particles, vaterite particles, and provided FTIR, XRD and XANES data where indicated in figure captions.

7.2. Particle Synthesis and Dialysis

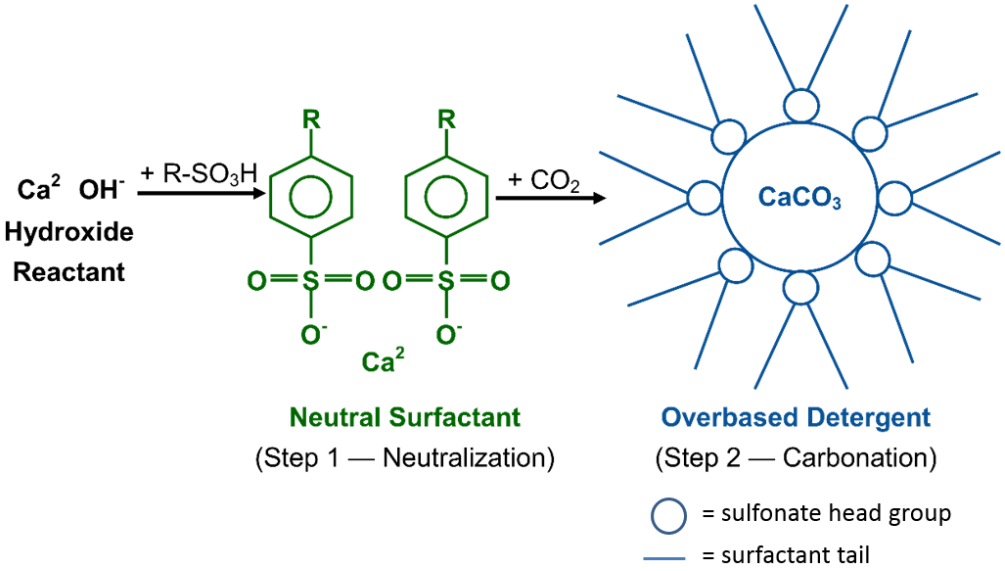

Figure 7.1 Outline of the synthesis process for the overbased fuel detergent particles, where R is a hydrocarbon chain (Schematic courtesy of T. Kathyola).

The wet chemical synthesis outlined in section 4.1.4 produced a viscous colloidal dispersion of the overbased detergent particles suspended in mineral oil. An example of the synthesised product is shown below in Figure 7.2. The calcium hydroxide used in the synthesis is not completely carbonated in order to produce an amorphous calcium carbonate structure. It has been postulated that any trace calcium hydroxide present, may form an amorphous shell surrounding the calcium carbonate core (2, 51). The calcium hydroxide shell is believed to present enough disorder that the amorphous calcium carbonate cannot crystallise, as it would not provide a template or nucleation site for crystallisation (51). This was observed by Cizaire et al (3), where Time of Flight Secondary Ion Mass Spectrometry (TOF-SIMS) and X-ray Photoelectron Spectroscopy (XPS) measurements showed a distinct separate calcium hydroxide signal present in the particles, with TOF-SIMS suggesting it is present on the particle surfaces, presumably stabilised by the surfactant.

7.2.1. Separation via Dialysis

The colloidal dispersion was dialysed using a latex ultrasound probe cover as a dialysis membrane to remove the particles from the mineral oil solvent. A schematic of this process is shown in section 4.1.4. Hexane was passed over the dialysis membrane for 24 hours to remove the mineral oil. This yielded a concentrated solution containing the colloidal fuel detergent particles, trace mineral oil, and hexane. This was then further diluted to a 1% solution by volume in hexane for further characterisation.

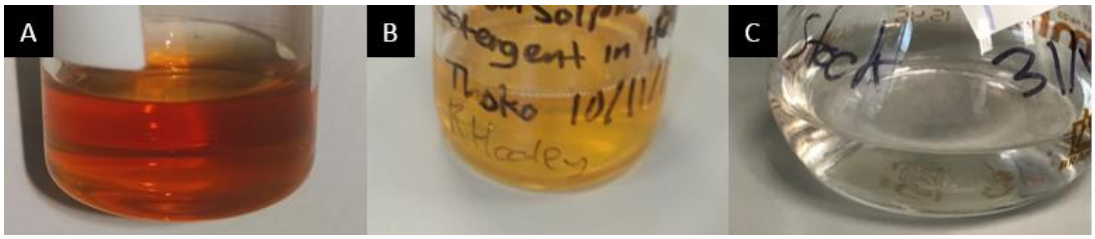

Figure 7.2 A) as-synthesised particles suspended in mineral oil, B) dialysed solution with trace mineral oil, C) diluted suspension used for CTEM/STEM imaging and bulk characterisation.

7.3. Bulk Characterisation

7.3.1. X-Ray Diffraction

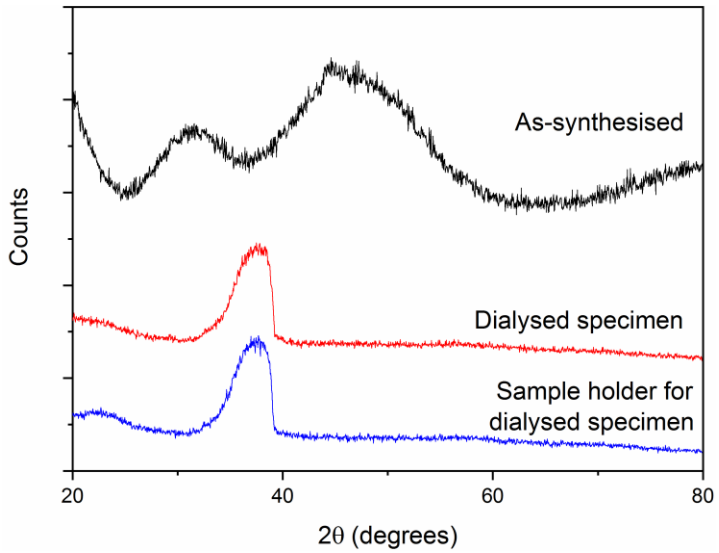

Figure 7.3 X-ray diffractogram of the dried as-synthesised and dialysed detergent particles. (XRD of as-synthesised particles provided by T. Kathyola).

XRD using the methods and equipment described in section 3.7.3 of both the dried as-synthesised and the dried dialysed detergents display no crystalline diffraction. This is in agreement with the manufacturers reports and previous research on this material system (2, 54) which states that the particles are amorphous. The as-synthesised specimen shows some amorphous scattering features, with scattering present at approximately ~30^{o} and ~40-50^{o} 2θ. This is most likely caused by scattering from amorphous calcium carbonate, Rodriguez-Blanco et al (158) observe similar broad humps in XRD of amorphous calcium carbonate. However, it is possible that there is a contribution from the mineral oil suspension medium, which would also display amorphous scattering. Due to the particle sizes present, this alone is not conclusive proof of an amorphous material, as a crystalline material with a similar particle size (of ~5-10 nm) would also show broad diffraction peaks.

The dialysed specimen is significantly more dilute than the as-synthesised specimen. XRD of this specimen does not show any useful information, as it is either not crystalline, too dilute, or the particle size is too small for coherent diffraction. The dialysed specimen exhibits a strong broad asymmetric peak at ~35^{o}, this is an artefact caused by the silicon sample holder scattering more strongly than the specimen, the as-synthesised specimen used a different sample holder due to the larger quantity of specimen and this scattering is not present. Despite this artefact, the dialysed specimen does not show any crystalline scattering peaks, and subtracting the background spectrum from the dialysed spectrum does not show any obvious amorphous scattering.

Both specimens display no crystalline diffraction information which suggests they are amorphous. However, it is possible that the specimen is crystalline but due to the particle sizes present is simply “X-ray amorphous” and thus requires structural investigation with more direct methods, including electron diffraction and phase contrast lattice imaging.

7.3.2. FTIR

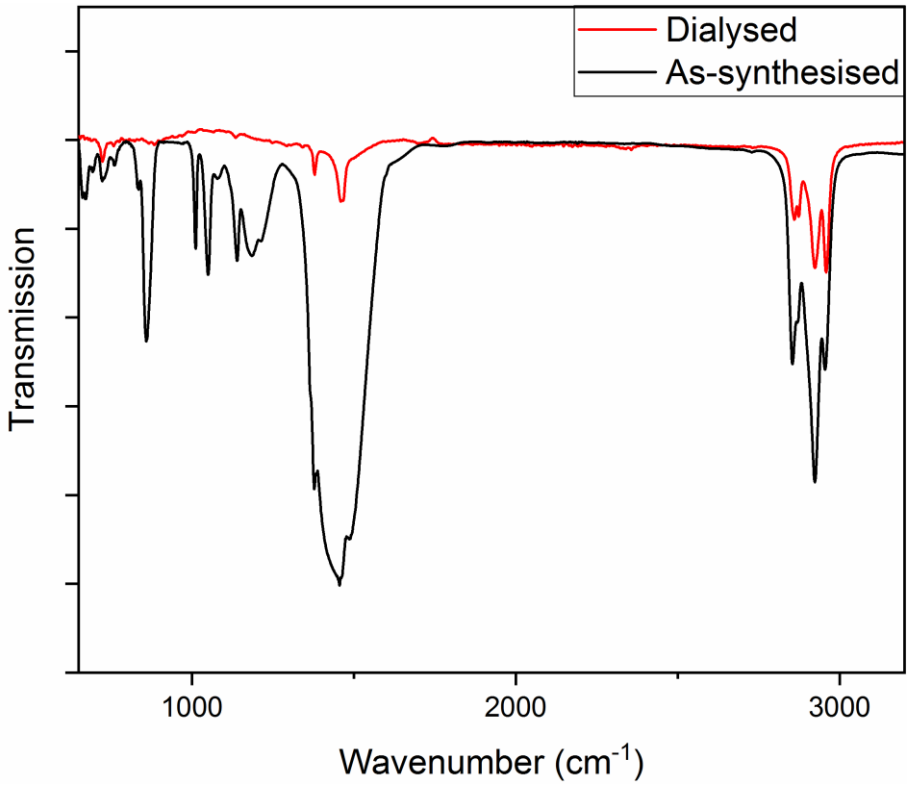

Figure 7.4 FTIR-ATR spectra of the as-synthesised and dialysed particles. (FTIR of as-synthesised particles courtesy of T. Kathyola).

The infrared spectra of the fuel detergent particles, shown in Figure 7.4 are complex, owing to the multiple organic and inorganic components of the mixture, including mineral oil, sulfonate surfactant, hexane and calcium carbonate. Reference spectra for the crystalline calcium carbonate polymorphs, the sulfonate surfactant, hexane and mineral oil have been previously shown in section 3.7.1 and these possess many overlapping features. The spectra show some significant differences before and after dialysis due to the concentration of the specimens; the as-synthesised specimen shows higher absorption in all peaks due to the higher concentration of mineral oil and detergent particles present.

The absorption peaks in the 650-1000 cm^{-1} region correspond to vibrations of the $CH=CH_2$ or CH=CH bonds in either the surfactant chain or the mineral oil, specifically out of plane bending vibrations in a long hydrocarbon chain. As

the intensity of these peaks is reduced following dialysis, it is suggested that mineral oil was a major component of this region of the spectrum.

In both spectra, the shape of the absorption band at ~1500 cm^{-1} does not conclusively determine whether the specimen is amorphous or crystalline, as all crystalline calcium carbonate polymorphs, amorphous calcium carbonate, the surfactant, mineral oil, and hexane all display absorption around 1500 cm^{-1}. These are attributed to C=C, CH_2 and CH_3 stretching vibrations in the hydrocarbon component, and asymmetric vibrations (v_3) in the CO_3 groups in the calcium carbonate (158). As all components overlap in the spectra, deconvolution to identify the influence of each component, as well as solving the structure of the calcium carbonate core would be a complex procedure.

The reduction in the hydrocarbon content following dialysis has revealed two small sharp absorption bands, at 1378 cm^{-1} and 1460 cm^{-1}. The 1378 cm^{-1} band is common to calcite, vaterite, the sulfonate surfactant, mineral oil and hexane, shown in section 3.7.1. The 1460 cm^{-1} band is common to aragonite, amorphous calcium carbonate, the sulfonate surfactant, mineral oil and hexane. Whilst this reduces the complexity of the spectrum, it is still not possible to fingerprint the form of calcium carbonate present.

7.3.3. X-ray Absorption Near Edge Structure

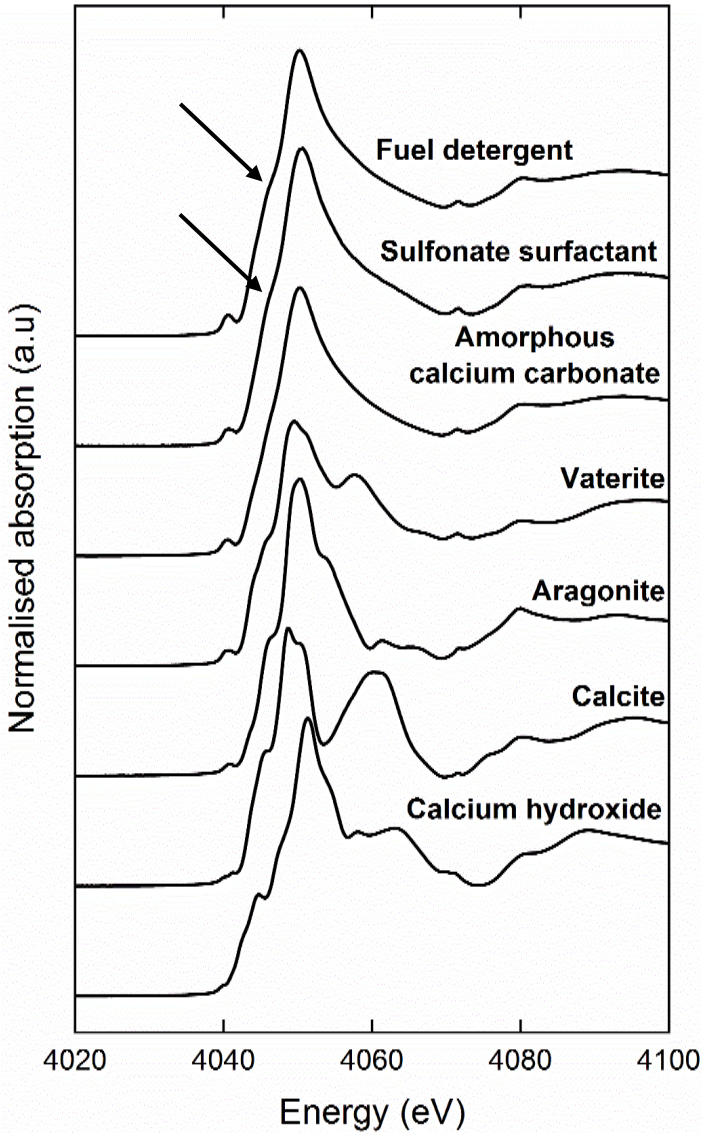

Figure 7.5 Ca *K*-XANES of the crystalline calcium carbonate polymorphs, amorphous calcium carbonate, fuel detergent particles and sulfonate surfactant (39).

The XANES plots in Figure 7.5 show the Ca *K*-absorption edge for the three crystalline anhydrous polymorphs of calcium carbonate, amorphous calcium carbonate (ACC), calcium hydroxide, the fuel detergent particles, and the calcium sulfonate surfactant. There is a clear difference between the XANES of the crystalline polymorphs and the calcium hydroxide, however the amorphous calcium carbonate, surfactant and fuel detergents display only very subtle differences in their absorption edges. The ACC, fuel detergents and surfactant show a slight difference at the shoulder of the main peak at

4050 eV (shown by the black arrow), where the ACC shows a more supressed peak at this energy compared to the fuel detergent and the surfactant.

Measurements of sulfonate surfactant stabilised overbased calcium carbonate micelles by Mansot et al (54) previously showed Ca *K*-XANES in agreement with those in Figure 7.5. The authors determined that the specimen was amorphous by analysing the radial distribution function from EXAFS measurements, where they found no ordering present at distances longer than 3.2 Å, rather than comparing the spectrum to a known amorphous calcium carbonate standard.

Total electron yield (TEY) XANES (as used in Figure 7.5) is a surface sensitive technique, with the measured electrons emitted from the top 1-2 nm of the specimen, thus it is possible that the TEY-XANES measurements above do not fully sample the centre of the particle cores. This may be why the TEY-XANES measurements of the fuel detergents show a clear component from the surfactant, which displays a Ca *K*-absorption edge as the sulfonate head group contains an ionically bonded calcium atom, resulting from the neutralisation reaction of sulfonic acid with calcium hydroxide (53).

In contrast to the spectra shown in Figure 7.5, Mansot's observations were based on transmission XANES measurements, and as such may have sampled the particle core to a greater extent. It is not possible to determine whether Mansot's measurements show this same shoulder from the surfactant at 4050 eV due to the poor energy resolution and poor print reproduction of the spectra in the publication.

The XANES of the fuel detergents suggest that it consists of a combination of ACC and surfactant XANES features, with no obvious contribution from the crystalline calcium carbonate polymorphs or calcium hydroxide. However, as the crystalline polymorphs and calcium hydroxide all show a shoulder at around 4050 eV, it is possible that there is a small fraction of crystalline calcium carbonate or hydroxide present in the specimen, though it is not currently possible to deconvolute their content, if any, in this complex material system.

7.3.4. Dynamic Light Scattering

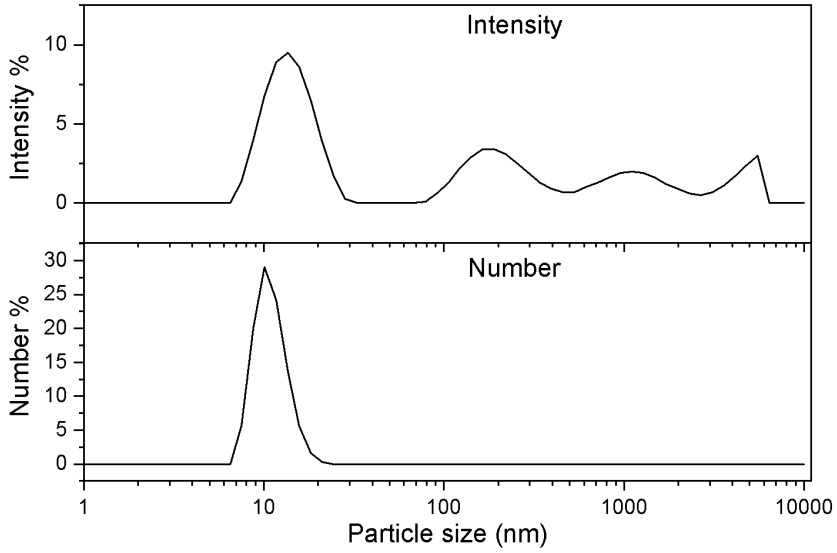

Figure 7.6 DLS intensity and number plots of the fuel detergent particles suspended in hexane, showing a primary particle peak at 7-20 nm and peaks from agglomeration above 100 nm.

DLS was performed on the fuel detergent specimen using a Malvern Instruments Zetasizer Nano ZS. The hydrodynamic diameters of the particles in Figure 7.6 show a primary particle size of 7-20 nm, with an intensity based mean particle size of ~11 nm, peaks in the intensity plot at larger particle sizes are indicative of agglomeration. However, the number plot in Figure 7.6 shows that the majority of the particles are monodisperse, with agglomerates only making up a small fraction of the total particles present, this is subsequently confirmed by ADF-STEM imaging. As DLS provides the hydrodynamic particle diameter, the surfactant head group and the hydrocarbon chain will be included in the measured particle size, as will any bound solvent molecules. DLS will therefore overestimate the particle size when compared to ADF-STEM (Figure 7.15), as the contrast in the ADF image only reveals the high atomic number calcium carbonate core, without directly revealing the surfactant.

7.3.5. Discussion

Results from bulk measurements suggest that the specimen is amorphous, however these techniques have limitations:

FTIR spectra of calcium carbonate and surfactant references have multiple overlapping components. For example; at ~700 cm^{-1}, calcite, aragonite, vaterite and the sulfonate surfactant all show a sharp absorption band with a similar intensity. This is assigned to a C-H bend in the surfactant and/or a symmetrical CO_3 vibration in the carbonate group. At 1400 cm^{-1} they all show a similar shaped broad absorption band from a C-O stretch in the calcium carbonates and/or a S=O stretch in the surfactant. This means that separating the contributions from multiple components is challenging, especially when the concentrations are not known. FTIR has been shown to detect trace components at concentrations around 0.5 wt%, however in this thesis FTIR is limited by the need to deconvolute complex spectra, rather than simply detecting trace components (200). XRD relies on particles having sufficient atomic planes to form coherent diffraction information, in this case, even if fully crystalline, the fuel detergent particles are small enough to be considered X-ray amorphous. XRD typically has a lower detection limit of ~5% by volume of crystalline material, and the lowest crystallite size to avoid Scherrer broadening is generally taken to be around 1 µm (161). TEY-XANES is surface sensitive and may not fully sample the particle core, but results are consistent with an amorphous calcium carbonate component and a sulfonate surfactant being present. XANES can detect trace but distinct elements at concentrations down to 1 ppm, but this may not be applicable for separating overlapping contributions or in noisy spectra (201). DLS probes the hydrodynamic particle diameter complete with surfactant and bound solvent. In addition, DLS does indicate that the majority of particles are in a monodisperse state. DLS does not have a sensitivity problem for characterising the fuel detergent particles, however it does not provide any chemical or structural information.

Bulk characterisation provides rapid insights into the structures and chemistry present, however these techniques lack sensitivity and specificity. The detection limits and operational drawbacks of the bulk measurements may have precluded the measurement of crystallinity in low concentrations. However, if bulk methods were able to detect crystallinity in this specimen, they would not be able to distinguish between partially crystalline cores

present in all particles and a low occurrence of crystallinity in discrete particles.

For more in-depth research, bulk methods must be correlated with more particle specific and sensitive techniques. CTEM and STEM imaging allow for the characterisation of these materials at multiple length scales with a high level of specificity, with investigations into single particles possible. However, as these particles contain calcium carbonate, electron beam damage has to be taken into account and minimised. Fluence thresholds and conditions previously developed in Chapter 6 were refined and used for in depth analysis via high resolution imaging.

7.4. Preliminary CTEM Characterisation

The dialysed fuel detergent particles were used for preliminary sample screening and method refinement, the intent of this preliminary research was to observe the specimen behaviour under irradiation and under different imaging conditions to optimise future analytical operation.

7.4.1. Bright Field CTEM Imaging

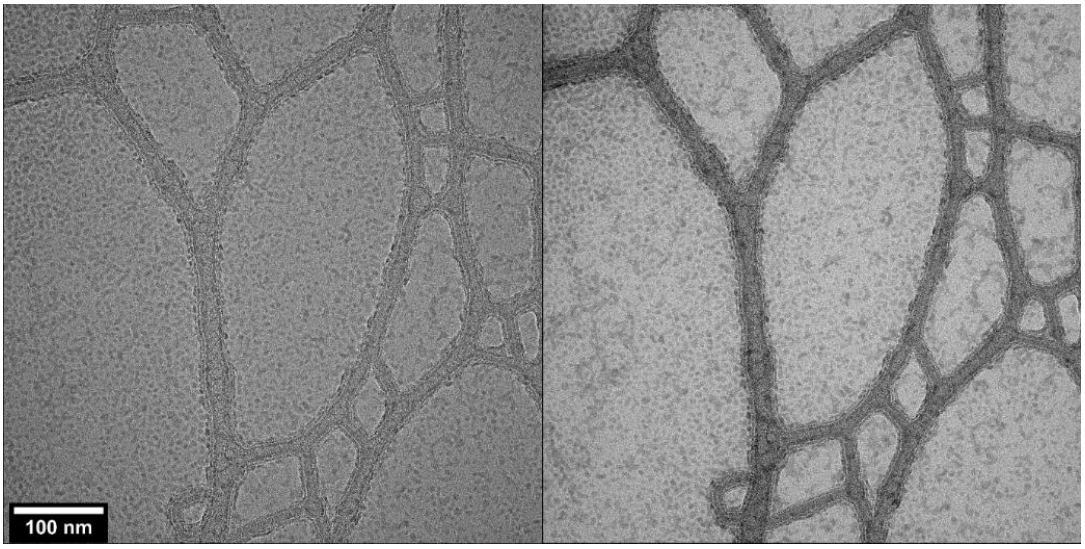

Figure 7.7 BF-CTEM image of fuel detergent particles supported on a ~3 nm ultrathin amorphous carbon film A) without and B) with an objective aperture inserted.

Bright field imaging presents a low contrast image, with particles faintly visible across an ultrathin carbon support film; when an objective aperture is inserted, amorphous scatter is reduced, and diffraction contrast is increased. However, this is not to a sufficient level for robust particle sizing, and no obvious diffracting crystallites are observed, suggesting an amorphous or poorly diffracting specimen. Low-dose operation is essential to avoid electron beam damage; however, this results in poor image contrast and a low signal to noise ratio, precluding easy focussing. This has implications for instrument alignment and electron beam damage, in that the specimen will be subject to an increased overall fluence whilst focussing adjustments are made.

7.4.2. Electron Diffraction

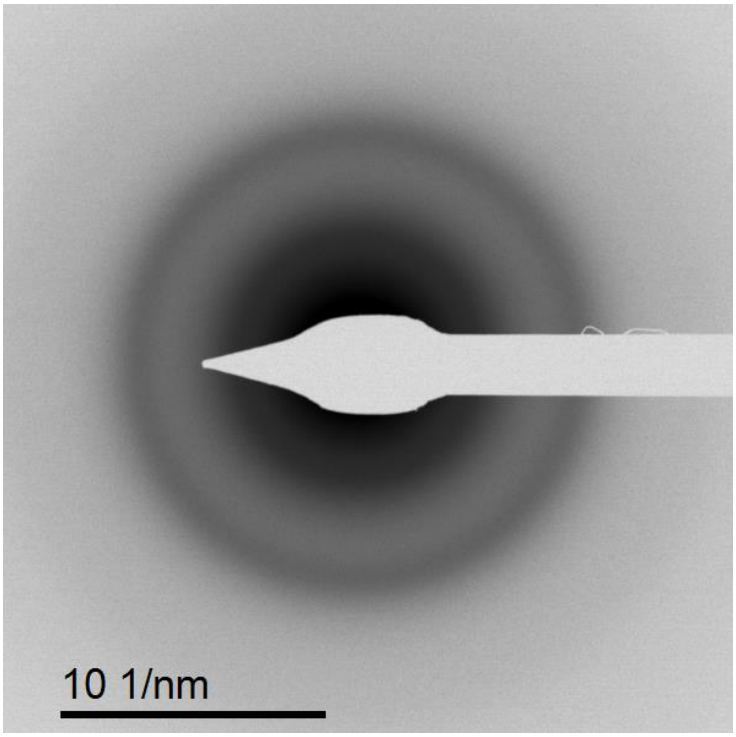

Figure 7.8 Selected area diffraction pattern from an area containing overbased fuel detergent particles. 200 nm selected area aperture, 150 µm condenser aperture.

As can be seen from the diffraction pattern in Figure 7.8, only diffuse scattering was observed, and no obvious crystallinity was detected. This is in agreement with the X-ray diffraction of both the as-synthesised, and dialysed specimens. This is not conclusive proof of an amorphous specimen as Scherrer broadening from ultra-fine (<5 nm) nanocrystalline particles would

also show diffuse bands in the diffraction pattern. Due to the lower detection limit of diffraction measurements (~5% crystallinity by volume), if crystallinity is present then it is limited in volume. As such diffraction should be used alongside direct measurements such as phase contrast lattice imaging to investigate whether crystallinity is indeed present.

7.4.3. Dark Field CTEM

Dark field imaging was used to provide contrast from scattering features, whether crystalline or amorphous, for an investigation into potential crystallinity and electron beam damage.

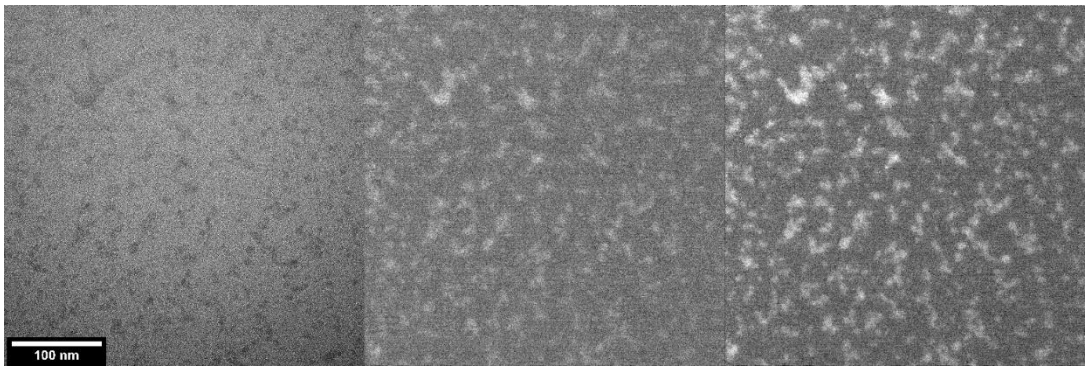

Figure 7.9 A) Bright field CTEM B-C) and dark field CTEM images of the same region of detergent particles. Fluence increases between image B and image C.

High contrast white features of enhanced intensity can be seen in the DF images (where the objective aperture is displaced over a typical crystalline diffraction range) in Figure 7.9B suggesting nanoscale crystallinity. However, as the number of high contrast features are seen to increase with further irradiation (Figure 7.9C), these may be induced by the electron beam. Without quantification of the fluxes and doses involved, it is not possible to know whether there was pre-existing crystallinity, or whether the observed crystallinity was induced by the electron beam.

7.5. High Resolution CTEM Imaging and Electron Beam Damage Study

Correlative dark field and bright field CTEM imaging in Figure 7.10 shows a crystalline particle. The DF image shows a particle which is larger and brighter

than the surrounding particles, the FFT of the associated bright field image shows that it is crystalline with a 2.6 Å *d*-spacing present.

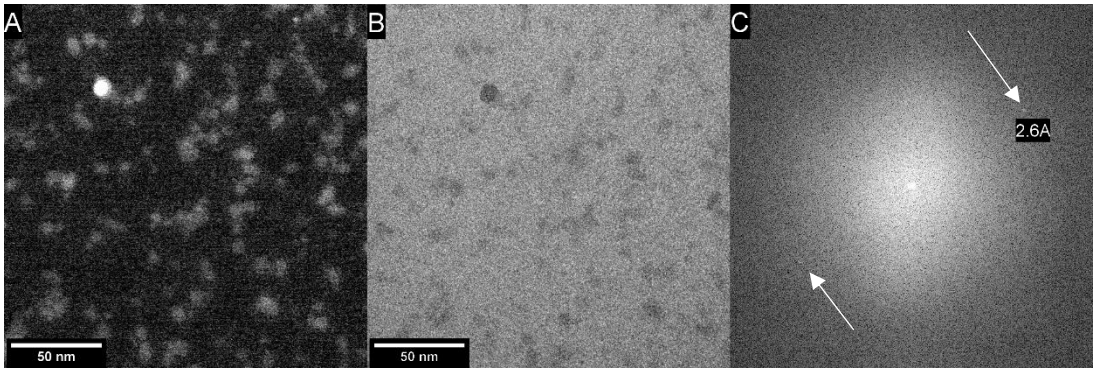

Figure 7.10 A) DF-CTEM and B) BF-CTEM image of the fuel detergent particles, C) associated FFT showing a 2.6 Å d-spacing, FFT image width 10 1/nm.

As there is an objective aperture inserted, the higher angle scattering is lost, and the phase contrast is heavily affected as high-resolution information is lost. As there is only one d-spacing present, it is not possible to fit a crystal structure with confidence or derive a zone axis. To acquire higher resolution information, the aperture must be removed or enlarged, which will make finding particles and focussing on them more challenging due to the supressed diffraction contrast.

An example of this is shown in Figure 7.11, where phase contrast CTEM imaging was used for high resolution characterisation of the fuel detergent particles, a crystalline particle was found and imaged at high resolution.

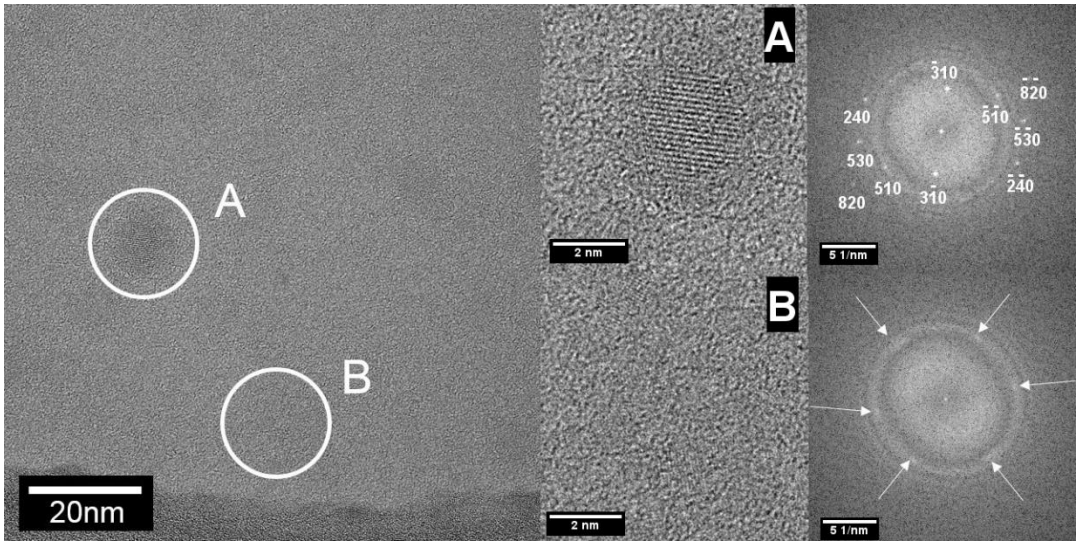

Figure 7.11 Phase contrast CTEM image of the detergent particles A) shows a particle with discrete crystallinity, with its FFT indicating a vaterite <001> zone axis. B) Shows the induced crystallisation of the amorphous particles after an estimated fluence of 4.5×10^7 $e^- nm^{-2}$, the arrows in the FFT correspond to the CaO {002} spots.

Here the time taken to focus and align properly on the crystalline particle (Figure 7.11A) was sufficient to induce crystallisation in adjacent amorphous particles (Figure 7.11B). As a result, low-dose operation is necessary to investigate the occurrence of crystalline particles and examine their structures. To derive the conditions for low-dose imaging, the electron beam damage of the fuel detergent particles was studied. This was done through 300 kV CTEM phase contrast imaging, in the same manner as in Chapter 6. However, for these particles, lattice imaging was used to measure the critical fluence leading to the onset of crystallisation of the particles, rather than the destruction of the calcite lattice as monitored by phase contrast lattice imaging, an example of this can be seen in Figure 7.12.

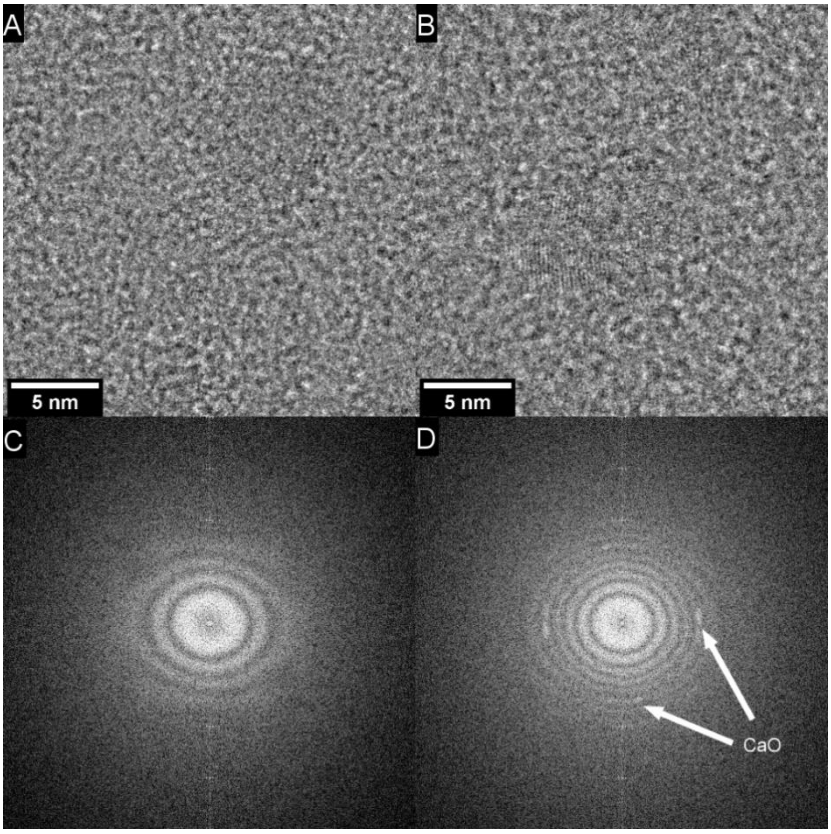

Figure 7.12 Electron beam damage observed in fuel detergent particles A) undamaged, taken at a fluence of ~5x10^{6} e^{-}nm^{-2} at 300 kV, B) following 3.5x10^{7} e^{-}nm^{-2} of irradiation at 300 kV in CTEM, C) FFT of A showing no crystallinity, D) FFT of B showing CaO crystallinity indicated by arrows. FFT image width 11 1/nm.

Through lattice imaging, it was seen that the detergent particles crystallised above an exposure of 3x10^{7} e^{-}nm^{-2} at 300 kV. The FFT displays crystallinity consistent with calcium oxide, commonly displaying the CaO {002} spots; crystalline calcium carbonate was not observed as an intermediate. Whilst this fluence threshold is only slightly higher than that derived for the breakdown of the calcite lattice image (2.7x10^{7} e^{-}nm^{-2}) (Chapter 6 section 6.2), this threshold is representative of the fluence required to form crystalline calcium oxide from amorphous calcium carbonate, rather than the destruction of crystallinity in crystalline calcite.

There are several differences between the crystalline calcite nanoparticles and the fuel detergent specimens, including particle thickness, particle size, and specimen cleanliness. It was previously demonstrated in Chapter 6 section 6.5 that specimen cleanliness impacts the lifetime of irradiated calcite

particles. The overbased detergent specimen has residual hydrocarbons present, from both the hexane solvent and mineral oil suspension medium, which may potentially increase the specimen lifetime under irradiation. Whilst a potential extension of irradiation lifetime is useful when imaging the specimen, the major drawback to poor cleanliness was that contamination deposition was rapid and highly visible. This deposition reduces imaged contrast and reduces the useable working time in imaged regions; an example of the extent of contamination build-up in the fuel detergent specimen is shown in Figure 7.13.

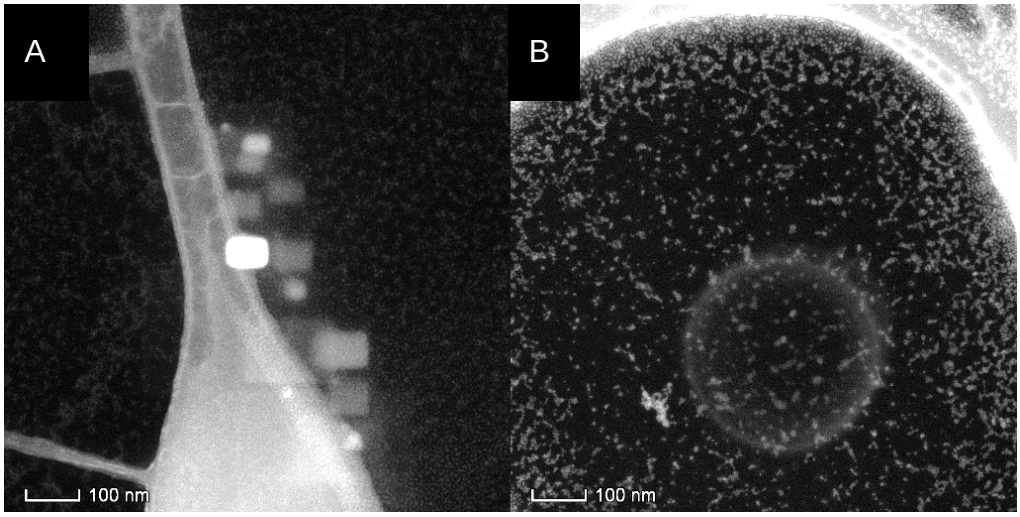

Figure 7.13 ADF-STEM image of hydrocarbon contamination deposits in dialysed fuel detergent specimens seen after A) STEM imaging and B) CTEM imaging.

The detergent particles are significantly smaller and hence thinner than the crystalline calcite nanoparticles (~5 nm as compared to ~55 nm), the inelastic mean free path (~80 nm for 300 kV electrons in calcite) is significantly larger than the particle thickness, thus there are fewer opportunities for inelastic scattering and the damage threshold should increase, however the elastic scattering contrast is also correspondingly reduced.

7.5.1. Summary

Whilst DF-CTEM is able to image the particles, with contrast afforded by amorphous scattering, it is not dose efficient due to the poor electron collection afforded by the displaced objective aperture and requires relatively long

imaging times to acquire sufficient signal. Under low fluence conditions or with short imaging times, the images are visibly noisy and lack contrast due to the inefficient electron collection. The use of a small objective aperture to form a dark field image can introduce randomly distributed, diffraction limited, bright features into the image, this means that the presence and distribution of nanoscale bright features cannot be used as an indication of any crystallinity (202). In addition, a small objective aperture precludes the use of phase contrast imaging. This is not an ideal method for CTEM operation, however this can be avoided by using ADF-STEM imaging, where due to more efficient electron collection efficiency using an annular detector based on a scintillator photomultiplier, a low probe current can be used, meaning that electron beam damage is less likely. In addition, ADF images can be formed simultaneously with phase contrast images, eliminating the need to remove and reinsert apertures.

Phase contrast CTEM is not an appropriate technique for the characterisation of the fuel detergent particles, owing to the low image contrast. This makes focussing and alignment challenging, even with a thin (~ 5 nm) amorphous support film, as these must be done on the specimen a significant dose is deposited and radiation damage is likely. To characterise these particles rigorously, the chances of irradiation damage must be minimised by working at fluences significantly below the measured damage thresholds. This can be achieved more reliably using STEM, where focussing and alignment can be performed using the Ronchigram, with the probe held off the specimen, and where dose efficient dark field imaging can be used simultaneously with phase contrast imaging. Despite STEM operation reducing the collection efficiency of phase contrast imaging compared to CTEM (87), this is outweighed by the operational and convenience benefits of STEM operation.

7.6. STEM Characterisation

STEM imaging was used for dose-efficient characterisation of the fuel detergent particles, including particle sizing, morphology and crystallinity. ADF-STEM imaging was used to measure morphology and particle size, and WABF-STEM was used to investigate the crystal structure through lattice

imaging. For imaging undertaken with a non-aberration corrected STEM system, the ADF collection angles were 17-100 mrad, with the bright field detector collection angle set to 7 mrad, the probe convergence angle was set to 10 mrad. This provided diffraction contrast from the ADF detector and phase contrast following the conditions outlined by Sader et al (87). For all measurements, the critical fluence threshold was taken to be the fluence required to form crystalline calcium oxide from amorphous particles ($3x10^7$ e^-nm^{-2}), as measured by 300 kV CTEM imaging in section 7.5. Specimens were prepared from drop casting following research from Mansot et al (54), who tested multiple methods to prepare TEM samples from overbased fuel detergent specimens: plunge-freezing in liquid ethane prior to fracturing, with carbon and platinum shadowing for near native state investigation; drop casting of particles suspended in pentane; and drop casting with platinum shadowing. Shadowing was used to enhance image contrast. They found that whilst there was some aggregation from solvent evaporation, the micelle cores were not affected by drop casting, and plunge freezing was not required.

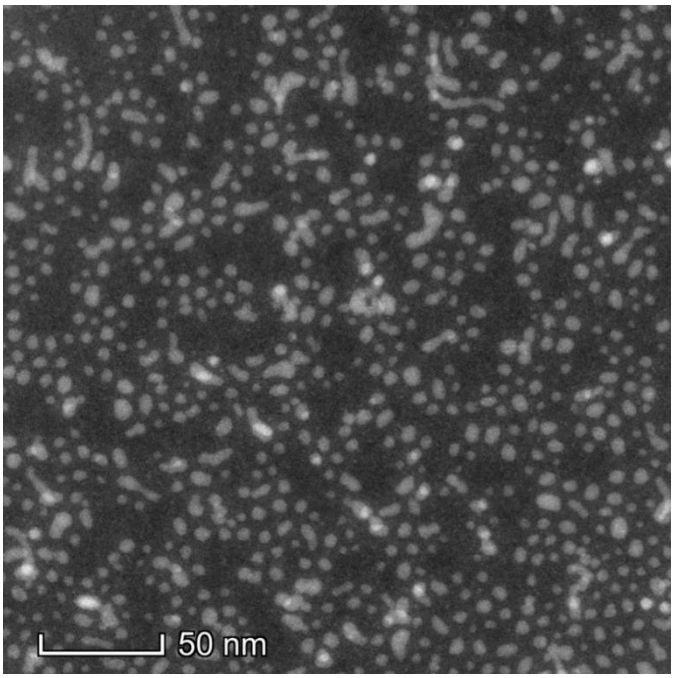

Figure 7.14 ADF-STEM image of overbased detergent particles, scan fluence is $2x10^4$ e^-nm^{-2}.

ADF-STEM imaging affords good contrast between the particles and the support film, making observations of particle size and morphology clear. Brighter features in ADF images are a result of enhanced scattering, either

from crystallinity or from thicker regions in the specimen. The particles are monodispersed, consistent with the DLS number plot (Figure 7.6B), and have a roughly circular morphology, however some elongated rod-like particles are observed. Multiple coexisting micelle morphologies have previously been observed by Almgren (203), where threadlike micelles have coexisted with both small micelles and vesicles. Presumably there is anisotropy in the surfactant concentration across the reaction mixture during synthesis, which may be related to mixing. The spherical particles seen here however have the manufacturer's desired morphology, as they have a smaller particle size, giving rapid dissolution, and higher stability in suspension, avoiding sedimentation.

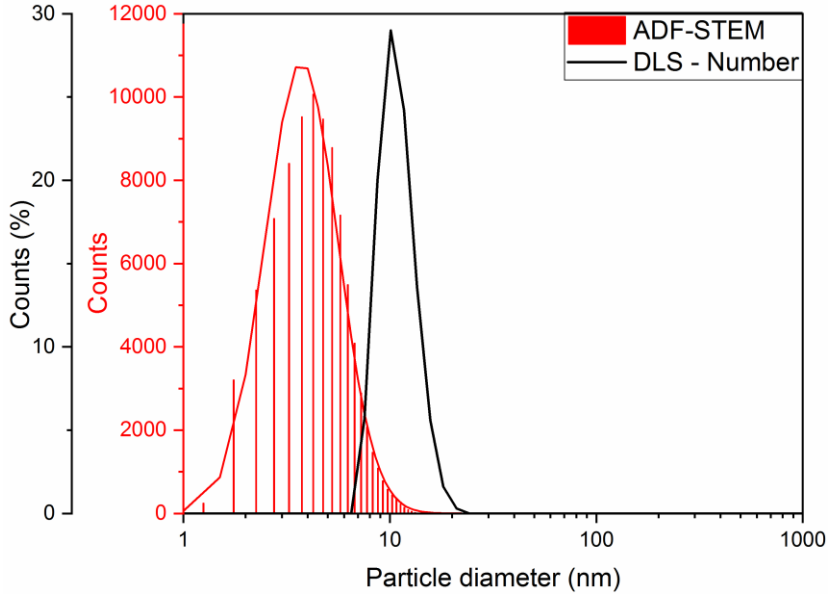

Figure 7.15 Particle size distribution of overbased detergent particles measured by ADF-STEM, overlaid with a lognormal distribution curve and the DLS number plot from Figure 7.6.

ADF imaging revealed an average particle-core size of 5.3 nm, with a standard deviation of 2.5 nm, as shown by Figure 7.15. This was measured automatically from ~90,000 particles identified in contrast segmented images processed in FIJI (177) and displays a lognormal distribution, this distribution is common for particles formed in an environment where particle coalescence occurs (187, 204).

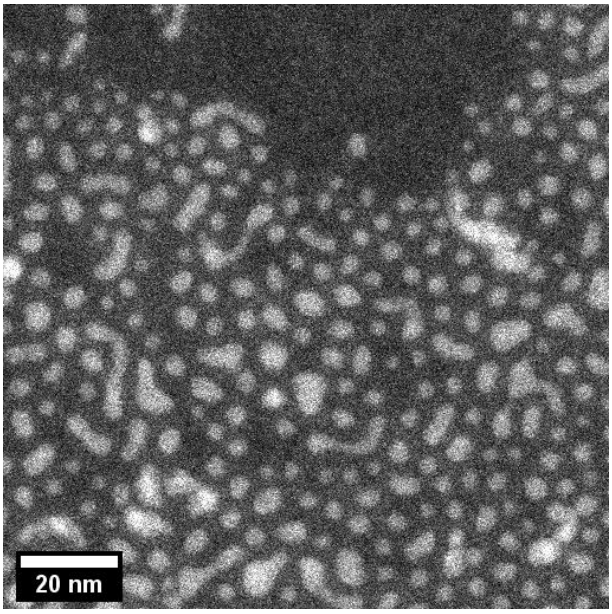

Figure 7.16 ADF STEM image of the detergent particles, showing the even separation between particles presumably due to the surfactant shell. Scan fluence ~ $1x10^4$ e^-nm^{-2}.

Figure 7.16 shows that there is a similar distance between the particles, with only a small number impinging on each other, this is assumed to be due to the surfactant shell separating the particles. This has the benefit of making image segmentation for particle sizing trivial, as particle overlap is minimised. The spacing between the particles is related to the chain length of the surfactant. When comparing the average particle diameter using DLS to that measured by STEM (11 nm compared to 5.3 nm shown in Figure 7.6). The DLS size measurement is larger due to this surfactant layer and the bound solvent layer. This would suggest the surfactant and solvent shell is ~3 nm in thickness. This is supported by measuring the nearest neighbour distance using an ImageJ/FIJI script (182) between the particles, which was revealed to be ~7 nm, which corresponds to a separation of ~3.5 nm on each side of a particle.

7.7. Application of Correlative BF and ADF-STEM

The contrast given by BF-STEM under low-dose conditions is not sufficient to identify particle size or morphology at low magnification. For more reliable analysis, ADF-STEM should be used concurrently. However, the intensity of an ADF-STEM image alone is not sufficient for identifying crystallinity, as enhanced contrast in these images is either due to increased thickness, or crystallinity. In some circumstances when a crystalline particle was well aligned, the lattice was detected in the ADF image, however for reliable lattice imaging the bright field detector was used as well.

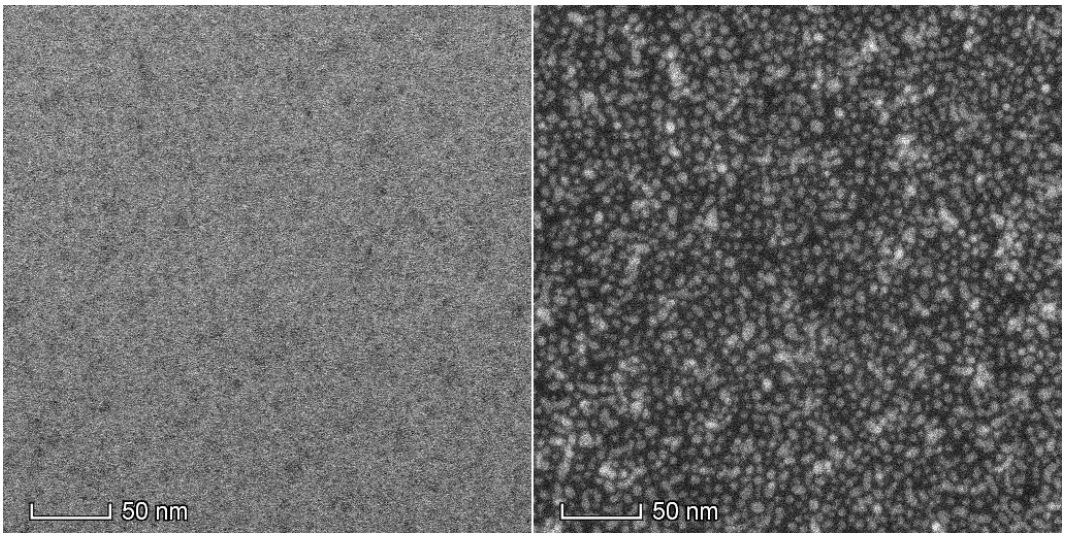

Figure 7.17 WABF and ADF-STEM image pair showing the contrast formed by each imaging method. Scan fluence = $3x10^3$ e^-nm^{-2}.

From Figure 7.17 the weak image contrast afforded by low magnification bright field imaging can be seen and with this image it is not possible to reliably ascertain particle size or dispersion. The dark field image taken of the same region shows enhanced contrast with particles clearly visible against the support film. From low magnification ADF images, differences in contrast can be seen in different particles and even inside some particles. This indicates that there are some more heavily scattering particles present, either these are thicker or are crystalline and hence diffracting.

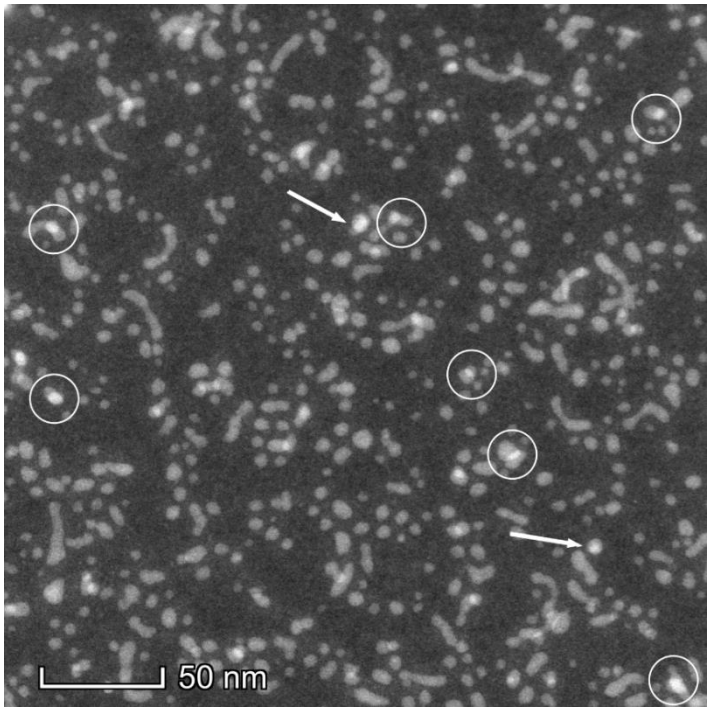

Figure 7.18 ADF-STEM image of the detergent particles showing particle superposition in the circled particles and potentially crystalline particles indicated with an arrow. Scan fluence = 2.5×10^4 $e^- nm^{-2}$.

The circled particles in Figure 7.18 show obvious superposition (particles on top of each other) and are hence thicker in localised regions as the contrast is not continuous across the particle. The particles indicated with an arrow in Figure 7.18 are less easily interpreted and would need to be investigated with high resolution imaging to ascertain their crystallinity. Due to particle superposition, ADF contrast alone cannot be used to determine crystallinity definitively, however it can be used as an indication of likely crystallinity when elevated contrast is seen across an entire particle.

When imaged by ADF-STEM, potentially crystalline particles (bright in ADF images) displayed a slightly larger particle size than the amorphous particles. Thus, under relatively low magnifications, particles likely to be crystalline could be readily observed and using this as an indicator, higher resolution imaging was then directed at these specific particles. This process is shown in Figure 7.19, where the low magnification image shows the process of identifying a potentially crystalline particle, followed by high resolution characterisation and indexing to the vaterite phase (in the case of Figure 7.19).

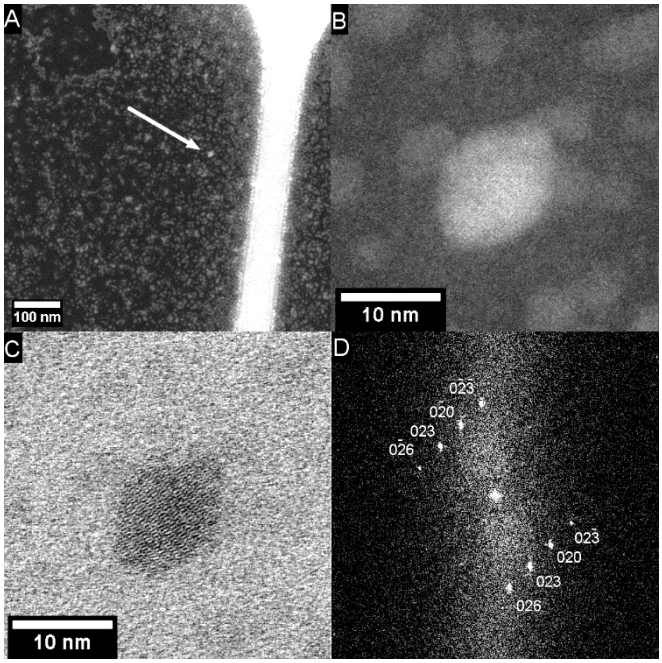

Figure 7.19 - A) Potentially crystalline particles can be visually identified from their size, morphology and enhanced diffraction contrast. B) High resolution imaging shows a larger particle that displays a different morphology to the surrounding amorphous particles. C) Simultaneously acquired BF-STEM phase contrast image provides a lattice image. D) FFT shows single crystal character and is indexed to the vaterite crystal structure viewed down the <100> zone axis. Total fluence $9x10^4$ e^-nm^{-2}. FFT image width 13 1/nm.

Throughout this study multiple crystalline particles were imaged; their crystal structures and morphologies were compared to investigate whether there was a preferential structure or morphology. It was found that all crystalline particles identified had the vaterite crystal structure, and displayed a different morphology and a larger size relative to the amorphous particles. Examples of discrete crystalline particles can be seen in Figure 7.19 and Figure 7.20, they all have a different appearance to the amorphous particles, which are smaller (~5 nm vs ~15 nm) and do not show significant scattering intensity.

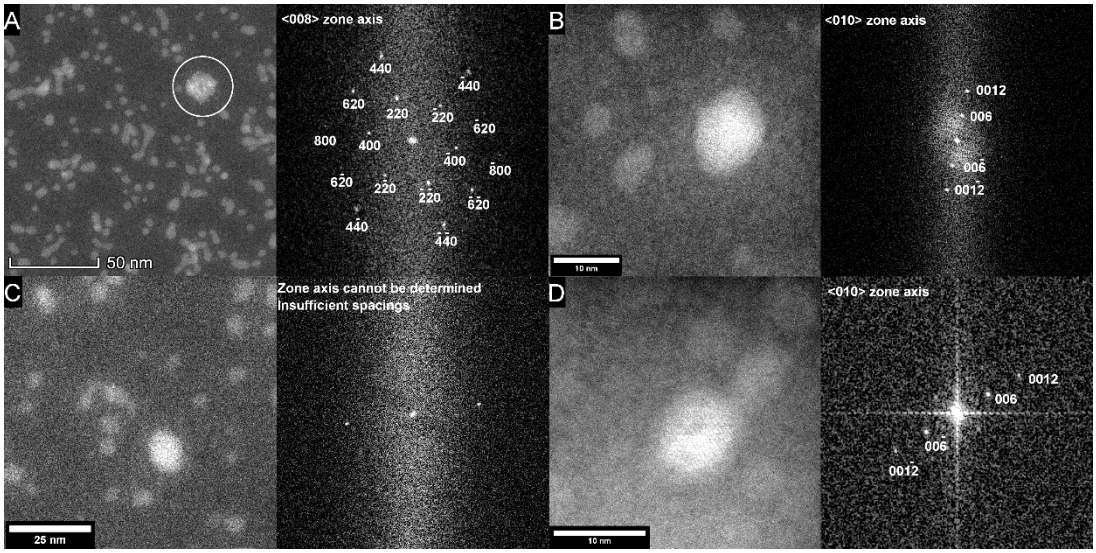

Figure 7.20 A-D) ADF-STEM images of crystalline particles with their corresponding FFTs (FFTs were calculated from the concurrent bright field STEM images) Fluences between $5x10^4$ - $9x10^4$ e^-nm^{-2}. FFT image width A) 19 1/nm, B) 26 1/nm D) 18 1/nm.

The FFTs images of the crystalline particles (~15 nm in diameter) were investigated and indexed where sufficient spots were present, the crystallinity was determined in all cases to be vaterite. Vaterite is known to form from the crystallisation of amorphous calcium carbonate as it is a metastable form with a reduced energetic stability (higher enthalpy relative to calcite) than aragonite and calcite (205).

The morphologies of the large crystalline particles appear to show some faceting, which can be seen more clearly in Figure 7.20A and C. However, the crystal habit is not well defined, due to the limited volume in which crystallisation has taken place. The local environment has been shown to affect vaterite crystal habit, including solvent viscosity, osmotic pressure and additives (19).

The larger size of crystalline particles (up to ~15 nm) may be due to multiple amorphous primary particles coalescing to form a larger particle, with nucleation and growth occurring within this larger particle. The measured lognormal particle size distribution is suggestive of coalescence (187). However, it is also possible that due to the random nature of the particle formation, that larger particles are formed without the merging of multiple

primary particles. These larger particles are more susceptible to crystallisation, due to the larger volume for nuclei to form in, and the higher chance that a nucleus can grow to reach the critical radius so as to become stable.

There are therefore several possible reasons for the presence of crystallinity in these larger particles:

- Larger particles would be subject to a lower degree of confinement (dimensional constraint) than smaller particles, and contain a larger volume of amorphous calcium carbonate. Meldrum et al (206) have demonstrated that the extent of confinement has direct impact on the progression of crystallisation, where crystallisation was supressed in heavily confined calcium carbonate systems, producing vaterite in moderately confined systems and calcite in low confinement systems. Thus, it has been shown that confinement extends the lifespan of amorphous calcium carbonate. The surfactant in the fuel detergent system is used to ensure confinement of the particles. By keeping the particle size as small as possible. The particles can then remain stable in an amorphous state for long durations as there is limited volume for nucleation to occur in.
- It is possible that the surfactant shell has been locally disrupted by processing contaminants, Stawski et al (207) have demonstrated that solvents can disrupt the surfactant shell on amorphous calcium carbonate particles and cause rapid nucleation and growth. By removing a fraction of the surfactant from the micelle, the particles are more likely to agglomerate and coalesce as the damaged surfactant shell is not able to maintain separation between impinging particles. Coalescence of particles would increase the volume and result in a higher chance of nucleation, and a larger volume for stable nuclei to grow in. The surfactant shell can be disrupted by the presence of a more polar solvent, which has previously been shown to affect the critical micelle concentration (CMC) and surface tension of a surfactant (208).

- It is possible that some particles were completely carbonated during synthesis, rather than the intended 90% carbonation, as ensuring thorough isotropic mixing in multiphase mixtures is challenging. This would remove the amorphous calcium hydroxide shell, which has been shown to induce crystallisation (51).

7.8. Partial Crystallinity

Several particles were observed which were thought to display partial crystallinity, with the possibility of a crystalline core being present, as observed by ADF-STEM imaging, in Figure 7.21. Probe corrected imaging was performed using a spherical aberration corrected 300 kV FEI Titan^3 Themis Z microscope at the Thermo Fisher Nanoport in Eindhoven. For imaging, a probe convergence semi-angle of ~20 mrad and probe size of ~70 pm were used, with a probe current of 10-20 pA. The BF collection semi-angle was 17 mrad and ADF collection semi-angles were 32-150 mrad, this gave comparable phase contrast and diffraction contrast conditions to the uncorrected STEM imaging shown previously.

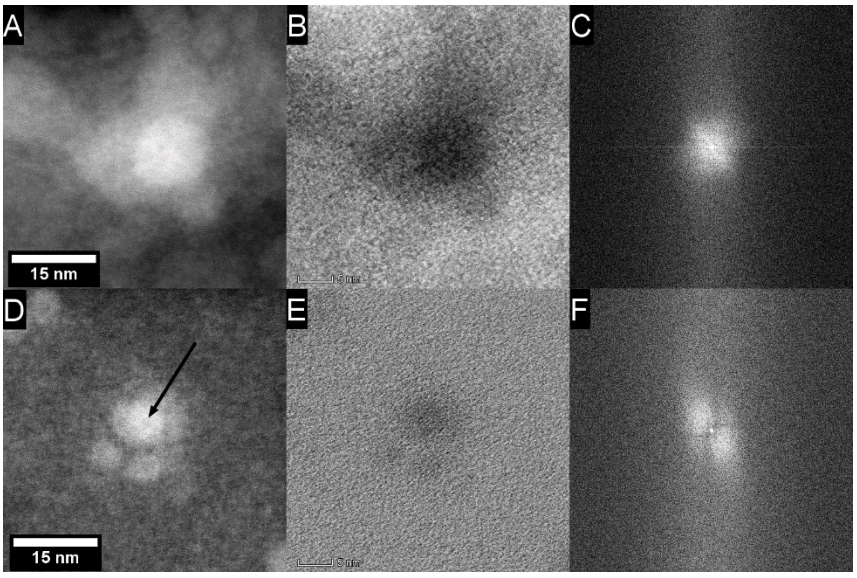

Figure 7.21 – (A+D) ADF-STEM image of particle with potential partial crystallinity in a bright core region (B+E) corresponding BF-STEM image and (C+F) FFT of bright field image. (15 nm scale bar) Fluence 9x10^4 e$^-$ nm^{-2}. FFT image width 12 1/nm.

Aberration corrected STEM imaging was used to investigate whether particles do have partial crystallinity, i.e. whether regions of individual particles can

show crystallinity independent of the rest of the particle. It was believed that the increased electron collection efficiency from a probe corrected STEM would reduce ambiguity from noisy images, and show any crystallinity more clearly if present (87).

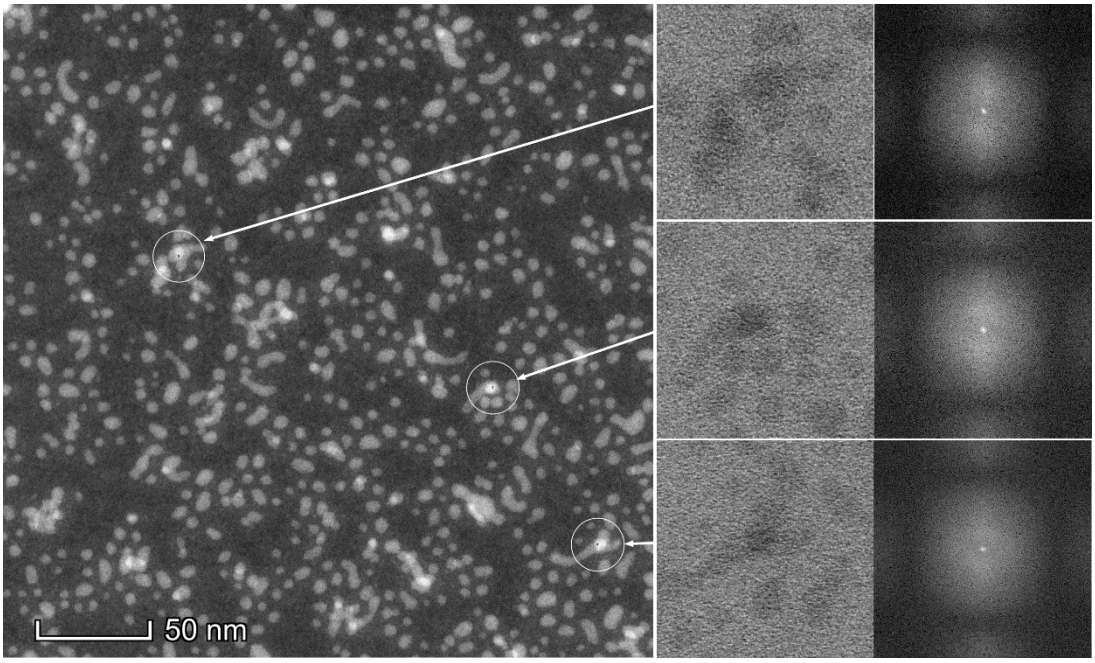

Figure 7.22 Probe corrected ADF-STEM and corresponding BF-STEM phase contrast images of particles thought to show partial crystallinity, the FFTs of the BF images do not show any crystallinity present. Scan fluence 2.5x10^{5} e^{-}nm^{-2}. FFT image width 5 1/nm.

Probe corrected imaging, shown in Figure 7.22, did not reveal any partial crystallinity present, the enhanced scattering contrast seen in parts of particles is presumably due to the thickness or superposition of particles overlapping resulting in increased scattering. If these particles were indeed crystalline, due to the many diffraction planes present in the vaterite structure and the coherence length of the electrons, it would be unlikely that the particles would be poorly aligned to avoid reaching any diffraction conditions. Thus, the particles are most likely not crystalline.

Partial crystallinity is an unlikely occurrence in particles of this size as the presence of any crystallinity would act as a heterogeneous nucleation site for crystal growth, requiring a lower free energy for stable growth than homogeneous nucleation. Once a stable nucleus has formed, the growth rate is related to supersaturation. Stawski et al (207) stated that in confined

calcium carbonate micelles the supersaturation can be high with respect to solid calcium carbonate phases, thus crystal growth in a micelle can proceed rapidly once a stable nucleus has formed. A system consisting of both amorphous and crystalline calcium carbonate would preferentially crystallise to reduce its energy. Wang et al (206) also state that the formation of a crystalline nucleus would rapidly destabilise an amorphous phase, leading to extensive crystallisation as diffusive growth occurs.

7.9. Quantification of Crystallinity

Following the detection of discrete crystallinity, and the discounting of partial crystallinity, it was decided that an attempt should be made to quantify its presence, this would give an indication of whether the difficulties in detecting crystallinity with bulk analytical techniques were due to the concentration of crystalline particles present. It would also be pertinent for future work to consider how the synthesis and storage conditions affect the incidence of discrete crystallinity, this can be achieved by developing CTEM/STEM based methods to measure the incidence of crystallinity.

Two STEM imaging strategies were used for the statistically significant quantification of crystallinity in the overbased detergent particles, these were: “random” spatial sampling and automated wide area mapping.

“Random” spatial sampling of multiple regions of the specimen was used to provide an approximate incidence of particle crystallinity. This was then compared to particles imaged using automated wide area mapping, where a 7x7 µm region of specimen was automatically imaged at a high magnification. This gives an indication of whether there was relative agreement of the incidence of crystallinity, an appreciation of the relative benefits and drawbacks of each technique, and potential directions for development of these imaging strategies for future use.

7.9.1. “Random” Spatial Sampling

In this thesis, “random” sampling was used as a baseline to compare the benefits of wide area mapping. This represents a qualitative comparison

between two different sampling strategies, “randomised” spatial sampling, and systematic sampling, each with drawbacks and benefits.

The benefits of “random” spatial sampling include:

- Large regions of the specimen could be covered rapidly, with unsuitable regions (large amounts of thick carbon support film) discarded prior to imaging.
- Bright field images could be rapidly assessed as they were acquired, allowing for “real-time” observations of crystallinity, giving an indication of the incidence of crystallinity.
- Prior to imaging, the Ronchigram can be used to rapidly focus and align, ensuring that each region is well aligned and in focus for the best chance of detecting crystallinity.
- Individual images could be rapidly screened following acquisition with multiple software packages and required relatively little storage space compared to the mapping files.

The downsides to manual “random” sampling include:

- The manual sampling approach is time consuming and involved, navigation, focussing and acquisition are all to be performed by the operator, this can lead to costly experiments.
- As the regions are chosen for sampling by a human, it cannot be considered truly random, meaning that unconscious bias is present when selecting regions to image.

The true incidence of crystallinity is not known; thus, an appropriate sampling frequency has not been developed. With further development and repeated measurements, it will be possible to produce a sampling frequency sufficient to capture a representative figure for the incidence of crystallinity.

For random sampling, ~50 non-adjoining regions within an area of ~20x20 µm were investigated with concurrent ADF and BF high resolution imaging with a pixel size of 70 pm. In each region the total number of particles in the ADF image were counted, and FFTs were taken of potentially crystalline particles

in the BF images to reveal the incidence of crystallinity. Particles deposited on the thicker regions of the carbon support film were not investigated, as they generally displayed low image contrast. The fluence received by the specimen was $2.5x10^5$ e^-nm^{-2}, with focussing carried out using the Ronchigram.

From these ~50 imaged regions, ~20,000 particles were counted and screened for crystallinity. From these 20,000 particles, 3 were found to be crystalline, as measured directly by the FFT, giving an approximate incidence of 1 crystalline particle in 7000.

7.9.2. Wide Area Mapping

Rather than match the sampling frequency to the incidence of crystallinity, which may not be spatially homogenous, a more intensive approach would be to sample all particles in a given specimen. Given enough time and image storage space, this would be possible, however the practicality of these measurements must be considered. This study took place using the Thermo-Fisher MAPS software package, which automates the operation of the microscope for specimen navigation, image collection using pre-set conditions, and image reconstruction to form a composite image. In this case, the MAPS software imaged a wide area of ~7x7 µm which was collected using low-dose ADF-STEM. Following this acquisition, the particles were counted using a threshold in FIJI, and the number of potentially crystalline particles was compared to the incidence of crystallinity extracted through random sampling.

Wide area mapping was used to increase the volume of the specimen sampled, and to investigate the prospects of introducing partial automation to the measurement of discrete crystallinity in the fuel detergent specimen. The aim of this was to increase the number of particles imaged, and reduce the unconscious bias present in operator led imaging. In this study, the mapping approach was compared to the randomised sampling, to compare the measured incidence of discrete crystallinity. Particles were determined to be potentially crystalline if; they showed enhanced scattering contrast compared to their neighbours, with contrast >20 % higher than surrounding particles as

measured by image grey levels; they were larger than the average particle size, ~15 nm compared to ~5 nm; and were not formed from obvious particle superposition, appearing as isolated single particles. All of these properties had been observed in particles known to be crystalline as measured through correlative ADF and WABF-STEM imaging, shown in section 7.7.

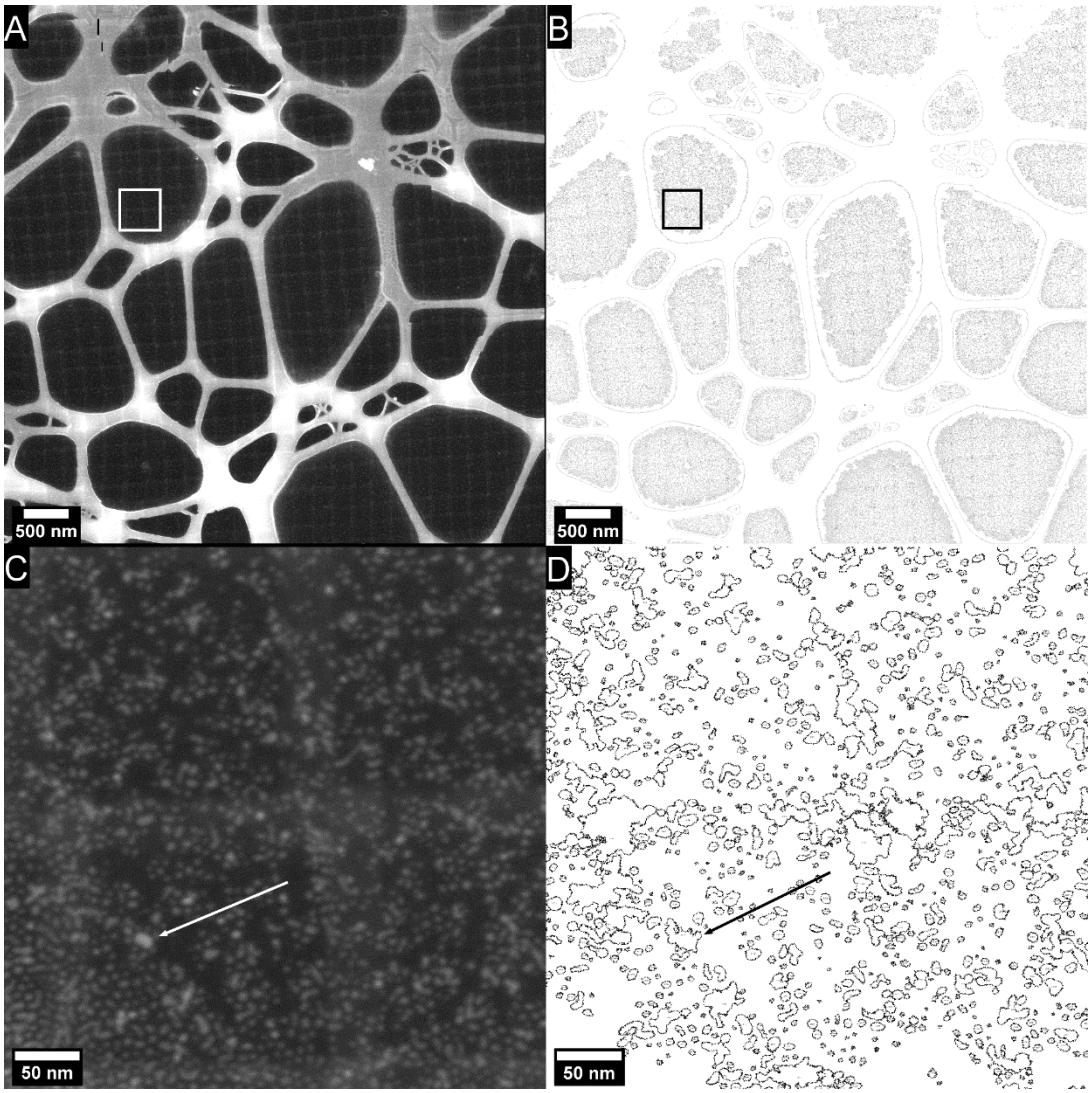

Figure 7.23 A) ADF-STEM image of the sampled 7x7 µm region, B) is image A with a threshold applied to show the locations of the counted particles with a black outline. C) is a magnified region of A corresponding to the white box in Image A, D) corresponds to Image C with the brightness threshold applied. Fluence $5x10^5$ e^-nm^{-2}.

For practical usage, the mapped region was segmented into smaller tiles, the particles were automatically counted using ImageJ/FIJI, and the number of potentially crystalline particles was manually counted. As concurrent bright field imaging was not possible, the crystallinity could not be directly measured.

Whilst this is not the same analysis method as the randomly sampled specimen, it is expected that the incidence of potentially crystalline particles would be higher than the incidence of actually crystalline particles, as it relies on subjectivity to determine likely crystallinity. For a particle to be considered potentially crystalline it should be visibly brighter than surrounding particles (~20% brighter as measured by FIJI), larger than average (typically 15 nm) and isolated i.e. not obviously overlapping adjacent particles as shown in section 7.8. Whilst subjective, these are the same criteria used when selecting regions containing particles likely to be crystalline for higher resolution studies when the microscope is manually operated (see section 7.9.1).

The main benefits of the automated image acquisition using MAPS were:

- Large regions of specimen could be imaged at high resolution without human intervention, this meant that unused instrument time including overnight, or weekend operation could be used to provide significant amounts of data which would be impractical or inefficient for manual collection, for example the 7x7 μm map required 9 hours of imaging to collect.
- As there is no human involvement on the selection of regions for high resolution imaging, bias is reduced when compared to manual non-randomised sampling. As the region mapped in this example is relatively small, the sampling frequency is also relatively small, however with sufficient time and data handling capacity more representative maps of multiple regions could be collected, increasing the sampling frequency to ensure that reliable sampling is undertaken. This would lead to a future goal of automatically imaging each particle in a specimen, in a manner similar to the single particle analysis techniques used for structural biology with cryo-TEM, this would eliminate operator bias from the sampling process.
- Whilst manual image processing is currently required, there is significant potential for automated image analysis, for example using ImageJ/FIJI scripting to use a grid of FFTs to find, extract and display the crystallographic orientation of high-resolution phase contrast CTEM

or STEM images. With further development, scripting or automation could allow for crystalline particles to be highlighted if not measured on individual images prior to map reconstruction.

There were several downsides to the wide area mapping approach used, these include:

- Current limitations of the Thermo Fisher MAPS image acquisition software meant that images could only be collected using one detector, in this case the ADF detector was used, whilst BF-STEM lattice imaging was lost, ADF imaging will show particles likely to be crystalline through their relative size and contrast compared to other particles. With further developments to the acquisition software, simultaneous multiple detector operation would provide more reliable measures of crystallinity.
- The image map produced by the mapping software was large, as such manipulating and processing these images was non-trivial i.e. the 7x7 µm map totalled 83,000 pixels per side and took up 100 Gb of storage space. In order to process this image with a standard desktop computer, it was segmented and processed in more manageable sections. Image processing would be more convenient if the sequentially acquired images were not assembled into a large map and were presented as individual images separately to the assembled map, or a substantially more powerful PC were used for image processing.
- Whilst automated mapping required significant imaging time (~15 hours), it was possible to leave the instrument unattended and collect images overnight for optimum experimental efficiency, however this left the instrument more vulnerable to hardware or software issues. The long acquisition time meant that instability in the lenses could lead to alignment drift, whilst this could easily be corrected when manually operated, this could not be done automatically.
- When the microscope was manually operated, Ronchigram focussing was used when moving between regions on the specimen, however it is not currently possible to automatically focus the microscope in this

manner between acquisitions. As these maps covered large areas, and the specimen was supported on a ~5 nm carbon film, the flexibility of the support meant that image focus varied across the map. As only the initial manual focus point and alignment is used for the entire map acquisition, image focus could not be guaranteed at significant distances from this initial point.

- The MAPS software package is commercially produced by the microscope manufacturer and is thus limited to use on their own hardware. Similar open-source software packages have been produced for automated electron microscopy and single particle analysis which are not tied to specific hardware, these include SerialEM (209) which is capable of TEM and STEM imaging, and Leginon (210) which is capable of TEM only.

The wide area mapping was able to count ~ 90,000 individual particles, of which approximately 30 were considered likely to be crystalline, giving an incidence of ~ 1 in 3000. Whilst this is a higher incidence than that extracted through random spatial sampling, it is considered to be a good match within an order of magnitude, considering the differences in sampling criteria and the relatively low number of samples taken using the manual sampling methodology.

7.9.3. Summary

Both sampling methods display different sources of experimental error, which must be considered prior to use. The random spatial sampling displays higher sampling error, as it is relies on the operator to remove conscious bias in area selection. However non-sampling errors are lower, as the data analysis is more definite, because the presence of crystallinity can be measured directly with phase contrast lattice imaging. Wide area mapping displays lower sampling errors as all particles in a chosen region are sampled. However, it displays more significant sources of error in the data analysis, as the presence of crystallinity is inferred from particle size, position and relative contrast rather than directly measured from lattice imaging.

It is assumed that the isolated crystalline particles are distributed in a homogeneous manner, however this is not known, as the distribution has not been studied. Thus, it is possible that both strategies are liable to overestimate or underestimate the incidence of crystallinity when the sampling frequency is insufficient. Whilst these imaging strategies have only been used once in this thesis due to time constraints, it demonstrates the potential applications of these techniques and allows for critical analysis of the benefits and errors inherent in each method. It is concluded that while both strategies have significant potential for development into robust quantification methods, both should use multiple repeats to produce a rigorous measurement of crystallinity and allow for quantitative analysis of crystallinity when various process conditions are changed.

When compared to the detection limits of conventional bulk analytical methods, the incidence of crystallinity identified by STEM is likely not detectable, especially when the multiple overlapping components are considered. For XRD, there is not sufficient crystalline material to show diffraction when compared to the amorphous background. FTIR would be able to detect the difference between amorphous calcium carbonate and vaterite (211), however the overlapping phase and surfactant fingerprints and low concentration of vaterite would make this highly challenging. These issues are common to XANES measurements, which is also hampered by the surface sensitivity of TEY measurements.

As the incidence of crystallinity detected was extremely low, it is unlikely that the presence of crystalline particles will significantly affect the overall product performance. However, it is possible that the long-term product stability is affected by the presence of crystalline particles, which may act as heterogeneous nucleation sites and promote the destabilisation of the formulated product through agglomeration and crystallisation.

7.10. Conclusions

Conventional bulk (particle averaging) spectroscopy and diffraction techniques suggest the overbased fuel detergent particles are amorphous as

they did not conclusively detect the presence of crystallinity. CTEM lattice imaging was able to detect the presence of vaterite crystallinity in relatively large (~15 nm) isolated particles, but imaging was limited by electron beam damage and weak image contrast, making CTEM operation challenging. Low-dose WABF and ADF-STEM imaging were also able to detect the presence of large (~15 nm) particles displaying vaterite crystallinity, two different sampling methods show this to occur in approximately 1 in 5000 particles.

ADF-STEM with WABF-STEM imaging is a dose efficient and effective characterisation method for the overbased fuel detergent particle system, and can provide specific information on particle morphology, core size, and crystallinity, neither of which can be reliably ascertained from bulk spectroscopy or diffraction methods. With these direct measurements, it will be possible to observe the influence of different processing or storage conditions on the stability and physical properties of this material system, which can be combined with measurements from bulk analytical methods to better inform industrial processing, formulation and quality control.

Chapter 8. Ex-Situ Process Monitoring Through Low-Dose Analytical Electron Microscopy

8.1. Introduction

This chapter encompasses an investigation into the solvent-induced destabilisation of the overbased calcium carbonate detergent particles characterised in the previous chapter. The aim of this study is to demonstrate the sensitivity and specificity of FTIR, DLS, XRD, SAED, and STEM imaging, with regards to characterising the solvent-induced structural variations and particle stability.

Previous scattering and spectroscopy studies have shown that polar solvents such as water, methanol and acetone affect the stability of the overbased detergents (8, 51, 212, 213). Both water and methanol are typically used in the detergent synthesis, but are removed in the final stages of the overbasing process (Chapter 4 section 4.1.4). It has been found that the addition of these two solvents as contaminants to the final products may weaken the interactions between the polar head groups of the calcium sulfonate surfactants (shown in Chapter 2 Figure 2.6) (51, 212, 213).

This chapter will show that the introduction of methanol as a contaminant results in the agglomeration and aggregation of the detergent particles over time. Ultimately leading to the crystallisation of poorly defined single crystals, whose growth was apparently facilitated by the attachment and subsequent templated crystallisation of the amorphous fuel detergent particles.

Herein, low-dose STEM imaging and electron diffraction in a FEI Titan^3 Themis were able to show the degradation of the fuel detergents within 24 hours, identifying that as they underwent agglomeration and aggregation, there is also crystallisation into vaterite. It was found that unlike electron microscopy, XRD, FTIR and DLS lacked the sensitivity required to show the early stages of the solvent-induced degradation process. This meant that the

specimen had to have significantly degraded before these techniques could detect any meaningful changes compared to an uncontaminated specimen.

The research in this chapter was carried out in collaboration with Dr Thokozile A. Kathyola (University of Leeds), who synthesised and dialysed the starting fuel detergent particles and also provided access to the FTIR spectrometer.

8.2. Methanol Contamination

Methanol is used as a solvent in the synthesis of the overbased detergent particles, it is removed from the reaction mixture through vacuum evaporation (shown in chapter 4 section 4.1.4) however, an unquantified residue of methanol may be left in the final product due to the efficiency of this separation. The impact of this impurity on the stability of the product is of interest to the manufacturers. To investigate this, a sample of dialysed fuel detergent particles suspended in hexane were dosed with ~10%vol of methanol and left to age for 5 days prior to FTIR spectroscopy and CTEM/STEM characterisation.

8.2.1. FTIR

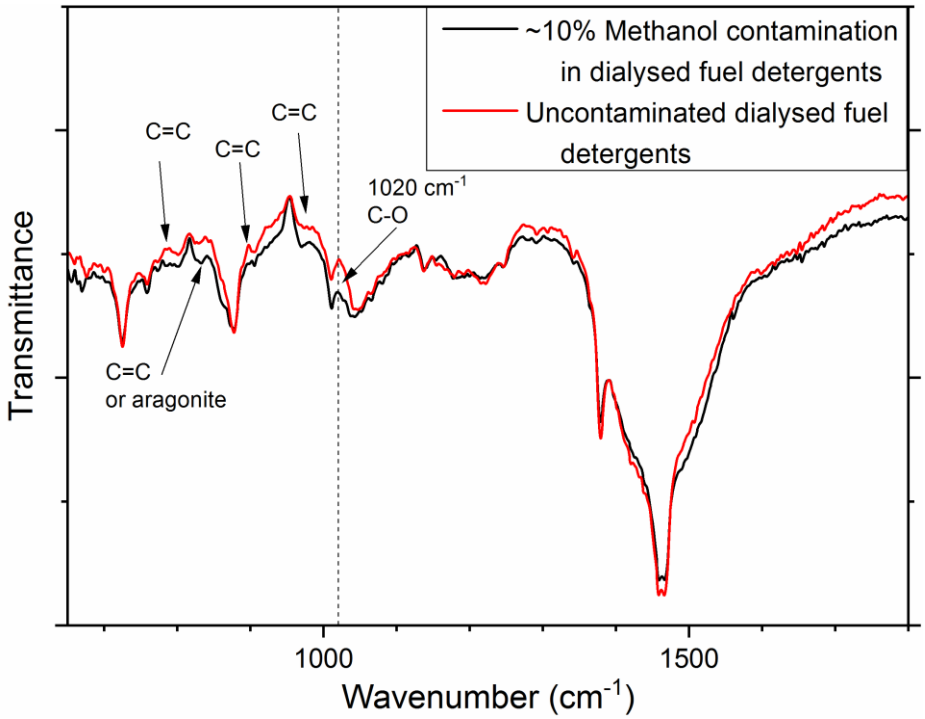

Figure 8.1 FTIR spectrum of the pure overbased detergents suspended in hexane, and detergents with a 10%vol methanol impurity suspended in hexane and aged for 5 days.

FTIR presented in Figure 8.1 shows that the addition of methanol has very subtle effects on the spectrum, with only a small reduction in transmission at 1020 cm^{-1} and a general reduction in transmittance between 800 and 1000 cm^{-1}, tentatively attributed to C=C stretches in the surfactant chain. However, the latter features may also be attributed to a noisy background in the spectrum, this would be caused by dilute specimens producing weak spectra, where the background becomes more significant. Methanol has an absorption peak in the region of 1020 cm^{-1}, and the reduced transmittance of the contaminated specimen is presumably due to the presence of methanol (214). From the FTIR alone it cannot be determined that there is a significant impact on the crystallinity or chemistry of the overbased detergent particles as there are no robustly identifiable changes to the spectrum, especially in the regions where the calcium carbonate polymorphs would appear.

8.2.2. STEM Imaging

While FTIR showed limited differences between the unmodified, and the methanol contaminated sample, the images obtained by STEM imaging showed large particles, alongside the nominally amorphous fuel detergent particles, shown in Figure 8.2.

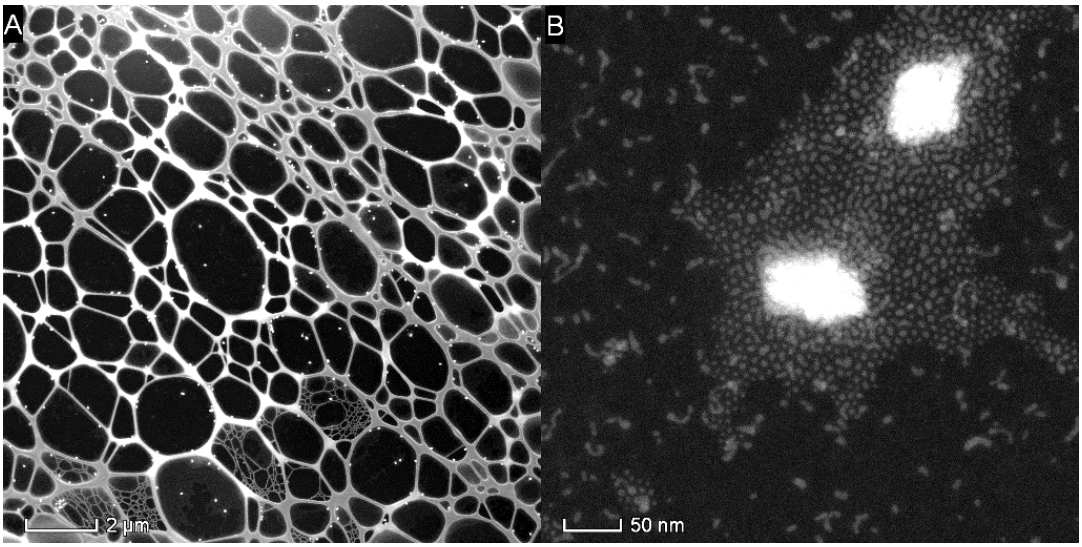

Figure 8.2 Low magnification ADF-STEM images of the methanol contaminated overbased detergent particles. A) shows the particles dispersed across the support film, B) shows the presence of both the typical overbased detergent particles plus large potentially polycrystalline deposits. Fluence $2.5x10^3$ e^-nm^{-2}.

The specimen displayed both amorphous detergent particles, and large crystalline particles of size ~50 x 100 nm displaying a roughly diamond-like morphology, with possible polycrystallinity (Figure 8.2B). The amorphous primary particle size of ~5 nm was found to be unaffected by methanol contamination.

8.2.3. EDX Spectroscopy

EDX spectroscopy and mapping performed in the FEI Titan^3 Themis at 300 kV was used to investigate the composition of the large particles, and to determine whether these particles were associated with any external contaminants deposited by the methanol solvent or otherwise.

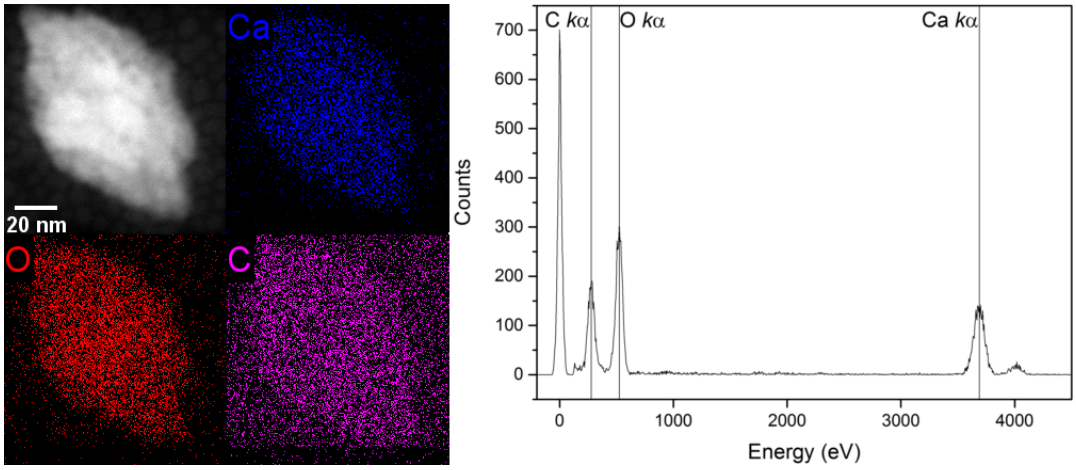

Figure 8.3 EDX map and spectrum from a large particle, showing the presence of calcium, carbon and oxygen. Fluence not quantified.

EDX mapping and the associated spectrum in Figure 8.3, shows that only calcium, carbon and oxygen are present in these particles, indicating that they are not contaminants deposited from the methanol solvent, and that they are likely formed from the crystallisation of the over-based detergent particles.

EDX spectroscopy did not show a significant sulfur presence, possibly this particle had only a monolayer of surfactant surrounding it, giving a weak signal. Some intensity is seen around the sulfur K_α region at 2300 eV, but this is not of significance when considering the background.

8.2.4. High Resolution STEM Imaging

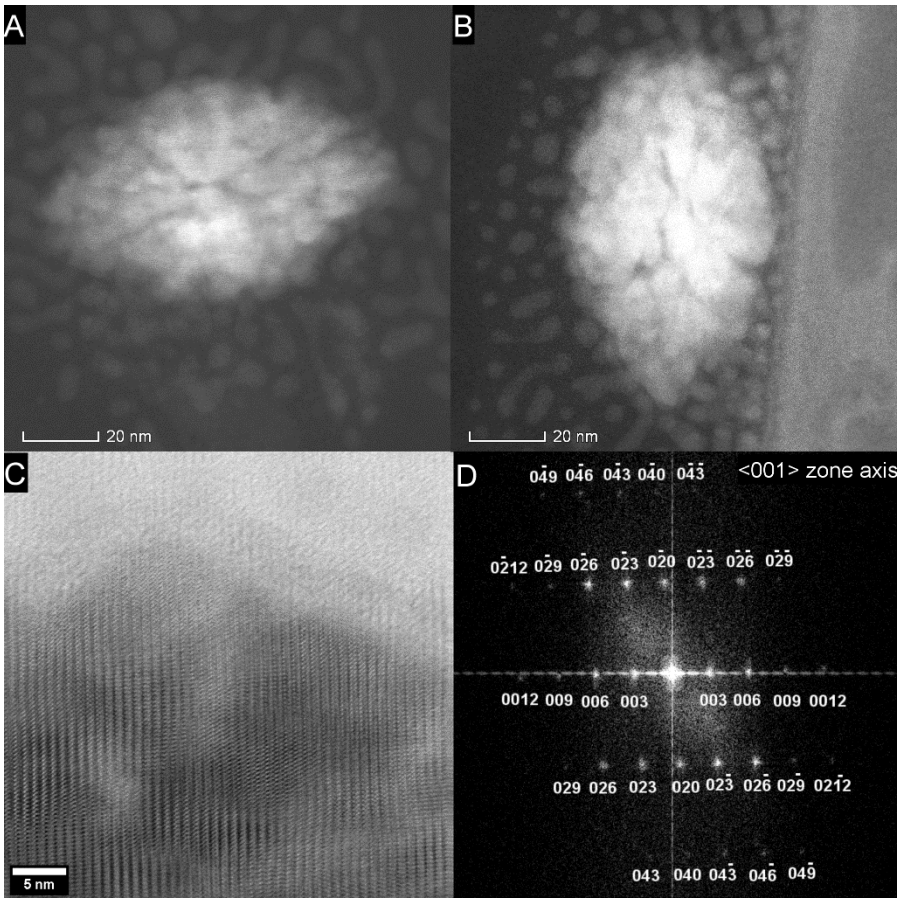

Figure 8.4 High resolution images of observed particles A+B) ADF-STEM, C) WABF-STEM image (contrast enhanced by superimposing a Fourier filtered image using the crystalline diffraction spots, D) FFT of (unprocessed) image C showing a single crystal pattern consistent with vaterite. Fluence A+B) 2.3×10^4 C) 4×10^6 $e^- nm^{-2}$. FFT image width 13 1/nm.

The high-resolution STEM imaging in Figure 8.4 shows crystalline particles. The ADF images suggests a polycrystalline particle growing from a central point, however the WABF image shows a clear lattice with continuity across the entire particle. The lattice continuity implies a single crystal, as is supported by the FFT, however the appearance of the particle does not. The crystallinity shown by the FFT indicated the presence of vaterite, which is consistent with the discrete crystallinity previously observed in section 7.6.

8.2.5. Selected Area Electron Diffraction

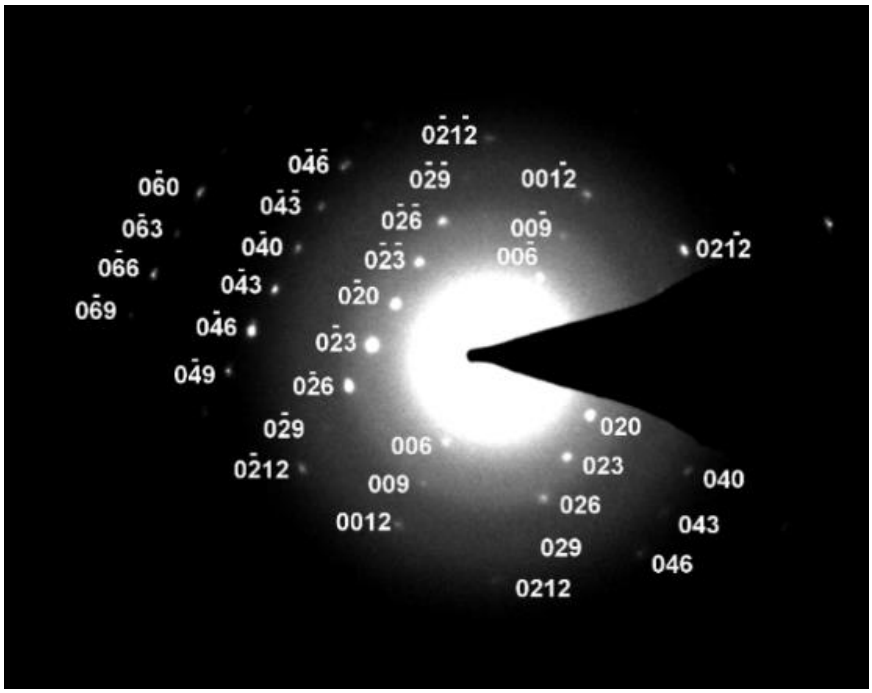

Figure 8.5 Diffraction pattern of crystalline particle, aligned along the vaterite <100> zone axis. Fluence not quantified. SADP image width 26 1/nm.

The electron diffraction pattern in Figure 8.5 correlates with the STEM imaging presented in Figure 8.4. Whilst the particles appear polycrystalline with a nodular structure, they produce a single crystal diffraction pattern consistent with the vaterite crystal structure. It is unknown whether the particles nodular appearance is due to oriented attachment of crystalline primary particles (mesocrystallinity) or due to a single crystal particle with attached amorphous particles. Electron diffraction may not be able to determine between the two proposed structures as the base crystal in Figure 8.6A would display a single crystal diffraction pattern and the amorphous particles would only contribute an amorphous background to the diffraction pattern. However the amorphous particles would contribute to the mottled appearance seen in the image. In Figure 8.6B, each small crystal would display a single crystal diffraction pattern, as the particles are crystallographically aligned the diffraction patterns would overlap and superimpose, appearing to form a single crystal diffraction pattern.

It would be possible to determine between the proposed strucutres if some of the mesocrystals were out of alignment, as this would manifest as streaking of the spots in the diffraction pattern consistent with misorientation.

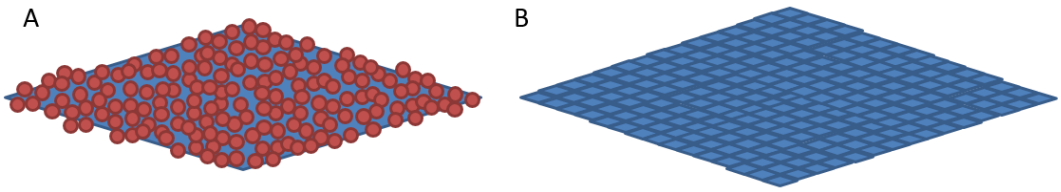

Figure 8.6 Schematic representations of A) Single crystalline particle with attached amorphous particles, B) mesocrystal consisting of crystallographically aligned crystalline primary particles. Red circles correspond to amorphous particles, blue polygons corresponds to crystalline particles.

8.2.6. Summary

FTIR spectra showed only subtle changes when the fuel detergent particles were contaminated with methanol, whereas STEM imaging demonstrated extensive crystallisation. Thus, FTIR spectroscopy did not have the sensitivity required to monitor product quality.

From the STEM images presented, the addition of ~2% by volume of methanol had a significant impact on the crystallinity of the overbased detergent particles. The images presented showed that they likely degraded through an agglomeration and aggregation process which led to crystallisation, as the particle morphology suggests the attachment of amorphous particles to a crystalline seed (seen in Figure 8.2B).

The presence of a high density of amorphous overbased detergent particles surrounding the large crystalline particles suggests that crystallisation may be occurring following agglomeration of the amorphous particles. This was noticed by Nielsen et al (215), where a crystalline calcium carbonate particle grew from the attachment of amorphous particles, which then crystallised using the crystalline particle as a seed.

The polycrystalline appearance of these particles may be related to the phenomenon of mesocrystallinity, where multiple single crystalline particles

aligned crystallographically (216, 217). From this they appear to display one single crystal diffraction pattern, despite being a polycrystalline particle. Mesocrystallinity has been postulated as a formation mechanism for biominerals, and organic additives have been shown to aid in orientation of particles, however there is significant debate around this topic (48, 216-219).

There are several possible mechanisms for the solvent-induced degradation of these particles:

- Roman et al (51) noted methanol to be a co-surfactant during particle synthesis, with the methanol molecules located near the interface between the surfactant head group and the carbonate core. The methanol molecules may intercalate between the surfactant tails, this would reduce the surfactant packing density (220). Reducing the surfactant packing density would affect the stability of the particles as the surfactant tails would not be able to repel other particles as well as a densely packed surfactant.
- Jao and Kreuz (221) stated that sulfonate micelles have rigid high tension interfaces, and the addition of methanol reduces the interfacial tension, presumably through the same process as noted by Roman et al (51). This would facilitate dynamic exchange, where species in micelles in close contact can diffuse between micelles, meaning that particles can grow through diffusion. This is unlikely, as the primary particle size was not seen to increase with methanol addition, however this could be investigated further using time-resolved dynamic light scattering and STEM imaging.
- Sun et al (213) investigated the effects of solvent polarity on the size of aggregates consisting of sulfonate surfactant stabilised particles. They found that the interaction between the head groups of the surfactant controlled the size of the micelle and the aggregation, and that introducing polar solvents reduced this interaction. As a consequence, they determined that if the interactions were weakened, then the micellar size would decrease, however the diameters of the micelles used in their study was of the

order of 220 nm, with a reduction of ~10%. It was determined that this effect was intensified by using more polar solvents, with the alcohol (1-heptanol in this case) having the largest impact. For the fuel detergent particles in this study, the particle size was not seen to change significantly, however a reduction in diameter of 10% would only correspond to a change of ~0.5 nm which may not be significant in DLS or imaging-based particle size measurements.

- Tavacoli et al (212) demonstrate that when water is added to a solution containing sulfonate stabilised particles, the water hydrogen bonds to the sulfonate head group. This weakens the interactions between the polar heads of the sulfonate and increases the spatial separation of the head groups, weakening the surfactant interaction with the core and thus reducing the steric separation of the particles. Presumably methanol can act in a similar manner.
- It is possible that addition of methanol may cause a fraction of the surfactant to leave the particle surface and preferentially stabilise the methanol. This would reduce the packing density of the surfactant and affect the steric separation, or encourage dynamic exchange.

From these postulated mechanisms, it is clear that methanol has a significant effect on the surfactant which stabilises the fuel detergent particles. For a more detailed understanding of the degradation process, time-resolved measurements must be taken. This will provide insights on the nanoscale phenomena occurring after methanol addition, which when coupled with bulk spectroscopy will inform on any chemical and structural changes occurring. Time-resolved measurements using both STEM imaging and bulk methods (FTIR, XRD and DLS) will also allow for technique sensitivity to be compared, for example if significant changes are seen in STEM imaging prior to detectable changes in XRD, FTIR or DLS then it raises the case for STEM to be considered as a tool for quality assurance and process analytics.

8.3. Time-resolved Measurements of Controlled Methanol Impurity Addition

Time-resolved observations provided information on the methanol induced (~2% by volume) degradation process, enabling understanding of how the amorphous particles degrade.

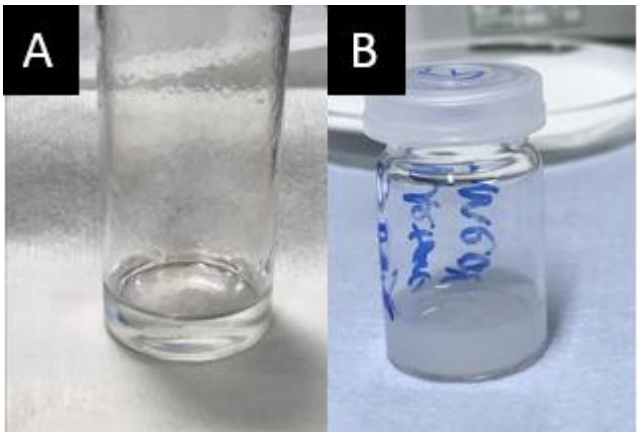

Figure 8.7 Fuel detergent particles suspended in hexane, A) prior to 2 vol% methanol addition, B) following 28 days of exposure to 2 vol% methanol.

After 28 days, the original fuel detergent particles had completely destabilised, the solution containing the particles had changed from clear and colourless to a white suspension. This can be seen in Figure 8.7 which shows extensive agglomeration or aggregation has occurred. Time-resolved measurements were undertaken between 0 and 28 days of methanol exposure.

8.3.1. Bulk Analysis

Bulk analysis using DLS, XRD and FTIR provided rapid complementary information to that provided by STEM imaging, however bulk techniques are not typically as sensitive or specific, as discussed in Chapter 7. Studying the degradation process of the overbased detergent particles provides an opportunity to compare the practical applicability of bulk analysis i.e. at what point are these techniques able to detect specimen degradation when compared to STEM imaging.

Dynamic Light Scattering

Dynamic Light Scattering gives an insight into the aggregation behaviour of the detergent particles when contaminated with methanol. Scattering intensity plots in Figure 8.8 show significant agglomeration present even in the stock uncontaminated sample, however with increasing time exposed to methanol, the size of these agglomerates is seen to increase. For example, between the 1- and 2-day samples, the agglomerate size increases from ~100 nm to ~300 nm and is approaching 1 µm after 10 days. This indicates that the methanol is inducing the agglomeration of the primary particles, though some agglomerates were present without additional contaminants.

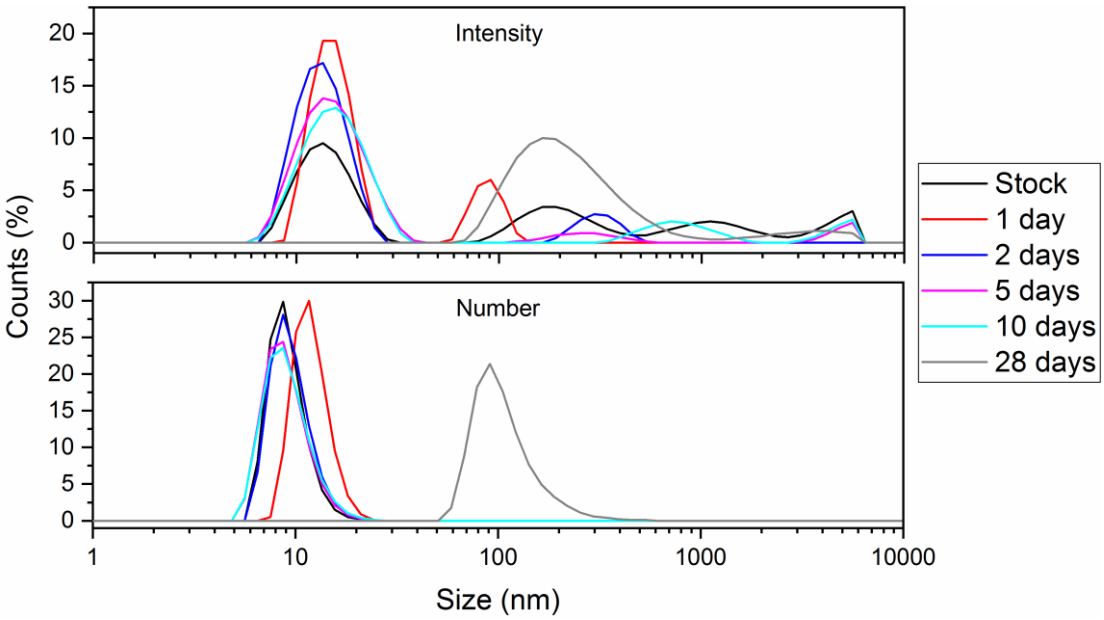

Figure 8.8 Intensity and number particle size measurements of stock and methanol contaminated specimens using DLS with particles dispersed in hexane.

The DLS intensity and number plots in Figure 8.8 show that the primary particle size remains centred around 10 nm for all time points except the 28-day aged specimen. The Intensity plot also shows the presence of agglomeration or aggregation giving 50-1000 nm clusters at all time points, though this is a low occurrence, as it is not reflected in the number plot, except at 28 days. The number plot shows that the primary particle size is generally unaffected by the presence of methanol.

A significant difference can be seen in the 28-day aged specimen in both the intensity and number plots. The 28-day specimen shows no 10 nm primary particles present, instead showing clusters of 50-200 nm dominating scattering. This suggests that the specimen has become significantly destabilised and that no un-aggregated, primary particles are detectable.

Whilst DLS allows for investigation of particle sizing and aggregation behaviour, it does not provide information on what form the particles have degraded into, whether they be amorphous or polycrystalline aggregates or single crystalline particles. As such DLS must be combined with chemical and structural analysis to form a more complete understanding of this process.

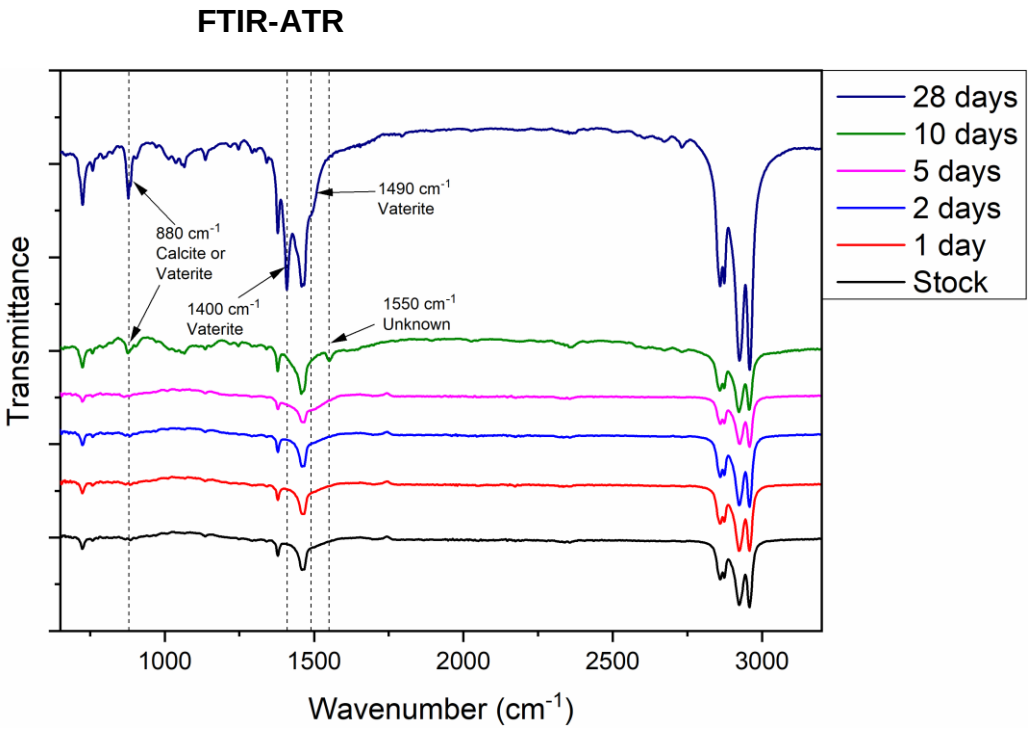

Figure 8.9 FTIR-ATR spectra of the fuel detergent particles at all time points, all measurements taken with the dialysed particles suspended in hexane.

The FTIR spectra, collected following methods previously outlined in section 4.2.4, are shown in Figure 8.9 and show little difference between the stock solution and the 5 day aged specimen, indicating no change is detected by FTIR. The specimens aged for 10 days and 28 days show an absorption band at ~880 cm^{-1} which cannot be specifically assigned, as calcite and vaterite

both show absorbance at this wavenumber, this indicates that some crystallinity is present though it cannot be determined. It is only after 28 days that the polymorph can be determined to be vaterite as two unique absorbance bands appear at 1400 and 1490 cm^{-1} (indicated in the spectra) that are only seen in vaterite.

In addition, a small absorption band is detected at 1550 cm^{-1} in the 10-day aged specimen, 1550 cm^{-1} tentatively corresponds to a C=C stretch in aromatic compounds. Whilst a benzene ring is present in the surfactant head group and aromatic compounds can be present in mineral oil, it is not known why this absorption feature is stronger in this individual spectrum. This feature does not correspond to calcium carbonate crystallinity, and is likely a contaminant on the spectrometer ATR crystal, or an artefact/noise in the spectrum.

No change is observed in the 2500-3000 cm^{-1} region, which is mostly attributed to the calcium sulfonate surfactant, trace mineral oil, and hexane solvent. The calcium carbonate polymorphs do not contribute in this region, and the surfactant, mineral oil or solvent are not expected to undergo chemical changes.

Ultimately, FTIR is only able to detect crystallisation after 10 days, and can only determine the polymorph after 28 days

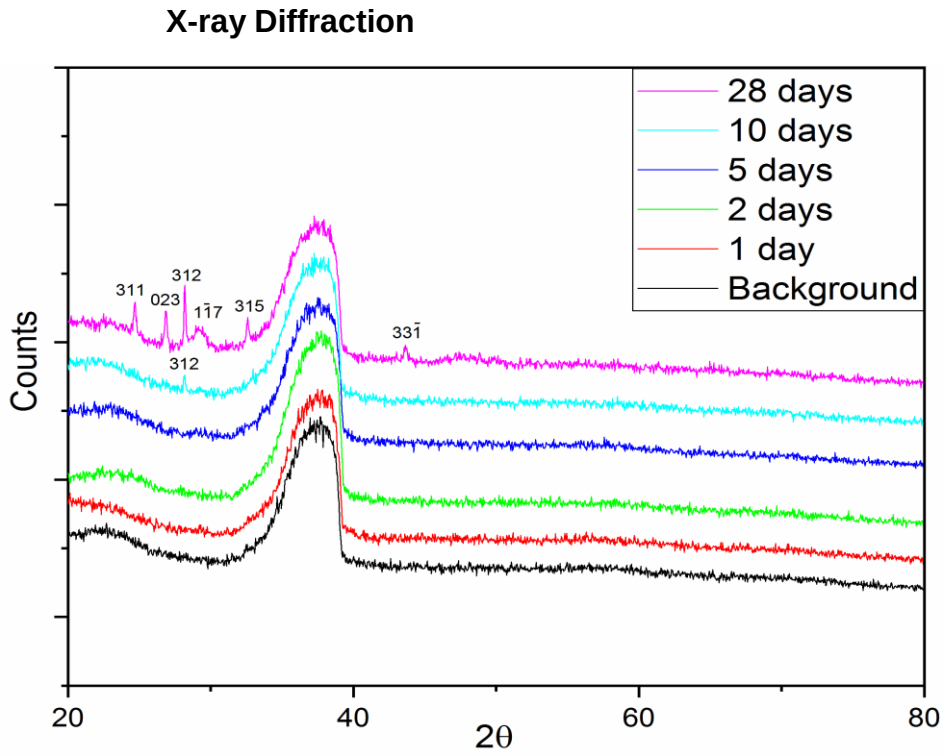

Figure 8.10 X-ray diffraction of the fuel detergent particles at all time points. Indexing was performed using the vaterite structure from Mugnaioli et al (34).

The XRD data shown in Figure 8.10 demonstrates that for methanol contaminated specimens, crystallinity is not detected up until they have aged for 10 days. For the 10-day aged specimen, crystallinity was detected, though as it is only one diffraction peak, accurate assignment is not possible.

More significant crystallinity was detected following 28 days of methanol exposure, and vaterite was clearly detected; the peak in the 10-day specimen was then attributed to be the vaterite (312) peak. The presence of vaterite is to be expected as vaterite is the first metastable structure formed from amorphous crystallisation (158). It is possible that vaterite was present prior to 10 days of aging, but the particle size and possibly volume fraction precluded X-ray diffraction identification. This is possible as low levels (1 in 5000 particles) of discrete crystallinity in the stock undamaged specimen were found to be vaterite, but was not detectable using X-ray diffraction (previously shown in section 7.3.1).

8.3.2. Summary

DLS shows that upon exposure to methanol, there was a loss of primary particles over time, with the tendency to form larger agglomerates. Primary particles were not detected in the 28-day aged specimen, and prior to this, the primary particle size was unaffected by the presence of methanol. XRD shows crystallinity was present at 10 days and 28 days, with vaterite detected in both instances. When used alongside the DLS results, it indicates that as the specimen destabilises and agglomerates, the specimen begins to crystallise from amorphous calcium carbonate into vaterite. Whilst discrete crystallinity has been found in some primary particles, it is not yet known whether these crystalline particles act as seeds for crystallisation in the agglomerates. FTIR is able to detect crystalline calcium carbonate after 10 days, however it is not able to determine between the crystalline polymorphs. After 28 days it shows vaterite characteristic absorption features at 1400 cm^{-1} and 1490 cm^{-1}.

Bulk analysis was able to determine the presence of vaterite following exposure to methanol at ~2% by volume, however it requires the specimen to be aged for 10 days to form sufficient vaterite for detection. More sensitive analysis using STEM imaging would inform on whether vaterite is present in the early stages of degradation, and on the degradation process leading up to the formation of vaterite. The specificity of STEM imaging would allow for a detailed investigation on how methanol affects individual particles, and on how they behave as a bulk system when altered by methanol.

8.3.3. STEM Imaging

Specimens which had been dialysed and diluted (as in Chapter 7) with no added contaminants, were found to undergo no destabilisation over the same or longer timescales as these aging experiments, demonstrating that the destabilisation is caused by the methanol contaminants. The characterisation of the uncontaminated particles was previously described in Chapter 7.

8.3.4. 1 Day

For a specimen aged for 1 day in the presence of methanol, significant agglomeration was seen. Loosely bound agglomerates of 50-200 nm diameter

were seen, with isolated primary particles also present. Despite this extensive agglomeration, widespread crystallinity was not observed, however discrete crystallinity in primary particles was still present. The incidence of discrete crystallinity was not quantified; however, it was not obviously different to non-contaminated specimens (i.e.1 in 5000 particles).

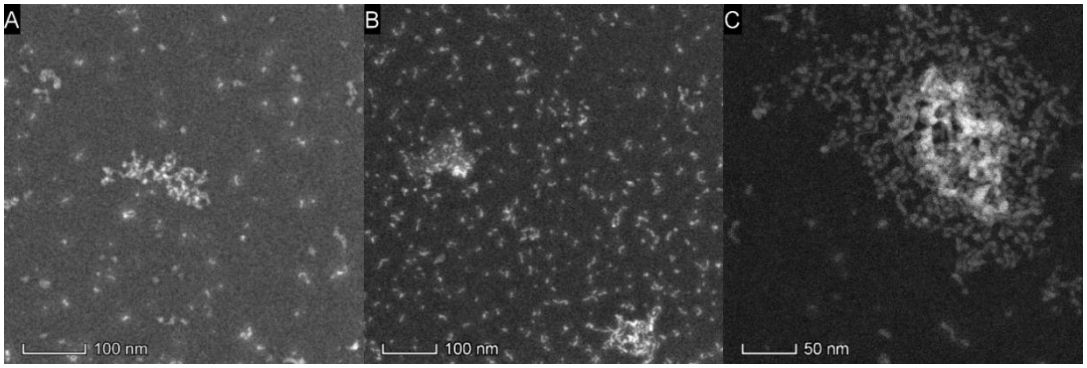

Figure 8.11 Low magnification ADF-STEM images of the detergent particles aged for 24 hours with methanol contamination, showing agglomeration. Fluence 1.5-6x10^{3} e^{-}nm^{-2}.

The images in Figure 8.11 show agglomeration present in the detergent particles, these agglomerates are approximately the same size as the crystalline particles previously imaged in Figure 8.2 and Figure 8.4. This agglomeration is likely the precursor to crystallinity, though the agglomerates pictured here were not crystalline. The agglomerates present in Figure 8.11 had not aggregated and densified, as individual primary particles can still be discerned.

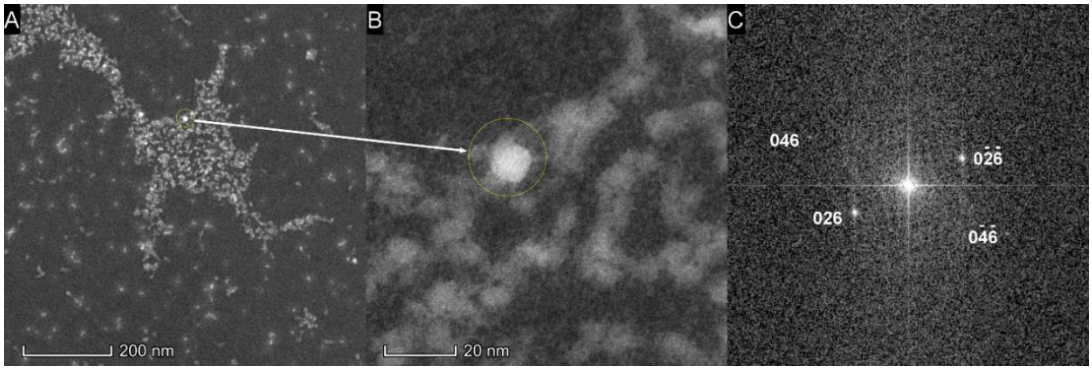

Figure 8.12 High resolution ADF images of the detergent particles aged for 24 hours with methanol contamination, showing discrete crystallinity in the circled particle. Total accumulated fluence 9x10^{4} e^{-}nm^{-2}. FFT image width 20 1/nm.

Discrete crystallinity was observed in individual particles inside some agglomerates, as pictured above in Figure 8.12B. Presumably if crystalline particles were present in agglomerates, then the crystalline particle may act as a seed crystal upon further aggregation and densification, allowing for subsequent crystal growth. However, as some agglomerates did not contain crystalline particles, homogeneous nucleation and subsequent growth from agglomerates composed of entirely amorphous particles may also be possible.

8.3.5. 2 Days

After 2 days, the loosely agglomerated particles were still present, however more densely aggregated particles were also seen, along with larger crystalline particles.

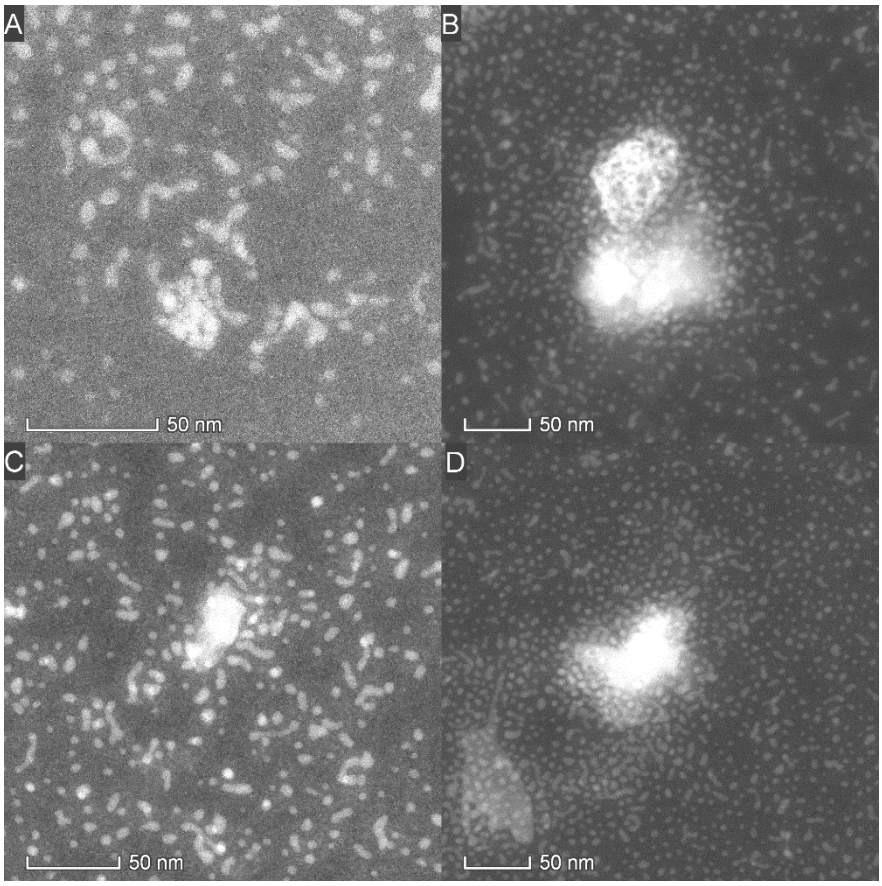

Figure 8.13 Low magnification ADF images of the detergent particles and aggregates. Total accumulated fluence of each image = 2.5×10^4 $e^- nm^{-2}$.

In Figure 8.13A-D, both aggregates and unaltered amorphous particles can be seen, these appear to be more densely compacted than the agglomerates

seen in Figure 8.11, and individual primary particles do not have well defined shapes. This would suggest that the agglomerates are growing and aggregating by consuming the smaller amorphous particles, through Ostwald ripening, driven by the reduction in surface energy.

In some cases, these aggregates were found to be crystalline, an example is shown below in Figure 8.14. Other aggregates did not display sufficient diffraction information to analyse the crystallinity properly i.e. they demonstrated spots in the FFT but could not be indexed.

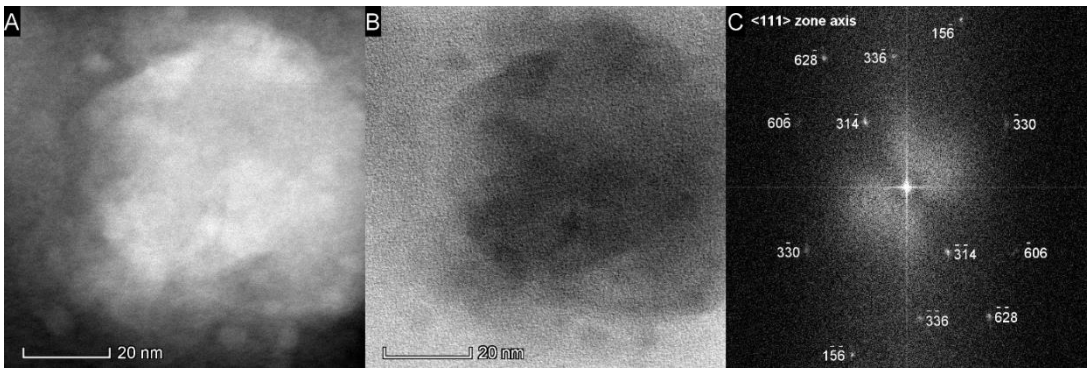

Figure 8.14 High resolution ADF and BF-STEM image of crystalline aggregate with associated FFT showing vaterite crystallinity aligned along the <111> zone axis. Total accumulated fluence = $9x10^4$ e^-nm^{-2}. FFT image width 15 1/nm.

From the images and FFT in Figure 8.14, the crystallinity of the aggregate can be seen, the FFT shows the presence of a single crystalline particle, however from the image, the particle appears to be a poorly defined aggregate without clear faceting or crystalline features. The crystallinity present is consistent with vaterite aligned along the <111> zone axis.

8.3.6. 5 Days

Following 5 days, two distinct crystalline particle morphologies were observed, flat plate-like structures and larger discrete crystalline particles. Presumably these different morphologies are formed from different crystallisation conditions, or as an intermediate morphology during the crystal growth process.

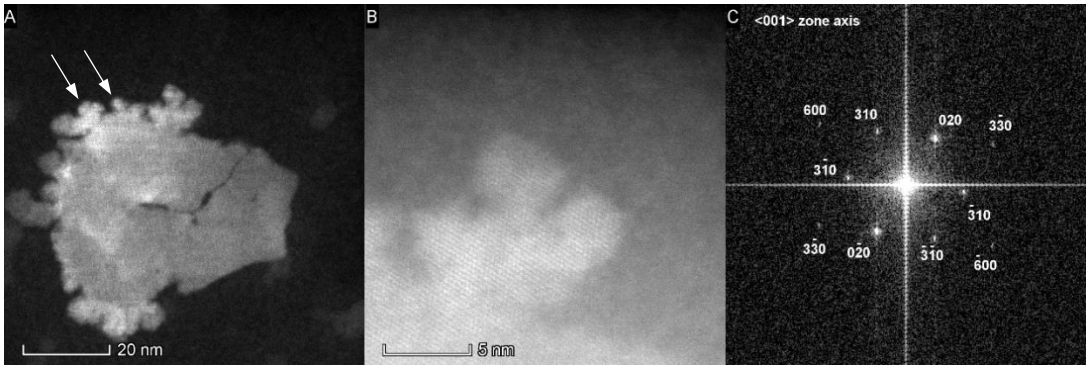

Figure 8.15 A) Low resolution ADF image, B) High resolution ADF image of the flat plate-like crystals and C) FFT of image B showing crystallinity consistent with vaterite. Total accumulated fluence A) = $9x10^4$ B) = $1.6x10^6$ e^-nm^{-2}. FFT image width 20 1/nm.

Figure 8.15 shows a flat plate-like particle which displays crystallinity consistent with vaterite as measured by the FFT. The particle appears to show multiple grains and ~3-5 nm growth nodules (indicated by arrows in Figure 8.15A) present, however the crystal lattice is seen to be continuous and aligned across the particle. The growth nodules visible in Image A and B are approximately the same size as the amorphous detergent particles ~4-5 nm. It is possible that these particles have undergone the same attachment process to the crystalline base particle as part of the growth process, as noticed by Nielsen et al (215), where amorphous particles become crystalline when they attach to the crystalline seed.

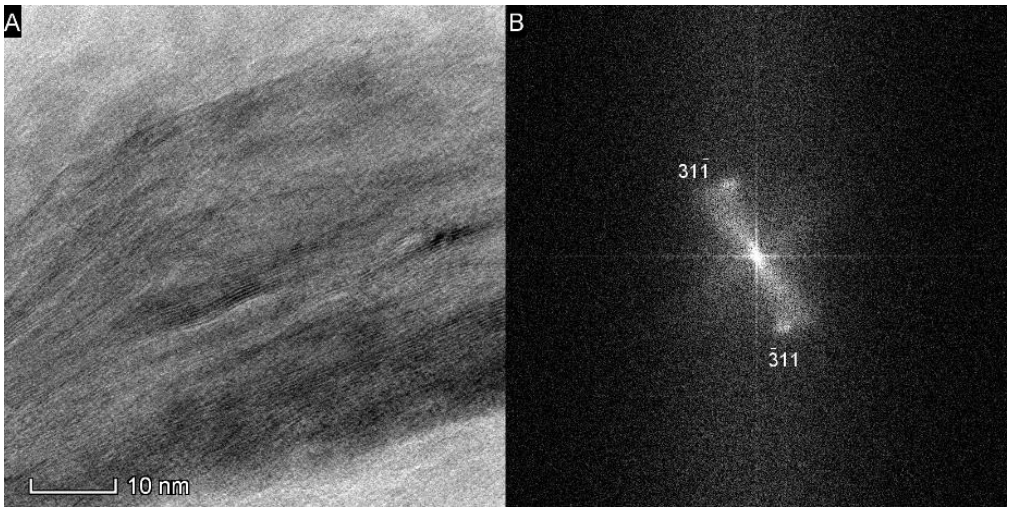

Figure 8.16 A) High resolution image of a stack of the layered particles shown in Figure 8.15 B) FFT of image A. Total accumulated fluence $1.8x10^5$ e^-nm^{-2}. FFT image width 10 1/nm.

Figure 8.16 shows what appears to be a stack of the layered particles, viewed end-on. Vaterite is known to form layered structures through spherulitic growth or as hexagonal plates, and the *d*-spacing shown is of the order of 3.7 Å which likely matches the (311) spacings of vaterite, however there is some error in the measurement due to the poor definition of the FFT spots.

Whilst it was initially thought this morphology was distinct from the flat plate-like vaterite shown in Figure 8.15, more developed layered particles were observed after longer aging times (Figure 8.22), and these displayed a similar appearance to Figure 8.16 when viewed end-on (Figure 8.24).

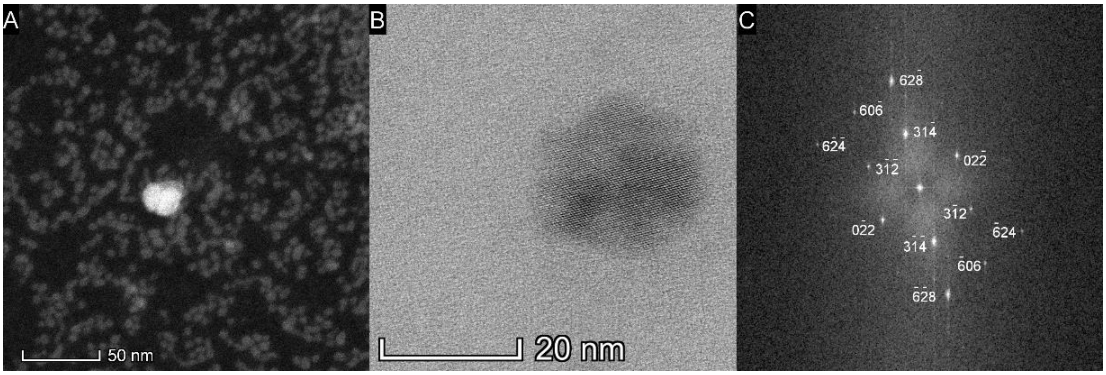

Figure 8.17 A) Low magnification ADF of discrete crystalline particles B) High resolution BF image and C) FFT of image B showing vaterite crystallinity aligned along the <111> zone axis. Total accumulated fluence $5x10^4$ e^-nm^{-2}. FFT image width 20 1/nm.

Figure 8.17 shows discrete crystalline particles with a poorly defined morphology, the particles appear nodular and potentially polycrystalline. The particle size is approximately 25 nm with the particles displaying a roughly circular morphology. The appearance of these particles is that of a densely packed aggregate, with particle interfaces seen in the bulk, however the FFT shows single crystalline character, consistent with vaterite.

8.3.7. 10 Days

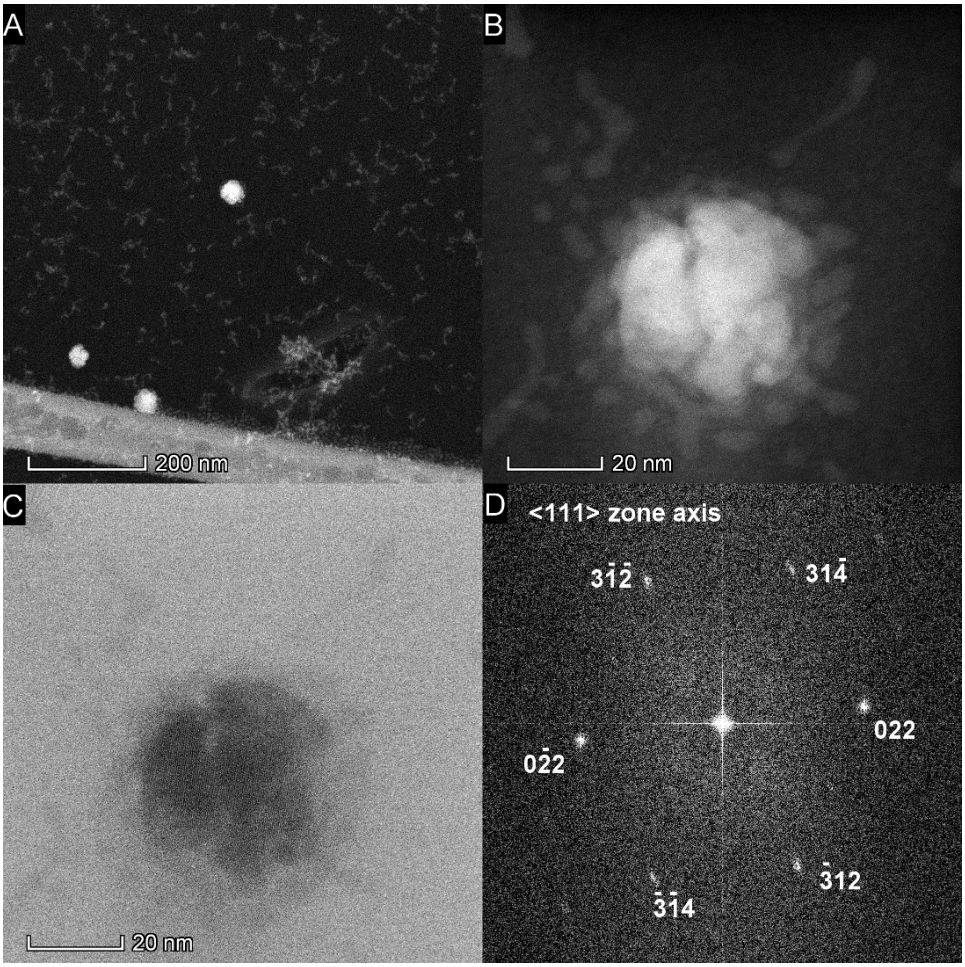

Figure 8.18 A-B) ADF-STEM images of crystalline particles C) simultaneously acquired phase contrast image D) FFT of C) showing the particle is vaterite is aligned along the <111> zone axis. Total accumulated fluence $9x10^4$ e^-nm^{-2}. FFT image width 10 1/nm.

The size of the discrete crystalline particles was seen to increase from ~25 nm after 5 days, to ~40 nm after 10 days, indicating further aggregation and growth. The crystallinity of these particles was the same with the single crystal vaterite character being unaffected by growth. The particles still display their nodular structure, especially clear in Figure 8.18 B) and C) where a continuous lattice can be seen crossing the boundaries inside the particle. In Figure 8.18B amorphous particles are seen surrounding the crystalline particle, presumably the amorphous particles adhere to the crystalline particle and then crystallise to lower the overall free energy. The amorphous particles surrounding the crystalline particle in Figure 8.18B appear to be distorted and more rod-like, it is possible that this is due to multiple particles coalescing. The weakening of

the surfactant shell by methanol disrupting the surface charge or surfactant packing efficiency would permit particles to come into contact with each other more easily, and this would permit coalescence or Ostwald ripening to occur.

The flat plate-like particles or layered structure seen in the 5-day aged specimen (Figure 8.15 and Figure 8.16) were not observed at 10 days. This is most likely due to limited sampling. It is possible they were present but due to their small quantity and sparse distribution, they were not seen.

8.3.8. 28 Days

The crystallisation of the fuel detergents into vaterite after 28 days was detected by FTIR and XRD, with DLS detecting a change in primary particle size from ~11 nm to >100 nm (shown in Figure 8.8). At this point STEM imaging was not necessary to detect the destabilisation of the fuel detergent particles, rather it was used to investigate whether there were any phenomena present that bulk measurements using FTIR, XRD and DLS could not detect.

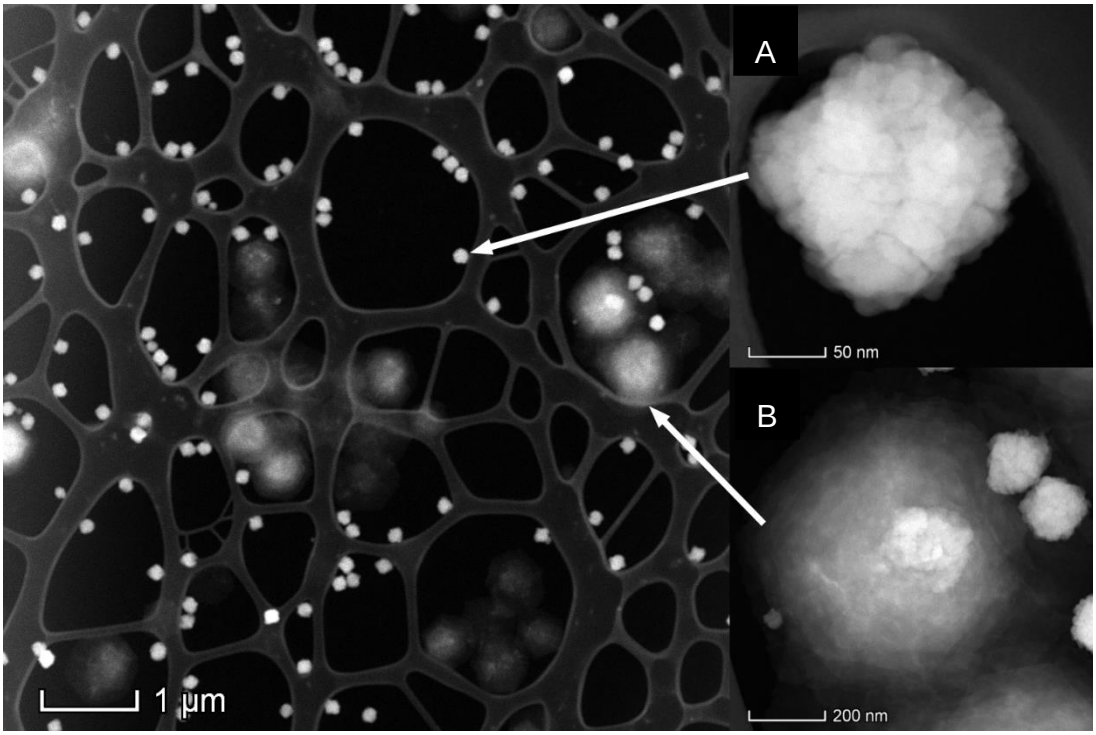

Figure 8.19 ADF-STEM image of crystalline particles formed from the overbased detergent particles, insets correspond to examples of the different particle morphologies observed. Fluence ~ $2x10^4$ e^-nm^{-2}.

From the ADF imaging in Figure 8.19, two different particle morphologies were observed. A) Near cubic particles with rough topology and nodular potentially polycrystalline appearance, with particle size of ~150 nm. B) Stacked plate-like hexagonal particles which were approximately 800 nm in diameter. The structures and compositions of these particles were examined by EDX mapping, electron diffraction, and high-resolution STEM imaging.

EDX Mapping

From the previously presented STEM images in Figure 8.19, it can be seen that there were two distinct morphologies present. Electron diffraction shown in Figure 8.21 and Figure 8.22 showed that the crystal structure of both particle morphologies is vaterite. As there are significant differences in morphology, it is likely the influence of the surfactant and changes in supersaturation during crystallisation have impacted the particle morphologies present. EDX mapping was used to show an approximate distribution of the surfactant, using the sulfur signal from the sulfonate head group, as seen in Figure 8.20.

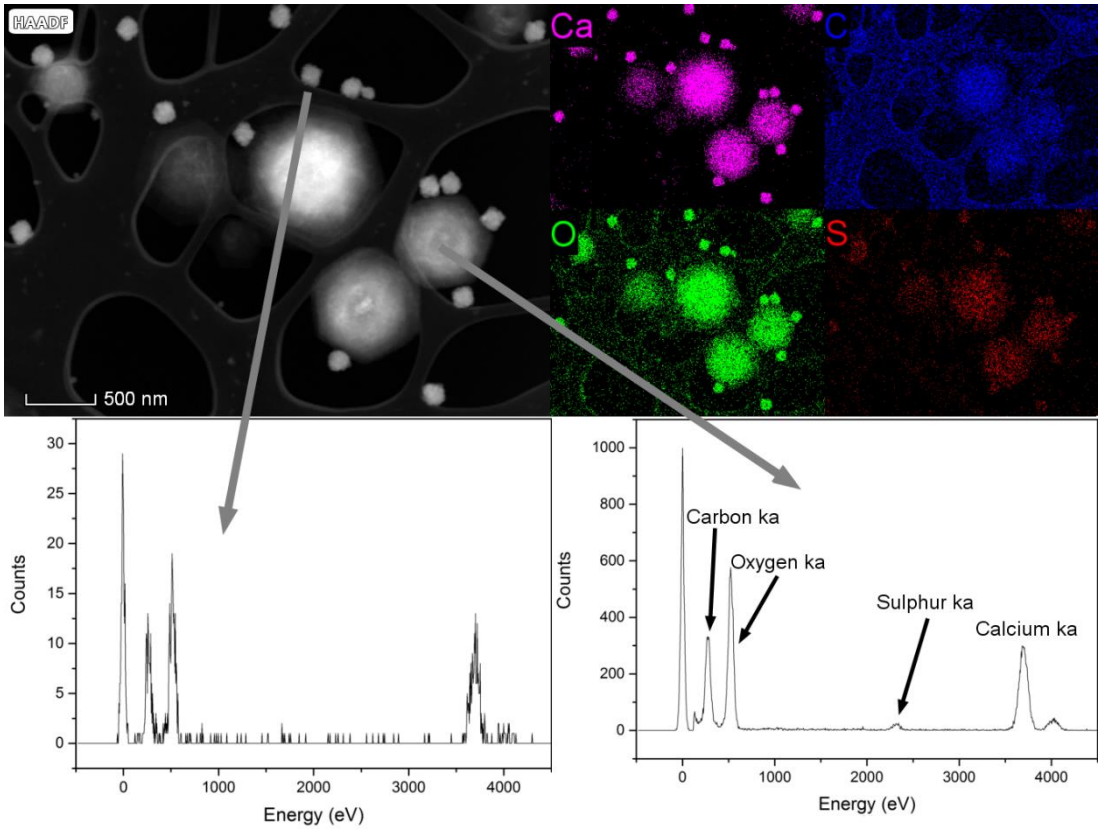

Figure 8.20 ADF-STEM image of hexagonal and cubic particles, with corresponding EDX map and spectra. The spectrum from the cubic particles was summed from the area of]5 cubic particles to improve the signal. The spectrum of the hexagonal particle was taken from one particle. Fluence not quantified.

EDX mapping and spectroscopy in Figure 8.20 showed that all particles present contained calcium, carbon and oxygen as expected. Sulfur is detected strongly in the hexagonal particles, it is likely that they have significant amounts of surfactant adhered, and that the crystallisation and growth of these particles was more strongly influenced or mediated by the surfactant.

The cubic particles did not show a significant amount of sulfur, however as they have a relatively low surface area compared to the hexagonal particles, they likely have less surfactant adhered to them, or display different growth faces with lower surface energy than the highly charged (001) face of vaterite (discussed later).

Cubic Particles

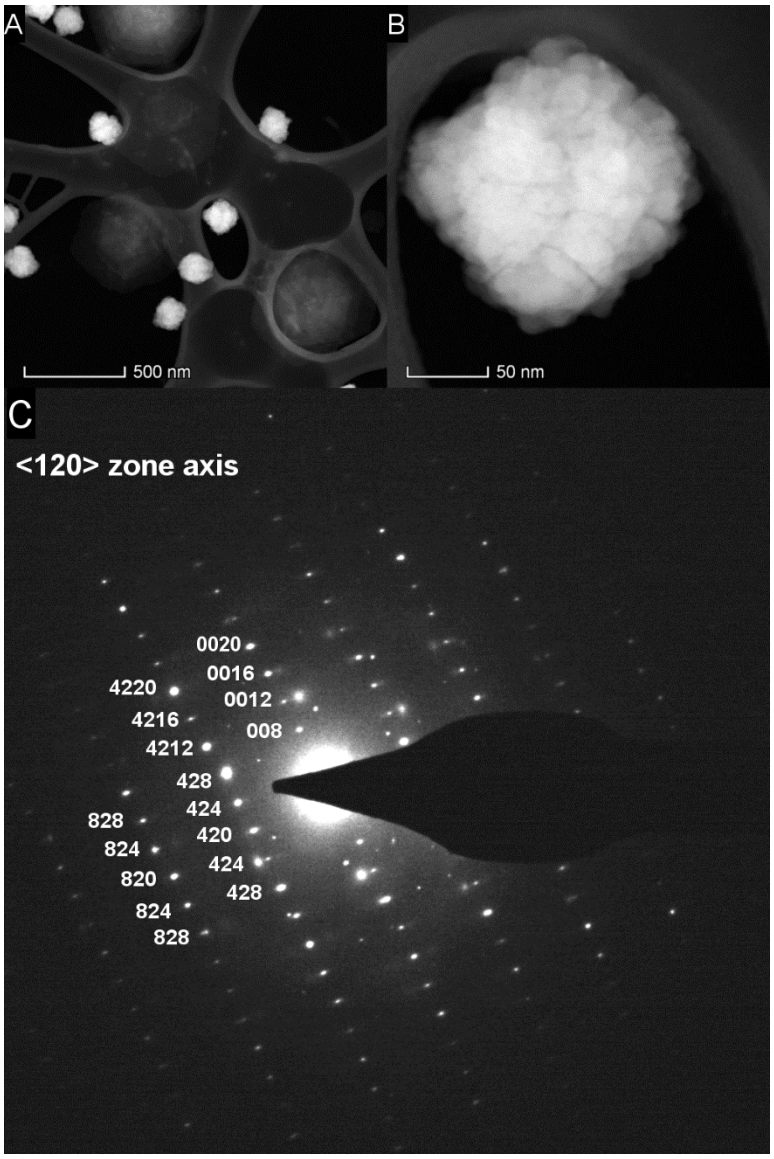

Figure 8.21 A-B) ADF STEM image of cubic particle, showing the rough topology and potential polycrystallinity. C) SADP showing single crystallinity in the particle, crystallinity corresponds to vaterite aligned along the <120> zone axis. Total accumulated fluence for ADF images = $2x10^4$ e^-nm^{-2}. SADP image width 41 1/nm.

The cubic particles displayed a single crystalline nature by electron diffraction, however the appearance is not typical of a single crystalline particle (Figure 8.21B). The particle appearance is more indicative of polycrystallinity, where multiple crystalline grains adhere together. High-resolution BF-STEM imaging (not shown) was able to demonstrate that the lattice was continuous across the particle, though from this is it not possible to determine whether it was one single lattice or multiple smaller lattices that were crystallographically aligned.

A similar morphology was observed by Ahmed et al (222) where the morphology was attributed to high reagent concentrations and rapid crystallisation. In their research, the particles were larger, however the particle appearance was similar, thus it is possible that the same process is occurring here. This is a likely explanation, as a similar morphology was observed first (after 2 days in Figure 8.14), where the concentration of amorphous calcium carbonate particles was highest. Rapid crystallisation has been known to cause occlusion of solvent and impurities, which in this case may include hexane or surfactant molecules (223).

The nodular uneven morphology may be related to the presence of occluded surfactant or solvent in the particles, which if held in internal voids may not be detected strongly via EDX due to their small volume. Organic molecules can be occluded in calcium carbonate crystals without affecting the crystal structures present, this is well known from biomineral studies (224). Kim et al (225) demonstrated the nanoscale occlusion of 13 wt% of an anionic polymer into a calcite crystal without impacting the crystallinity present. The occlusions have a similar appearance to the darker regions in the ADF-STEM image in Figure 8.21B, presumably as diffraction contrast is reduced in the less dense or less crystalline occlusions. Gries et al (226) showed that aragonite single crystals can accommodate polymer or protein filled voids without influencing the single crystal character too.

Hexagonal Particles

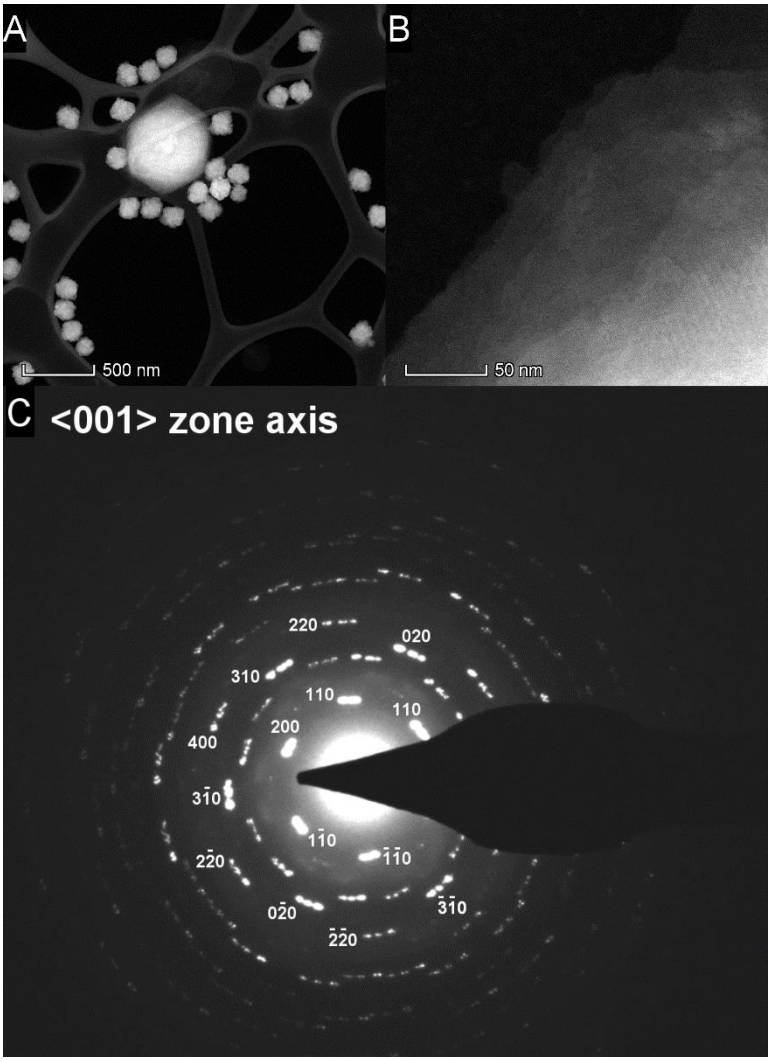

Figure 8.22 A) ADF-STEM image of hexagonal particle, B) higher magnification ADF-STEM image showing the layered structure C) SADP showing single crystallinity with angular mismatch between layers, crystallinity corresponds to vaterite aligned along the <001> zone axis. Fluence ~ $2x10^4$ e^-nm^{-2}. SADP image width 16 1/nm.

Hexagonal particles show a layered structure, with slight angular mismatch of up to 12^o between layers, as shown by the radial distribution of the spots in the diffraction pattern in Figure 8.22. The diffraction pattern confirms the hexagonal plates are oriented with the (001) basal planes perpendicular to the electron beam, thus parallel with the support film.

Hexagonal vaterite particles have been previously described by Andreassen et al (227), where they attribute the plate-like structure to polymer stabilisation of the (001) basal plane, leading to thin hexagonal particles. As the EDX

mapping shows the presence of sulfur in these particles, it is possible that the sulfonate surfactant has mediated this crystallisation by acting in the same manner. Gehrke et al (228) have previously shown that ammonium ions (NH_4^+) neutralised the highly charged (001) face of vaterite and supressed growth along this direction, resulting in flat hexagonal particles. Pouget et al (229) also observed the formation of flat hexagonal vaterite particles. Using cryo-TEM they observed that the hexagonal particles were initially polycrystalline, which then transformed into a single crystal structure templated by the ammonium ion stabilised (001) face. This was determined by diffraction measurements, where the particles displayed a hexagonal morphology prior to a single crystal character.

Huang et al (230) showed that the surfactant concentration can affect the stacking behaviour of the hexagonal plates. Low surfactant concentrations form a monomer layer on the (001) face, the hydrophobic interactions between the surfactants then force the hexagonal plates into alignment. At high surfactant concentrations (above the critical micelle concentration) the surfactant will form micelles on the surface, the micelles do not array neatly on the surface and other hexagonal vaterite particles cannot stack, instead they grow thicker as the (001) face is not stabilised or neutralised. This is demonstrated in Figure 8.23, where stacking is shown for different surfactant concentrations.

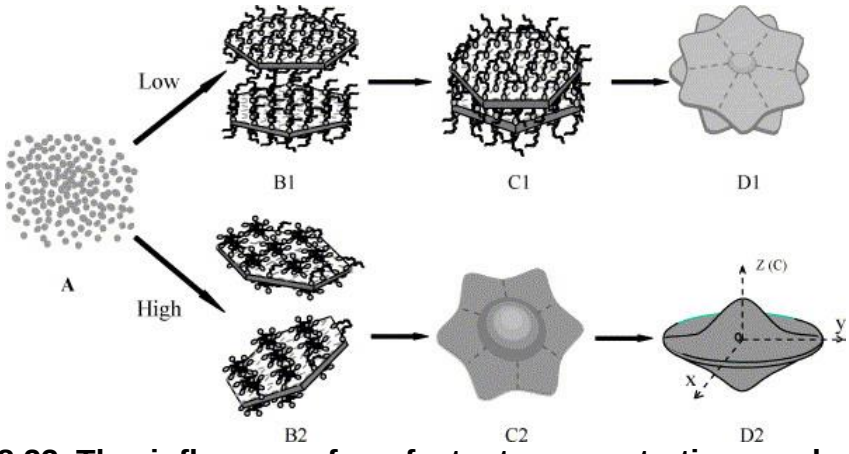

Figure 8.23 The influence of surfactant concentration on hexagonal vaterite stacking. B1-D1 low concentration, B2-D2 high concentration (230).

The stacking can be more clearly seen on hexagonal particles which are not lying with the (001) face perpendicular to the electron beam. An example is seen in Figure 8.24 where the layers have separated and the gaps between them are visible.

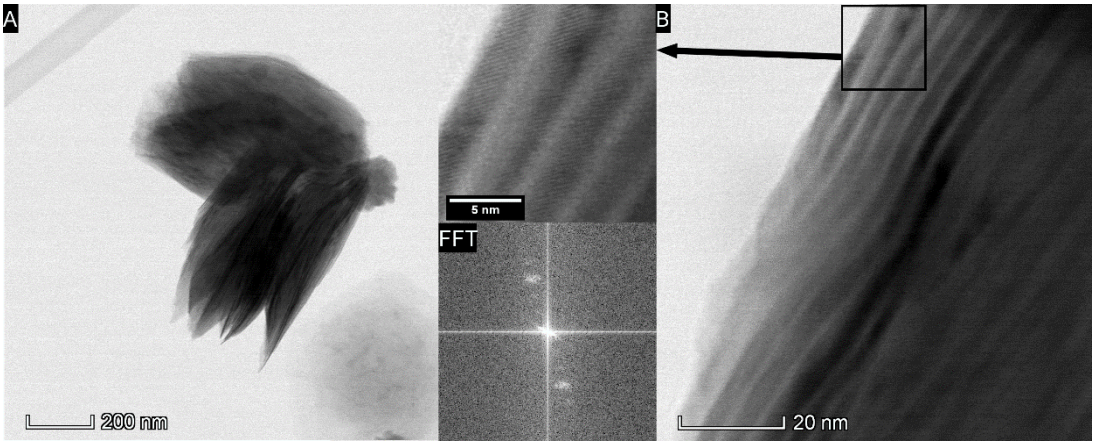

Figure 8.24 A) BF-STEM image of hexagonal particle stack B) High resolution BF-STEM image of the stack, showing layering present, Inset shows the lattice in the layers and their crystallographic alignment. FFT shows crystallinity is present. Fluence $9x10^4$ e^-nm^{-2}.

The ~3 nm separation between layers can be seen clearly in Figure 8.24B, where the dark layers are crystalline and brighter layers are likely the surfactant layers, with the plates are stacked along the (001) direction, as indicated by the electron diffraction in Figure 8.22C. A lattice can be seen in the layers (Figure 8.24 inset and FFT) which has a 3.24 Å *d*-spacing, matching the (023) plane in vaterite. This lattice is crystallographically oriented across the surfactant layers, as the FFT is taken from multiple layers but displays only one orientation.

8.3.9. Summary

The addition of polar solvents i.e. methanol as opposed to apolar hexane, have been shown to increase the polarity of the micelle interface, which may affect the surfactant packing density and thus impact the micelle stability (231). If the surfactant coating is compromised, the particle stability is reduced, the particles are not able to sterically repel each other to the same extent, which may lead to coalescence and aggregation. Coalescence was found in the primary particles, where rod-like morphologies were seen, and agglomerates then aggregates were seen to occur prior to crystallisation.

Pouget et al (229) state that crystallisation from amorphous calcium carbonate nanoparticles begins with agglomeration, leading to aggregation, and then nucleation in the larger amorphous particles. The degradation of the fuel detergent particles displays this same progression, with agglomeration (1 day) hours, aggregation (2 days) and crystallisation (2 to 5 days).

Whilst the degradation process and events leading up to the crystallisation can be easily explained, the cause of the multiple morphologies of vaterite is more challenging. Vaterite is known to produce many morphologies, including spherulites, florets, hexagons, dumbbells, and rods (19, 20, 42, 43, 158, 206, 222, 227, 229, 232). These morphologies have been demonstrated to form with or without the use of additives, and in amorphous or solution crystallisation (227).

8.4. Conclusions

Bulk analytical techniques alone were not found to be appropriate tools for the observation of the methanol induced degradation process of the fuel detergent particles. Whilst these tools are commonly used for process analysis, they lacked the sensitivity and specificity required in this case. STEM imaging and electron diffraction were able to demonstrate the destabilisation process from the atomic scale, to the single nanoparticle level, and up to the micro-scale. This makes a compelling case for STEM imaging to be considered as a tool for ex-situ process analysis and quality control.

STEM imaging has shown that the degradation of the fuel detergents when contaminated with methanol occurred by agglomeration, then aggregation and finally by templated crystallisation. This led to the destabilisation of the suspended particles and their eventual sedimentation, and has major implications on the efficacy of the formulated product. This degradation process informs the formulation and synthesis of this product to minimise methanol contamination during storage and use. This will also allow for future research into the effects of processing and storage conditions on the stability of this product and related colloidal material systems.

Chapter 9. Conclusions and Future Work

9.1. Conclusions

The overall aim of this thesis was to use transmission electron microscopy for high spatial resolution characterisation of calcium carbonate overbased fuel detergent particles. This was achieved by the observation and quantification of electron beam damage in a model system before attempting to image a more complex fuel detergent specimen with low-dose STEM.

The first aspect of this study presented in Chapter 5 involved the synthesis and characterisation of calcite nanoparticles to use as a model system. Upon 200 kV irradiation electron beam damage was found to occur in a progressive manner by radiolysis, which caused mass loss of CO_2 with outgassing, pore formation and the formation of polycrystalline CaO. Several indicators of degradation by electron beam damage were identified and then quantified with respect to incident electron flux, where it was shown that there was no fluence rate dependence of damage. The degradation of the crystalline lattice as observed by high resolution phase contrast imaging, and the reduction of O:Ca ratio measured by EDX spectroscopy were chosen to be the most useful indicators of electron beam damage in calcite nanoparticles.

Following this, in Chapter 6, the damage indicators were used to optimise the microscope operating conditions, by adjusting acceleration voltage, illumination mode and specimen cleanliness. It was found that there were no obvious benefits to operating at 80 kV rather than 300 kV, as for example, the increased peak intensity in EDX spectra was cancelled out by the reduction in specimen lifetime. Imaging in STEM was found to increase the specimen lifetime significantly from 2.7×10^7 $e^- nm^{-2}$ to over 1.8×10^8 $e^- nm^{-2}$. However, this was attributed to hydrocarbon contamination build-up supressing radiation damage, rather than there being an inherent benefit of STEM itself. This improvement was only present when hydrocarbon contamination was deposited on the specimen, there was a reduction in damage threshold to ~10^7 $e^- nm^{-2}$ for STEM imaging when the specimen was thermally cleaned of contaminants.

In Chapter 7 fuel detergent particles were characterised using the optimised microscope operating conditions. Prior to in-depth analysis the onset of electron beam damage was quantified and was found to occur at similar fluences to calcite, aragonite, and vaterite, with the amorphous calcium carbonate particles degrading to form crystalline calcium oxide. The nominally amorphous fuel detergent particles were found to have a core size of ~5 nm and display crystallinity in ~1 in 5000 particles, as measured by random sampling and automated wide-area mapping.

The final aspect of this study, in Chapter 8, was to investigate the relative sensitivity of low-dose STEM imaging compared to conventional laboratory-based techniques. This was achieved by investigating the degradation of the fuel detergent particles when a polar solvent was introduced as a contaminant. STEM imaging was able to provide information on the agglomeration, aggregation and crystallisation of the fuel detergents into vaterite prior to the benchmark laboratory analytical techniques (FTIR, XRD and DLS). This makes a compelling case for STEM imaging to be used for process monitoring and quality control in the fuel detergent synthesis.

Ultimately the outcome of this thesis is the determination that low-dose STEM is able to provide high resolution insights into the structures present in fuel detergent particles. It was necessary to use a model system to gain an appreciation of the damage processes at work and manipulate the microscope operating conditions to minimise its impact, prior to the in-depth analysis.

9.2. Summary

Transmission electron microscopy, both conventional and scanning can provide valuable insights into the structures and compositions of electron beam sensitive materials, provided that the influence of electron beam damage is considered. In this thesis, the electron beam damage of calcite nanoparticles was observed and measured in order to optimise microscope operation conditions for use on calcium carbonate-based materials. STEM imaging was found to have a higher sensitivity and specificity when detecting and quantifying discrete crystallinity in nominally amorphous calcium

carbonate fuel detergent particles. In addition, STEM imaging and electron diffraction were able to demonstrate the solvent-induced degradation of the fuel detergent specimen, with higher sensitivity than commonly used bulk analytical techniques.

9.3. Future work

Following the research undertaken in this thesis, there are several opportunities for further development, these include:

Liquid Cell or Cryogenic CTEM/STEM Characterisation of the Fuel Detergent Particles

The current specimen preparation route involved drop-casting the fuel detergent particles and drying them prior to imaging. This is not representative of the environment in which they are stored or in use. Native state analysis using a liquid cell, or near native state imaging in cryogenic conditions would provide complementary information in a more representative environment. Whilst the use of conventional liquid cell and cryogenic TEM holders present several challenges including:

- Relatively thick (~microns) silicon nitride windows or ice encapsulation reduce the image contrast and analytical signals from the large background scattering and signal absorption. Graphene encapsulated liquid cell systems are under development, and these may provide a more suitable environment for the characterisation of the fuel detergent particles.
- Radiolysis of the water or solvent carrying the particles can change the local chemistry, e.g. pH, and may also create reactive species which can reduce or oxidise materials.

If liquid cell operation could be coupled with long duration time-resolved imaging, it may be possible to observe the solvent-induced degradation process in real-time.

Application of STEM Imaging to Process Analysis of the Fuel Detergent Particles

The introduction of a methanol contaminant provided valuable insights into the solvent-induced degradation of the fuel detergent particles. However, with further time, a comprehensive study into how industrial processing conditions affect the commercial product would also be of interest. When coupled with a design of experiments approach, it could inform the manufacturers of the most significant variables in the synthesis of the particles. As STEM imaging has been shown to be sensitive down to the individual nanoparticle level, it would be pertinent to demonstrate the impact of minor processing variations on the levels of discrete crystallinity present, the particle core size and shape, and the dispersity present.

Automated Quantification of Discrete Crystallinity

Through the integration of scripted image analysis with the automated microscope control and mapping software used in this study, it would be possible to automate and quantify the incidence of discrete crystallinity in a nanoparticle specimen. The functionality to determine the presence of crystallinity in an image is currently available, however if integrated with mapping software this could provide useful process analytics with limited human involvement and subjectivity. This would make quantification by STEM imaging a more rigorous and less intensive method, which could rapidly provide information on the incidence of crystallinity, along with particle core size under low-dose conditions.

General Applications and Opportunities

From this thesis it is clear that STEM can be used for the high-resolution characterisation of calcium carbonate-based material systems. It is capable of providing valuable insights into the interaction of calcium carbonate and surfactants in an industrial setting, and displays a higher sensitivity and specificity than conventional bulk analytical techniques and spectroscopies. As such it has the potential for wider application outside of the study of fuel detergent particles, some examples of these applications are outlined below:

- There is interest in the nanoscale interactions between biopolymers and proteins with calcium carbonate in biominerals (225). Insights into local crystalline ordering or texturing would provide information on how polymers attach to crystal surfaces, or whether there are preferential orientations or facets for attachment, and how they can be manipulated to form biomimetic materials.
- If coupled with liquid cell operation, the STEM imaging conditions proposed in this thesis can be used to screen the polymorphs produced in the early stages of calcium carbonate crystallisation studies (18). Allowing for direct observations on how changing crystallisation conditions affects the crystal structure and habit formed in-situ.
- Low-dose-STEM imaging may be used to provide information on the phenomenon of mesocrystallinity, where high resolution imaging must be coupled with diffraction measurements to indicate whether a material is displaying mesocrystallinity or is a single crystal (218, 219). It may also be possible to couple imaging with elemental spectroscopy for spatially resolved chemical analysis of surfactant or polymer networks to identify how the distribution of organic additives impacts mesocrystallinity, or oriented attachment.

References

1. Meldrum, F.C. Calcium carbonate in biomineralisation and biomimetic chemistry. *International Materials Reviews.* 2003, **48**(3), pp.187-224.
2. Hudson, L.K., Eastoe, J. and Dowding, P.J. Nanotechnology in action: Overbased nanodetergents as lubricant oil additives. *Advances in Colloid and Interface Science.* 2006, **123–126**, pp.425-431.
3. Cizaire, L., Martin, J.M., Le Mogne, T. and Gresser, E. Chemical analysis of overbased calcium sulfonate detergents by coupling XPS, ToF-SIMS, XANES, and EFTEM. *Colloids and Surfaces A: Physicochemical and Engineering Aspects.* 2004, **238**(1–3), pp.151-158.
4. Crewe, A.V. A New Kind Of Scanning Microscope. *Journal de Microscopie.* 1963, **2**, pp.369-371.
5. Crewe, A.V., Wall, J. and Welter, L.M. A High-Resolution Scanning Transmission Electron Microscope. *Journal of Applied Physics.* 1968, **39**(13), pp.5861-5868.
6. Egerton, R.F., Li, P. and Malac, M. Radiation damage in the TEM and SEM. *Micron.* 2004, **35**(6), pp.399-409.
7. Egerton, R. A Modest Proposal for the Propagation of Information Concerning Radiation Damage in the TEM, and as Fodder for Pasturized Professors. *Microscopy Today.* 2013, **21**(6), pp.70-72.
8. Belle, C., Gallo, R., Jacquet, F., Hoornaert, P. and Roman, J.P. The overbasing of detergent additives: The behaviour of promoters and determination of factors controlling the overbasing reaction. *Lubrication Science.* 1992, **5**(1), pp.11-31.
9. Roman, J.P., Hoornaert, P., Faure, D., Biver, C., Jacquet, F. and Martin, J.M. Formation and Structure of Calcium Carbonate Particles in Reverse Microemulsions. *Journal of Colloid and Interface Science.* 1991, **144**(2), pp.324-339.
10. Nielsen, M.H., Lee, J.R.I., Hu, Q., Yong-Jin Han, T. and De Yoreo, J.J. Structural evolution, formation pathways and energetic controls during template-directed nucleation of CaCO3. *Faraday Discussions.* 2012, **159**(0), pp.105-121.
11. Carr, F.P., Frederick, D.K. and Staff, U.b. Calcium Carbonate. *Kirk-Othmer Encyclopedia of Chemical Technology.* 2014, pp.1-7.
12. Bartczak, Z., Argon, A.S., Cohen, R.E. and Weinberg, M. Toughness mechanism in semi-crystalline polymer blends: II. High-density polyethylene toughened with calcium carbonate filler particles. *Polymer.* 1999, **40**(9), pp.2347-2365.
13. Siesholtz, H.W. and Cohan, L.H. Calcium Carbonate Extender Pigments. *Industrial & Engineering Chemistry.* 1949, **41**(2), pp.390-395.

14. Stirnimann, T., Di Maiuta, N., Gerard, D.E., Alles, R., Huwyler, J. and Puchkov, M. Functionalized Calcium Carbonate as a Novel Pharmaceutical Excipient for the Preparation of Orally Dispersible Tablets. *Pharm Res.* 2013, **30**(7), pp.1915-1925.

15. Pavlík, V. Effect of carbonates on the corrosion rate of cement mortars in nitric acid. *Cement and Concrete Research.* 2000, **30**(3), pp.481-489.

16. Matschei, T., Lothenbach, B. and Glasser, F.P. The role of calcium carbonate in cement hydration. *Cement and Concrete Research.* 2007, **37**(4), pp.551-558.

17. Rae Cho, K., Kim, Y.-Y., Yang, P., Cai, W., Pan, H., Kulak, A.N., Lau, J.L., Kulshreshtha, P., Armes, S.P., Meldrum, F.C. and De Yoreo, J.J. Direct observation of mineral-organic composite formation reveals occlusion mechanism. *Nat Commun.* 2016, **7**.

18. Verch, A., Morrison, I.E.G., Locht, R.v.d. and Kröger, R. In situ electron microscopy studies of calcium carbonate precipitation from aqueous solution with and without organic additives. *Journal of Structural Biology.* 2013, **183**(2), pp.270-277.

19. Sims, S.D., Didymus, J.M. and Mann, S. Habit modification in synthetic crystals of aragonite and vaterite. *Journal of the Chemical Society, Chemical Communications.* 1995, (10), pp.1031-1032.

20. Wagterveld, R.M., Yu, M., Miedema, H. and Witkamp, G.J. Polymorphic change from vaterite to aragonite under influence of sulfate: The “morning star” habit. *Journal of Crystal Growth.* 2014, **387**, pp.29-35.

21. Wilbur, K.M. and Watabe, N. Experimental Studies in Calcification in Molluscs and the Alga Coccolithus Huxleyi. *Annals of the New York Academy of Sciences.* 1963, **109**(1), pp.82-112.

22. Myszka, B., Schüßler, M., Hurle, K., Demmert, B., Detsch, R., Boccaccini, A.R. and Wolf, S.E. Phase-specific bioactivity and altered Ostwald ripening pathways of calcium carbonate polymorphs in simulated body fluid. *RSC Advances.* 2019, **9**(32), pp.18232-18244.

23. Davis, B.L. and Adams, L.H. Kinetics of the calcite ⇌ aragonite transformation. *Journal of Geophysical Research (1896-1977).* 1965, **70**(2), pp.433-441.

24. Ihli, J., Wong, W.C., Noel, E.H., Kim, Y.-Y., Kulak, A.N., Christenson, H.K., Duer, M.J. and Meldrum, F.C. Dehydration and crystallization of amorphous calcium carbonate in solution and in air. *Nat Commun.* 2014, **5**.

25. Wang, J. and Becker, U. Energetics and kinetics of carbonate orientational ordering in vaterite calcium carbonate. *American Mineralogist.* 2012, **97**(8-9), pp.1427-1436.

26. Graf, D. Crystallographic tables for the rhombohedral calcites. *American Mineralogist.* 1961, **46**, p.34.

27. Valenzano, L., Torres Fernando, J., Doll, K., Pascale, F., Zicovich-Wilson Claudio, M. and Dovesi, R. *Ab Initio Study of the Vibrational Spectrum and Related Properties of Crystalline Compounds; the Case of CaCO3 Calcite*. Zeitschrift für Physikalische Chemie. 2006, 220, p.893.

28. Aquilano, D., Otálora, F., Pastero, L. and García-Ruiz, J.M. Three study cases of growth morphology in minerals: Halite, calcite and gypsum. *Progress in Crystal Growth and Characterization of Materials.* 2016, **62**(2), pp.227-251.

29. De Villiers, J.P.R. Crystal Structures of Aragonite, Strontianite, and Witherite. *American Mineralogist.* 1971, **56**(5-6), pp.758-767.

30. Zeng, M., Kim, Y.-Y., Anduix-Canto, C., Frontera, C., Laundy, D., Kapur, N., Christenson, H.K. and Meldrum, F.C. Confinement generates single-crystal aragonite rods at room temperature. *Proceedings of the National Academy of Sciences.* 2018, **115**(30), pp.7670-7675.

31. Hu, Z., Shao, M., Cai, Q., Ding, S., Zhong, C., Wei, X. and Deng, Y. Synthesis of needle-like aragonite from limestone in the presence of magnesium chloride. *Journal of Materials Processing Technology.* 2009, **209**(3), pp.1607-1611.

32. Higuchi, T., Fujimura, H., Yuyama, I., Harii, S., Agostini, S. and Oomori, T. Biotic Control of Skeletal Growth by Scleractinian Corals in Aragonite–Calcite Seas. *PLOS ONE.* 2014, **9**(3), p.e91021.

33. Christy, A.G. A Review of the Structures of Vaterite: The Impossible, the Possible, and the Likely. *Crystal Growth & Design.* 2017, **17**(6), pp.3567-3578.

34. Mugnaioli, E., Andrusenko, I., Schüler, T., Loges, N., Dinnebier, R.E., Panthöfer, M., Tremel, W. and Kolb, U. Ab Initio Structure Determination of Vaterite by Automated Electron Diffraction. *Angewandte Chemie International Edition.* 2012, **51**(28), pp.7041-7045.

35. Kabalah-Amitai, L., Mayzel, B., Kauffmann, Y., Fitch, A.N., Bloch, L., Gilbert, P.U.P.A. and Pokroy, B. Vaterite Crystals Contain Two Interspersed Crystal Structures. *Science.* 2013, **340**(6131), pp.454-457.

36. Le Bail, A., Ouhenia, S. and Chateigner, D. Microtwinning hypothesis for a more ordered vaterite model. *Powder Diffraction.* 2012, **26**(1), pp.16-21.

37. Demichelis, R., Raiteri, P., Gale, J.D. and Dovesi, R. The Multiple Structures of Vaterite. *Crystal Growth & Design.* 2013, **13**(6), pp.2247-2251.

38. Kathyola, T., Chang, S.-Y., Willneff, E., Willis, C., Cibin, G., Wilson, P., Kroner, A., Shotton, E., Dowding, P. and Schroeder, S. *In situ monitoring of the reactive crystallization of calcium carbonate in*

multiphase systems. American Chemical Society. 2018, 255. Available from: http://eprints.whiterose.ac.uk/135171/

39. Kathyola, T.A. *Solvent mediated reactive crystallisation of calcium carbonate - the effects of non-aqueous solvents on the structure of calcium sulfonate obverbased detergents*. PhD thesis, University of Leeds, 2018.

40. Gauldie, R.W., Sharma, S.K. and Volk, E. Micro-raman spectral study of vaterite and aragonite otoliths of the coho salmon, Oncorhynchus kisutch. *Comparative Biochemistry and Physiology Part A: Physiology.* 1997, **118**(3), pp.753-757.

41. Wehrmeister, U., Soldati, A.L., Jacob, D.E., Häger, T. and Hofmeister, W. Raman spectroscopy of synthetic, geological and biological vaterite: a Raman spectroscopic study. *Journal of Raman Spectroscopy.* 2010, **41**(2), pp.193-201.

42. Ismaiel Saraya, M.E.-S. and Rokbaa, H.H.A.E.-L. Formation and Stabilization of Vaterite Calcium Carbonate by Using Natural Polysaccharide. *Advances in Nanoparticles.* 2017, **06**(04), pp.158-182.

43. Trushina, D.B., Bukreeva, T.V., Kovalchuk, M.V. and Antipina, M.N. CaCO3 vaterite microparticles for biomedical and personal care applications. *Materials Science and Engineering: C.* 2014, **45**, pp.644-658.

44. Bukreeva, T.V., Marchenko, I.V., Borodina, T.N., Degtev, I.V., Sitnikov, S.L., Moiseeva, Y.V., Gulyaeva, N.V. and Kovalchuk, M.V. Calcium carbonate and titanium dioxide particles as a basis for container fabrication for brain delivery of compounds. *Doklady Physical Chemistry.* 2011, **440**(1), p.165.

45. Addadi, L., Raz, S. and Weiner, S. Taking Advantage of Disorder: Amorphous Calcium Carbonate and Its Roles in Biomineralization. *Advanced Materials.* 2003, **15**(12), pp.959-970.

46. Weiner, S., Levi-Kalisman, Y., Raz, S. and Addadi, L. Biologically formed amorphous calcium carbonate. *Connect Tissue Res.* 2003, **44 Suppl 1**, pp.214-218.

47. Sawada, K. *The mechanisms of crystallization and transformation of calcium carbonates*. Pure and Applied Chemistry. 1997, 69, p.921.

48. Jacob, D.E., Wirth, R., Soldati, A.L., Wehrmeister, U. and Schreiber, A. Amorphous calcium carbonate in the shells of adult Unionoida. *Journal of Structural Biology.* 2011, **173**(2), pp.241-249.

49. Pouget, E.M., Bomans, P.H.H., Goos, J.A.C.M., Frederik, P.M., de With, G. and Sommerdijk, N.A.J.M. The Initial Stages of Template-Controlled CaCO3 Formation Revealed by Cryo-TEM. *Science.* 2009, **323**(5920), pp.1455-1458.

50. Marković, I., Ottewill, R.H., Cebula, D.J., Field, I. and Marsh, J.F. Small angle neutron scattering studies on non-aqueous dispersions of calcium carbonate. *Colloid and Polymer Science.* 1984, **262**(8), pp.648-656.

51. Roman, J.-P., Hoornaert, P., Faure, D., Biver, C., Jacquet, F. and Martin, J.-M. Formation and structure of carbonate particles in reverse microemulsions. *Journal of Colloid and Interface Science.* 1991, **144**(2), pp.324-339.

52. Lynch, C.S. *Suspending colloidal calcium carbonate in hydrocarbon oils*. Google Patents. 1966. Available from: https://www.google.com/patents/US3242078

53. Rolfes, A. and Jaynes, S. *Process for making overbased calcium sulfonate detergents using calcium oxide and a less than stoichiometric amount of water*. 2001.

54. Mansot, J.L., Hallouis, M. and Martin, J.M. Colloidal antiwear additives 1. Structural study of overbased calcium alkylbenzene sulfonate micelles. *Colloids and Surfaces A: Physicochemical and Engineering Aspects.* 1993, **71**(2), pp.123-134.

55. Egerton, R.F., McLeod, R., Wang, F. and Malac, M. Basic questions related to electron-induced sputtering in the TEM. *Ultramicroscopy.* 2010, **110**(8), pp.991-997.

56. Hobbs, L.W. Radiation Effects in Analysis of Inorganic Specimens by TEM. In: Hren, J. et al. eds. *Introduction to Analytical Electron Microscopy*. Springer US, 1979, pp.437-480.

57. Egerton, R.F. Choice of operating voltage for a transmission electron microscope. *Ultramicroscopy.* 2014, **145**, pp.85-93.

58. Murooka, Y. and Walls, M. Beam damage in an anisotropic material (CaCO3) in STEM. *Institue of physics, conference series.* 1991, **119**, pp.121-124.

59. Hobbs, L.W. Radiation damage in electron microscopy of inorganic solids. *Ultramicroscopy.* 1978, **3**, pp.381-386.

60. Egerton, R.F. Electron energy-loss spectroscopy in the TEM. *Reports on Progress in Physics.* 2009, **72**(1).

61. Hobbs, L.W. Electron-beam sensitivity in inorganic specimens. *Ultramicroscopy.* 1987, **23**(3), pp.339-344.

62. Cazaux, J. Correlations between ionization radiation damage and charging effects in transmission electron microscopy. *Ultramicroscopy.* 1995, **60**(3), pp.411-425.

63. Itoh, N. Formation of lattice defects by ionising radiation in alkali halides. *J. Phys. Colloques.* 1976, **37**(C7), pp.C7-27-C27-37.

64. Kabler, M.N. and Williams, R.T. Vacancy-interstitial pair production via electron-hole recombination in halide crystals. *Physical Review B.* 1978, **18**(4), pp.1948-1960.

65. Egerton, R.F. *Electron Energy-Loss Spectroscopy in the Electron Microscope.* Plenum Press, 1996.

66. Egerton, R.F. Mechanisms of radiation damage in beam-sensitive specimens, for TEM accelerating voltages between 10 and 300 kV. *Microsc Res Tech.* 2012, **75**(11), pp.1550-1556.

67. Hren, J. *Introduction to Analytical Electron Microscopy.* Springer, 1979.

68. Chiu, W. and Jeng, T.W. Electron radiation sensitivity of protein crystals. *Ultramicroscopy.* 1982, **10**(1), pp.63-69.

69. Rodriguez-Navarro, C., Ruiz-Agudo, E., Luque, A., Rodriguez-Navarro, A.B. and Ortega-Huertas, M. Thermal decomposition of calcite: Mechanisms of formation and textural evolution of CaO nanocrystals. *American Mineralogist.* 2009, **94**(4), pp.578-593.

70. Egerton, R.F. Scattering delocalization and radiation damage in STEM-EELS. *Ultramicroscopy.* 2017, **180**, pp.115-124.

71. Cater, E.D. and Buseck, P.R. Mechanism of decomposition of dolomite, Ca0.5Mg0.5CO3, in the electron microscope. *Ultramicroscopy.* 1985, **18**(1), pp.241-251.

72. Egerton, R.F. Control of radiation damage in the TEM. *Ultramicroscopy.* 2013, **127**, pp.100-108.

73. Li, P. *Electron irradiation damage to organic light emitting materials*. MSc thesis, University of Alberta, 2003.

74. Holmes, J.L., Bachus, K.N. and Bloebaum, R.D. Thermal effects of the electron beam and implications of surface damage in the analysis of bone tissue. *Scanning.* 2000, **22**(4), pp.243-248.

75. Höche, T., Gerlach, J.W. and Petsch, T. Static-charging mitigation and contamination avoidance by selective carbon coating of TEM samples. *Ultramicroscopy.* 2006, **106**(11), pp.981-985.

76. Hren, J.J. Specimen contamination in analytical electron microscopy: Sources and solutions. *Ultramicroscopy.* 1978, **3**, pp.375-380.

77. Isabell, T.C. and Fischione, P.E. Applications of Plasma Cleaning for Electron Microscopy of Semiconducting Materials. *MRS Online Proceedings Library.* 1998, **523**, pp.null-null.

78. Wall, J. Contamination in the STEM at ultra high vacuum. *Scanning electron microscopy.* 1980, **1980**, pp.99-106.

79. Ramachandra, R., Demers, H. and de Jonge, N. Atomic-resolution scanning transmission electron microscopy through 50-nm-thick silicon nitride membranes. *Applied Physics Letters.* 2011, **98**(9), p.093109.

80. Börrnert, F., Fu, L., Gorantla, S., Knupfer, M., Büchner, B. and Rümmeli, M.H. Programmable Sub-nanometer Sculpting of Graphene with Electron Beams. *ACS Nano.* 2012, **6**(11), pp.10327-10334.

81. Sidorov, M. Marriage Of Focused and Broad Ion Beam: Sample Preparation Optimized for High Performance Analytical (S)TEM. *Microscopy and Microanalysis.* 2002, **8**(Supplement S02), pp.560-561.

82. Chen, C.L., Arakawa, K. and Mori, H. Effect of Pt on the electron-irradiation-induced decomposition of sapphire. *Scripta Materialia.* 2010, **63**(4), pp.355-358.

83. Ward, M.B., Kapitulčinová, D., Brown, A.P., Heard, P.J., Cherns, D., Cockell, C.S., Hallam, K.R. and Ragnarsdóttir, K.V. Investigating the role of microbes in mineral weathering: Nanometre-scale characterisation of the cell–mineral interface using FIB and TEM. *Micron.* 2013, **47**, pp.10-17.

84. Egerton, R.F., Konstantinova, T. and Zhu, Y. Analysis of Beam-Sensitive Materials

by Electrons and X-rays. In: Hawkes, P.W. ed. *Advances in Imaging and Electron Physics*. Elsevier, 2015, pp.70-80.

85. Rose, A. *Vision: Human and Electronic.* Plenum Press, 1973.

86. Rose, H. Phase Contrast in Scanning Transmission Electron Microscopy. *OPTIK.* 1974, **39**(4), pp.416-436.

87. Sader, K., Brown, A., Brydson, R. and Bleloch, A. Quantitative analysis of image contrast in phase contrast STEM for low dose imaging. *Ultramicroscopy.* 2010, **110**(10), pp.1324-1331.

88. S'ari, M., Blade, H., Brydson, R., Cosgrove, S.D., Hondow, N., Hughes, L.P. and Brown, A. Toward Developing a Predictive Approach To Assess Electron Beam Instability during Transmission Electron Microscopy of Drug Molecules. *Molecular Pharmaceutics.* 2018, **15**(11), pp.5114-5123.

89. Hoffmann, R., Wochnik, A.S., Betzler, S.B., Matich, S., Griesshaber, E., Schmahl, W.W. and Scheu, C. TEM preparation methods and influence of radiation damage on the beam sensitive CaCO3 shell of Emiliania huxleyi. *Micron.* 2014, **62**, pp.28-36.

90. Golla-Schindler, U., Benner, G., Orchowski, A. and Kaiser, U. In situ observation of electron beam-induced phase transformation of CaCO3 to CaO via ELNES at low electron beam energies. *Microsc Microanal.* 2014, **20**(3), pp.715-722.

91. Eddleston, M.D., Bithell, E.G. and Jones, W. Transmission electron microscopy of pharmaceutical materials. *Journal of Pharmaceutical Sciences.* 2010, **99**(9), pp.4072-4083.

92. Cattle, J., ari, M.S., Hondow, N., Abellán, P., Brown, A.P. and Brydson, R.M.D. Transmission electron microscopy of a model crystalline organic, theophylline. *Journal of Physics: Conference Series.* 2015, **644**(1), p.012030.

93. Burrage, B.J. and Pitkethly, D.R. Aragonite Transformations Observed in the Electron Microscope. *Physica Status Solidi (b).* 1969, **32**(1), pp.399-405.

94. Towe, K.M. Ultrastructure of calcite decomposition in vacuo. *Nature.* 1978, **274**, p.239.

95. Eddisford, P., Brown, A. and Brydson, R. Identifying and quantifying the mechanism of electron beam induced damage and recovery in hydroxyapatite. *Journal of Physics: Conference Series.* 2008, **126**(1), p.012008.

96. Martin, J., Beauparlant, M., Sauvé, S. and L'Espérance, G. On The threshold conditions for electron beam damage of asbestos amosite fibers in the transmission electron microscope (tem). *Journal of Occupational and Environmental Hygiene.* 2016, pp.1-35.

97. Walls, M. and Tence, M. EELS study of beam induced decomposition of calcite in the STEM. *IOP Conference Series EMAG89.* 1989, **98**(6), p.4.

98. Murooka, Y. and Yuan, J. Irradiation damage in an anisotropic material (calcite). *Proceedings of the 13th international congress on electron microscopy.* 1994, **1**, pp.751-752.

99. Kimoto, K. Practical aspects of monochromators developed for transmission electron microscopy. *Microscopy (Oxford, England).* 2014, **63**(5), pp.337-344.

100. Buban, J.P., Ramasse, Q., Gipson, B., Browning, N.D. and Stahlberg, H. High-resolution low-dose scanning transmission electron microscopy. *Journal of Electron Microscopy.* 2010, **59**(2), pp.103-112.

101. Stevens, A., Yang, H., Carin, L., Arslan, I. and Browning, N.D. The potential for Bayesian compressive sensing to significantly reduce electron dose in high-resolution STEM images. *Microscopy (Oxf).* 2014, **63**(1), pp.41-51.

102. Kovarik, L., Stevens, A., Liyu, A. and Browning, N.D. Implementing an accurate and rapid sparse sampling approach for low-dose atomic resolution STEM imaging. *Applied Physics Letters.* 2016, **109**(16), p.164102.

103. Jones, L., Yang, H., Pennycook, T.J., Marshall, M.S.J., Van Aert, S., Browning, N.D., Castell, M.R. and Nellist, P.D. Smart Align—a new tool for robust non-rigid registration of scanning microscope data. *Advanced Structural and Chemical Imaging.* 2015, **1**(1), p.8.

104. Jones, L., Wenner, S., Nord, M., Ninive, P.H., Løvvik, O.M., Holmestad, R. and Nellist, P.D. Optimising multi-frame ADF-STEM for high-precision atomic-resolution strain mapping. *Ultramicroscopy.* 2017, **179**, pp.57-62.

105. Egerton, R.F. Radiation damage to organic and inorganic specimens in the TEM. *Micron.* 2019, **119**, pp.72-87.

106. Freeman, H.M., Perez, J.P.H., Hondow, N., Benning, L.G. and Brown, A.P. Beam-induced oxidation of mixed-valent Fe (oxyhydr)oxides (green rust) monitored by STEM-EELS. *Micron.* 2019, **122**, pp.46-52.

107. Ilett, M., Brydson, R., Brown, A. and Hondow, N. Cryo-analytical STEM of frozen, aqueous dispersions of nanoparticles. *Micron.* 2019, **120**, pp.35-42.

108. Hondow, N., Brydson, R., Wang, P., Holton, M.D., Brown, M.R., Rees, P., Summers, H.D. and Brown, A. Quantitative characterization of nanoparticle agglomeration within biological media. *Journal of Nanoparticle Research.* 2012, **14**(7), p.977.

109. Taylor, K.A. and Glaeser, R.M. Electron Diffraction of Frozen, Hydrated Protein Crystals. *Science.* 1974, **186**(4168), pp.1036-1037.

110. Adrian, M., Dubochet, J., Lepault, J. and McDowall, A.W. Cryo-electron microscopy of viruses. *Nature.* 1984, **308**(5954), pp.32-36.

111. Bartesaghi, A., Merk, A., Banerjee, S., Matthies, D., Wu, X., Milne, J.L.S. and Subramaniam, S. 2.2 Å resolution cryo-EM structure of β-galactosidase in complex with a cell-permeant inhibitor. *Science.* 2015, **348**(6239), pp.1147-1151.

112. Mao, Y., Wang, L., Gu, C., Herschhorn, A., Désormeaux, A., Finzi, A., Xiang, S.-H. and Sodroski, J.G. Molecular architecture of the uncleaved HIV-1 envelope glycoprotein trimer. *Proceedings of the National Academy of Sciences.* 2013, **110**(30), pp.12438-12443.

113. Henderson, R. Avoiding the pitfalls of single particle cryo-electron microscopy: Einstein from noise. *Proceedings of the National Academy of Sciences.* 2013, **110**(45), pp.18037-18041.

114. Cabra, V. and Samsó, M. Do's and Don'ts of Cryo-electron Microscopy: A Primer on Sample Preparation and High Quality Data Collection for Macromolecular 3D Reconstruction. *Journal of Visualized Experiments : JoVE.* 2015, (95), p.52311.

115. Evans, J.E., Hetherington, C., Kirkland, A., Chang, L.-Y., Stahlberg, H. and Browning, N. Low-dose aberration corrected cryo-electron microscopy of organic specimens. *Ultramicroscopy.* 2008, **108**(12), pp.1636-1644.

116. S'ari, M., Cattle, J., Hondow, N., Brydson, R. and Brown, A. Low dose scanning transmission electron microscopy of organic crystals by scanning moiré fringes. *Micron.* 2019, **120**, pp.1-9.

117. Su, D. and Zhu, Y. Scanning moiré fringe imaging by scanning transmission electron microscopy. *Ultramicroscopy.* 2010, **110**(3), pp.229-233.

118. Busch, H. Berechnung der Bahn von Kathodenstrahlen im axialsymmetrischen elektromagnetischen Felde. *Annalen der Physik.* 1926, **386**(25), pp.974-993.

119. Ruska, E. The development of the electron microscope and of electron microscopy. *Reviews of Modern Physics.* 1987, **59**(3), pp.627-638.

120. Ruska, E. The emergence of the electron microscope: Connection between Realization and First Patent Application, Documents of an Invention. *Journal of Ultrastructure and Molecular Structure Research.* 1986, **95**(1–3), pp.3-28.

121. Knoll, M. and Ruska, E. Beitrag zur geometrischen Elektronenoptik. I. *Annalen der Physik.* 1932, **404**(5), pp.607-640.

122. Knoll, M. and Ruska, E. Das Elektronenmikroskop. *Zeitschrift für Physik.* 1932, **78**(5-6), pp.318-339.

123. Abbe, E. VII.—On the Estimation of Aperture in the Microscope. *Journal of the Royal Microscopical Society.* 1881, **1**(3), pp.388-423.

124. Weinberger, P. Revisiting Louis de Broglie's famous 1924 paper in the Philosophical Magazine. *Philosophical Magazine Letters.* 2006, **86**(7), pp.405-410.

125. Von Ardenne, M. *Improvements in electron microscopes* 1939.

126. Crewe, A.V., Wall, J. and Langmore, J. Visibility of Single Atoms. *Science.* 1970, **168**(3937), pp.1338-1340.

127. Isaacson, M.S. Seeing single atoms. *Ultramicroscopy.* 2012, **123**, pp.3-12.

128. Erdman, N. and Bell, D.C. Introduction to the Theory and Advantages of Low Voltage Electron Microscopy. In: Brooks, S. et al. eds. *Low Voltage Electron Microscopy*. 2012.

129. Krumeich, F. *TEM electron diffraction.* https://www.microscopy.ethz.ch/TEMED.htm: ETH Zurich, 2017.

130. Bell, D.C. and Erdman, N. *Low Voltage Electron Microscopy, Principles and Applications.* Wiley, 2013.

131. Rodenburg, J. *The Ronchigram.* [Online]. 2004. [Accessed 13/07/2018].

132. Alexander, D. *Looking Through the Fish-Eye - The Electron Ronchigram.* [Online]. 2012. [Accessed 13/07/2018].

133. Muller, D.A. and Weyland, M. Tuning the convergence angle for optimum STEM performance. *FEI Nanosolutions.* 2005, **1**, pp.24-35.

134. Williams, D. and Carter, C. *Transmission Electron Microscopy.* 2 ed. New York: Springer, 2009.

135. Mitchell, D.R.G. *Contrast Transfer Function.* [Online]. 2017. [Accessed 30/07/2018].

136. Kirkland, J. *Advanced Computing in Electron Microscopy.* Springer US, 2010.

137. Barthel, J. and Thust, A. Quantification of the Information Limit of Transmission Electron Microscopes. *Physical Review Letters.* 2008, **101**(20), p.200801.

138. Marko, M. and Rose, H. The Contributions of Otto Scherzer (1909–1982) to the Development of the Electron Microscope. *Microscopy and Microanalysis.* 2010, **16**(4), pp.366-374.

139. Lynch, K.M., Marchuk, N. and Elwin, M.L. Chapter 22 - Digital Signal Processing. In: Lynch, K.M. et al. eds. *Embedded Computing and Mechatronics with the PIC32*. Oxford: Newnes, 2016, pp.341-374.

140. Rose, H. and Kisielowski, C.F. On the Reciprocity of TEM and STEM. *Microscopy and Microanalysis.* 2005, **11**(S02), pp.2114-2115.

141. Krumeich, F., Müller, E. and Wepf, R.A. Phase-contrast imaging in aberration-corrected scanning transmission electron microscopy. *Micron.* 2013, **49**, pp.1-14.

142. Humphreys, C.J. Fundamental concepts of stem imaging. *Ultramicroscopy.* 1981, **7**(1), pp.7-12.

143. Baumann, F.H. Very low angle annular dark field imaging in the scanning transmission electron microscope: A versatile tool for micro- and nano-characterization. *Journal of Vacuum Science & Technology B.* 2012, **30**(4), p.041804.

144. Fulz, B. and Howe, J. *Transmission Electron Microscopy and Diffractometry of Materials.* 4 ed. Springer, 2013.

145. Pennycook, S.J., Jesson, D.E., McGibbon, A.J. and Nellist, P.D. High angle dark field STEM for advanced materials. *Journal of Electron Microscopy.* 1996, **45**(1), pp.36-43.

146. Bell, D. and Garratt-Reed, A. *Energy Dispersive X-ray Analysis in the Electron Microscope.* Taylor & Francis, 2003.

147. McCarthy, J., Friel, J. and Camus, P. Impact of 40 Years of Technology Advances on EDS System Performance. *Microscopy and Microanalysis.* 2009, **15**(6), pp.484-490.

148. Lechner, P., Fiorini, C., Hartmann, R., Kemmer, J., Krause, N., Leutenegger, P., Longoni, A., Soltau, H., Stötter, D., Stötter, R., Strüder, L. and Weber, U. Silicon drift detectors for high count rate X-ray spectroscopy at room temperature. *Nuclear Instruments and Methods in Physics Research Section A: Accelerators, Spectrometers, Detectors and Associated Equipment.* 2001, **458**(1), pp.281-287.

149. Metchnik, V. and Tomlin, S.G. On the Absolute Intensity of Emission of Characteristic X Radiation. *Proceedings of the Physical Society.* 1963, **81**(5), p.956.

150. Kociak, M. and Stephan, O. Mapping plasmons at the nanometer scale in an electron microscope. *Chemical Society Reviews.* 2014, **43**(11), pp.3865-3883.

151. Egerton, R.F., Yang, Y.Y. and Chen, F.Y.Y. EELS of "thick" specimens. *Ultramicroscopy.* 1991, **38**(3-4), pp.349-352.

152. Malis, T., Cheng, S.C. and Egerton, R.F. EELS log-ratio technique for specimen-thickness measurement in the TEM. *Journal of Electron Microscopy Technique.* 1988, **8**(2), pp.193-200.

153. Liao, Y. *ELNES and EXELFS.* [Online]. 2018. [Accessed 22/11].

154. Brown, A.P., Hillier, S. and Brydson, R.M.D. Quantification of Fe-oxidation state in mixed valence minerals: a geochemical application of EELS revisited. *Journal of Physics: Conference Series.* 2017, **902**, p.012016.

155. Egerton, R.F. and Malac, M. EELS in the TEM. *Journal of Electron Spectroscopy and Related Phenomena.* 2005, **143**(2-3 SPEC. ISS.), pp.43-50.

156. Murooka, Y., Walls, M. and Rodenburg, J. High Resolution Time Resolved EELS of CaCO3. *Transactions of the Royal microscopical Society.* 1990, **1**, pp.185-188.

157. Junejo, U. *Working principle of ATR spectrometer.* https://upload.wikimedia.org/wikipedia/commons/2/28/Schematic_of_ATR-FTIR_Spectrometer.png: Wikimedia Commons, 2017.

158. Rodriguez-Blanco, J.D., Shaw, S. and Benning, L.G. The kinetics and mechanisms of amorphous calcium carbonate (ACC) crystallization to calcite, via vaterite. *Nanoscale.* 2011, **3**(1), pp.265-271.

159. Bhattacharjee, S. DLS and zeta potential – What they are and what they are not? *Journal of Controlled Release.* 2016, **235**, pp.337-351.

160. Stetefeld, J., McKenna, S.A. and Patel, T.R. Dynamic light scattering: a practical guide and applications in biomedical sciences. *Biophysical reviews.* 2016, **8**(4), pp.409-427.

161. Williams, T. A Needle in the X-Ray Haystack, Detection Limits in Powder XRD of Geological Materials. In: *Geological Society of America 2007 Annual Meeting*, *Denver*. GSA, 2007.

162. Maia, L.F., Fernandes, R.F., Almeida, M.R. and de Oliveira, L.F.C. Rapid assessment of chemical compounds from Phyllogorgia dilatata using Raman spectroscopy. *Revista Brasileira de Farmacognosia.* 2015, **25**(6), pp.619-626.

163. Bowley, H., Gardiner, D., Gerrard, D., Graves, P., Louden, J. and Turrell, G. *Practical Raman Spectroscopy.* Heidelberg: Springer-Verlag, 1989.

164. Nanophoton. *Schematic of Raman Microscopy.* [Online]. 2019. [Accessed 06/05/2019].

165. Gunasekaran, S., Anbalagan, G. and Pandi, S. Raman and infrared spectra of carbonates of calcite structure. *Journal of Raman Spectroscopy.* 2006, **37**(9), pp.892-899.

166. Porto, S.P.S., Giordmaine, J.A. and Damen, T.C. Depolarization of Raman Scattering in Calcite. *Physical Review.* 1966, **147**(2), pp.608-611.

167. Carpenter, M. *Helium Atmosphere Chamber for Soft X-ray Spectroscopy of Biomolecules*. MS thesis, University of California, Davis, 2010.

168. Calvin, S. *XAFS for Everyone.* Taylor & Francis, 2013.

169. Hari, B., Ding, X., Guo, Y., Deng, Y., Wang, C., Li, M. and Wang, Z. Multigram scale synthesis and characterization of monodispersed cubic calcium carbonate nanoparticles. *Materials Letters.* 2006, **60**(12), pp.1515-1518.

170. Kitamura, M., Konno, H., Yasui, A. and Masuoka, H. Controlling factors and mechanism of reactive crystallization of calcium carbonate polymorphs from calcium hydroxide suspensions. *Journal of Crystal Growth.* 2002, **236**(1-3), pp.323-332.

171. Shivkumara, C., Singh, P., Gupta, A. and Hegde, M.S. Synthesis of vaterite CaCO3 by direct precipitation using glycine and L-alanine as directing agents. *Materials Research Bulletin.* 2006, **41**(8), pp.1455-1460.

172. Markovic, I., Ottewill, R.H., Cebula, D.J., Field, I. and Marsh, J.F. Small Angle Neutron Scattering Studies on Non-Aqueous Dispersions of Calcium Carbonate - The Guinier Approach. *Colloid and Polymer Science.* 1984, **262**(8), pp.648-656.

173. van Wijngaarden, G.D. and Brons, H.M.J. *Preparation of a Basic Salt*. Office, U.S.P. United States: Shell Oil Company. 1989. Available from: https://www.google.com.ar/patents/US4869837

174. Alcock, K. *Preparation of overbased calcium sulphonates*. Google Patents. 1984. Available from: https://www.google.com/patents/EP0121024A1?cl=en

175. Tuschel, D. Selecting an Excitation Wavelength for Raman Spectroscopy. *Spectroscopy.* 2016, **31**(3), pp.14-23.

176. Lawaetz, A.J. and Stedmon, C.A. Fluorescence intensity calibration using the Raman scatter peak of water. *Applied spectroscopy.* 2009, **63**(8), pp.936-940.

177. Rueden, C.T., Schindelin, J., Hiner, M.C., DeZonia, B.E., Walter, A.E., Arena, E.T. and Eliceiri, K.W. ImageJ2: ImageJ for the next generation of scientific image data. *BMC Bioinformatics.* 2017, **18**(1), p.529.

178. Mitchell, D.R.G. DiffTools: Electron diffraction software tools for DigitalMicrograph™. *Microsc Res Tech.* 2008, **71**(8), pp.588-593.

179. Ritchie, N.W.M. Getting Started with NIST DTSA-II. *Microscopy Today.* 2011, **19**(1), pp.26-31.

180. Bance, U.R., Drummond, I.W., Finbow, D., Harden, E.H. and Kenway, P. Hydrocarbon contamination in vacuum dependent scientific instruments. *Vacuum.* 1978, **28**(10), pp.489-496.

181. Soong, C., Hoyle, D., Malac, M. and Egerton, R. The Sources of Contamination of TEM Samples and Means for its Reduction. *Microscopy and Microanalysis.* 2012, **18**(2), pp.1480-1481.

182. *Nearest Neighbor Distances Calculator.* https://icme.hpc.msstate.edu/mediawiki/index.php/Nearest_Neighbor_Distances_Calculation_with_ImageJ, 2016.

183. Buckman, J. Use of automated image acquisition and stitching in scanning electron microscopy: Imaging of large scale areas of materials at high resolution. *Microscopy and Analysis.* 2014, **January 2014**, pp.s13-16.

184. Donnelly, F.C., Purcell-Milton, F., Framont, V., Cleary, O., Dunne, P.W. and Gun'ko, Y.K. Synthesis of CaCO3 nano- and micro-particles by dry ice carbonation. *Chemical Communications.* 2017, **53**(49), pp.6657-6660.

185. Abramoff, M., Magalhaes, P. and Ram, S. Image processing with ImageJ. *Biophotonics International.* 2004, **11**(7), pp.36-42.

186. *ImageJ.* US National Institue of Health, 1997.

187. Bergmann, R.B. and Bill, A. On the origin of logarithmic-normal distributions: An analytical derivation, and its application to nucleation and growth processes. *Journal of Crystal Growth.* 2008, **310**(13), pp.3135-3138.

188. Stenn, K. and Bahr, G.F. Specimen damage caused by the beam of the transmission electron microscope, a correlative reconsideration. *Journal of Ultrastructure Research.* 1970, **31**(5), pp.526-550.

189. Barber, D.J. and Wenk, H.R. Microstructures in carbonates from the Alnø and Fen carbonatites. *Contributions to Mineralogy and Petrology.* 1984, **88**(3), pp.233-245.

190. Rodriguez-Navarro, C., Luque, A., Ruiz-Agudo, E. and Ortega-Huertas, M. A TEM and 2D-XRD study of the thermal decomposition of Calcite. *Spanish Mineralogical Society.* 2008, **9**, pp.223-224.

191. Hooley, R.W.M., Brown, A.P., Kulak, A.N., Meldrum, F.C. and Brydson, R.M.D. A Quantitative Evaluation of Electron Beam Sensitivity in Calcite Nanoparticles. *Journal of Physics: Conference Series.* 2017, **902**(1), p.012005.

192. Brydson, R. *Aberration-Corrected Analytical Transmission Electron Microscopy.* Wiley, 2011.

193. Egerton, R.F., Wang, F. and Crozier, P.A. Beam-Induced Damage to Thin Specimens in an Intense Electron Probe. *Microscopy and Microanalysis.* 2006, **12**(01), pp.65-71.

194. Jones, L. and Downing, C. The MTF & DQE of Annular Dark Field STEM: Implications for Low-dose Imaging and Compressed Sensing. *Microscopy and Microanalysis.* 2018, **24**(S1), pp.478-479.

195. Fryer, J.R. Radiation damage in organic crystalline films. *Ultramicroscopy.* 1984, **14**(3), pp.227-236.

196. Muller, D.A. and Silcox, J. Radiation damage of Ni3Al by 100 keV electrons. *Philosophical Magazine A.* 1995, **71**(6), pp.1375-1387.

197. Fryer, J.R. and Holland, F. High Resolution Electron Microscopy of Molecular Crystals. III. Radiation Processes at Room Temperature. *Proceedings of the Royal Society of London. A. Mathematical and Physical Sciences.* 1984, **393**(1805), p.353.

198. Sagawa, R., Hashiguchi, H. and Kondo, Y. Low Dose Ptychographic STEM Observation Using Fast Pixelated Detector. *Microscopy (Oxf).* 2018, **67**(suppl_2), pp.i27-i27.

199. Yücelen, E., Lazić, I. and Bosch, E.G.T. Phase contrast scanning transmission electron microscopy imaging of light and heavy atoms at the limit of contrast and resolution. *Scientific Reports.* 2018, **8**(1), p.2676.

200. Chan, K.L.A. and Kazarian, S.G. Detection of trace materials with Fourier transform infrared spectroscopy using a multi-channel detector. *Analyst.* 2006, **131**(1), pp.126-131.

201. Leri, A.C. and Ravel, B. Sample thickness and quantitative concentration measurements in Br K-edge XANES spectroscopy of organic materials. 2014, (1600-5775 (Electronic)).

202. Buseck, P., Cowley, J. and Eyring, L.R. *High-Resolution Transmission Electron Microscopy: and Associated Techniques.* Oxford University Press, 1989.

203. Almgren, M. Mixed micelles and other structures in the solubilization of bilayer lipid membranes by surfactants. *Biochimica et Biophysica Acta (BBA) - Biomembranes.* 2000, **1508**(1), pp.146-163.

204. Comsa, G.-H. Remarks on the size distribution function of ultrafine metal particles. *J. Phys. Colloques.* 1977, **38**(C2), pp.C2-185-C182-190.

205. Radha, A.V., Forbes, T.Z., Killian, C.E., Gilbert, P.U.P.A. and Navrotsky, A. Transformation and crystallization energetics of synthetic and biogenic amorphous calcium carbonate. *Proceedings of the National Academy of Sciences of the United States of America.* 2010, **107**(38), pp.16438-16443.

206. Wang, Y., Zeng, M., Meldrum, F.C. and Christenson, H.K. Using Confinement To Study the Crystallization Pathway of Calcium Carbonate. *Crystal Growth & Design.* 2017, **17**(12), pp.6787-6792.

207. Stawski, T.M., Roncal-Herrero, T., Fernandez-Martinez, A., Matamoros-Veloza, A., Kröger, R. and Benning, L.G. “On demand” triggered crystallization of CaCO3 from solute precursor species stabilized by the water-in-oil microemulsion. *Physical Chemistry Chemical Physics.* 2018, **20**(20), pp.13825-13835.

208. Prajapati, K. and Patel, S. Micellisation of surfactants in mixed solvent of different polarity. *Archives of Applied Science Research.* 2012, **4**(1), pp.662-668.

209. Schorb, M., Haberbosch, I., Hagen, W.J.H., Schwab, Y. and Mastronarde, D.N. Software tools for automated transmission electron microscopy. *bioRxiv.* 2018, p.389502.

210. Carragher, B., Kisseberth, N., Kriegman, D., Milligan, R.A., Potter, C.S., Pulokas, J. and Reilein, A. Leginon: An Automated System for Acquisition of Images from Vitreous Ice Specimens. *Journal of Structural Biology.* 2000, **132**(1), pp.33-45.

211. M. Al Omari, I. Rashid, N. Qinna, Jaber, A. and A. Badwan. Calcium Carbonate. In: Brittain, H. ed. *Profiles of Drug Substances, Excipients and Related Methodology*. Burlington: Academic Press, 2016, pp.31-132.

212. Tavacoli, J.W., Dowding, P.J., Steytler, D.C., Barnes, D.J. and Routh, A.F. Effect of Water on Overbased Sulfonate Engine Oil Additives. *Langmuir.* 2008, **24**(8), pp.3807-3813.

213. Sun, J.-X., Hu, Z.-S. and Hsu, S.M. The Effect of Concentration, Solvent, and Temperature on Aggregation of a Commercial Calcium Sulfonate Additive as Studied by FTIR and Light Scattering Techniques. *Tribology Transactions.* 1997, **40**(4), pp.633-638.

214. Smith, A.L. *The Coblentz Society Desk Book of Infrared Spectra.* 2 ed. Kirkwood, MO: The Coblentz Society, 1982.

215. Nielsen, M.H., Li, D., Zhang, H., Aloni, S., Han, T.Y.-J., Frandsen, C., Seto, J., Banfield, J.F., Cölfen, H. and De Yoreo, J.J. Investigating Processes of Nanocrystal Formation and Transformation via Liquid Cell TEM. *Microscopy and Microanalysis.* 2014, **20**(2), pp.425-436.

216. Kim, Y.-Y., Schenk, A.S., Ihli, J., Kulak, A.N., Hetherington, N.B.J., Tang, C.C., Schmahl, W.W., Griesshaber, E., Hyett, G. and Meldrum, F.C. A critical analysis of calcium carbonate mesocrystals. *Nat Commun.* 2014, **5**.

217. Rodriguez-Navarro, C., Kudlacz, K., Cizer, O. and Ruiz-Agudo, E. Formation of amorphous calcium carbonate and its transformation into mesostructured calcite. *CrystEngComm.* 2015, **17**(1), pp.58-72.

218. Sturm, E.V. and Cölfen, H. Mesocrystals: structural and morphogenetic aspects. *Chemical Society Reviews.* 2016, **45**(21), pp.5821-5833.

219. Song, R.-Q. and Cölfen, H. Mesocrystals—Ordered Nanoparticle Superstructures. *Advanced Materials.* 2010, **22**(12), pp.1301-1330.

220. Lim, Y., Stanimirova, R., Xu, H. and Petkov, J. Sulphonated methyl ester, a promising surfactant for detergency in hard water conditions. *Household and Personal Care Today.* 2016, **11**(4), pp.47-52.

221. Jao, T.-C. and Kreuz, K.L. Characterization of Inverted Micelles of Calcium Alkarylsulfonates by Some Pyrene Fluorescence Probes. In: *Phenomena in Mixed Surfactant Systems*. American Chemical Society, 1986, pp.90-99.

222. Ahmed, J., Menaka and Ganguli, A.K. Controlled growth of nanocrystalline rods, hexagonal plates and spherical particles of the vaterite form of calcium carbonate. *CrystEngComm.* 2009, **11**(5), pp.927-932.

223. Beckmann, W. and Budde, U. PHARMACEUTICALS | Crystallization. In: Wilson, I.D. ed. *Encyclopedia of Separation Science*. Oxford: Academic Press, 2000, pp.3729-3738.

224. Gower, L.B. Biomimetic Model Systems for Investigating the Amorphous Precursor Pathway and Its Role in Biomineralization. *Chemical Reviews.* 2008, **108**(11), pp.4551-4627.

225. Kim, Y.-Y., Ganesan, K., Yang, P., Kulak, A.N., Borukhin, S., Pechook, S., Ribeiro, L., Kröger, R., Eichhorn, S.J., Armes, S.P., Pokroy, B. and Meldrum, F.C. An artificial biomineral formed by incorporation of copolymer micelles in calcite crystals. *Nature Materials.* 2011, **10**, p.890.

226. Gries, K., Kröger, R., Kübel, C., Fritz, M. and Rosenauer, A. Investigations of voids in the aragonite platelets of nacre. *Acta Biomaterialia.* 2009, **5**(8), pp.3038-3044.

227. Andreassen, J.-P., Beck, R. and Nergaard, M. Biomimetic type morphologies of calcium carbonate grown in absence of additives. *Faraday Discussions.* 2012, **159**(0), pp.247-261.

228. Gehrke, N., Cölfen, H., Pinna, N., Antonietti, M. and Nassif, N. Superstructures of Calcium Carbonate Crystals by Oriented Attachment. *Crystal Growth & Design.* 2005, **5**(4), pp.1317-1319.

229. Pouget, E.M., Bomans, P.H.H., Dey, A., Frederik, P.M., de With, G. and Sommerdijk, N.A.J.M. The Development of Morphology and Structure in Hexagonal Vaterite. *Journal of the American Chemical Society.* 2010, **132**(33), pp.11560-11565.

230. Huang, J.H., Mao, Z.F. and Luo, M.F. Effect of anionic surfactant on vaterite CaCO3. *Materials Research Bulletin.* 2007, **42**(12), pp.2184-2191.

231. Moyá, M.L., Rodríguez, A., del Mar Graciani, M. and Fernández, G. Role of the solvophobic effect on micellization. *Journal of Colloid and Interface Science.* 2007, **316**(2), pp.787-795.

232. Schuler, T. and Tremel, W. Versatile wet-chemical synthesis of non-agglomerated CaCO3 vaterite nanoparticles. *Chemical Communications.* 2011, **47**(18), pp.5208-5210.

Appendix

Pores are seen to form in image E on the following page, manifesting as bright spots around the edges of the particles. The diffraction pattern taken under the same fluence does not display crystalline calcium oxide, indicating that pore formation precedes the detection of calcium oxide in electron diffraction. Pore formation is seen around the edges of the particles, beginning in image E and continuing throughout the rest of the time resolved images. By image H, when calcium oxide is detected in the diffraction pattern, pores can be seen extensively in the BF-CTEM images, indicating significant radiolysis damage has occurred.

Time resolved diffraction patterns taken alongside the BF-CTEM images are shown in the following pages, as the specimen is irradiated it is possible to see the formation of polycrystalline calcium oxide. This manifests as diffraction rings which are indicated more clearly by black arrows in image H. These rings are subtle as there is only a limited amount of crystalline calcium oxide present, with further irradiation the radiolysis damage progresses, and the rings become more prominent as the calcite diffraction spots decay. The intensity of the diffraction spots was not measured, nor was the intensity of the diffraction rings, only the appearance of the rings was measured, this being the fluence at which the rings are considered visible and are detected as bumps in a line profile, as described in section 4.3.2.

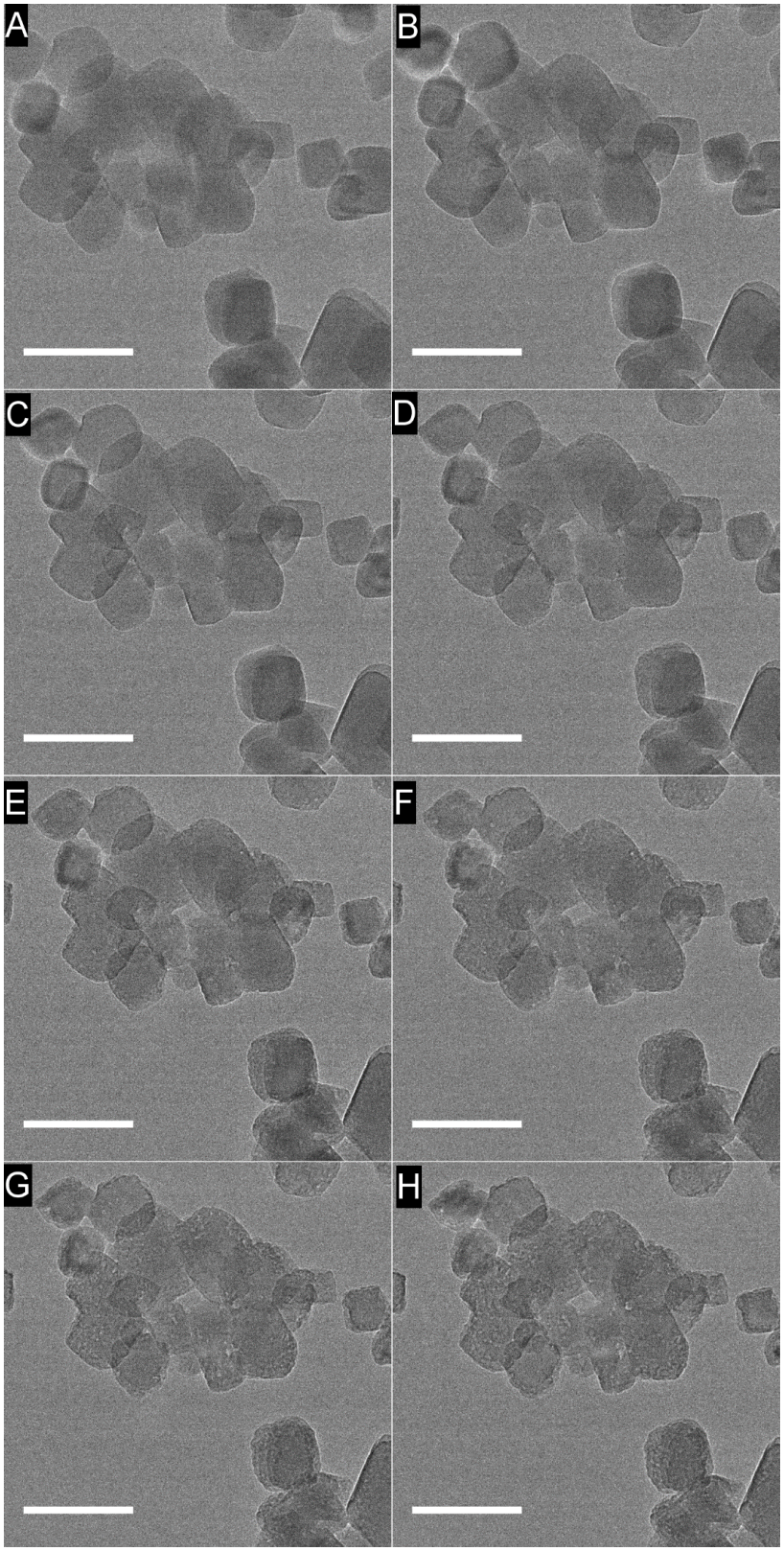

A

Fluence is nominally zero, all particles are pristine and no CaO is visible in the SAED

B

Fluence = 5.4×10^5 $e^- nm^{-2}$

C

Fluence = 1.08×10^6 $e^- nm^{-2}$

D

Fluence = 1.61×10^6 $e^- nm^{-2}$

E

Fluence = 2.2×10^6 $e^- nm^{-2}$

By this point, pores are visible around the edges of the particles, but no damage is detected in the SAED (following page)

F

Fluence = 2.7×10^6 $e^- nm^{-2}$

G

Fluence = 3.23×10^6 $e^- nm^{-2}$

H

Fluence 3.76×10^6 $e^- nm^{-2}$

CaO (111) and (200) rings are visible in SADPs

Degradation of particles under 200 kV irradiation measured by BF-CTEM imaging. Scale bar is 100nm. Fluence rate 1×10^5 $e^- nm^{-2} s^{-1}$

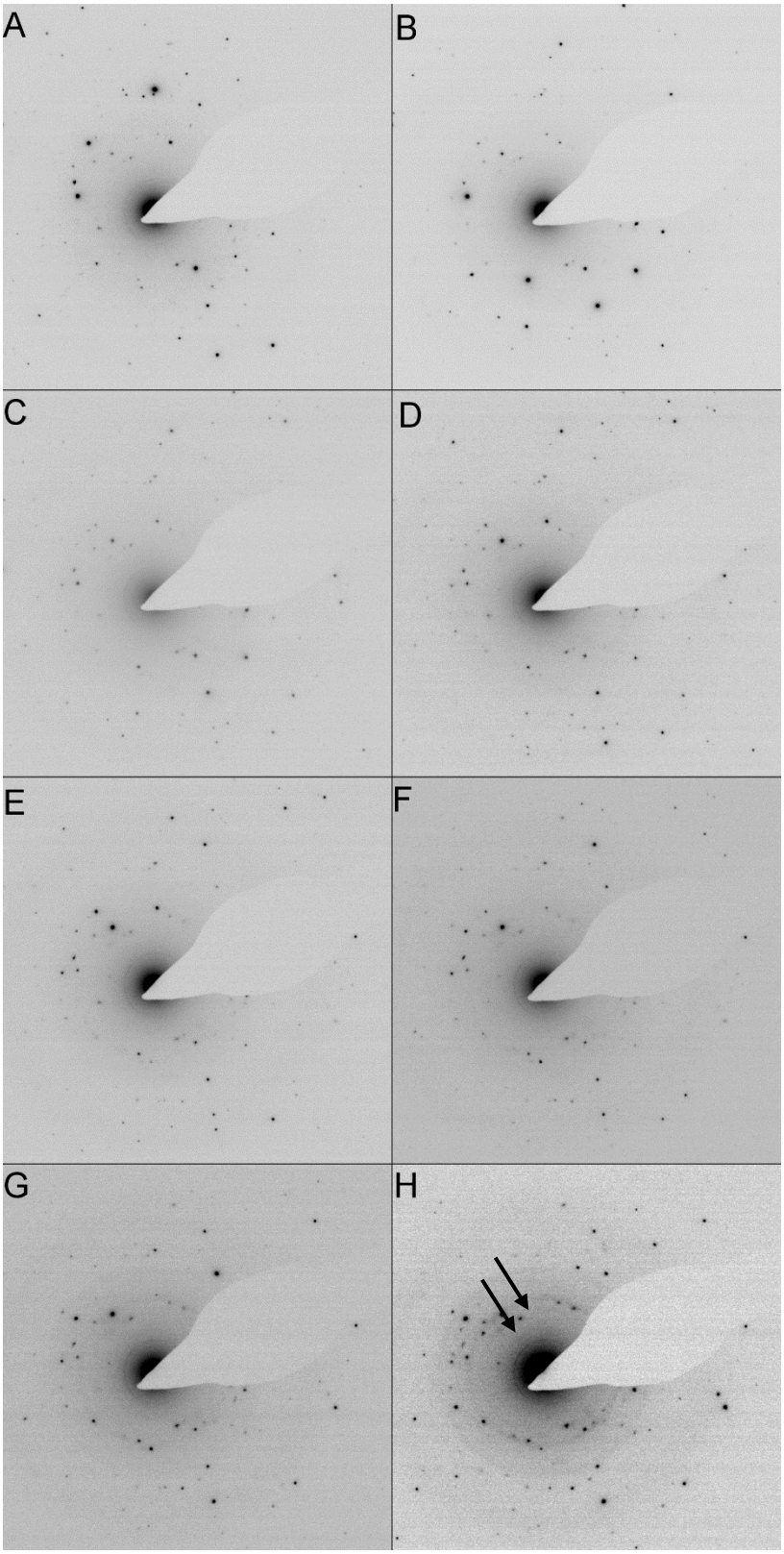

A

Fluence is nominally zero, all particles are pristine and no CaO is visible in the SAED

B

Fluence = 5.4×10^5 $e^- nm^{-2}$

C

Fluence = 1.08×10^6 $e^- nm^{-2}$

D

Fluence = 1.61×10^6 $e^- nm^{-2}$

E

Fluence = 2.2×10^6 $e^- nm^{-2}$

By this point, pores are visible around the edges of the particles but no damage is detected in the SAED

F

Fluence = $2.7 \times 10^6 e^- nm^{-2}$

G

Fluence = 3.23×10^6 $e^- nm^{-2}$

H

Fluence 3.76×10^6 $e^- nm^{-2}$

CaO (111) and (200) rings are visible, as indicated by the black arrows

Time-resolved SADPs showing the onset of calcium oxide nucleation under electron irradiation. Calcium oxide rings corresponding to the (111) and (200) planes are indicated. Fluence rate 1×10^5 $e^- nm^{-2} s^{-1}$. SADP image width is 26 1/nm.